a framework for seismic risk assessment based on artificial neural networks

Zhiyi Wang

université PARIS-SACLAY

CentraleSupélec

NNT : 2018SACLC089

A framework for seismic risk assessment based on artificial neural networks

Thèse de doctorat de l'Université Paris-Saclay
préparée à CentraleSupélec

École doctorale n°573 approches interdisciplinaires, fondements, applications et innovation (Interfaces)
Spécialité de doctorat : sciences et technologies industrielles

Thèse présentée et soutenue à Gif-sur-Yvette, le 27 novembre 2018, par

M. Zhiyi WANG

Composition du Jury :

Jean-François Semblat Professeur, ENSTA Paristech	Président
Paolo Bazzurro Professeur, IUSS Pavia	Rapporteur
Jean-Marc Bourinet Professeur associé (HDR), Sigma Clermont	Rapporteur
Michael Beer Professeur, Leibniz University Hannover	Examinateur
Fernando Lopez-Caballero Professeur associé, CentraleSupélec, Université Paris-Saclay	Examinateur
Nicola Pedroni Professeur associé (HDR), Politecnico di Torino	Co-encadrant
Irmela Zentner Ingénieure-chercheur experte, EDF R&D	Co-encadrante
Enrico Zio Professeur, CentraleSupélec, Université Paris-Saclay	Directeur de thèse

Thèse de doctorat

Acknowledgement

This Ph.D. thesis cannot be finished without the help from all the people around me. First of all, I would like to express my gratitude to Professor Enrico ZIO, for making this interesting topic possible for a Ph.D. thesis and for his supervision during these three years on this work. His scientific knowledge and expertise help build the basis and improve the quality of this thesis.

The second person who contributes a lot is Dr. Irmela ZENTNER, for her guidance all along these three years. Regular discussions with her ensure the correct direction of the thesis and guarantee the quality of the realized work. Thanks to her for accepting me as an internship student for a research internship regarding 'the spatial variability of seismic ground motions in the soil-structure interaction', which brings me into the domain of the earthquake engineering. After my two years' experience in Germany, thanks to Irmela, I am able to work in EDF for these three years on this topic.

The third person to be mentioned here is Dr. Nicola PEDRONI. His expertise in artificial neural networks enables me to discover the world of metamodels, and relevant techniques concerning the adaptive learning of metamodels. It is really a pity that he had left for Turin on the half of the thesis.

I will not forget my friends and colleagues, both from EDF and CentraleSupélec, for their continuous support, not only for the technical suggestions about the finite elements simulations with Code_Aster, programing with Python, but also for interesting discussions about the life of Ph.D. students, about the French and Chinese culture, etc.

Finally, I would like to express my sincere gratitude to my wife Yajie and my parents. Without their support and encouragements, I cannot finish that easily all these years of adventures in France and Germany. I will be very happy to be able to go back to China and stay close with you.

In Paris, 12 September, 2018,

Zhiyi

Abstract

Seismic probabilistic risk assessment (SPRA) is one of the most widely used methodologies to assess and to ensure the performance of critical infrastructures, such as nuclear power plants (NPPs), faced with earthquake events. SPRA adopts a probabilistic approach to estimate the frequency of occurrence of severe consequences of NPPs under seismic conditions. This PhD thesis is focused on the first two steps of the SPRA framework, namely seismic fragility analysis and probabilistic seismic hazard analysis (PSHA).

A comprehensive seismic fragility analysis should account for various information in the computation of fragility curves: numerical simulation results, experts judgments and post-earthquake observations. This requires a methodology not only to integrate all these information in the fragility analysis, but also to be able to reduce the computational burden of numerical simulations by finite element method. On the other hand, the computation of the ground motion prediction equations (GMPEs), which is the key element in PSHA, depends to a certain extent on the proposed functional forms. However, this can be a limitation because one cannot ensure whether the existing functional forms can be generalized for a new seismic intensity measure (IM). Considering these aspects, the application of methods based on artificial neural networks (ANNs) has been investigated in the computation of fragility curves and GMPEs in the thesis.

The thesis provides discussions on the following aspects: (i) Construction of metamodels with ANNs to build the relations between seismic IMs and engineering demand parameters of the structures, for the purpose of accelerating the fragility analysis. The uncertainty related to the substitution of FEMs models by ANNs is investigated. (ii) Proposal of a Bayesian-based framework with adaptive ANNs, to take into account different sources of information, including numerical simulation results, reference values provided in the literature and damage data obtained from post-earthquake observations, in the fragility analysis. (iii) Computation of GMPEs with ANNs. The epistemic uncertainties of the GMPE input parameters, such as the magnitude and the averaged thirty-meter shear wave velocity, are taken into account in the developed methodology. (iv) Calculation of the annual failure rate by combining results from the fragility and hazard analyses. The fragility curves are determined by the adaptive ANN, whereas the hazard curves are obtained from the GMPEs calibrated with ANNs. The proposed methodologies are applied to various industrial case studies, such as the KARISMA benchmark and the SMART model.

Résumé

L'étude probabiliste de sûreté (EPS) parasismique est l'une des méthodologies les plus utilisées pour évaluer et assurer la performance des infrastructures critiques, telles que les centrales nucléaires, sous excitations sismiques. L'EPS adopte une approche probabiliste pour estimer la fréquence d'occurrence des conséquences graves des centrales nucléaires dans les conditions sismiques. Cette thèse de doctorat porte sur les deux premières étapes de l'EPS parasismique, à savoir l'analyse de la fragilité et l'évaluation de l'aléa sismique.

Un calcul complet de courbes de fragilité doit prendre en compte des informations diverses: résultats de simulations numériques, jugements fournis par des experts et les observations post-sismiques. Cela nécessite une méthodologie non seulement pour intégrer toutes ces informations dans l'analyse de fragilité, mais aussi pour pouvoir réduire le coût de calcul de simulations numériques par la méthode des éléments finis. En outre, dans l'évaluation de l'aléa sismique, la méthode classique pour établir les lois d'atténuation, qui prédisent les mouvements sismiques au sol, dépend des formes fonctionnelles proposées. Cependant, cela peut être une limitation car il faut déterminer si les formes fonctionnelles existantes peuvent être généralisées pour une nouvelle intensité sismique. Compte tenu de ces aspects, l'application de méthodes basés sur les réseaux de neurones artificiels a été étudiée dans le calcul de courbes de la fragilité et des lois d'atténuation dans la thèse.

La thèse discute sur les aspects suivants:

(i) Construction de méta-modèles avec les réseaux de neurones pour établir les relations entre les intensités sismiques et les paramètres de demande des structures, afin d'accélérer l'analyse de fragilité. Basé sur les résultats des simulations par la méthode des éléments finis, les intensités sismiques les plus influentes sont identifiées par une procédure de sélection pilotée par des coefficients de corrélation semi-partielle. L'incertitude liée à la substitution des modèles des éléments finis par les réseaux de neurones est étudiée. Il a été découvert que l'incertitude de prédiction du réseau de neurones se compose de deux parties. La première partie est due à la simplification des excitations sismiques dans les entrées du réseau de neurones, et elle est directement intégrée dans le calcul de la probabilité de défaillance. D'autre part, la deuxième partie est l'incertitude statistique liée à la distribution des entrées (c'est-à-dire les intensités sismiques). Cette dernière incertitude statistique est utilisée pour le calcul des intervalles de confiance.

(ii) Proposition d'une méthodologie bayésienne avec réseaux de neurones adaptatifs, afin de prendre en compte les différentes sources d'information, y compris les résultats des simulations numériques, les valeurs de référence fournies dans la littérature et les évaluations

post-sismiques, dans le calcul de courbes de fragilité. Dans cette méthodologie, un réseau de neurones est entraîné de manière adaptative basé sur son incertitude de prédiction, afin de mieux sélectionner un nombre réduit de mouvements sismiques représentant l'ensemble de l'espace de signaux sismiques. Les paramètres de fragilité calculés par la simulation du réseau de neurones donnent une estimation de la capacité médiane a priori et l'incertitude aléatoire. Les données des observations post-sismiques sont utilisées pour construire la fonction de vraisemblance.

(iii) Calcul des lois d'atténuation avec les réseaux de neurones. Les incertitudes épistémiques des paramètres d'entrée de lois d'atténuation, tels que la magnitude et la vitesse moyenne des ondes de cisaillement de trente mètres, sont prises en compte dans la méthodologie développée. Un entraînement ANN basé sur les moindres carrés généralisés est proposé pour gérer les termes non diagonaux dans la maximisation de la fonction de vraisemblance. La méthode proposée est validée sur une base de données simulée et est également appliquée à la base de données RESORCE. Les résultats de l'application montrent que les écarts-types des GMPE peuvent être réduits de 4 à 16%.

(iv) Calcul du taux de défaillance annuel en combinant les résultats des analyses de fragilité et de l'aléa sismique. Les courbes de fragilité sont déterminées par le réseau de neurones adaptatif, tandis que les courbes d'aléa sont obtenues à partir des lois d'atténuation construites avec les réseaux de neurones. Les résultats de l'application montrent que, grâce à la réduction des écarts-types de la loi d'atténuation avec la modélisation de l'incertitude des entrées, un faible aléa sismique est obtenu. Ainsi, les valeurs de taux de défaillance annuels sont plus faibles pour les endommagements considérés.

Contents

List of Figures

List of Tables

Part I

Thesis

Chapter 1

Introduction

Performance-based earthquake engineering (PBEE) aims at designing and constructing civil facilities according to their performances under extreme seismic loads. Decisions of the design of such structures depend not only on the construction cost, but also on their performance related to the damage control and life safety [Ghobarah 2001]. Consistent with the principle of PBEE, seismic probabilistic risk assessment (SPRA) is one of the most widely used methodologies to assess and to ensure the performance of critical infrastructures, such as nuclear power plants (NPPs), faced with earthquake events. SPRA adopts a probabilistic approach to estimate the frequency of occurrence of severe consequences (radiological release, etc.) of NPPs under seismic conditions. In the framework of SPRA, the uncertainties from the earthquake randomness and physical variables are propagated through an engineering model, to compute the frequency of failure. The methodology of SPRA consists of the following four main steps [EPRI 1994], illustrated in Figure 1.1:

1. Probabilistic seismic hazard analysis (PSHA) which produces the hazard curves describing the annual frequency of exceeding one seismic intensity measure (IM).
2. Component fragility analysis which develops fragility curves, to estimate the conditional probability of failure of one component of the NPP at a given seismic IM.
3. System and accident-sequence analysis to evaluate the influence of the failure of one component on the key events (radiological release for example). This can be realized with the event tree and the fault tree analyses.
4. Consequence analysis combining the hazard curves and the fragility curves to compute the frequency of occurrence of the key events.

A complete SPRA covers a wide range of research areas, including (i) Seismology, which evaluates the seismicity of a region of interest; (ii) Structural analysis, which computes the response of a structure or its components under seismic loads; (iii) Uncertainty quantification, which propagates the uncertainty from earthquake excitations and material properties of the structure; (iv) Reliability and system engineering, which takes into account the interaction and interdependence between components to estimate the probability of failure of the key events. This thesis involves the first two aspects of the SPRA methodology, namely fragility analysis and PSHA, to conduct the seismic risk assessment. Methods based on artificial neural networks are employed, in order to (i) improve the computational efficiency of the

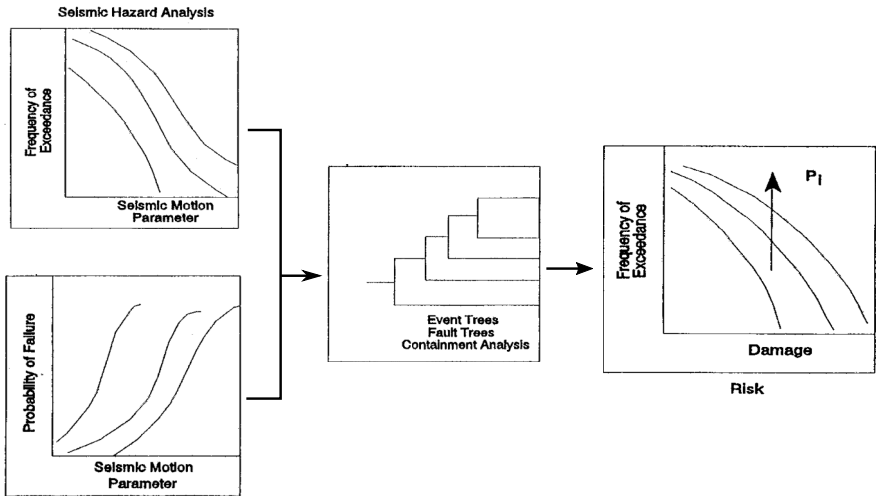

Figure 1.1: Framework of seismic probabilistic risk assessment [EPRI 1994]

simulations and (ii) to provide more flexibility of the model of the ground motion prediction equations. Bayesian updating is also combined with artificial neural networks to integrate different sources of information in fragility analysis.

Fragility Analysis

The computation of fragility curves requires realistic estimation of the structure performance subject to seismic excitations via the quantification and the propagation of uncertainties. Kennedy et al. [1980] proposed in the 1980s a systematic methodology to develop fragility curves based on safety factors. In this method, the uncertainties are divided into two categories: aleatory (or inherent) uncertainties and epistemic uncertainties. Meanwhile, a lognormal model is employed for the computation of the conditional probability of failure. The aleatory uncertainty describes the randomness of the ground motion or the material properties, whereas the epistemic uncertainty originates from the lack of knowledge and provides the confidence intervals for the fragility curves. Based on the lognormal assumption, the computation of the fragility curves is simplified to determine two parameters: the median capacity and the logarithmic standard deviation. However, one hypothesis hidden behind the product of the safety factor is that the response relations are linear [Zentner et al. 2017], which is not necessarily correct in the reality.

Numerical simulations based on finite element method (FEM) are widely used to conduct fragility analysis. A simulation-based fragility estimation procedure needs a large number of FEM simulations to evaluate the probability of failure at given values of IMs. The Monte Carlo estimation is the most fundamental simulation-based approach to evaluate the probability of failure pointwisely at given seismic intensity measures, if sufficient simulation results are available. Nevertheless, this is difficult to achieve in the reality, due to the complexity of the FEM model of the industrial facility and the associated computational burden to carry

out numerical analyses. One way to improve the computational efficiency is to construct metamodels, which can be used to replace the time-consuming FEM models. Metamodels, such as artificial neural networks, represent an ensemble of statistical algorithms which catch input-output relations of physical models, and make predictions according to these relations. With well-constructed metamodels, the computational cost of numerical simulations can be largely reduced.

Statistical analysis can be also carried out to determine the fragility parameters if real recorded data or experimental observations are provided [Straub and Kiureghian 2008; EPRI 2014]. Due to the fact that a numerical model cannot contain all the structural details and damage mechanisms, these empirical data provide additional information about the behavior of the structure and can be used for a more accurate estimation of fragility curves. Bayesian statistics are often used in fragility analysis to integrate the empirical data.

Hazard Analysis

Apart from the vulnerability of the structure assessed from the fragility analysis, the earthquake information that the structure should withstand is another indispensable element in seismic risk assessment: which level of earthquake should be used to perform the analysis for an area of interest? What is the annual occurrence of an earthquake which exceeds a certain intensity level? All these questions are answered by seismic hazard analysis.

Rather than using a deterministic worst-case earthquake which a site of interest can encounter, the probabilistic hazard analysis adopts a probability-based framework to consider all the earthquake events which may occur on this site [Baker 2008]. PSHA starts with the identification of possible earthquake sources and the characterization of the distribution of earthquake magnitude and source-to-site distance. The ground motions prediction equations (GMPEs) are later constructed to compute the IM as a function of parameters of the earthquake source, path and site conditions. The total probability theorem is finally applied to calculate the probability of exceedance of the IM with respect to fixed intensity levels.

One of the key steps of PSHA is the computation of the GMPEs. This latter task is often achieved by employing a mixed-effects model with supposed functional forms. The particular functional forms adopted in the GMPEs can be a limitation, since it is difficult to determine whether the existing forms can be generalized for a new IM. Data-driven GMPE approaches have been developed recently to overcome this difficulty [Derras et al. 2014; Hermkes et al. 2014]. In addition, the epistemic uncertainty associated to the earthquake magnitude and the site soil condition Vs_{30} is not accounted for in classical GMPE computations. Kuehn and Abrahamson [2017] show that the ignorance of such uncertainty can lead to an overestimation of the GMPE variance, and this can, thus, impact the final hazard curves. The Bayesian regression has been used by Kuehn and Abrahamson [2017] to consider the epistemic

uncertainty associated to source and site-related parameters.

Objective and Organization of the Thesis

This PhD thesis aims at using data-driven artificial neural networks in the computation of fragility curves and ground motion prediction equations. Bayesian updating is also used for the consideration of post-earthquake evaluation data in the fragility analysis. It provides discussions on the following aspects:

1. Construction of metamodels with ANNs to build the relations between seismic intensity measures and structural damage measures. The metamodels are used to replace FEM models to accelerate the fragility analysis. The uncertainty related to the substitution of FEMs models by ANNs is investigated.
2. Proposal of a Bayesian-based framework to take into account different sources of information, including numerical simulation results, reference parameter values provided in the literature and damage data obtained from post-earthquake observations, for the computation of fragility curves.
3. Computation of GMPEs with ANNs. The epistemic uncertainties of the GMPE input parameters, such as the magnitude and the averaged thirty-meter shear wave velocity, are taken into account in the developed methodology.
4. Calculation of the annual failure rate by the convolution of the fragility curves and hazard curves. The fragility curves are computed with the adaptive ANN, whereas the hazard curves are obtained from the GMPEs calibrated with ANNs.

The subjects covered by the thesis is summarized in Figure 1.2. The thesis is organized as follows: Chapter 2 presents fundamental theories of the artificial neural networks, more precisely the multi-layer perceptron, which is used as a non-linear regression tool throughout the thesis. Two other advanced ANN training techniques, namely ANN training with correlated residuals and adaptive ANN training, are also explained. These ANN training techniques will be applied in the chapters that follow.

Chapter 3 describes a methodology of simulation-based seismic fragility analysis which employs ANNs to substitute FEM simulations. This methodology starts from the selection of the most influential seismic IMs as the inputs of the ANN metamodel and ends with the investigation of the impact of ANN prediction uncertainty on the fragility curves. The fragility curves are finally computed by pointwise Monte-Carlo estimations with the fast-running ANN metamodel.

Chapter 4 gives details of the Bayesian framework which incorporates simulation results, post-earthquake observations and parameters values referred in literature in the seismic fragility analysis. The prior fragility parameters are estimated from the numerical simulation

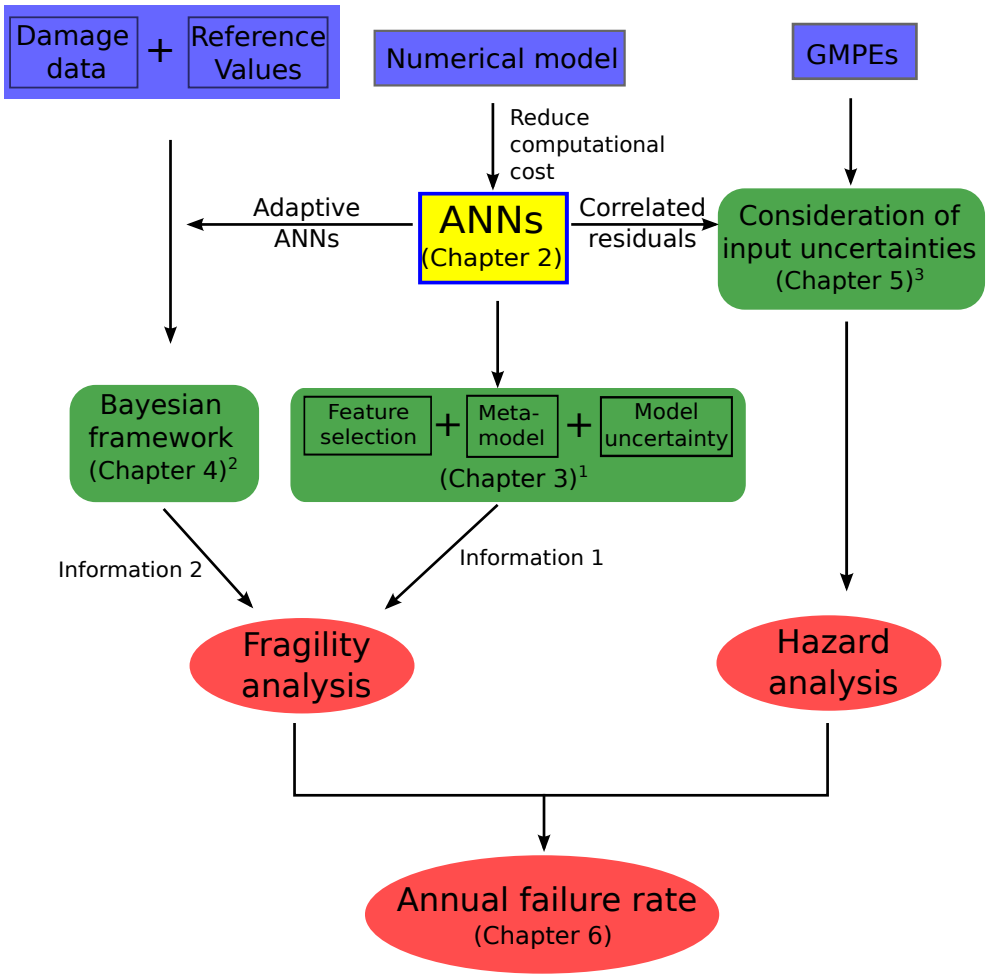

[1]The corresponding paper of Chapter 3: Wang, Z., Pedroni, N., Zentner, I. and Zio, E. (2018). Seismic fragility analysis with artificial neural networks: Application to nuclear power plant equipment. Eng. Struct., 162:213-225.

[2]The corresponding paper of Chapter 4: Wang, Z., Zentner, I. and Zio, E. (2018). A Bayesian framework for estimating fragility curves based on seismic damage data and simulations by adaptive neural networks. Nucl. Eng. Des., 338:232-246.

[3]The corresponding paper of Chapter 5: Wang, Z., Zentner, I. and Zio, E. Ground motion prediction equations by artificial neural networks with input uncertainties. (submitted)

Figure 1.2: Summary of the work accomplished in the PhD thesis

results provided by adaptive artificial neural networks, whereas the observational data are used to construct the likelihood function. The posterior distribution of the seismic capacity of the structure or equipment is obtained by applying Bayes' theorem.

Chapter 5 deals with the computation of GMPEs with ANNs by taking into consideration the epistemic uncertainties in the magnitude and Vs_{30} values provided by the earthquake database. The input epistemic uncertainty is modeled by the first order second moment

approach. This latter modeling introduces additional off-diagonal element in the variance-covariance matrix, which requires training the ANN based on generalized least-squares. The GMPEs with the consideration of the input uncertainty are computed and compared to the classical GMPEs, i.e. the GMPEs without considering the input uncertainty.

The annual failure rate is computed in Chapter 6. The fragility curves are computed with the adaptive ANN proposed in Chapter 4. The hazard curves are constructed from the GMPEs obtained in Chapter 5. After the consideration of the input uncertainties in the GMPEs, the annual failure rate is calculated and compared with the failure rate which is computed from the GMPEs without accounting for the input uncertainties.

Finally, the conclusion of the PhD thesis and the perspectives of future researches are provided in the Conclusion chapter.

Bibliography

Baker, J. W. (2008). An introduction to probabilistic seismic hazard analysis (PSHA). Technical report, Stanford University.

Derras, B., Bard, P. Y., and Cotton, F. (2014). Towards fully data driven ground-motion prediction models for Europe. *Bull. Earthquake Eng.*, 12:495–516.

EPRI (1994). Methodology for developing seismic fragilities. Technical report, Electric Power Research Institute EPRI, Palo Alto, CA. Report TR-103959.

EPRI (2014). Assessment of the use of experience data to develop seismic fragilities. Technical report, Electric Power Research Institute EPRI, Palo Alto, CA. Report 3002002933.

Ghobarah, A. (2001). Performance-based design in earthquake engineering: state of development. *Eng. Struct.*, 23:878–884.

Hermkes, M., Kuehn, N. M., and Riggelsen, C. (2014). Simultaneous quantification of epistemic and aleatory uncertainty in GMPEs using gaussian process regression. *Bull. Earthquake Eng.*, 12:449–466.

Kennedy, R., Cornell, C., Campell, R., Kaplan, S., and Perla, H. (1980). Probabilistic seismic safety study of an existing nuclear power plant. *Nucl. Eng. Des.*, 59:315–338.

Kuehn, N. M. and Abrahamson, N. A. (2017). The effect of uncertainty in predictor variables on the estimation of ground-motion prediction equations. *Bull. Seismol. Soc. Am.*, 108:358–370.

Straub, D. and Kiureghian, A. D. (2008). Improved seismic fragility modeling from empirical data. *Struct. Saf.*, 30:320–336.

Zentner, I., Gündel, M., and Bonfils, N. (2017). Fragility analysis methods: Review of existing approaches and application. *Nucl. Eng. Des.*, 323:245–258.

Chapter 2

Artificial Neural Networks

As the main statistical tool used in the thesis, the basic theory of the artificial neural networks (ANNs), in particular the multi-layer perceptron, is presented in this chapter. The backward-propagation algorithm, which is used to compute the first order derivative of the ANNs models, is briefly recalled in the first place. Furthermore, an ANN training method, based on the generalized least-squares, is explained in order to consider correlated residuals in the training process. Finally, the principle of the adaptive training of ANNs, which is largely used by other metamodels such as Kriging in reliability analysis, is described. These training methods will be used in the sequel of the thesis either in the construction of metamodels for fragility analysis, or in the computation of the ground motion prediction equations using ANNs.

Contents

2.1 A Classical ANN model: Multi-layer Perceptron

2.1.1 Overview

Inspired by biological neural networks in human brains, the artificial neural network (ANN) is one of the most widely statistical tools to perform regression and classification analyses. The mathematical model of neural networks based on threshold logic was first proposed by McCulloch and Pitts in 1943 [McCulloch and Pitts 1943; Hastie et al. 2008]. In the work of Rosenblatt [1962], the perceptron models, which are considered as the basic units of the human brain, are explained in very detail, including the basic assumptions and mathematical theories. Similar neural network models were used later as classifiers by Widrow and Hoff [1960]. Since the mid 1980s, ANNs have been largely applied as non-linear regression models, when the famous back-propagation algorithm was proposed by Rumelhart et al. [1986]. However, other models such as support vector machines gradually took the place of ANNs in machine learning due to the simplicity of the models and the efficiency to conduct statistical analyses. ANNs regained their importance in the artificial intelligence in the late 2000s because of the advent of the deep learning [LeCun et al. 2015]. They become nowadays very powerful tools with very wide applications in robotics, cognitive recognition, image identification, natural language processing, statistical classification and regression.

Basic types of neural networks are feed-forward neural networks (FNNs) and recurrent neural networks (RNNs), shown in Figure 2.1. In FNNs, the information is propagated in one direction, from the input side to the output side. Unlike FNNs, at least one feed-back connection exists in the RNN, which means that the results of the hidden layer or the output layer units are fed back into the input side for further computations, so that this structure is in particular useful to construct models for dynamic time sequences. In this thesis, we are focused on the application of multi-layer perceptrons (MLPs), the most fundamental model of FNNs, to perform non-linear regressions in seismic risk assessment.

A MLP model structure consists of multiple neural layers and connections between every two adjacent layers (Figure 2.2a). Weights and biases are associated to the connections to determine the whole MLP performance. A neural layer contains one or several neural units with their corresponding activation functions (Figure 2.2b). In general, the neural layers can be divided into 3 categories:

1. Input layer. The input layer receives the input data from the training datasets, and therefore takes the same number of neurons as the input parameters. A linear activation function is associated to the units in the input layer.

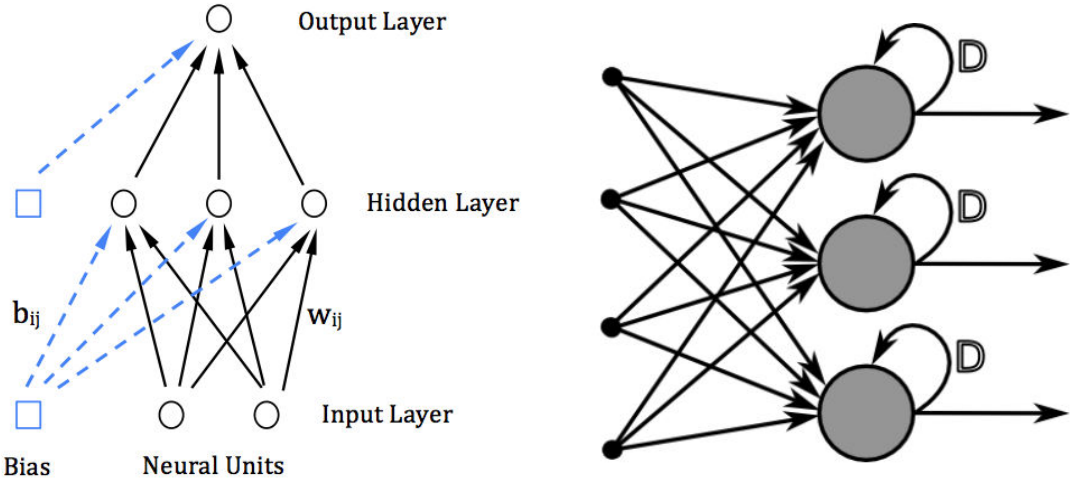

(a) Feed-forward neural network (b) Recurrent neural network

Figure 2.1: Basic artificial neural network structure

2. Output layer. The output layer returns the calculation results of the MLP model. The number of the neurons is determined by the dimension of the outputs of the datasets. Activation functions in the output layer units can be linear or sigmoid functions for regression models, and softmax functions for classification models [Reed and Marks 1998].
3. Hidden layer. The hidden layer is not necessary in the single-layer perceptron network, but should be present in the multi-layer perceptron. In most cases sigmoid functions are applied in the hidden layer units. Possible sigmoid functions are the logistic function[1] and the hyperbolic tangent function.

For the purpose of simplicity but without loss of generality, a m-input-1-output neural network model is used to illustrate the working mechanism of a neural unit (Figure 2.3). m inputs are multiplied with their respective weights before arriving at an adder. The adder transmits the sum of the inputs and the bias to the activation function: a sigmoid function. The sigmoid function can preserve the quasi-linearity when its entry remains small, and the non-linearity shows up when its input value becomes larger. Therefore, the prediction of this neural unit is calculated by

$$\hat{y_k} = \varphi(\sum_{i=1}^{m} w_{ki}x_i + b_k) = \varphi(v_k), \tag{2.1.1}$$

where w_{ki} is the corresponding weight for the input component x_i, b_k represents the bias, $v_k = \sum_{i=1}^{m} w_{ki}x_i + b_k$ denotes the weighted sum of the inputs arriving at the neuron, and $\varphi(\cdot)$

[1]Logistic function is defined as $f(x) = \dfrac{1}{1+\mathrm{e}^{-x}}$.

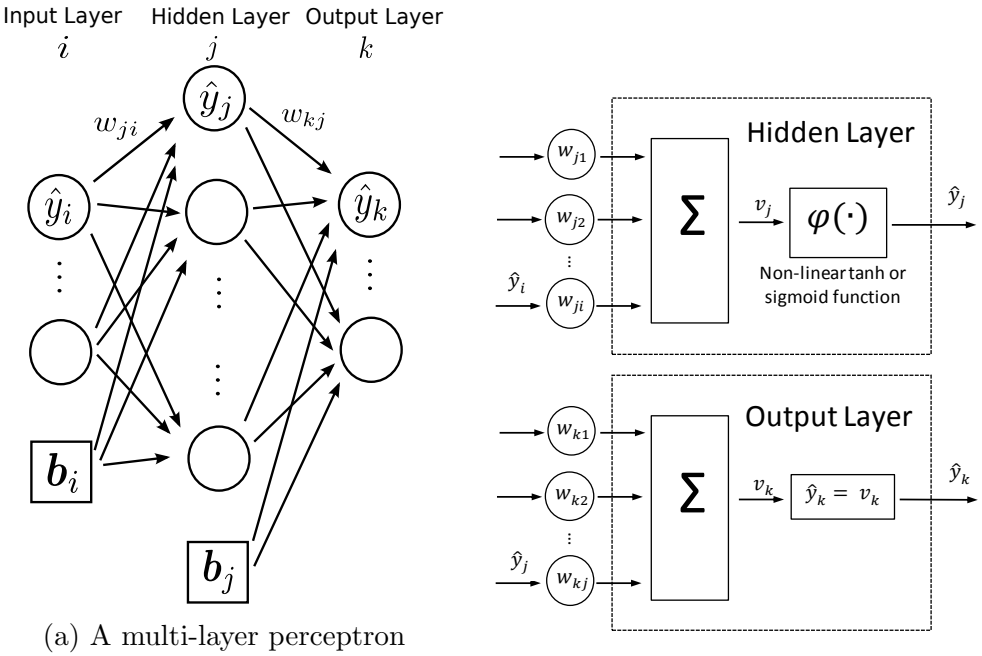

(a) A multi-layer perceptron model

(b) Activation functions

Figure 2.2: Illustration of the multi-layer perceptron

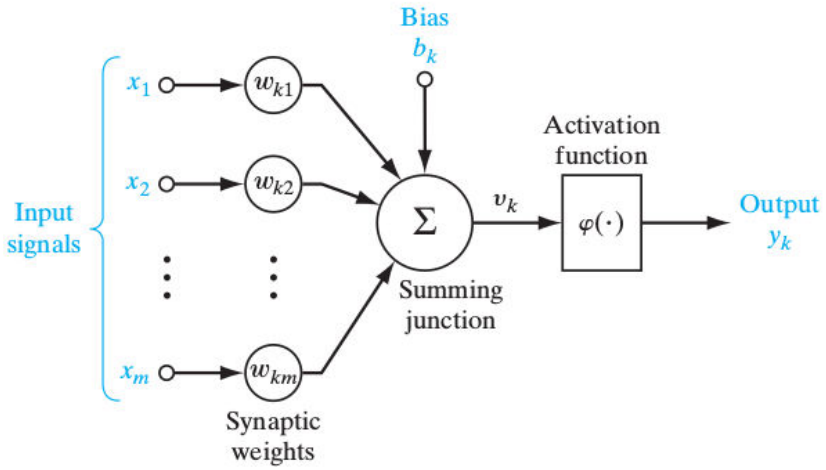

Figure 2.3: Working mechanism of a neural unit [Haykin 2008]

is the selected sigmoid function. Therefore, the output $\hat{y}_k$ of a MLP shown in Figure 2.2 is computed by

$$\begin{aligned}\hat{y}_k &= \sum_{j=1}^{q} w_{kj}\hat{y}_j + b_j \\ &= \sum_{j=1}^{q} w_{kj}(\varphi(\sum_{i=1}^{p} w_{ji}\hat{y}_i + b_i)) + b_j \\ &= \sum_{j=1}^{q} w_{kj}(\varphi(\sum_{i=1}^{p} w_{ji}x_i + b_i)) + b_j,\end{aligned} \tag{2.1.2}$$

in which p and q are the numbers of neurons in the input layer and hidden layer, respectively.

In the sequel of this thesis, the vector[2] $\underline{w}$ is used to represent all the model parameters, including weights and biases. Before training the MLP, the MLP structure should be decided first.

Concerning the MLP structure, one crucial problem is to determine the number of hidden layers and the number of neurons in every hidden layer. Without enough hidden layer elements, the MLP model cannot show sufficient non-linearity. In this case, the MLP model is underfitted and the predictions of the model cannot well approximate the statistical tendency of the data. Nevertheless, if the MLP model consists of too may neurons, it tends to be overfitted: the model prediction is accurate for the training data; However, when it is used to provide predictions for another independent dataset, its performance is very poor. It is obvious that if the weight numbers exceed the total training data size, the MLP can return exactly the target value (Figure 2.4). A MLP with appropriate hidden layer parameters is thus decisive for a correct surrogate model. This can be certainly achieved by running MLP with all the possible combinations of hidden layer counts and hidden layer size, and choose the one with the minimal error, if the computational cost is affordable. However, there still exit some conclusions which facilitate the decision of the MLP structure.

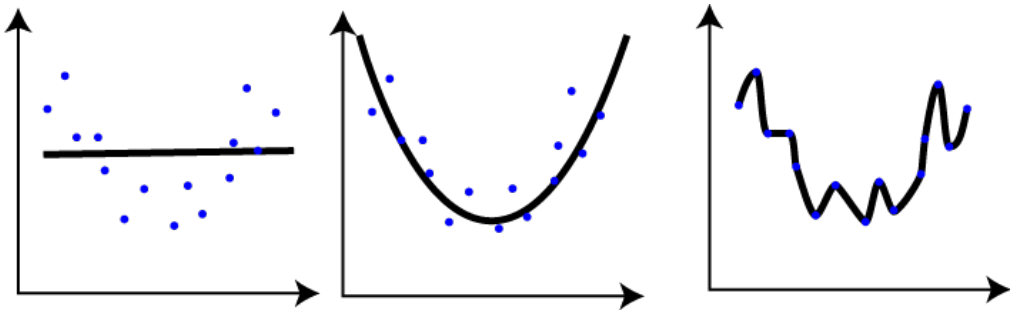

Figure 2.4: Quality of training of a MLP: underfitting (left); appropriate-fitting (center); overfitting (right)

How many hidden layers should be adopted in a MLP? Lippmann [1987]; Lapedes and Farber [1988] showed that two hidden layers are adequate to classify regions with any convex shape and to approximate any bounded continuous function. In addition, Kolmogorov's theorem states that a continuous multivariate function can be represented by a superposition of one dimensional functions of the same input variables [Kolmogorov 1957; Sprecher 1965; Cybenko 1989], which indicates that one hidden layer should be sufficient for universal approximation. However, several researchers pointed out some counterexamples where MLP with single hidden layer does not give satisfactory non-linear regression results. One can refer to Reed and Marks [1998] for these examples in detail. In spite of the existence of coun-

[2]In this thesis, we follow the French tensor notation for vectors and matrices. For example, a vector $\boldsymbol{x}$ is denoted with one underline ($\underline{x}$), whereas a matrix $\boldsymbol{x}$ is denoted with two underlines ($\underline{\underline{x}}$).

terexamples, it is recognized that single hidden layer MLP can approximate most continuous bounded functions.

How many hidden layer units should be used in a MLP model? The number of hidden layer units depend on the input and output numbers, the number of training examples and training algorithms. Compare to the number of the hidden layers, there exit less scientific proofs to provide a clear answer. Some 'rules of thumb' are provided concerning the number of hidden layer units. It is written in some literature and manual that the neuron number in the hidden layer should be between number of the input and the output, their average number for example. This statement is questionable because the size of training examples is not taken into consideration. It is well recognized that, with conventional training algorithms, the model is easy to be overfitted if the weight number is larger than the number of training cases. However, according to Weigend [1994]; Tetko et al. [1995]; Sarle [1995], in using regularization method such as the early stopping, the MLP tends to perform better with larger hidden layer units number. But still, it does not make too much sense if the number of unknown weights exceeds the size of the total training examples. For a MLP structure with one hidden layer, it is possible to make a loop of different hidden unit numbers and the best hidden number number is selected considering the prediction error on a validation dataset, which is not used to train the MLP.

2.1.2 ANN Training

The performance of the ANN[3] is evaluated by the error function, which calculates the difference between the ANN predictions and the real simulation results. The most commonly used error function in the ANN training is the sum-of-square error (SSE), which computes the sum of square of prediction errors over all the input data [Bishop 1995]. For an ANN with one single output, the SSE error writes

$$e(\underline{x};\underline{w}) = \frac{1}{2}\sum_{p=1}^{N}(\hat{y}_k(\underline{x}^p;\underline{w}) - y_k(\underline{x}^p))^2, \tag{2.1.3}$$

where $\underline{x}^p$ is the p-th input data[4], $\hat{y}_k(\underline{x}^p;\underline{w})$ is the ANN prediction, in which the symbol $\hat{}$ is used to denote all the results computed by ANNs. N is the total data size of the input datasets. $y_k(\underline{x}^p)$ is the 'real' results from observations, experiments or simulations of a physical model. It is also call 'target' in many literatures. For a n-output ANN model, the

[3]It has to be mentioned that in the next parts of the thesis, without specification, the acronym 'ANN' stands for the MLP model.

[4]In this thesis, in order to make a clear description of datasets, the upper index is used to indicate a specific data example in the datasets, whereas the lower index indicates one component, more specifically, one feature of the dataset.

SSE is calculated over all the output components (Eq.2.1.4):

$$e(\underline{x};\underline{w}) = \frac{1}{2}\sum_{p=1}^{N}\sum_{k=1}^{n}(\hat{y}_k(\underline{x}^p;\underline{w}) - y_k(\underline{x}^p))^2. \tag{2.1.4}$$

The ANN is trained in order to minimize the SSE:

$$\underline{w}^* = \arg\min_{\underline{w}}(e(\underline{x};\underline{w})). \tag{2.1.5}$$

The SSE function actually acts as an objective function from the optimization point of view. As a result, the ANN training can be regarded as solving the optimization problem (Eq.2.1.5), i.e. finding the optimal weights $\underline{w}^*$ that minimize the SSE function. Therefore, Eq.2.1.5 can be solved based on gradient-based optimization methods if the gradient vector $\underline{g} = \dfrac{\partial e(\underline{x};\underline{w})}{\partial \underline{w}}$ can be obtained. The back-propagation algorithm, proposed by Rumelhart et al. [1986], helps compute very efficiently the gradient vector $\underline{g}$.

Let us consider an ANN composed of one input layer, one hidden layer and one output layer. The configuration of this ANN is shown in Figure 2.2. The activation functions in the input layer and the output layer are linear, whereas hyperbolic tangent sigmoid functions are used in the hidden layer. The weights between the input layer i, the hidden layer j are denoted by w_{ji}, and w_{kj} are used for the weights between the hidden layer j and the output layer k. The outputs for neural nodes in the layer i, j, k are called $\hat{y}_i$, $\hat{y}_j$, $\hat{y}_k$, respectively. v_j, v_k represent the results after the adder in the hidden and the output layer (Figure 2.2b). With the inputs of the ANN, one can calculate progressively the output $\hat{y}_i$, $\hat{y}_j$ of each layer, and finally the output $\hat{y}_k$ of the network (Eq.2.1.2). This procedure is called **forward propagation**, because the calculation flow starts from the inputs and propagates towards the outputs.

As the SSE is a summation function over all the training cases, a SSE for every training case can be defined separately:

$$e(\underline{x};\underline{w}) = \sum_{p} e^p(\underline{x}^p;\underline{w}), \tag{2.1.6}$$

$$e^p(\underline{x}^p;\underline{w}) = \frac{1}{2}\sum_{k=1}^{n}(\hat{y}_k(\underline{x}^p;\underline{w}) - y_k(\underline{x}^p))^2. \tag{2.1.7}$$

In this way, the derivative of the total SSE is also the sum of the derivative of the single SSE for every training example:

$$\frac{\partial e(\underline{x};\underline{w})}{\partial \underline{w}} = \sum_{p}\frac{\partial e^p(\underline{x}^p;\underline{w})}{\partial \underline{w}}. \tag{2.1.8}$$

Let us first focus on the computation of the derivative of $e^p(\underline{x}^p; \underline{w})$ with respect to the weights $w_{\alpha\beta}$ between the layer α and the layer β [5]. In the sequel, we will substitute the notation $e^p(\underline{x}^p; \underline{w})$ by e^p for simplicity.

Let us define a new variable $\delta = \dfrac{\partial e^p}{\partial v}$ (v is the weighted sum of the neural outputs, as shown in Figure 2.2b.). According to the back-propagation algorithm, the calculation flow of δ is backwards:

$$\delta : \begin{cases} \delta_k = \hat{y}_k - y_k & \text{For } \delta \text{ of the output layer k;} \\ \delta_j = \varphi'_j \sum_k \delta_k w_{kj} & \text{For } \delta \text{ of the hidden layer j.} \end{cases} \tag{2.1.9}$$

The details of the derivation of the back-propagation algorithm are explained in the Appendix. δ is initialized in the output layer, and transmitted back towards the input layer with Eq.2.1.9 (Figure 2.5). It is the reason why this algorithm is called '**back-propagation algorithm**'. This algorithm, in particular Eq.2.1.9 is also valid for multiple hidden layers.

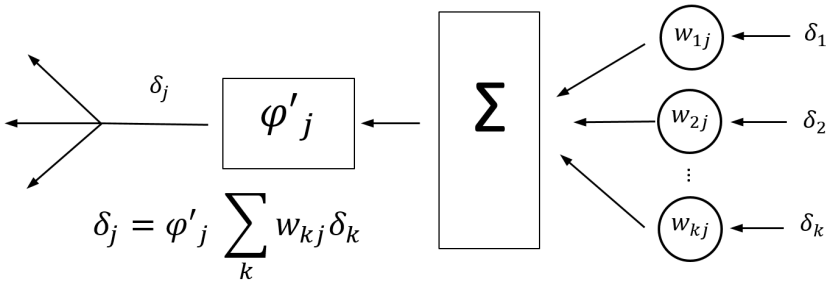

Figure 2.5: Backward propagation of δ

Then the derivative $\dfrac{\partial e^p}{\partial w_{\alpha\beta}}$ is calculated with 3 steps:

1. Apply a training case input vector $\underline{x}^p$ to the network, and propagate forward the input to get output $\hat{y}$ at neurons on every layer.
2. On the output layer, compute δ for all nodes with $\delta_k = \hat{y}_k - y_k$. And backward propagate δ according to Eq.2.1.9 from the output layer to the input layer.
3. Evaluate the derivative with the equation

$$\frac{\partial e^p}{\partial w_{\alpha\beta}} = \delta_\alpha \hat{y}_\beta. \tag{2.1.10}$$

[5] It is worth mentioning that Greek alphabets α, β are used to denote ANN weights between layer α and β in a general way: They are not restricted in the case of one-hidden-layer ANN.

In the end, the derivative for the total training dataset is computed by

$$g_{\alpha\beta} = \frac{\partial e}{\partial w_{\alpha\beta}} = \sum_p \frac{\partial e^p}{\partial w_{\alpha\beta}}. \tag{2.1.11}$$

With the computed gradient vector $\underline{g}$, all the gradient-based first order optimization methods (gradient descent, conjugated gradient descent, etc.) and second order methods (Gauss-Newton algorithm, Levenberg-Marquardt algorithm and Broyden-Fletcher-Goldfarb-Shanno algorithm, etc.) can be applied to train the ANN. These algorithms are explained in very detail in the books of Bishop [1995]; Reed and Marks [1998].

To train an ANN, the total dataset is usually divided into two parts: a training dataset and a test dataset. The ANN training is performed on the training dataset. Then, the trained ANN is validated on the test dataset to check its capability of generalization. In order to prevent overfitting, a commonly used strategy is to split again a validation dataset from the initial training dataset. The ANN training is performed on the reduced training dataset. During the ANN training, the performance and the error of the ANN are checked on the validation set. The training of the ANN is stopped when the error of the validation dataset reaches its minimum. This strategy is called **early stopping**. After applying the early stopping strategy, the trained ANN is still needed to be tested on the test dataset.

2.1.3 Prediction Uncertainty

Like any regression model, there exist uncertainties associated to the predictions provided by ANN models. One possibility to compute these prediction intervals (PIs) is to use bootstrap [Efron 1982; Zio 2006]. Bootstrap is a method introduced by B. Efron to estimate the property (mean, variance, etc.) of one statistic estimator if its probability distribution is unknown. This method consists in running a series of simulations with data resampled from the input space with replacement (so the same data patterns may appear several times in the inputs) and estimating the statistical characteristics from the simulation results. This method is the easiest way to evaluate the ANN PIs, but not the most efficient way.

Another approximate approach is the **delta method**, which is more efficient and can give satisfactory estimations of the PIs. Assuming a normal distribution of the ANN training error, this method relies on the linear Taylor expansion of the ANN model and estimates the PIs of the corresponding linear model [Chryssoloiuris et al. 1996; Rivals and Personnaz 2000; Dybowski and Gant 2001; Hui 2011]. In this way, the Hessian matrix of the ANN is approximated by the product of the Jacobian matrices.

Mathematically, the PIs are computed with the standard deviations (Stds) of the ANN training error σ_{ANN} and the gradient vector $\underline{h}_{k'} = \dfrac{\partial \hat{y}_{k'}}{\partial \underline{w}}$, where the index k' stands for the k'th ANN output, as defined in Eq.2.1.4. The computation of $\underline{h}^i_{k'}$ for the ith training example

can also be achieved with the backward-propagation algorithm:

$$\begin{aligned} &\tilde{\delta}^i_{k',k} = \delta^{\text{Kron}}_{kk'} && \text{For } \tilde{\delta} \text{ of the output layer k;} \\ &\tilde{\delta}^i_{k',j} = \varphi'_j \textstyle\sum_k [\tilde{\delta}_{k',k} \cdot w_{kj}] && \text{For } \tilde{\delta} \text{ of the hidden layer j;} \\ &h^i_{k',\alpha\beta} = \tilde{\delta}^i_{k',\alpha} \cdot \hat{y}^i_\beta, \end{aligned} \tag{2.1.12}$$

where $\delta^{\text{Kron}}_{kk'}$ represents the Kronecker delta applied to k and k', namely it equals to 0 when $k \neq k'$ and its value is 1 if $k = k'$. In the case that the ANN has only one single output, the computation of $\underline{h}$ can be simplified as:

$$\underline{h}^i = \frac{\partial \hat{y}^i}{\partial \underline{w}} = \frac{\partial \hat{y}^i}{\partial E(\underline{x};\underline{w})} \frac{\partial E(\underline{x};\underline{w})}{\partial \underline{w}} = \frac{\underline{g}}{\hat{y}^i - y^i}. \tag{2.1.13}$$

The Jacobian matrix $\underline{\underline{J}}$ of the ANN training data is, hence, constructed as

$$\underline{\underline{J}} = \begin{bmatrix} \underline{h}^1 & \underline{h}^2 & \cdots & \underline{h}^i & \cdots & \underline{h}^N \end{bmatrix}^T, \tag{2.1.14}$$

where $\underline{\underline{J}}$ is a $N \times Q$ matrix, with N the number of the ANN training examples and Q the number of the weighting parameters in the ANN, and ^{T} is used to denote matrix transpose. Consequently, the prediction uncertainties of ANNs are calculated as

$$s^2 = \sigma^2_{\text{ANN}} + \sigma^2_{\text{ANN}} \underline{h}^T_{\text{test}} (\underline{\underline{J}}^T \underline{\underline{J}})^{-1} \underline{h}_{\text{test}}, \tag{2.1.15}$$

where s denotes the Std of the ANN predictions. Hence, the $100(1-\gamma)\%$ PIs are $\hat{y} \pm s q_{\gamma/2,N-Q}$, in which $q_{\gamma/2,N-Q}$ denotes the $(1-\gamma/2)$ quantile for a student distribution with $N-Q$ degrees of freedom.

The computation of PIs based on the delta method is tested on the following case: a random noise with distribution $\mathcal{N}(0,\sigma^2)$ is add to a sine function $\sin(x)$, so that

$$y(x) = \sin(x) + \varepsilon, \quad \text{with} \quad \varepsilon \sim \mathcal{N}(0,\sigma^2). \tag{2.1.16}$$

An ANN model with one hidden layer and four hidden layer neural units is used to calibrate the sine model. Datasets are generated with $\sigma = 0.1$, with x evenly distributed on the interval $[0, 2\pi]$. Eighty generated (x, y) pairs (Figure 2.6a) are used to train the ANN, and another 100 datasets are used for the test and the prediction. The prediction intervals are computed with the delta method. The results of the regression and the prediction intervals are shown in Figure 2.6b.

From Figure 2.6b it can be observed that the regression model calibrated by the ANN is satisfactory: the ANN returns a regression model which follows well the sine function. The

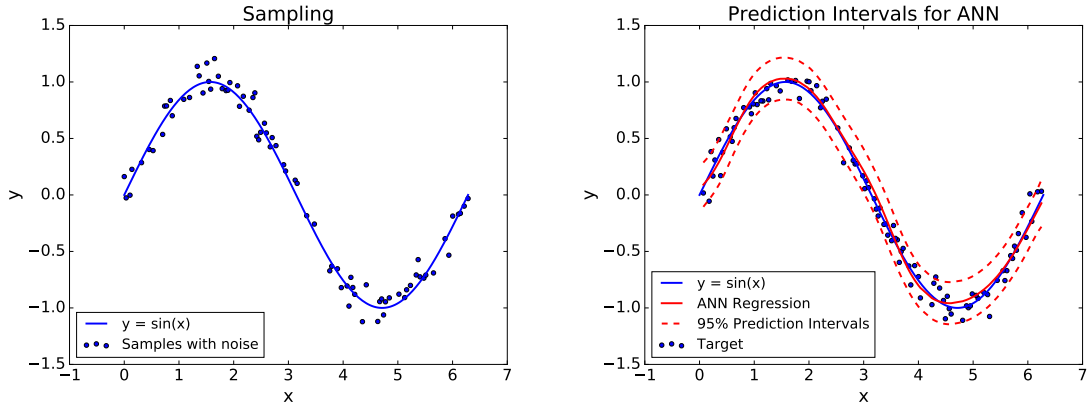

(a) Sampling of $y = \sin(x) + \varepsilon$, with $\sigma = 0.1$ (b) Prediction intervals

Figure 2.6: An illustrative example for the estimation of ANN PIs with the delta method

calculated prediction intervals are also credible: Among 100 test datasets, 95 data are located within the 95% prediction intervals, and 5 points are outside. This is reasonable because for a 95% prediction interval, one prediction has 5% probability to be dropped outside the interval. Therefore for 100 data, 5 points in average can be located outside. The concept of the prediction intervals will be used later in the adaptive learning of an ANN metamodel.

2.2 Training of ANNs with Correlated Residuals

An assumption hidden behind the cost function of Eq.2.1.4 for the classical ANN training is that the residuals $\hat{y}^i - y^i$ are statistically independent and identically distributed (IID). In case that the residuals are correlated, this correlation should be accounted for in the cost function of the ANN training. This section is dedicated to introduce a training method to take into consideration the correlation between the residuals. The method will be eventually used in the computation of the ground motion prediction equations, in which the variance-covariance matrix of the residuals is not diagonal. The covariance matrix is assumed **known** a priori in this section.

The cost function $\tilde{e}$ of the ANN with the correlated residuals reads as follows:

$$\tilde{e}(\underline{x};\underline{w}) = \frac{1}{2}\sum_{k=1}^{n}\left[\underline{\hat{y}}_k(\underline{x};\underline{w}) - \underline{y}_k(\underline{x})\right]^T\left[\underline{\underline{C}}_k^{-1}\right]\left[\underline{\hat{y}}_k(\underline{x};\underline{w}) - \underline{y}_k(\underline{x})\right]. \tag{2.2.1}$$

Different from Eq.2.1.4, the outputs and the targets of the ANN training are denoted in the vector forms $\underline{\hat{y}}$ and $\underline{y}$, respectively. $\underline{\underline{C}}_k$ is the known variance-covariance matrix of the residuals for the kth output. In the traditional ANN training, $\underline{\underline{C}}_k = \underline{\underline{I}}_N$, in which $\underline{\underline{I}}_N$ is the identity matrix of size $N \times N$. Therefore, the training of the ANN is to find the weighting

parameters that minimize the modified cost function:

$$\underline{w}^* = \arg\min_{\underline{w}} \frac{1}{2} \sum_{k=1}^{n} \left[\hat{\underline{y}}_k(\underline{x};\underline{w}) - \underline{y}_k(\underline{x})\right]^T \left[\underline{\underline{C}}_k^{-1}\right] \left[\hat{\underline{y}}_k(\underline{x};\underline{w}) - \underline{y}_k(\underline{x})\right]. \tag{2.2.2}$$

In statistics, Eq.2.2.2 is a typical cost function of a generalized least-squares (GLS) problem.

The minimization of Eq.2.2.2 can be achieved by simply applying $\frac{\partial \tilde{e}}{\partial \underline{w}} = 0$:

$$\frac{\partial \tilde{e}}{\partial \underline{w}} = 0 \Rightarrow \sum_{k=1}^{n} \left[\frac{\partial \hat{\underline{y}}_k}{\partial \underline{w}}\right]^T \left[\underline{\underline{C}}_k^{-1}\right] \left[\hat{\underline{y}}_k(\underline{x};\underline{w}) - \underline{y}_k(\underline{x})\right] = \underline{0}. \tag{2.2.3}$$

Recalling that the ANN prediction $\hat{\underline{y}}_k$ is nonlinear with respect to $\underline{w}$, computing the zero roots of Eq.2.2.3 requires employing the iterative Newton-Raphson method. By linearizing the ANN output at the $(j+1)$th iteration: $\hat{\underline{y}}_k(\underline{x};\underline{w}^{j+1}) = \hat{\underline{y}}_k(\underline{x};\underline{w}^j) + [\frac{\partial \hat{\underline{y}}_k}{\partial \underline{w}}|_{\underline{w}^j}](\underline{w}^{j+1} - \underline{w}^j)$ and omitting high order terms, Eq.2.2.3 becomes:

$$\sum_{k=1}^{n} \left[\underline{\underline{J}}_k^j\right]^T \left[\underline{\underline{C}}_k^{-1}\right] \left[\underline{\underline{J}}_k^j \Delta \underline{w}^j - \underline{r}_k^j\right] = \underline{0}, \tag{2.2.4}$$

in which the Jacobian matrix defined in Eq.2.1.13 is reused to denote the derivatives, $\Delta \underline{w}^j = \underline{w}^{j+1} - \underline{w}^j$, and the residual vector $\underline{r}_k^j$ is calculated by $\underline{r}_k^j = \underline{y}_k - \hat{\underline{y}}_k(\underline{w}^j)$. In this way, the updating of the weighting parameters $\Delta \underline{w}^j$ at the iteration j is computed by

$$\Delta \underline{w}^j = \left[\sum_{k=1}^{n} [\underline{\underline{J}}_k^j]^T [\underline{\underline{C}}_k^{-1}] [\underline{\underline{J}}_k^j]\right]^{-1} \left[\sum_{k=1}^{n} [\underline{\underline{J}}_k^j]^T [\underline{\underline{C}}_k^{-1}] [\underline{r}_k^j]\right]. \tag{2.2.5}$$

Eq.2.2.5 is the Gauss-Newton optimization algorithm applied to a GLS problem. An additional damping parameter λ, as used in the Levenberg–Marquardt algorithm, is added in Eq.2.2.5 to stabilize the numerical optimization:

$$\Delta \underline{w}^j = \left[\sum_{k=1}^{n} [\underline{\underline{J}}_k^j]^T [\underline{\underline{C}}_k^{-1}] [\underline{\underline{J}}_k^j] + \lambda \underline{\underline{I}}_Q\right]^{-1} \left[\sum_{k=1}^{n} [\underline{\underline{J}}_k^j]^T [\underline{\underline{C}}_k^{-1}] [\underline{r}_k^j]\right]. \tag{2.2.6}$$

Eq.2.2.6 approaches the classical gradient descent for $\lambda \to +\infty$ [Marquardt 1963]. The value of λ can either be set to a fixed value, or be varied for different iterations according to the proposal of Marquardt [1963].

The proposed algorithm is validated with two simple test cases. The dataset used is a generated database for the peak ground accelerations (PGAs). The dataset consists of 893

sets of PGA values, as well as the information on the source, path and site of the corresponding 893 earthquakes, with the moment magnitude M_w, Joyner-Boore distance R_{jb} and the first thirty shear-wave velocity Vs_{30}[6]. Therefore, the ANN used for this dataset is constructed with three input neurons and one output neuron.

In the first test case, the identity matrix $\underline{\underline{I}}$ is assigned to $\underline{\underline{C}}$. Then, the training of the corresponding ANN is the same as a classical neural network. The evolution of the cost function with the proposed algorithm (Eq.2.2.6) is compared to that of the Broyden-Fletcher-Goldfarb-Shanno (BFGS) algorithm, which is a commonly used ANN training algorithm. Five neural nodes are used in the hidden layer of the ANN. The comparison is illustrated in Figure 2.7. It can be observed that the minimum value of the cost function (the mean square error) computed by the proposed GLS ANN algorithm is almost the same as that calculated by BFGS.

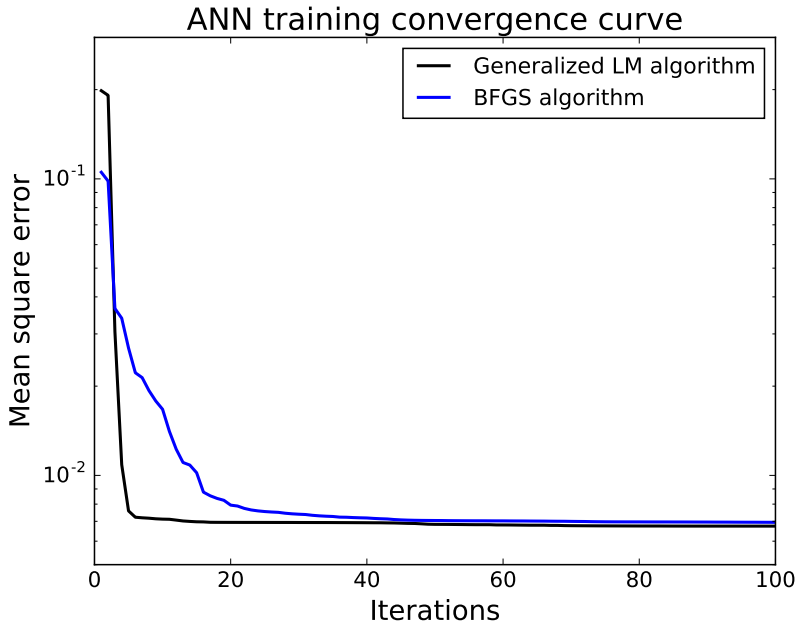

Figure 2.7: Test case one: Comparison of the performance of the proposed algorithm (generalized LM algorithm as legend) with BFGS

The second test case consists in training an ANN with a pre-assumed variance-covariance matrix. A simple structure of the ANN is selected, so that we can write the analytical expression of the ANN prediction and use an existing python package 'Scipy.optimize' (option BFGS) to perform the numerical minimization. The values of the weights and biases computed from the GLS ANN training algorithm are compared to the results from Scipy. The dataset used to train the ANN stays the same as the first case study. The matrix $\underline{\underline{C}}$ is constructed following the procedure of the construction of the variance-covariance matrix in

[6]The dataset is in fact the first realization in the generated database, which is explained in detail in Chapter 5. One can refer to Chapter 5 for more descriptions about the data.

the ground motion prediction equations, with $\tau = 0.2$ and $\phi = 0.3$. More details regarding the construction of such matrix can be found in Chapter 5. The number of the hidden layer neurons are chosen to be two. Therefore, the analytical expression of the ANN prediction writes[7]:

$$\begin{aligned}\hat{y} =& w_{11}^2 * \tanh(w_{11}^1 * M_w + w_{12}^1 * \ln R_{jb} + w_{13}^1 * \ln Vs_{30} + b_1^1) + \\ & w_{12}^2 * \tanh(w_{21}^1 * M_w + w_{22}^1 * \ln R_{jb} + w_{23}^1 * \ln Vs_{30} + b_2^1) + b_1^2.\end{aligned} \tag{2.2.7}$$

The result of the comparison is reported in Table 2.1. It can be concluded that the ANN parameters computed with the proposed GLS ANN training algorithm are almost the same as those computed by Scipy. The accuracy of the GLS ANN training algorithm is thus validated.

Table 2.1: Test case two: Comparison of the proposed GLS ANN training results to results computed by Scipy optimization tool.

	b_1^1	b_2^1	w_{11}^1	w_{12}^1	w_{13}^1	w_{21}^1	w_{22}^1	w_{23}^1	b_1^2	w_{11}^2	w_{12}^2
ANN	2.138	0.646	-0.23	3.542	-1.394	0.313	-0.427	-0.081	-1.173	0.173	2.501
Scipy	2.138	0.646	-0.23	3.539	-1.392	0.313	-0.427	-0.081	-1.175	0.173	2.503

2.3 Adaptive Training of ANNs

2.3.1 State of the Art

Besides the classical training algorithms, adaptive training techniques of statistical metamodels have been developed recently. The main idea is to build metamodels iteratively by adding in the training dataset the samples selected by a learning function (e.g. with metamodel prediction closest to the failure threshold). The iterative training is stopped until the required accuracy is reached. The enrichment of the design of experiments (DoE) can be achieved by a crude selection of candidates in the initial Monte-Carlo (MC) population according to the learning function. Such enrichment strategy has been applied in AK-MCS (Active Kriging - MC Simulation) [Echard et al. 2011; Zheng et al. 2017], adaptive support vector machine (ASVM) [Pan and Dias 2017], adaptive polynomial chaos expansion (APCE) [Marelli and Sudret 2018], etc. However, this strategy depends to a certain extent on the initial MC population: the estimated quantity of interest can be biased if the initial population does not cover the area of interest. An alternative is to enrich the training data with advanced sampling techniques. Additional training points are selected from the population generated from importance sampling (IS), Markov chain Monte-Carlo (MCMC) or directional simulation (DS) to better cover the region of interest. Typical works on the adaptive metamodeling

[7]The ANN inputs M_w, $\ln R_{jb}$ and $\ln Vs_{30}$ in Eq.2.2.7 are pre-processed in projecting them into $[-1, 1]^3$ space.

based on advanced sampling techniques are CQ2RS for polynomial response surfaces [Gayton et al. 2003]; ^{2}SMART [Bourinet et al. 2011], ASVR (Adaptive Support Vector Regression) [Bourinet 2016] and other adaptive models based on SVM (Support Vector Machine) classification and regression [Hurtado 2001; Bourinet 2013]; Meta-IS [Dubourg et al. 2013; Cadini et al. 2015], AK-IS [Echard et al. 2013], MetaAK-IS^2 [Cadini et al. 2014] for Kriging, etc.

A few works have also been realized to combine the adaptive learning with ANNs. Orthogonal factorial designs are proposed by Shao and Murotsu [1997] to select learning data of ANNs. However, a minimum distance between data has to be set in this method to prevent the local concentration of the selected points. This critical distance varies from case to case, and it is difficult in general to estimate this distance when the performance function is a black box. The performance of ANNs combined with DS is investigated in more detail in Hurtado and Alvarez [2001]. Both DS and IS are adopted in Schueremans and Gemert [2005] to adaptively select training data. The difference of the radius between the ANN and the limit state function is used in Schueremans and Gemert [2005] as a criterion to enrich the DoE. Also based on DS, the learning function in Most and Bucher [2006] is the uncertainty of the radius calculated by the ANNs trained repeatedly with the same training data. This idea is in fact similar to the Bootstrap method but without the resampling of the training data. The performance of adaptive ANNs trained based on IS is compared to MC-IS estimation in Chojaczyk et al. [2015] to show its accuracy and computational efficiency. The application of the subset simulation to the ANN adaptive learning is proposed in Papadopoulos et al. [2012] and later further studied in Pedroni and Zio [2017] with IS to find the optimal instrumental probability density distribution. Xiao et al. have proposed an ANN adaptive training strategy where the uncertainties of the ANN predictions with the Jackknifing resampling [Xiao et al. 2018]. The learning function in this work is a combination of ANN prediction uncertainties and a distance metric.

Despite these works, it seems that ANN adaptive learning is less used in practice compared to Kriging and SVM. The reason stems from two aspects: (i) The uncertainty on the ANN prediction is not straightforwardly provided, unlike Kriging and SVM. The prediction uncertainty is directly given in the outputs of Kriging, and the most probable misclassified point can be also easily identified in the SVM margin. Bootstrap [Efron 1982], as adopted in APCE, is a universal approach to evaluate the prediction uncertainty. However, Bootstrap requires a number of retrainings of the metamodel and can be, thus, computationally demanding; (ii) In order to avoid overfitting, the number of training data should exceed the number of unknown weighting parameters in the ANN. This makes ANNs less attractive because the size of the initial population in the ANN adaptive training could be large, especially for high dimensional inputs.

2.3.2 ANN Adaptive Training Strategy

The basic idea of the adaptive ANNs is the same as the adaptive strategies used in Kriging, SVM and PCE. It aims to ensure the performance of the ANNs in the area of interest, for example in the proximity of the failure threshold or in the region where the original ANN shows poor performance, rather than to train the ANN with every sampling in the initial MC population, which is not necessary and computationally costly. ANNs are trained iteratively in the adaptive training strategy. The training dataset is enriched in every iteration by a **learning function** U, i.e. a selection criterion, so that more and more data in the area of interest are selected. The principle of the adaptive ANN, shown in Figure 2.8, is described in what follows:

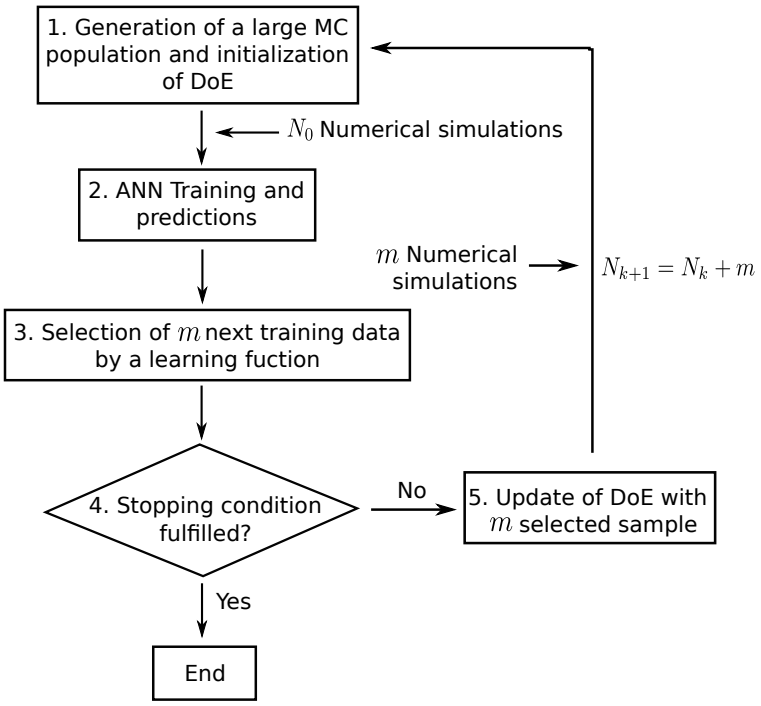

Figure 2.8: Basic principle of the adaptive ANN training

1. *Generation of a large MC population and initialization of the DoE.* A large size of input samples of the ANN should be generated to provide candidates to be selected by the adaptive learning. The size of the MC population is denoted by N_{MC}. Moreover, an initial DoE is required to perform the first training of the ANN. Among N_{MC} inputs, N_0 sets of inputs are randomly selected to call the physical computational model. N_0 should be larger than the number of the unknown parameters (weights and biases) of the ANN. This forms the first DoE to train the ANN.

2. *Start of the iterative ANN training.* For iteration k ($k \geqslant 0$), ANN is trained with the training data of the DoE. The ANN predictions $\hat{y}_k(\underline{x}^i)$ can be computed. The values of the learning function can also be calculated for every input data $\underline{x}^i$ in the total MC population,

with respect to the ANN trained at the current iteration.

3. *Selection of next m training samples with the learning function.* The learning function U helps select the m next samples. These samples are added in the training dataset and they will be used to train the ANN in the next training iteration. An example of the typical learning functions is the U function of AK-MCS proposed by Echard et al. [2011] for applications of structural reliability problems.

4. *Stopping condition verification.* A **stopping condition** should be set to check the accuracy of the ANN. The iterative training is stopped if the stopping condition is fulfilled.

5. *Update of DoE with m selected best points.* If the stopping condition in step 4 is not fulfilled, the DoE is enriched with the m best points selected in step 3. Then, m numerical simulations of the physical computational model are performed, and the results are added to train the ANN. After the DoE update, the total number of the available data to train the ANN at the iteration $k+1$ is: $N_{k+1} = N_k + m$.

2.3.3 Application Examples

In this subsection, the ANN adaptive training is applied to three reliability problems with a proposed learning function. These three examples are selected from Echard et al. [2011]; Pan and Dias [2017] involving nonlinear performance functions and high dimensional problems. In reliability analysis, the probability of failure of a system is evaluated based on a function G representing the system performance, considering a vector of uncertain input variables $\underline{x}$. The state of the system is characterized by the sign of the performance function $G(\underline{x})$: A failure is indicated by a negative value. In this way, the probability of failure of the system is computed as

$$P_f = \int \mathbf{1}[G(\underline{x}) < 0] f_{\underline{X}}(\underline{x}) \mathrm{d}\underline{x}, \tag{2.3.1}$$

where $f_{\underline{X}}(\underline{x})$ is the joint probability density function (PDF) of $\underline{x}$ and $\mathbf{1}[G(\underline{x}) < 0]$ is the indicator function. Therefore, the limit state of the system is described by the surface $G(\underline{x}) = 0$. Monte Carlo (MC) simulation is one of the most widely applied numerical resolutions to estimate P_f. The probability of failure is calculated by the proportion of the failure counts in the total number of MC simulations N:

$$\hat{P}_f = \frac{1}{N} \sum_{i=1}^{N} \mathbf{1}[G(\underline{x}) < 0]. \tag{2.3.2}$$

When P_f is small, the computational efficiency of the MC simulation can be very low, since it requires a large number of calls of the performance function $G(\underline{x})$ to provide an accurate evaluation of the probability of failure. To overcome this inconvenience, the adaptive training of ANN is applied with the following learning function and stopping condition:

1. *Learning function:* A searching zone S_k at the kth iteration is defined in order to avoid the local concentration of the m samples to be selected. S_k is defined by the set of $\underline{x}$ whose prediction uncertainty $s(\underline{x})$ is larger than the maximum s of the training set:

$$S_k = \left\{\underline{x} : s_k(\underline{x}) > s_{\text{train},k}\right\}, \tag{2.3.3}$$

$$s_{\text{train},k} = \max(s_k(\underline{x}) \text{ for } \underline{x} \text{ in the training set}). \tag{2.3.4}$$

   The prediction uncertainty $s_k(\underline{x})$ can be computed with the delta method (Eq.2.1.15), with respect to the ANN trained at the iteration k. K-means clustering [Hastie et al. 2008] is then applied to divide the input data in the searching zone S_k into m clusters. The learning function used is the same as that proposed by Echard et al. [2011] in AK-MCS:

$$U(\underline{x}) = \frac{|\hat{G}(\underline{x})|}{s(\underline{x})} = \frac{|\hat{y}(\underline{x}) - y_{\text{crit}}|}{s(\underline{x})}, \tag{2.3.5}$$

   where $\hat{G}(\underline{x})$ is the performance function approximated by the ANN, whereas y_{crit} represents the failure threshold of the system. Afterwards, in each cluster, the sample with the smallest U value is selected to be the next best point and is added to the DoE.

2. *Stopping condition:* A classical stopping condition of the adaptive ANN is applied:

$$\varepsilon = \frac{|P_{f,k-1} - P_{f,k}|}{P_{f,k}} < \varepsilon_{\text{crit}}. \tag{2.3.6}$$

   This criterion checks the convergence of the $\hat{P}_f$ computed between two successive iterations. $\varepsilon_{\text{crit}}$ is the convergence threshold depending on the specific test case. It can be set to 0.5% for example.

The total workflow the ANN adaptive training with the proposed learning function and stopping condition is illustrated in Figure 2.9. In the subsequent parts of this subsection, the proposed adaptive ANN training is compared to other existing algorithms, including AK-MCS, ASVM, IS-ANN, DS-ANN, etc., in terms of the computational efficiency and the accuracy. In every example, the probability of failure with direct MC estimation is also computed and serves as reference.

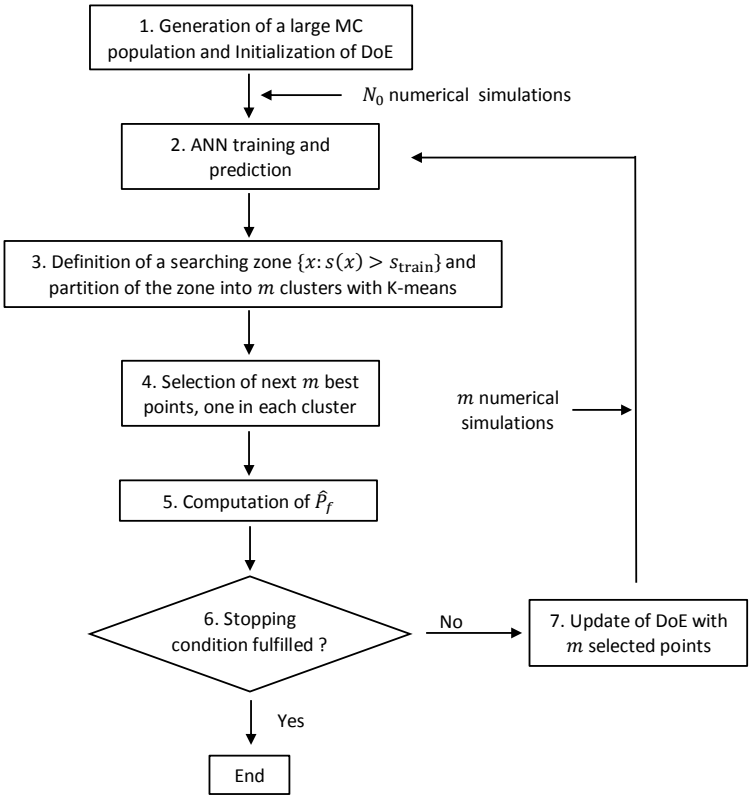

Figure 2.9: The adaptive ANN training algorithm for reliability problems

Example 1: A Four-branch Series System

A four-branch series system is used as the first example [Echard et al. 2011; Pan and Dias 2017]. The performance function of the system reads:

$$G(\underline{x}) = \min \left\{ \begin{array}{l} 3 + 0.1(x_1 - x_2)^2 - (x_1 + x_2)/\sqrt{2} \\ 3 + 0.1(x_1 - x_2)^2 + (x_1 + x_2)/\sqrt{2} \\ (x_1 - x_2) + k/\sqrt{2} \\ -(x_1 - x_2) + k/\sqrt{2} \end{array} \right\}, \tag{2.3.7}$$

where x_1, x_2 are independent random variables following the standard normal distribution $\mathcal{N}(0, 1)$. The cases with $k = 6$ and $k = 7$ are considered. The ANN used in this example has hidden layer neurons number $h = 5$, as in Most and Bucher [2006]. For the stopping condition, $\varepsilon_{\text{crit}}$ is set to 0.5%. The DoE is initialized with $N_0 = 24$, with $m = 3$ points to be selected at every iteration for DoE update. The searching zone, clustering and the update of the DoE are illustrated in Figure 2.10.

The performance of the adaptive ANN in both cases $k = 6$ and 7 is presented in Table 2.2 and Table 2.3, and compared to other advanced adaptive learning techniques used in Echard et al. [2011]; Pan and Dias [2017]; Schueremans and Gemert [2005]. The comparison

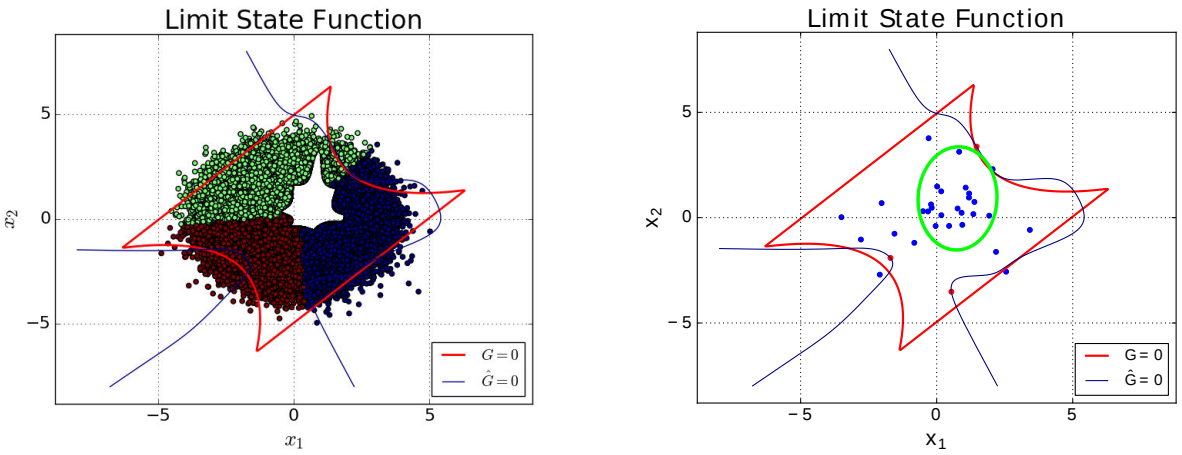

(a) Searching zone and clustering

(b) Update of the DoE

Figure 2.10: Illustration of the selection of the next best points with the adaptive ANN algorithm at iteration 3 for $k = 7$: (a) searching zone and its partition into 3 clusters. One color represents one cluster. $\hat{G} = 0$ is the limit state predicted by the ANN; (b) update of DoE with red points selected at the current iteration. Blue points stand for the old DoE. The region with a concentration of the training data indicated by the green circle is not included in the searching zone in (a).

is with respect to the total number of calls to $G(\underline{x})$ and the final estimated $\hat{P}_f$. We compute also the relative error ε_{P_f} between the $\hat{P}_f$ estimated by different metamodels and by direct MC estimation. The training data selected by the adaptive ANN and the final prediction of the adaptive ANN for $k = 7$ are shown in Figure 2.11 and Figure 2.12, respectively. The evolutions of the probability of failure of both cases $k = 6$ and 7 are plotted in Figure 2.13. For a better visualization, the probability of failure computed at every iteration in Figure 2.13 is normalized with respect to the final $\hat{P}_f = 4.73 \times 10^{-3}$ for $k = 6$ and $\hat{P}_f = 2.34 \times 10^{-3}$ for $k = 7$.

For $k = 6$, the adaptive ANN converges with 97 calls to the performance function. The predicted probability of failure is 4.732×10^{-3}, with 4.1% error relative to the $\hat{P}_f$ calculated by direct MC simulation with 10^6 calls. For the case $k = 7$, the adaptive ANN is stopped with 81 calls to $G(\underline{x})$. The predicted probability of failure is 2.34×10^{-3}, with 3.7% relative error to the direct MC estimation with 10^6 calls. It can be concluded that the performance of the proposed adaptive ANN is comparable to AK-MCS and ASVM-MCS: although it is less accurate than AK-MCS and ASVM-MCS, the relative errors 4.1% and 3.7% are still satisfactory. Besides, Kriging and SVM can be more accurate than ANNs for an analytical separable problem, because Kriging is an exact interpolator of the training data, and hard-margin SVM can also used to make zero classification error of the training samples. However, ANNs try to find an average regression curve for the training samples, which may introduce some errors on the signs of the predicted $\hat{G}(\underline{x})$. On the other hand, the adaptive ANN converges slightly faster than AK-MCS and ASVM-MCS. Compared to other algorithms based on ANNs, the adaptive

ANN-MCS proposed in this section shows clearly better performance in both computational efficiency and prediction accuracy.

Table 2.2: Performance of the adaptive ANN for the four-branch series system: $k = 6$

Method	N_c	$\hat{P}_f$	ε_{P_f}	CoV	Comments
MC	10^6	4.544×10^{-3}	-	1.48%	
Adaptive ANN-MCS	97	4.732×10^{-3}	4.1%	1.45%	
MC	10^6	4.40×10^{-3}	-	1.50%	Pan and Dias [2017]
ASVM-MCS	99	4.46×10^{-3}	1.36%	1.50%	
MC	10^6	4.416×10^{-3}	-	1.50%	Echard et al. [2011]
AK-MCS	126	4.416×10^{-3}	0%	1.50%	
IS-ANN	52	5.7×10^{-3}	22.5%	-	
DS-ANN	165	4.1×10^{-3}	7.2%	-	

Table 2.3: Performance of the adaptive ANN for the four-branch series system: $k = 7$

Method	N_c	$\hat{P}_f$	ε_{P_f}	CoV	Comments
MC	10^6	2.256×10^{-3}	-	2.10%	
Adaptive ANN-MCS	81	2.34×10^{-3}	3.7%	2.06%	
MC	10^6	2.15×10^{-3}	-	2.15%	Pan and Dias [2017]
ASVM-MCS	89	2.13×10^{-3}	0.93%	2.16%	
MC	10^6	2.233×10^{-3}	-	2.11%	Echard et al. [2011]
AK-MCS	96	2.233×10^{-3}	0%	2.11%	
IS-ANN	125	2.9×10^{-3}	29.9%	-	
DS-ANN	67	1.0×10^{-3}	55.2%	-	

Concerning the limit state function $\hat{G}(\underline{x}) = 0$ predicted by the adaptive ANN (Figure 2.12), it provides a global satisfactory approximation to the original limit state $G(\underline{x}) = 0$ except for the region close to the four corners. As stated in Pan and Dias [2017], this is linked to the initial MC population in which few samples can be found in the proximity of the four corners. From Figure 2.11 we can also see that, due to the definition of the searching zone, the selected training data are quasi-uniformly distributed along the limit state. The small concentration of the training data in the middle of the safety area (around the point (0, 0)) is related to the N_0 random selection of the initial DoE. As the number of the training examples should always be larger than the number of weighting parameters in ANNs, this phenomenon is difficult to be avoided in the adaptive ANN approach.

Example 2: Dynamic Response of a Mechanical Oscillator

The second example consists of a single degree-of-freedom undamped mechanical oscillator (Figure 2.14), with 6 independently distributed random variables [Echard et al. 2011; Pan and Dias 2017]. The parameters about the probability distributions of the 6 parameters are listed in Table 2.4. The performance function of the oscillator reads:

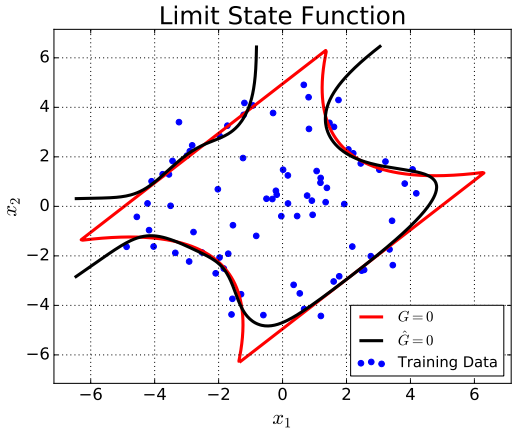

Figure 2.11: Example 1: The limit state function prediction by the adaptive ANN and the selected training data, $k = 7$

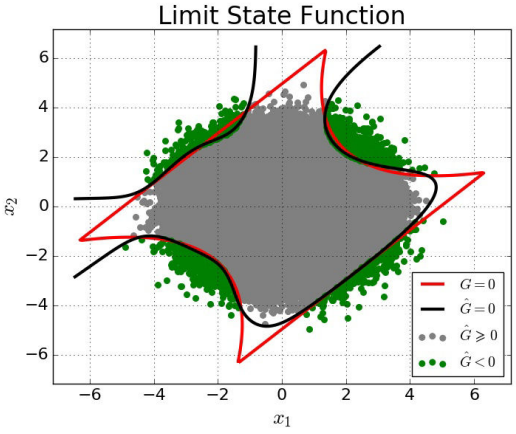

Figure 2.12: Example 1: Predictions on the initial MC population with the adaptive ANN, $k = 7$

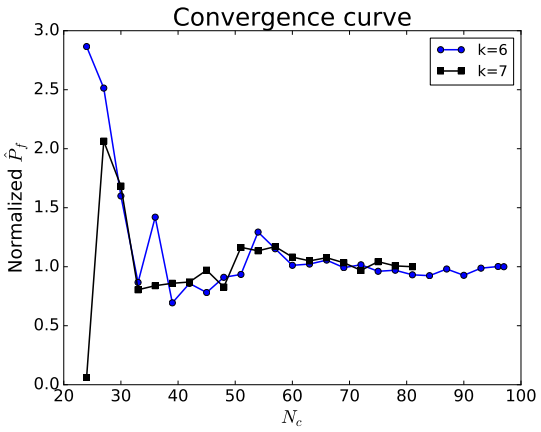

Figure 2.13: Example 1: Convergence of the estimated $\hat{P}_f$

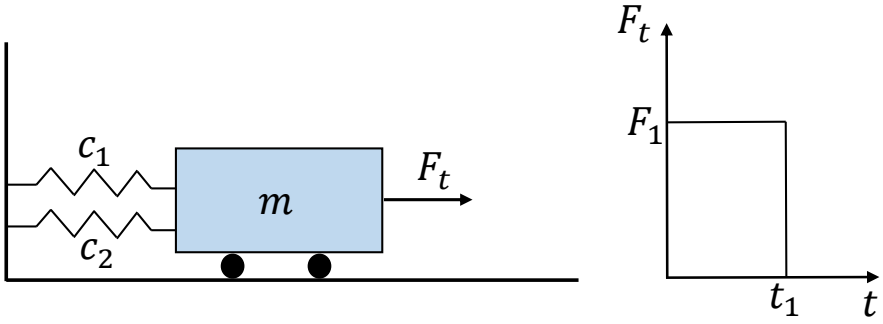

Figure 2.14: Example 2: A single degree of freedom oscillator

$$G(c_1, c_2, m, r, t_1, F_1) = 3r - \left| \frac{2F_1}{m\omega_0^2} \sin(\frac{\omega_0^2 t_1}{2}) \right|, \tag{2.3.8}$$

where $\omega_0 = \sqrt{\frac{c_1 + c_2}{m}}$.

In this example, $h = 4$ is selected for the number of neurons in the hidden layer of the

ANN, according to an empirical rule of thumb $h \approx (n_{\text{input}} + n_{\text{output}})/2$. The size of the initial MC population is 10^6. The number of the initial DoE is $N_0 = 40$ and $m = 3$ data are added into the DoE at every iteration. For the stopping condition, $\varepsilon_{\text{crit}}$ is set to be 0.5%. The results of the adaptive ANN and the comparison with other models are given in Table 2.5, and the convergence curve of the adaptive ANN algorithm for this example is shown in Figure 2.15.

Table 2.4: Example 2: Uncertain parameters

Parameter	PDF	Mean	Standard Deviation
m	Normal	1	0.05
c_1	Normal	1	0.1
c_2	Normal	0.1	0.01
r	Normal	0.5	0.05
F_1	Normal	1	0.2
t_1	Normal	1	0.2

Similar to the first example, the proposed adaptive ANN shows satisfactory performance also in this case study. The algorithm is stopped after 58 calls to the performance function and the estimated probability of failure is 0.0282, with 0.7% error relative to the direct MC estimation. In comparison with other methods, the performance of the adaptive ANN is comparable to ASVM-MCS and AK-MCS. Besides, compared to other ANN adaptive learning algorithms such as IS-ANN and DS-ANN, the adaptive ANN-MCS shows better accuracy and efficiency. This example validates the proposed adaptive ANN-MCS algorithm for a moderate dimensional problem.

Table 2.5: Example 2: Performance of the adaptive ANN for the mechanical oscillator

Method	N_c	$\hat{P}_f$	ε_{P_f}	CoV	Comments
MC	10^6	0.0284	-	0.58%	
Adaptive ANN-MCS	58	0.0282	0.70%	0.58%	
MC	10^6	0.0287	-	0.58%	Pan and Dias [2017]
ASVM-MCS	56	0.0279	2.87%	0.59%	
MC	7×10^4	0.0283	-	2.21%	Echard et al. [2011]
AK-MCS	58	0.0283	0%	2.21%	
IS-ANN	68	0.031	8.71%	-	
DS-ANN	86	0.028	1.06%	-	

Example 3: High Dimensional Example

The last example is a high dimensional example proposed in Rackwitz [2001]. It is used to check whether the adaptive ANN can handle an analytical high dimensional problem. The

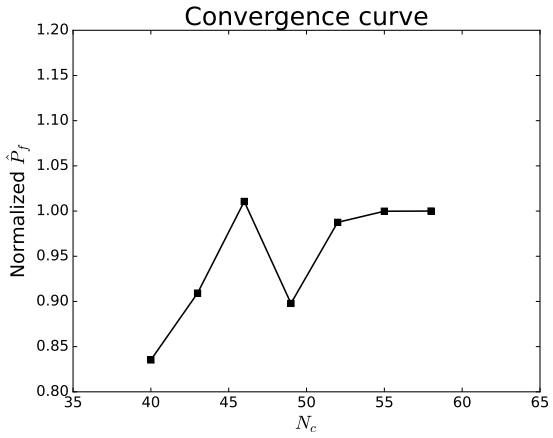

Figure 2.15: Example 2: Convergence of the estimated $\hat{P}_f$

performance function of this problem is given by:

$$G(x_1, ..., x_n) = n + 3\sigma\sqrt{n} - \sum_{i=1}^{n} x_i, \tag{2.3.9}$$

where variables x_i are mutually independent and they follow lognormal distributions with unit means and standard deviation $\sigma = 0.2$. n is the dimension of the problem. Two n values are considered in this study: $n = 40$ and $n = 100$. The initial MC population is 10^6, the same as the previous two examples. The number of hidden layer neurons is chosen to be 5, in order to provide a reasonable initial DoE size compared to AK-MCS and ASVM-MCS. For the stopping condition, $\varepsilon_{\text{crit}}$ is again set to 0.5%. The initial DoE size is $N_0 = 250$ for $n = 40$ and $N_0 = 600$ for $n = 100$. For both cases, 10 data are added to DoE at every iteration. The results for the adaptive ANN in these two problems are summarized in Table 2.6 and compared to AK-MCS and ASVM-MCS. The convergence curve for $n = 100$ is plotted in Figure 2.16.

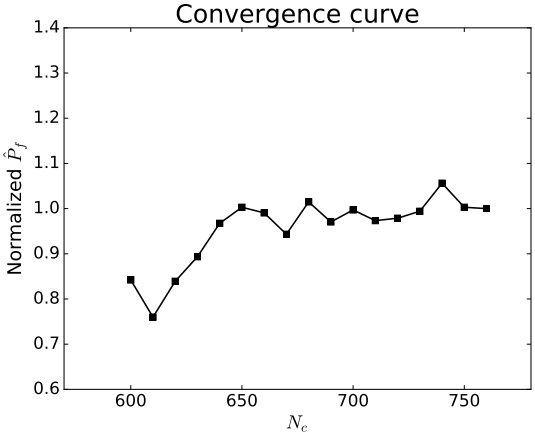

Figure 2.16: Example 3: Convergence of the estimated $\hat{P}_f$ for $n = 100$

Table 2.6: Example 3: Performance of the adaptive ANN for the high dimensional problem

Method	n	N_c	$\hat{P}_f$	ε_{P_f}	CoV	Comments
MC	40	10^6	2×10^{-3}	-	2.23%	
	100	10^6	1.782×10^{-3}	-	2.27%	
Adaptive ANN-MCS	40	320	1.965×10^{-3}	1.75%	2.25%	
	100	760	1.691×10^{-3}	5.11%	2.43%	
MC	40	10^6	1.82×10^{-3}	-	2.24%	Pan and Dias [2017]
	100	10^6	1.73×10^{-3}	-	2.40%	
ASVM-MCS	40	341	1.78×10^{-3}	2.20%	2.37%	
	100	810	1.72×10^{-3}	0.58%	2.41%	
MC	40	3×10^5	1.813×10^{-3}	-	4.3%	Echard et al. [2011]
	100	3×10^5	1.647×10^{-3}	-	4.5%	
AK-MCS	40	112	1.813×10^{-3}	0%	4.3%	
	100	153	1.647×10^{-3}	0%	4.5%	

The adaptive ANN converges with 320 calls to the $G(\underline{x})$ for $n = 40$ and at 760 calls for $n = 100$. The errors of the probability of failure are respectively 1.75% and 5.11% relative to the direct MC estimates with 10^6 calls. In comparison to AK-MCS and ASVM-MCS, all three methods lead to satisfactory estimation of the probability of failure, for both 40 and 100 dimensional cases. The adaptive ANN provides comparable performance to ASVM-MCS. However, AK-MCS shows better convergence speed and accuracy than the other two methods. Due to the interpolation property of Kriging, the relative error is zero and the convergence speed is much higher than the adaptive ANN and ASVM. It has to be mentioned that the initial MC population for AK-MCS is 3×10^5, less than 10^6 adopted in ASVM and adaptive ANN. It can be also seen that N_c increases with the dimension of the problem for adaptive ANNs because of the initial DoE size. With $h = 5$, the initial DoE size for the adaptive ANN is already quite large. In contrast to AK-MCS in which the increase of the dimension has little influence on the convergence speed [Echard et al. 2011], the size of the initial DoE in the adaptive ANN depends on the dimension of the problem. If all the input parameters are mutually independent and if no dimensionality reduction method can be applied, adaptive ANNs are less attractive in terms of computational efficiency.

The proposed adaptive ANN training algorithm has been tested on three examples involving nonlinear multi-failure region, moderate dimension and high dimension problems, and its performance has been compared to other advanced techniques. The results reveal that the adaptive ANN-MCS shows satisfactory performance in terms of computational efficiency and prediction accuracy, so that it can be a good alternative to other adaptive algorithms such as AK-MCS and ASVM-MCS. Based on the obtained results, some discussions are provided in this section:

1. In both accuracy and efficiency, the performance of adaptive ANN-MCS is comparable to AK-MCS and ASVM-MCS in the considered test cases, and it performs much better than DS-ANN and IS-ANN. In addition, once the delta method has been implemented to compute the prediction uncertainty of the ANN, the implementation of the proposed adaptive ANN is straightforward.
2. The performance of the ANN is slightly less competitive than Kriging and SVM for separable problems (e.g. the three mentioned case studies) in terms of accuracy, due to its inherent regression property. Kriging is an exact interpolator of the training data, whereas hard-margin SVMs can be adopted for zero misclassification of the training data. In spite of that, the adaptive ANN-MCS provides satisfactory accuracy compared to these two methods for the three considered test cases.
3. Without advanced samplings to generate additional candidates to approach the limit state, the accuracy of the adaptive ANN-MCS depends to a certain degree on the initial MC population. Therefore, the initial MC population should be large enough to cover the limit state of the performance function. Otherwise, the ANN metamodel loses the local detail of the limit state, e.g. the four sharp corners in the first example.
4. The stopping condition used in the adaptive ANN is less strict than AK-MCS and ASVM. This makes ANN converge quickly despite the large initial size of DoE. If a similar criterion is applied to AK-MCS and ASVM, their convergence speed could be higher, as discussed in Echard et al. [2011]; Pan and Dias [2017].

2.4 Summary

Different training methods of artificial neural networks, which build the basis of the applications of ANNs in different subjects studied in this thesis, are summarized and presented in this chapter. The chapter starts with the explanation of the classical training method of ANNs based on gradient-based optimization methods. The gradient of the ANN cost function can be computed efficiently by the back-propagation algorithm. The computation of the uncertainty of the ANN predictions with the delta method is also discussed. This prediction uncertainty will be further investigated when the ANN is used to substitute the finite element model for the seismic fragility analysis in Chapter 3. Furthermore, considering correlated residuals, an ANN training algorithm based on the GLS principle is derived. This latter GLS ANN training will be used for the computation of ground motion prediction equations in Chapter 5. In the end, the basis of the adaptive training strategy of ANNs is introduced. The principle of the ANN adaptive learning will be used in Chapter 4, for a better selection of the training data to cover the whole input space.

Appendix

2.A Back-propagation Algorithm

The back-propagation algorithm to compute the ANN gradient $\underline{g}$ is derived in what follows. Let us first focus on the computation of the derivative of $e^p(\underline{x}^p;\underline{w})$ with respect to the weights w_{kj} between the hidden layer and the output layer. In the sequel, we will substitute the notation $e^p(\underline{x}^p;\underline{w})$ by e^p for simplicity. With the chain rule, the derivative is calculated by

$$\frac{\partial e^p}{\partial w_{kj}} = \frac{\partial e^p}{\partial v_k}\frac{\partial v_k}{\partial w_{kj}}. \tag{2.A.1}$$

From our notation convention, v_k^p should have been used in Eq.2.A.1 because the derivative is calculated for a specific training example p. This upper index is omitted here for simplicity and it is also omitted in the following for $\hat{y}$.

Because $v_k = \sum_j w_{kj}\hat{y}_j$ (Figure 2.2b), the second term on the right of Eq.2.A.1 can be computed easily:

$$\frac{\partial v_k}{\partial w_{kj}} = \hat{y}_j. \tag{2.A.2}$$

Let us introduce another notation for simplicity:

$$\delta_k = \frac{\partial e^p}{\partial v_k}. \tag{2.A.3}$$

By substituting Eqs.2.A.2,2.A.3 into Eq.2.A.1, we obtain

$$\frac{\partial e^p}{\partial w_{kj}} = \delta_k\hat{y}_j. \tag{2.A.4}$$

The chain rule is applied again for the computation of δ_k:

$$\delta_k = \frac{\partial e^p}{\partial \hat{y}_k}\frac{\partial \hat{y}_k}{\partial v_k}. \tag{2.A.5}$$

According to Eq.2.1.7 and $\hat{y}_k = v_k$ in Figure 2.2b for the output layer, with one training example p, the result of δ_k is written as:

$$\delta_k = \hat{y}_k - y_k. \tag{2.A.6}$$

The same strategy is applied to compute the derivative of e^p with respect to w_{ji} between the input layer and the hidden layer:

$$\frac{\partial e^p}{\partial w_{ji}} = \frac{\partial e^p}{\partial v_j}\frac{\partial v_j}{\partial w_{ji}} = \delta_j\hat{y}_i. \tag{2.A.7}$$

δ_j is calculated in a similar way as Eq.2.A.5:

$$\delta_j = \frac{\partial e^p}{\partial v_j} = \frac{\partial e^p}{\partial \hat{y}_j}\frac{\partial \hat{y}_j}{\partial v_j}. \tag{2.A.8}$$

The second term of Eq.2.A.8 can be computed easily considering $\hat{y}_j = \varphi(v_j)$ (Figure 2.3):

$$\frac{\partial \hat{y}_j}{\partial v_j} = \varphi'(v_j), \tag{2.A.9}$$

where $\varphi'(\cdot)$ is the derivative of the hyperbolic tangent function $\varphi(\cdot)$. $\varphi'(v_j)$ is later denoted by φ'_j for simplicity. The first term in Eq.2.A.8 can be expressed with δ_k:

$$\frac{\partial e^p}{\partial \hat{y}_j} = \sum_k \frac{\partial e^p}{\partial \hat{v}_k}\frac{\partial v_k}{\partial \hat{y}_j} = \sum_k \delta_k w_{kj}. \tag{2.A.10}$$

Therefore, final expressions are derived for δ_j and $\dfrac{\partial e^p}{\partial w_{ji}}$:

$$\delta_j = \varphi'_j \sum_k \delta_k w_{kj}, \tag{2.A.11}$$

$$\frac{\partial e^p}{\partial w_{ji}} = \delta_j \hat{y}_i. \tag{2.A.12}$$

From Eq.2.A.11 one can observe that, in order to compute δ_j in the hidden layer, it is necessary to compute firstly δ_k in the output layer, where comes from the name of the backward propagation algorithm.

Bibliography

Bishop, C. M. (1995). *Neural Networks for Pattern Recognition*. Oxford University Press.

Bourinet, J.-M. (2013). Reliability assessment with sensitivity-based adaptive SVM surrogates. In *Proceedings of the 11th ICOSSAR Conference*.

Bourinet, J.-M. (2016). Rare-event probability estimation with adaptive support vector regression surrogates. *Reliab. Eng. Syst. Safe.*, 150:210–221.

Bourinet, J.-M., Deheeger, F., and Lemaire, M. (2011). Assessing small failure probabilities by combined subset simulation and Support Vector Machines. *Struct. Saf.*, 33:343–353.

Cadini, F., Gioletta, A., and Zio, E. (2015). Improved metamodel-based importance sampling for the performance assessment of radioactive waste repositories. *Reliab. Eng. Syst. Safe.*, 134:188–197.

Cadini, F., Santos, F., and Zio, E. (2014). An improved adaptive kriging-based importance technique for sampling multiple failure regions of low probability. *Reliab. Eng. Syst. Safe.*, 131:109–117.

Chojaczyk, A. A., Teixeira, A. P., Neves, L. C., Cardoso, J. B., and Soares, C. G. (2015). Review and application of artificial neural networks models in reliability analysis of steel structures. *Struct. Saf.*, 52:78–89.

Chryssoloiuris, G., Lee, M., and Ramsey, A. (1996). Confidence interval prediction for neural network models. *IEEE T. Neural. Networ.*, 7(1):229–232.

Cybenko, G. (1989). Approximation by superpositions of a sigmoidal function. *Mathematics of Control, Signals and Systems*, 2:303–314.

Dubourg, V., Sudret, B., and Deheeger, F. (2013). Metamodel-based importance sampling for structural reliability analysis. *Probab. Eng. Mech.*, 33:47–57.

Dybowski, R. and Gant, V. (2001). *Clinical Applications of Artificial Neural Networks*. Cambridge University Press.

Echard, B., Gayton, N., and Lemaire, M. (2011). Ak-mcs: An active learning reliability method combining kriging and monte carlo simulation. *Struct. Saf.*, 33:145–154.

Echard, B., Gayton, N., Lemaire, M., and Relun, N. (2013). A combined Importance Sampling and Kriging reliability method for small failure probabilities with time-demanding numerical models. *Reliab. Eng. Syst. Safe.*, 11:232–240.

Efron, B. (1982). The jackknife, the bootstrap and other resampling plans. *Society for industrial and applied mathematics*, 3.

Gayton, N., Bourinet, J., and Lemaire, M. (2003). CQ2RS: a new statistical approach to the response surface method for reliability analysis. *Struct. Saf.*, 25:99–121.

Hastie, T., Tibshirani, R., and Friedman, J. (2008). *The Elements of Statistical Learning - Data Mining, Inference, and Prediction*. Springer.

Haykin, S. (2008). *Neural Networks and Learning Machines*. Pearson Prentice Hall.

Hui, C. L. P. (2011). *Artificial Neural Networks - Application*. InTech.

Hurtado, J. E. (2001). Filtered importance sampling with support vector margin: A powerful method for structural reliability analysis. *Struct. Saf.*, 191:113–132.

Hurtado, J. E. and Alvarez, D. A. (2001). Neural-network-based reliability analysis: a comparative study. *Comput. Methods Appl. Mech. Eng.*, 191:113–132.

Kolmogorov, A. N. (1957). On the representation of continuous functions of many variables as superpositions of continuous functions of one variable and addition. *Doklay Akademii Nauk USSR*, 14:953–956.

Lapedes, A. and Farber, R. (1988). How neural nets work. *Neural Information Processing Systems (Denver 1987)*, pages 442–456.

LeCun, Y., Bengio, Y., and Hinton, G. (2015). Deep learning. *Nature*, 521:436–444.

Lippmann, R. P. (1987). An introduction to computing with neural nets. *ASSP Magazine*, page 4–22.

Marelli, S. and Sudret, B. (2018). An active-learning algorithm that combines sparse polynomial chaos expansions and bootstrap for structural reliability analysis. *Struct. Saf.*, 75:67–74.

Marquardt, D. W. (1963). An algorithm for least-squares estimation of nonlinear parameters. *J. Soc. Indust. Appl. Math.*, 11:431–441.

McCulloch, W. and Pitts, W. (1943). A logical calculus of the ideas immanent in nervous activity. *B. Math. Biophys*, 5(4):115–133.

Most, T. and Bucher, C. (2006). Adaptive response surface approach using artificial neural networks and moving least squares. In *17 th International Conference on the Application of Computer Science and Mathematics in Architecture and Civil Engineering*.

Pan, Q. and Dias, D. (2017). An efficient reliability method combining adaptive Support Vector Machine and Monte Carlo Simulation. *Struct. Saf.*, 67:85–95.

Papadopoulos, V., Giovanis, D. G., Lagaros, N. D., and Papadrakakis, M. (2012). Accelerated subset simulation with neural networks for reliability analysis. *Comput. Methods Appl. Mech. Eng.*, 223–234:70–80.

Pedroni, N. and Zio, E. (2017). An Adaptive Metamodel-Based Subset Importance Sampling approach for the assessment of the functional failure probability of a thermal-hydraulic passive system. *Appl. Math. Model.*, 48:269–288.

Rackwitz, R. (2001). Reliability analysis — a review and some perspectives. *Struct. Saf.*, 23:365–395.

Reed, R. D. and Marks, R. J. (1998). *Neural Smithing*. The MIT Press.

Rivals, I. and Personnaz, L. (2000). Construction of confidence intervals for neural networks based on least squares estimation. *Neural Networks*, 13:463–484.

Rosenblatt, F. (1962). *Principles of Neurodynamics: Perceptrons and the Theory of Brain Mechanisms*. Spartan.

Rumelhart, D., Hinton, G., and Williams, R. (1986). *Learning internal representations by error propagation in Parallel Distributed Processing: Explorations in the Microstructure of Cognition*. The MIT Press.

Sarle, W. S. (1995). Stopped training and other remedies for overfitting. In *Proceedings of the 27th Symposium on the Interface*, pages 352–360.

Schueremans, L. and Gemert, D. V. (2005). Benefit of splines and neural networks in simulation based structural reliability analysis. *Struct. Saf.*, 27:246–261.

Shao, S. and Murotsu, Y. (1997). Structural reliability analysis using a neural network. *Jpn. Soc. Mech. Eng. Int. J.*, 40:242–246.

Sprecher, D. A. (1965). On the structure of continuous functions of several variables. *Transaction of the American Mathematical Society*, 115(3):340–355.

Tetko, I. V., Livingstone, D. J., and Luik, A. I. (1995). Neural network studies. 1. comparison of overfitting and overtraining. *Journal of Chemical Information and Computer Sciences*, 35:826–833.

Weigend, A. S. (1994). On overfitting and effective number of hidden units. In *Proceedings of the 1993 Connectionist Models Summer School*, page 335–342.

Widrow, B. and Hoff, M. E. (1960). Adaptive switching curcuits. *IRE WESCON Convention record*, 4:96–104.

Xiao, N.-C., Zuo, M. J., and Zhou, C. (2018). A new adaptive sequential sampling method to construct surrogate models for efficient reliability analysis. *Reliab. Eng. Syst. Safe.*, 169:330–338.

Zheng, P., Wang, C., Zong, Z., and Wang, L. (2017). A new active learning method based on the learning function U of the AK-MCS reliability analysis method. *Eng. Struct.*, 148:185–194.

Zio, E. (2006). A study of the bootstrap method for estimating the accuracy of artificial neural networks in predicting nuclear transient processes. *IEEE T. Nucl. Sci.*, 53(3):1460–1478.

Chapter 3

Seismic Fragility Analysis with Artificial Neural Network Metamodels

The conditional probability of failure, illustrated by means of fragility curves, is usually computed adopting a lognormal assumption to reduce the computational cost. In this chapter, an artificial neural network (ANN) is constructed to improve the computational efficiency for the calculation of structural outputs. The following aspects are addressed: (a) Selection of IMs as inputs of the ANN. The most relevant IMs are selected with a forward selection approach based on semi-partial correlation coefficients; (b) Quantification and investigation of the ANN prediction uncertainty computed with the delta method. It consists of an aleatory component from the simplification of the seismic inputs and an epistemic model uncertainty from the limited size of the training data. The aleatory component is integrated in the computation of fragility curves, whereas the epistemic component provides the confidence intervals; (c) Computation of fragility curves with Monte Carlo method and verification of the validity of the lognormal assumption. This methodology is applied to estimate the probability of failure of an electrical cabinet in a reactor building studied in the framework of the KARISMA benchmark.

Contents

3.1 Introduction

In the seismic probabilistic risk assessment (SPRA) methodology, fragility curves are computed as conditional probabilities of failure of structures, or critical components, for given values of a seismic intensity measure (IM), such as the peak ground acceleration (PGA) [EPRI 1994]. The core damage frequency of the plant is, then, calculated by the convolution of the fragility curves with the hazard curves in fault tree and event tree analysis [EPRI 1994]. The computation of fragility curves requires a realistic estimation of the structure performance subject to seismic excitations via the quantification and the propagation of uncertainties existing in earthquake ground motions, structural material properties, etc. These uncertainties are categorized into two groups [Kennedy et al. 1980]: aleatory uncertainties, which reveal the inherent randomness of variables or stochastic processes, and epistemic uncertainties, which originate from the lack of knowledge about the model and provide a family of confidence interval curves for the fragility estimation.

In practice, a fragility curve is calculated as the conditional probability that the engineering demand parameter (EDP) exceeds a critical threshold, for a given seismic IM: [Mai et al. 2017; Zentner et al. 2017]:

$$P_f(\alpha) = P(y > y_{\text{crit}}|\alpha), \tag{3.1.1}$$

where y is the EDP, such as inter-story drift, y_{crit} is the failure threshold and α represents the seismic IM. This conditional probability can be evaluated pointwise for different α values with the Monte Carlo method [Mai et al. 2017; Noh et al. 2015], as well as with methods based on the lognormal hypothesis [Kennedy et al. 1980; Lallemant et al. 2015; Shinozuka et al. 2000]. However, both methods require a few hundred heavy numerical simulations with the finite element method (FEM).

One way to improve the computational efficiency consists in building a metamodel to calibrate the statistical relation between seismic inputs and structural outputs. In fact, it is difficult to directly use stochastic ground motions to construct the metamodels, because the high-dimensionality of the inputs of such metamodels requires a very large size of training data

to accurately approximate the input-output relation [Gidaris et al. 2015]. An alternative is to use seismic IMs as inputs of the metamodels to represent ground motions. Various functional models based on the calibration of IMs-EDP relation have been proposed [Cornell et al. 2002; Perrault 2013; Xu and Gardoni 2016]. According to these works, a nonlinear regression metamodel seems more suitable to provide adequate nonlinearity in the IMs-EDP relation. However, with this approach, the simplification of the continuous stochastic ground motion by a small set of IMs may not allow to describe all the random variability in the earthquake motion [Zentner and Borgonovo 2014]. Therefore, it cannot ensure the performance of the metamodels.

Some studies regarding the application of metamodels in fragility analysis have been realized recently. Most works focus on using seismic IMs to characterize earthquake accelerations. Metamodels are constructed to calibrate the relation between EDPs and uncertain inputs of the structural models, including IMs and material parameters. The construction of the metamodels is either achieved by decomposing the nonlinear input-output relation with high-dimensional model representation (HDMR) [Zentner and Borgonovo 2014; Unnikrishnan et al. 2013], or realized with polynomial regression [Buratti et al. 2010; Seo and Linzell 2013; Seo et al. 2012; Saha et al. 2016; Park and Towashiraporn 2014] or other more advanced statistical tools, such as artificial neural networks (ANNs) [Lagaros and Fragiadakis 2007; Lagaros et al. 2009; Mitropoulou and Papadrakakis 2011; Ferrario et al. 2015; Calabresea and Lai 2013], LASSO regression [Mangalathu et al. 2017], Bayesian networks [Gehl and D'Ayala 2016], merging multivariate adaptive regression splines, radial basis function network, support vector regression [Ghosh et al. 2013], Kriging [Gidaris et al. 2015; Jia and A.Taflanidis 2013; Lopez-Caballero and Khalil 2018], etc. On the other hand, earthquake accelerations are also used directly as inputs of the metamodel in Mai et al. [2016] to predict structural response time histories. The construction of the metamodel is divided into two steps: the first step is to extract the characteristics of earthquake motions with nonlinear auto-regression; then the polynomial chaos expansion is applied to these characteristics to construct the metamodel. EDPs are computed from the structural response time histories, and fragility curves can be thus obtained. Although this method seems different from the classical metamodeling with IMs, the idea remains the same: the nonlinear auto-regression serves as a tool to extract the features of earthquake motions and past values of the structural displacement, whereas these features are represented by the IMs in the classical approaches. Besides regression methods, classification models like logistic regression, random forests and support vector machine are utilized in Ataei and Padgett [2015] to predict directly the probability of failure from the uncertain inputs. Despite the fact that seismic fragility analyses have been successfully performed with different types of metamodels, the following two points are rarely discussed: (i) Systematic selection of pertinent IMs to represent seismic ground motions; (ii) Quantification

of the prediction uncertainty of the metamodels.

In this chapter, a computationally efficient methodology for the application of ANNs to characterize the IMs-EDP relation is proposed, from the selection of the most relevant IMs to the quantification of ANN prediction uncertainties. A more efficient feature selection method based on the semi-partial correlation coefficient is proposed in this work. The uncertainty in the ANN predictions is also investigated: it consists of an aleatory component from the simplification of the seismic inputs and an epistemic uncertainty due to the paucity of the training data. The former is considered in the computation of $P_f(\alpha)$, whereas the latter is used in the estimation of confidence intervals.

3.2 Simulation-based Fragility Analysis

A simulation-based fragility analysis is composed of 3 main steps:

1. Structure modeling. This step consists in establishing a set of mathematical partial differential equations to describe the mechanical behavior of the underlying model.
2. Numerical simulation and calculation of the EDP. Numerical simulations are performed to propagate the uncertainties and to compute the EDP. FEM is the most widely used numerical resolution method.
3. Computation of the conditional probability of failure of the structure. This step is realized by applying a statistical analysis to the IM-EDP data cloud (α, y) computed from the numerical simulation results.

In this section, the computation of the EDP and the calculation of the conditional probability of failure are further discussed. Two commonly used methods for the computation of the conditional probability are presented. These two methods will be applied to calculate the fragility curves in an industrial complex case study in this chapter.

3.2.1 Computation of the Engineering Demand Parameter

Mechanical model The mechanical model to compute the EDP of a structure or a critical component can be described as:

$$y = f(\underline{a}(t)), \tag{3.2.1}$$

where $\underline{a}(t)$ represents the seismic ground acceleration. The resolution of Eq.3.2.1 is usually time-consuming, especially when the structural model is very complex. In this way, one needs to resort to the metamodel to reduce the computational cost of the numerical simulations.

Metamodel In this chapter, a metamodel established for IMs-EDP relation is desired. It is used to replace the mechanical model in order to improve the computational efficiency:

$$\hat{y} = \hat{f}(\mathrm{IM}_1, \mathrm{IM}_2, ..., \mathrm{IM}_k), \tag{3.2.2}$$

where the symbol '$\wedge$' denotes the results calculated from the metamodel. The regression of the metamodel leads to a reduction of the variability in the metamodel prediction: $y = \hat{y} + \varepsilon$. The existence of the residual ε not only comes from the lack-of-fit of the metamodel, but also has more specific interpretations:

1. The metamodel cannot show sufficient nonlinearity to replace the mechanical model. The residual value can be very high if a linear metamodel is wrongly selected to substitute a nonlinear mechanical model.
2. IMs are adopted to represent the inherent randomness of ground motions $\underline{a}(t)$, which gives rise to a loss of information in the input variables. Different ground motion time histories with the same set of IM values lead to different structural responses, in contrast to a deterministic response predicted by the metamodel. Consequently, ε should be present for the training data in the metamodeling process. That is also the main reason why a nonlinear regression model like ANN is preferred, rather than an exact interpolation model, such as Kriging with classical kernels (Gaussian kernel, Matern kernel, etc.).
3. The number of the training data for the development of the metamodel is usually limited due to the computational cost of FEM simulations.

These facts show the necessity of the quantification of the metamodel prediction uncertainty, in order to provide reliable applications of metamodels to critical structures such as NPPs.

3.2.2 Computation of Fragility Curves

This section is dedicated to recall the basis of two methods in the computation of fragility curves: the Monte Carlo Method and the regression method. These two methods can be applied to compute the conditional probability of failure when the data cloud (α, y) is provided.

Monte Carlo (MC) method In this method, N seismic records with the same IM level α are collected. Structural analyses for all N seismic motions are performed, and the probability of failure for the seismic IM level α is calculated as:

$$P_{\mathrm{MC}}(\alpha) = \frac{1}{N} \sum_{i=1}^{N} \mathbf{1}[y_{\mathrm{crit}} - y^i(\alpha) < 0], \tag{3.2.3}$$

where $\mathbf{1}[y_{\mathrm{crit}} - y^i(\alpha) < 0]$ equals 1 if $y_{\mathrm{crit}} - y^i(\alpha) < 0$, otherwise it equals 0.

Regression method with lognormal assumption The lognormal assumption is commonly adopted to compute the conditional probability of failure. The regression method (Reg), or 'cloud analysis', is based on the linear regression of the data cloud (α, y) in the log-log space [Zentner et al. 2017; Cornell et al. 2002; Ellingwood and Kinali 2009].

$$\ln y = c \ln \alpha + \ln b + \varepsilon, \tag{3.2.4}$$

where b and c are regression parameters determined from the data cloud $(\ln \alpha, \ln y)$, and the residual ε follows a normal distribution $\mathcal{N}(0, \beta^2_{R|IM})$. $\beta_{R|IM}$ is calculated as:

$$\beta_{R|IM} = \sqrt{\frac{\sum_{i=0}^{N} (\varepsilon^i - \bar{\varepsilon})^2}{N-2}}, \tag{3.2.5}$$

in which $\bar{\varepsilon}$ is the mean of the regression residuals and N denotes the size of the data (α, y). The conditional probability of failure can be, thus, calculated:

$$P_f(\alpha) = \mathbf{\Phi}\left(\frac{\ln b\alpha^c - \ln y_{\text{crit}}}{\beta_{R|IM}}\right), \tag{3.2.6}$$

where $\mathbf{\Phi}(\cdot)$ is the cumulative distribution function of the standard normal distribution $\mathcal{N}(0, 1)$.

Both methods MC and Reg are used in the sequel of this paper to compute fragility curves. In particular, the pointwise MC method serves to confirm the validity of the lognormal assumption.

3.3 Description of the ANN-based Seismic Fragility Analysis

The global procedure for the estimation of the fragility curves with ANNs is illustrated in Figure 3.1. The basic stages are: (1) Preparation of data set by performing FEM simulations. (2) Feature selection to extract the most important IMs as inputs of the ANN. (3) ANN training and validation. (4) ANN uncertainty quantification. (5) Computation of fragility curves with ANN simulation results.

3.3.1 Preparation of Data Set

This step is achieved by conducting a series of numerical simulations with the FEM. The soil-structure interaction (SSI) should be considered to offer a best estimate of the structural response. The number of simulations is thus limited due to the computational complexity of the FEM analysis, with the presence of the SSI. The basic working flow is divided into the following 5 steps illustrated in Figure 3.2:

1. Generation of synthetic seismic motions at the bedrock. This can be realized by gener-

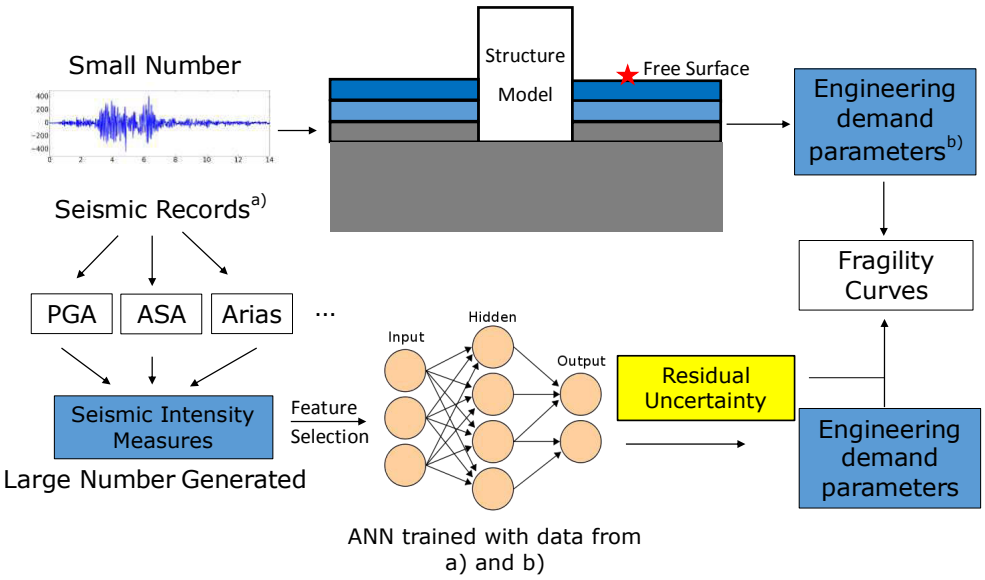

Figure 3.1: Work flow for the computation of fragility curves with ANN

ating a set of seismic motions compatible with the spectral acceleration predicted by the ground motion prediction equations (GMPEs).

2. Convolution of the bedrock accelerations to the free surface. The convolution is performed using a 1D column of soil with the consideration of soil degradation. The degradation of the soil during the earthquake is accounted for by the equivalent linear method (ELM) based on the 1D soil column [Yoshida et al. 2002].
3. After the convolution, surface ground motions and their corresponding degraded soil profiles are obtained. The ground motions obtained on the free surface are coherent with the site-specific degraded soil profiles. The latter is utilized as the input of the SSI analysis, whereas IMs of the ground motions on the free surface can be extracted.
4. SSI analysis is conducted and structural response time histories can be thus obtained.
5. The EDPs are computed by the post-processing of the structural response time histories.

Consequently, the data set IMs-EDP is available for the feature selection and further for the construction of the ANN metamodel.

3.3.2 Feature Selection

Before the training of the ANNs, it is important to select a subset of IMs whose impact on the EDP is dominant. This step, named feature selection, is crucial in the metamodel construction phase to ensure the performance of the ANNs. On the one hand, an IM irrelevant to the output should not be considered as a feature; on the other hand, with the limited size of available training data, a smaller input dimension simplifies the ANN structure and improves the generalization capacities of the network [Bishop 1995]. The feature selection approach

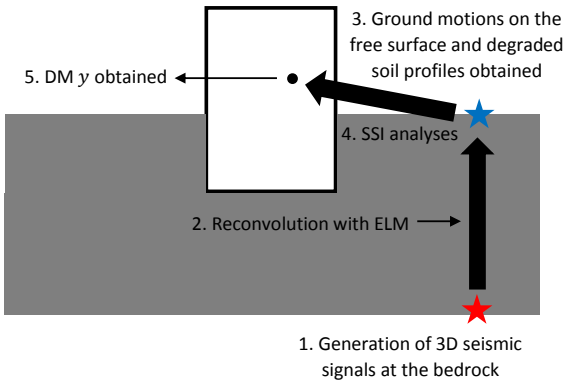

Figure 3.2: Work flow of FEM simulations

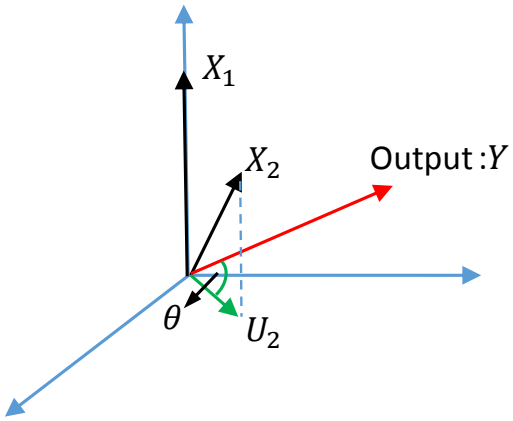

Figure 3.3: Computation of SPCC – $\cos(\theta)$

applied in Ferrario et al. [2015] is a wrapper approach based on the genetic algorithm (GA). The wrapper approach relies on the metamodel to select the best subset of the features (i.e. relevant IMs) [Kohavi and John 1997]. However, one disadvantage of the wrapper approach is its computational burden, because this method requires a large number of repeated trainings of the ANNs.

Filter approach based on semi-partial correlation coefficients A filter approach is proposed in this paper to improve the computational efficiency of the wrapper feature selection. In machine learning, the filter approach describes a group of methods used to select the features regardless of the metamodel. Therefore, it can be regarded as a sensitivity analysis between inputs and outputs. In the context of fragility analysis, the main difficulty in applying such an approach is the dependence between all the IMs. This correlation should be considered in the execution of the filter approach to discard the redundant information.

For this purpose, a forward selection algorithm driven by semi-partial correlation coefficients (SPCCs) is used to rank the importance of the IMs. As shown in Figure 3.3, in order to eliminate the dependence, the IM X_2 is projected onto the orthogonal space of the reference IM X_1. The SPCC calculates the correlation (the cosine value of the angle θ) between the projection U_2 and Y. The orthogonal relation between random variables (RVs) is interpreted by the statistical linear independence between them. Therefore, if IMs follow lognormal distributions, the orthogonal projections can be realized by means of Cholesky factorization on the correlation coefficient matrix of the underlying normally distributed RVs [Ditlevesen and Madsen 2005]. The adopted forward selection algorithm is as follows:

1. Define the input and the output of the algorithm: the input is the feature set $S_0 = \{X_1, \cdots, X_k\}$ ($X_i = \ln \mathrm{IM}_i$) and the output is ranked feature set S^*. Initialize the output set $S_0^* = \emptyset$.

2. Begin the iteration i (i starts from 0): for each feature X_j in S_i, compute the SPCC between X_j and the Output Y ($\ln \mathrm{EDP}$), by projecting X_j onto the orthogonal space of the ranked feature set S_i^* (i.e. conditional to S_i^*). Select the feature with the largest SPCC value:

$$j^* = \arg\max_j \mathrm{SPCC}(X_j, Y|S_i^*); \tag{3.3.1}$$

$$R_i^{\mathrm{SP}} = \mathrm{SPCC}(X_{j^*}, Y|S_i^*). \tag{3.3.2}$$

When $i = 0$, $\mathrm{SPCC}(X_j, Y|\emptyset)$ actually computes the linear correlation coefficient between X_j and Y.

3. Subtract the selected X_{j^*} from the feature set: $S_i \ominus X_{j^*} \rightarrow S_{i+1}$, and add X_{j^*} into the output set: $S_i^* \oplus X_{j^*} \rightarrow S_{i+1}^*$.
4. Set $i = i + 1$ and return to Step 2 until all the IMs are selected in S^*.

The IMs are ranked in S^* according to their importance to the output, and one can select the first few IMs to train the ANN.

3.3.3 ANN Training and Validation

For the ANN training, the available data set is divided into 3 independent subsets:

- Training subset (e.g. 60% of the total data), which is used to determine the optimal weighting parameters $\underline{w}^*$ that minimize the cost function of the ANN model.

- Validation subset (e.g. 20% of the total data), which supervises the training process. The ANN training is stopped when the validation error reaches its minimum to avoid overfitting [Bishop 1995; Pedroni et al. 2010]. This strategy is called early stopping.

- Test subset (e.g. 20% of the total data), which is independent of the training and validation subsets. The test subset is not used in the ANN training, but used afterwards to evaluate the generalization capacity of a trained ANN metamodel.

The ANN is suggested to be trained with IMs-EDP in log-log space to facilitate the consideration of the ANN uncertainties into the fragility curves. The performance of the ANN can be evaluated by the root-mean-square error (RMSE). Once trained and validated, the ANN substitutes the FEM model to accelerate the computation process.

3.3.4 ANN Uncertainty Quantification

The prediction uncertainty s of the ANN is computed with the delta method described in Chapter 2.1.3:

$$s^2 = \sigma_{\mathrm{ANN}}^2 + \sigma_{\mathrm{ANN}}^2 \underline{h}_{\mathrm{test}}^T (\underline{\underline{J}}^T \underline{\underline{J}})^{-1} \underline{h}_{\mathrm{test}}. \tag{3.3.3}$$

The source of the ANN prediction uncertainty comes from two aspects: (i) The selected

IMs cannot completely represent the variability of the ground motion. This eventually reduces the variability of the output. (ii) The ANN accuracy due to the limited size of data to train ANNs. It is the statistical uncertainty linked to the ANN model. Let us return to the two components in s^2: the first fixed part σ^2_{ANN} represents the ANN training error, and the second part $\sigma^2_{\text{ANN,stat}} \triangleq \sigma^2_{\text{ANN}} \underline{h}^T_{\text{test}} (\underline{\underline{J}}^T \underline{\underline{J}})^{-1} \underline{h}_{\text{test}}$ depends on the training and the test data.

1. The first term σ^2_{ANN} estimates the difference between the FEM simulation results and the predictions of the ANN. Given that a nonlinear regression returns a regular hyper-surface in a high dimensional space, the predictions of the ANN show always less variability than the original FEM data. As discussed in Section 3.2.1, this phenomenon is mainly due to the loss of the inherent seismic randomness in the input variables, so that the nature of σ^2_{ANN} can be regarded as the aleatory uncertainty not explained by the ANN input parameters.
2. The second term $\sigma^2_{\text{ANN,stat}}$ is the statistical uncertainty linked to the limited data used to train and test the ANNs. The information of the training data is included in the $\underline{\underline{J}}$ matrix and $\underline{h}_{\text{test}}$ incorporates the influence of the test data. It is thus considered as the epistemic uncertainty, and it provides the confidence intervals of the fragility curves.

These two aspects are illustrated with a simple case study in Figure 3.4. In fact, σ_{ANN} should have contained also an epistemic uncertainty contribution from the insufficient nonlinearity of the ANN. However, the high flexibility of the ANN architecture offers an universal approximation capacity to continuous bounded functions [Reed and Marks 1999]. If the number of the hidden layer units is correctly determined, the error from the ANN nonlinearity can be considered less important compared to the aleatory randomness neglected in its inputs. This can be observed from Figure 3.4: in spite of the existence of the unidentified input z, the ANN regression curve stays very close to $y = \sin(x)$ curve in the training data region. Consequently, this epistemic contribution is assumed negligible in this study. Next section presents the computation of fragility curves with the consideration of these two uncertainties.

3.3.5 Fragility Curves with ANN simulation results

The marginal distributions of the IMs are known through the GMPEs [Campbell and Bozorgnia 2008]. Correlation models are also available in the literature [Baker 2007]. Based on GMPEs and correlation models, seismic IMs can be generated directly as inputs of the ANN. One advantage of using IMs as inputs of metamodels is that no seismic ground motions are in need for ANN simulations.

Given the large number of simulation results provided by ANN, fragility curves can be computed with methods MC and Reg. This also allows confirming the validity of the lognormal assumption used in the fragility analysis. It is important to take into account the ANN prediction uncertainty, because the regression of the ANN reduces the statistical variability

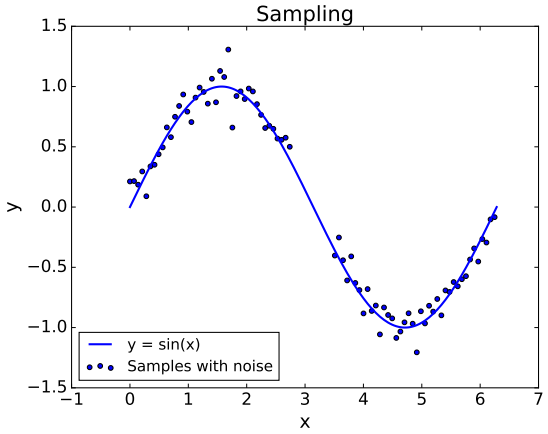

(a) ANN Training data

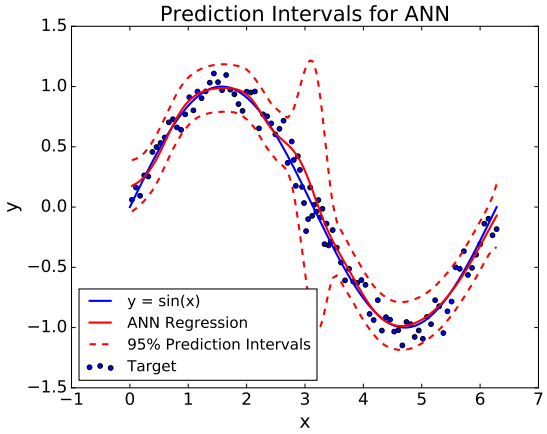

(b) ANN Test results

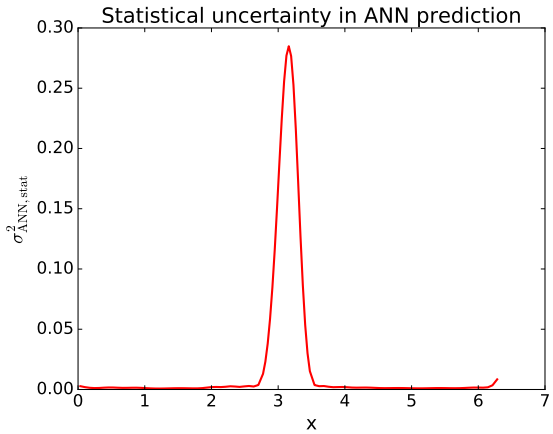

(c) ANN statistical uncertainty

Figure 3.4: An illustrative example for ANN prediction uncertainties: (a) 80 sparse training data $y = \sin(x) + z$, with $z \sim \mathcal{N}(0, 0.1^2)$. An ANN is trained with (x, y). z is assumed to be the unidentified input. No training data are generated near $x = 3$, for the purpose of checking the property of $\sigma_{\text{ANN,stat}}$. (b) ANN is trained, with $\sigma_{\text{ANN}} = 0.0931$, close to the Std of z. The ANN is then tested on 100 uniformly regenerated data. (c) $\sigma_{\text{ANN,stat}}$ with a peak near $x = 3$, where no training data exist. It can be concluded that $\sigma_{\text{ANN,stat}}$ captures the scarcity of the training data.

of the EDPs, and thus the aleatory uncertainty of the fragility curves. As a consequence, methods MC and Reg should be adapted with the consideration of the ANN prediction uncertainty.

For the Reg method, as the ANN is trained in log-log space, the aleatory residual uncertainty σ^2_{ANN} can be integrated directly into the expression of the lognormal CDF (Eq.3.2.6). The basic steps consist of:

1. Generation of IMs as inputs of the ANN. Select one IM α as the parameter of the fragility curve.
2. Conduct ANN simulations with the generated IMs. The ANN outputs $\hat{y}$ are obtained.
3. Apply Reg method on data $(\alpha, \hat{y})$ and determine the regression parameters b, c, $\beta^{\text{ANN}}_{R|IM}$.

4. Compute the conditional probability of failure with the consideration of σ^2_{ANN}:

$$P_f(\alpha) = \mathbf{\Phi}\left(\frac{\ln b\alpha^c - \ln y_{\text{crit}}}{\beta_{\text{Total}}}\right) = \mathbf{\Phi}\left(\frac{\ln b\alpha^c - \ln y_{\text{crit}}}{\sqrt{(\beta^{\text{ANN}}_{R|IM})^2 + \sigma^2_{\text{ANN}}}}\right). \tag{3.3.4}$$

A similar idea concerning the consideration of this metamodel uncertainty has been used in Gidaris et al. [2015] for Kriging.

For the MC estimation based on the ANN simulation data, no analytical expression can be derived. One has to resort to the sampling of the residual, for both aleatory and epistemic parts. The basic steps are:

1. Generation of N groups of seismic IMs as inputs of the ANN, conditional to the IM α used as the independent parameter of the fragility curve.
2. Conduct ANN simulations with the generated IMs. The ANN outputs $\hat{y}$ are obtained.
3. Sampling of N residuals ε_{ANN} following $\mathcal{N}(0, \sigma^2_{\text{ANN}})$, and sampling of $\varepsilon^{\gamma}_{\text{ANN,stat}}$, the γ percentile of $\mathcal{N}(0, \sigma^2_{\text{ANN,stat}})$.
4. Computation of the conditional probability of failure $P_{\text{MC}}(\alpha)$ and the γ confidence interval $\tilde{P}^{\gamma}_{\text{MC}}(\alpha)$:

$$P_{\text{MC}}(\alpha) = \frac{1}{N}\sum_{i=1}^{N} \mathbf{1}[\ln y_{\text{crit}} < \ln \hat{y}^i(\alpha) + \varepsilon^i_{\text{ANN}}]; \tag{3.3.5}$$

$$\tilde{P}^{\gamma}_{\text{MC}}(\alpha) = \frac{1}{N}\sum_{i=1}^{N} \mathbf{1}[\ln y_{\text{crit}} < \ln \hat{y}^i(\alpha) + \varepsilon^i_{\text{ANN}} + \varepsilon^{\gamma}_{\text{ANN,stat}}]. \tag{3.3.6}$$

5. Repeat the steps 1-4 for different α values.

$P_{\text{MC}}(\alpha)$ can be compared with $P_f(\alpha)$ to confirm the assumption of lognormality of the fragility curve. For the purpose of simplicity, the adapted Reg and MC methods in the ANN-based fragility analysis are denoted as 'Modified Reg' and 'Modified MC', respectively. In the sequel, the described methodology is illustrated with an industrial test case studied in the KARISMA benchmark.

3.4 Case Study: KARISMA benchmark

3.4.1 Kashiwazaki-Kariwa FEM Analysis

In 2007, the Japanese Kashiwazaki-Kariwa (K-K) NPP was affected by the Niigataken-Chuetsu-Oki earthquake (NCOE) with a magnitude $M_w = 6.6$ and an epicenter distance of 16 km. The structure of the K-K NPP is shown in Figure 3.6. In this paper, we are interested in the reliability of a hypothetical electrical cabinet located on the fifth floor of

the Unit 7 reactor building of the NPP (Figure 3.6). The finite element model for the Unit 7 consists of 92,000 degrees of freedom with 10,700 nodes and 15,600 elements, including bar, beam, and different shell elements. The constitutive law of the materials is considered as linear. The NPP model is embedded 23 meters in the soil, which is accounted for in the SSI analysis. The structural analyses are carried out with Code_Aster, a finite element analysis open-source software developed by EDF group [1], while the soil part is solved with MISS based on the boundary element method (BEM) [2].

FEM analyses are performed according to the approach described in Chapter 3.3.1. 100 triplets of 3D synthetic ground motions are generated at the bedrock with $Vs_{30} = 720$ m/s and used for the uncertainty propagation. Given the NCOE scenario, the generation of the synthetic ground motions are based on scenario spectra predicted by the Campbell-Bozorgnia 2008 (C&B 2008) GMPE Campbell and Bozorgnia [2008]. One example of the 3D generated ground motions are shown in Figure 3.5. In order to obtain sufficient failure cases for the fragility analysis, the synthetic seismic motions at the bedrock are scaled with a factor of three. After analyses with ELM, 100 triplets of ground motions on the free surface and 100 degraded soil profiles are obtained.

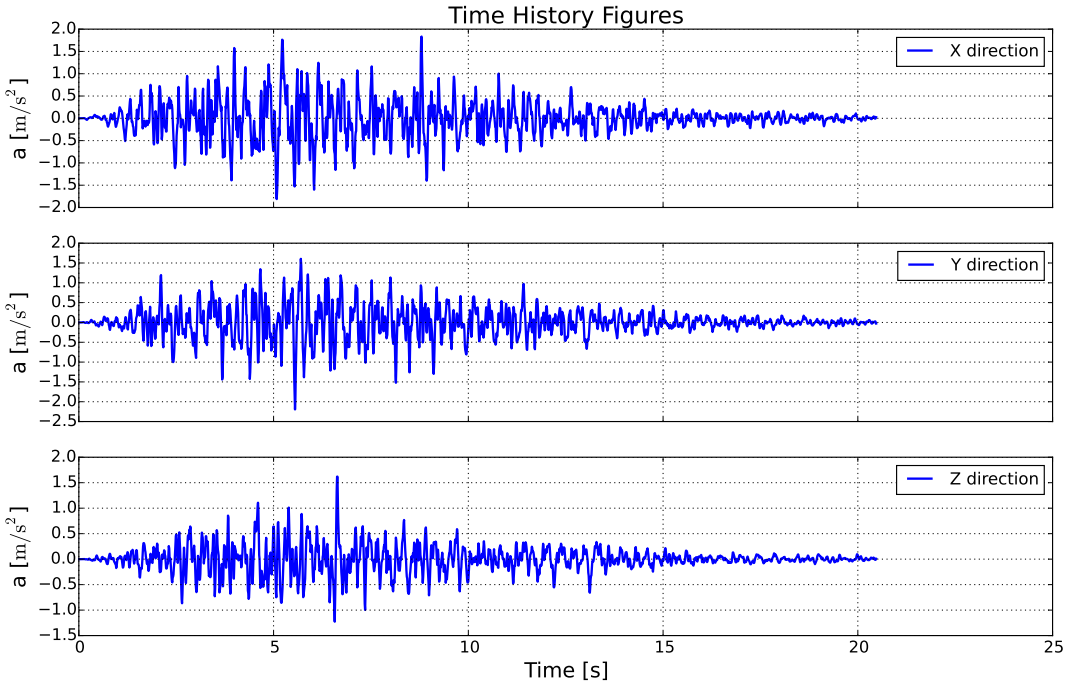

Figure 3.5: Example of generated 3D earthquake ground motions

The impedances of the soil and the seismic forces should have been computed for each

[1] Open-source Finite Element code developed by EDF group, http://www.code-aster.org.

[2] A software in earthquake engineering and structural dynamics developed by the laboratory MSSMAT, Ecole Centrale Paris, http://www.mssmat.ecp.fr/miss.

soil profile using BEM. However, the high complexity of the embedded foundation makes it hard to achieve: it takes 24 hours to run the BEM simulation for one soil profile. In order to reduce the computational cost, the 3D seismic signals at the bedrock are regrouped into four soil classes according to their PGA values: i. PGA∈[0, 0.5g) ii. PGA∈[0.5g, 1.0g) iii. PGA∈[1.0g, 1.5g) iv. PGA∈[1.5g, $+\infty$). The degraded soil profiles are averaged within each class and four soil profiles are obtained to represent four different degradation levels. The SSI analyses are performed with the 100 ground motions on the free surface, as well as the impedances and seismic forces calculated from the four soil profiles, to compute the floor accelerations of the K-K NPP.

Anchorage failure of the electrical cabinet is considered in this study. The capacity is given by the floor spectral acceleration of the anchorage point around 4Hz, the assumed natural frequency of the cabinet. The maximum value of the floor spectral accelerations in the two horizontal directions, averaged over a frequency interval around 4Hz to account for the uncertainty, is defined as the EDP y:

$$y = \frac{1}{4.5 - 3.5} \max_{i=X,Y} \int_{3.5}^{4.5} S^e_{a,i}(f)\mathrm{d}f, \tag{3.4.1}$$

where $S^e_{a,i}$ denotes the spectral acceleration of the electrical equipment in the i-th direction. Figure 3.7 shows the 100 calculated EDPs as a function of the geometric mean of the PGAs of the horizontal seismic motions on the free surface.

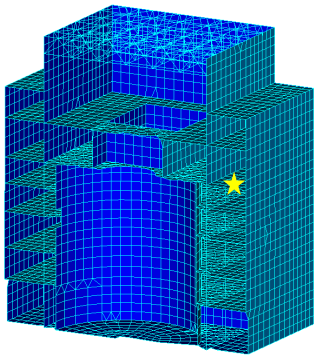

Figure 3.6: Location of the electrical cabinet in the K-K model (indicated by the star symbol)

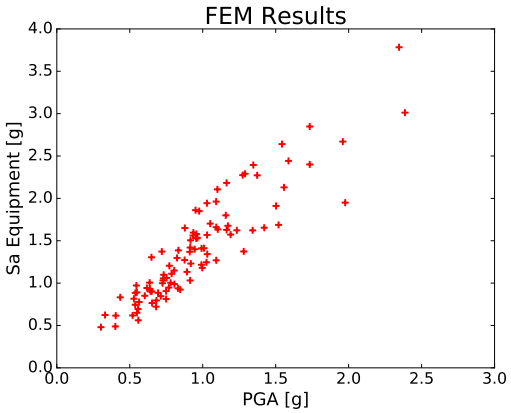

Figure 3.7: Point cloud of EDPs (Eq.3.4.1) calculated with FEM

3.4.2 Data Analysis

The 100 IMs-EDP obtained from FEM simulations can be used for the construction and the training of the ANN metamodel. Eight classical IMs are chosen as candidates for the inputs of the ANN metamodel. The eight IMs include the commonly used seismic intensity

indicators PGA, PGV, PGD, $\mathrm{PS}_a(f_0)$, CAV, Arias intensity I_A, as well as the predominant period T_p used in Stewart et al. [2001] and the ASA proposed in Biasio et al. [2015]. These IMs are presented in detail in Table 3.1. The geometric means of IMs in the two horizontal directions are used as scalar IMs for 3D ground motions. The integration domain of the ASA is slightly modified compared to its initial definition in Biasio et al. [2015], to consider the uncertainty on the natural frequency of the electrical cabinet. The correlation coefficients

Table 3.1: Definitions of classical seismic intensity measures

Intensity Measures	Definitions	Comments
PGA (peak ground acceleration)	$\max \lvert a(t) \rvert$	$a(t)$: seismic acceleration
PGV (peak ground velocity)	$\max \lvert v(t) \rvert$	$v(t)$: seismic velocity
PGD (peak ground displacement)	$\max \lvert u(t) \rvert$	$u(t)$: seismic displacement
$\mathrm{PS}_a(f_0)$ (pseudo-spectral acceleration)	Spectral acceleration	f_0=4Hz, damping 5%
ASA (average spectral acceleration)	$\int_{3.5}^{4.5} \mathrm{PS}_a(f)\mathrm{d}f$	f: frequency
T_p (predominant period)	$\arg\max_T \mathrm{PS}_a(\frac{1}{T})$	$T = 1/f$
CAV (cumulative absolute velocity)	$\int_0^{t_{\max}} \lvert a(t) \rvert \mathrm{d}t$	$t_{\max}$: total seismic duration
I_A (Arias intensity)	$\frac{\pi}{2g} \int_0^{t_{\max}} a(t)^2 \mathrm{d}t$	$g = 9.81\mathrm{m/s}^2$

ρ between the eight IMs and the EDP defined by 3.4.1 are listed in Table 3.2. It can be observed that, among all the eight chosen IMs, ASA is the most relevant IM to the EDP, whereas there is a very weak correlation for T_p.

Table 3.2: Correlation coefficients between IMs and EDP

Intensity Measures	PGA	PGV	PGD	PS_a	ASA	T_p	CAV	I_A
ρ	0.913	0.693	0.420	0.920	0.950	0.093	0.889	0.890

The statistical distributions of the eight selected IMs are examined to check their lognormality. The eight proposed IMs are normalized and compared to $\mathcal{N}(0,1)$. The normalization is realized by

$$\alpha_{\mathrm{Norm}} = \frac{\ln \alpha - \mu_{\ln \alpha}}{\sigma_{\ln \alpha}}, \tag{3.4.2}$$

where $\mu_{\ln \alpha}$ and $\sigma_{\ln \alpha}$ denote the mean and the Std of $\ln \alpha$, respectively. For simplicity of illustration, the probability plots of three IMs (PGA, ASA and I_A) are shown in Figure 3.8. Besides, the values of the coefficients of determination R^2 of the probability plots are given in Table 3, for all the eight IMs: the closer to the lognormal distribution the IM is, the closer to 1 the value of R^2 will be. It can be concluded that it is reasonable to apply the lognormal distribution model to all eight IMs.

Table 3.3: Coefficients of determination of the probability plots

Intensity Measures	PGA	PGV	PGD	PS_a	ASA	T_p	CAV	I_A
R^2	0.9877	0.9970	0.9915	0.9866	0.9896	0.9823	0.9912	0.9913

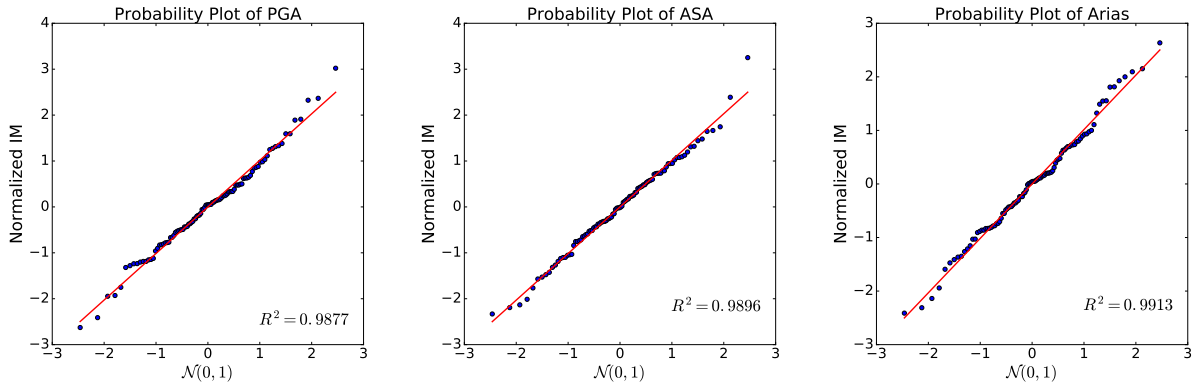

(a) Probability plot for PGA (b) Probability plot for ASA (c) Probability plot for I_A

Figure 3.8: Probability plots for PGA, ASA and I_A to check their lognormality

3.4.3 Selection of Relevant IMs and Determination of ANN Structures

Feature selection Due to the limited size of the data set (100 IMs-EDP), it is necessary to apply feature selection to obtain a reliable ANN metamodel with good generalization capabilities. A very complex ANN with a large number of unknown weights can easily to be overfitted, given the underlying data set. The features (IMs) are selected with the SPCC filter approach proposed in Section 3.3.2. The result after the feature selection with SPCC is illustrated in Figure 3.9. From the forward selection result, ASA and I_A are selected as the relevant features because the R^{SP} for the other IMs are less than 0.05, so that they can be regarded as non-influential if ASA and I_A have already been considered.

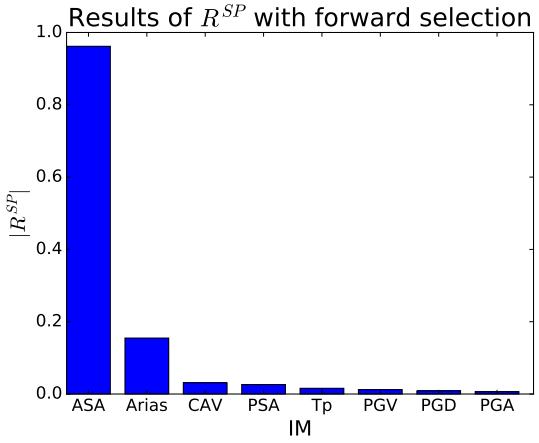

Figure 3.9: Results of forward selection

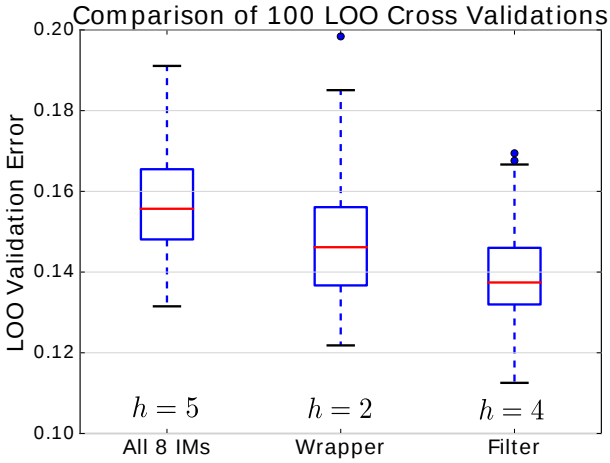

Figure 3.10: LOO cross-validation results for different ANNs

The number of the neurons h in the hidden layer should be determined additionally. For this purpose, the total set of 100 data is separated into 2 subsets: 80 data for training and cross-validation (T-CV data), and 20 data for test. The 20 test data are not used to determine the structure of the ANN, but used later to evaluate the generalization capacity of the trained

ANN. 4-fold cross-validation based on 80 T-CV data is executed on ANNs with $h = 1, 2, \dots 8$ of hidden neurons, respectively, in order to select the optimal number: The ANN structure with the smallest 4-fold cross-validation error is chosen for the final metamodel. The optimal value of h determined by the described approach is 4.

Comparison of selected features We compare our results to the features selected with the wrapper approach based on GA used in Ferrario et al. [2015]. The final feature subset selected by GA is ASA and CAV, with $h = 2$ in the hidden layer. It can be observed that both approaches select similar seismic IMs: ASA, the most efficient IM in this study (Table 3.2), and an IM concerning the integration of the ground motion acceleration over the signal duration (I_A or CAV).

In order to highlight the necessity of the feature selection, the leaving-one-out (LOO) cross-validation is carried out with the ANN structures determined by the feature selection procedures, as well as the ANN without dimensionality reduction (i.e. with all eight IMs. The number of hidden nodes is $h = 5$). With random initializations of ANN weighting parameters, 100 LOO cross-validations have been performed. The box-plot of the LOO cross-validation error is shown in Figure 3.10. From the results, one can observe that the ANN models determined by feature selections show more accuracy. In addition, the ANN model with the filter approach performs best in the LOO cross-validation.

Therefore, in the sequel of this paper, the ANN is trained with two inputs (ASA and I_A), four hidden layer nodes and one output, which is computed according to Eq. 3.4.1. Point clouds and fragility curves will be plotted with ASA, which is the most efficient IM in this study.

3.4.4 Results of the ANN Training

Training results Training based on the back-propagation algorithm is carried out with the ANN structure determined by the filter approach. The ANN toolbox used in this study is an open-source python package 'Neurolab' with the implemented delta method for the quantification of ANN prediction uncertainties. The 80 T-CV data in Chapter 3.4.3 is again divided into 2 subsets: 60 data for training and 20 data for validation. Early stopping is applied on the validation set to avoid overfitting. The generalization capacity of the ANN is examined on the 20 test data. The ANN is trained in *log-log space*. The results of the ANN training are shown in Figure 3.11. From Figure 3.11, one can conclude that the training results are satisfactory. Most of the results in the 'prediction-target' space are located in the neighborhood of the dashed diagonal line. The point clouds of the ANN training and test compared to the FEM output are shown in Figure 3.12a and Figure 3.12a, respectively. Both reveal a globally satisfactory prediction quality: the ANN predictions remain coherent

with the FEM results. In fact, with a regression model like ANN, it is not possible to obtain the exact prediction results. In addition, it has to be pointed out that the dispersion of the ANN predictions is reduced compared to the FEM results. This is due to the loss of the aleatory uncertainty by reducing ground motions to two IMs in the ANN metamodeling. The underestimated variability in the ANN predictions will reduce the uncertainty in the fragility curve. The histogram of the normalized ANN training residuals is plotted in Figure 3.13. It can be observed that its distribution is close to $\mathcal{N}(0,1)$, so that the assumption of normality of the ANN residuals in the delta method can be considered reasonable in this study.

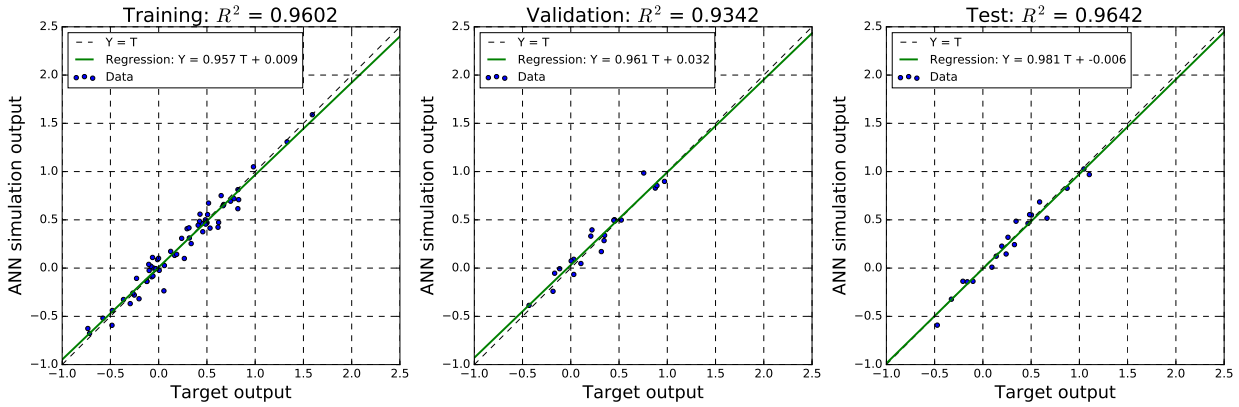

(a) Training set (b) Validation set (c) Test set

Figure 3.11: ANN training results

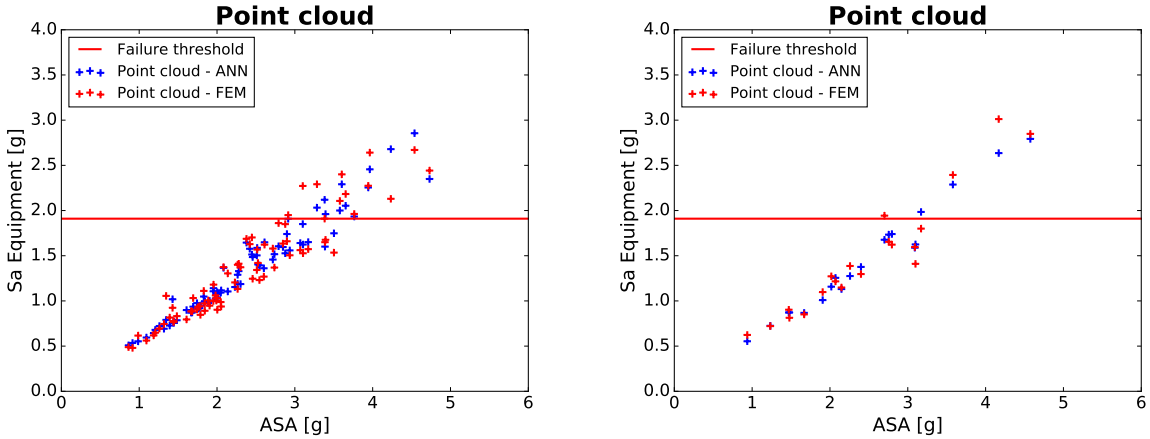

(a) ANN training and validation point cloud (b) ANN test point cloud

Figure 3.12: Point Clouds of ANN predictions for 80 T-CV dataset and 20 test dataset

Comparison with other metamodels The training results of the ANN are compared with those of other metamodels, including Kriging with Gaussian kernel (an interpolation model), Kriging with Gaussian and White noise kernel (a regression model) and quadratic response surface. The metamodels are constructed with 80 T-CV data and tested on 20 test

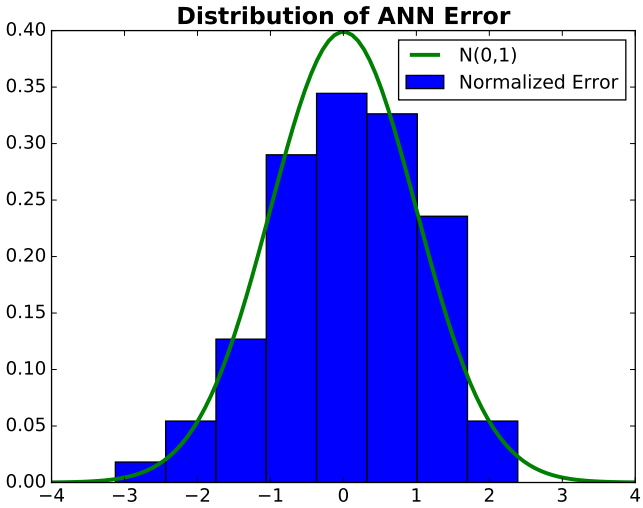

Figure 3.13: Distribution of ANN training residuals

data, using the python toolbox scikit-learn. The RMSE between metamodel predictions and FEM outputs is used to evaluate the accuracy of the different metamodels. The seismic IMs used are ASA and I_A, the same used for the ANN. The results are reported in Table 3.4.

Table 3.4: Training and test results for different metamodels

Model	RMSE Training (80 data)	RMSE Test (20 data)
ANN	0.141	0.135
Kriging interpolation[3]	0	0.43
Kriging regression[4]	0.153	0.145
Quadratic response surface	0.151	0.151

Several conclusions can be drawn from Table 3.4: (i) Kriging interpolation is not an appropriate metamodel for this study, since the test error is much larger than other models. The reason has already been discussed in Chapter 3.2.1: the zero residual in the training of Kriging overfits the model. The generalization capability of the interpolation Kriging model is thus very limited with the underlying data. (ii) Once the residual is present in the training data of the Kriging regression, the performance of the Kriging is largely improved. (iii) Quadratic response surface offers less nonlinearity than ANN, which is why its errors are larger. (iv) Overall, ANN shows slightly better performance than other considered metamodels.

Consideration of ANN prediction uncertainties The ANN model is validated in the previous subsections. Let us show in this part the necessity of the incorporation of the σ_{ANN} in the fragility curves. We focus on the 80 T-CV data used to train the ANN. Based on

[3]With Gaussian kernel.
[4]With a mixture of Gaussian kernel and white noise kernel.

the same 80 seismic inputs, one can obtain 80 structural outputs y and $\hat{y}$, from FEM and ANN simulations respectively. Fragility curves are computed with Reg method (Eq.3.2.6) for data set (α, y) and $(\alpha, \hat{y})$. The fragility curves are calculated for α =ASA and $\alpha = I_A$, respectively, in order to provide further discussions. At the same time, the 'modified Reg' method (Eq.3.3.4) is applied to the data set $(\alpha, \hat{y})$ to compute fragility curves, accounting for the aleatory residual uncertainty of the ANN predictions. From Figure 3.14, it can be seen

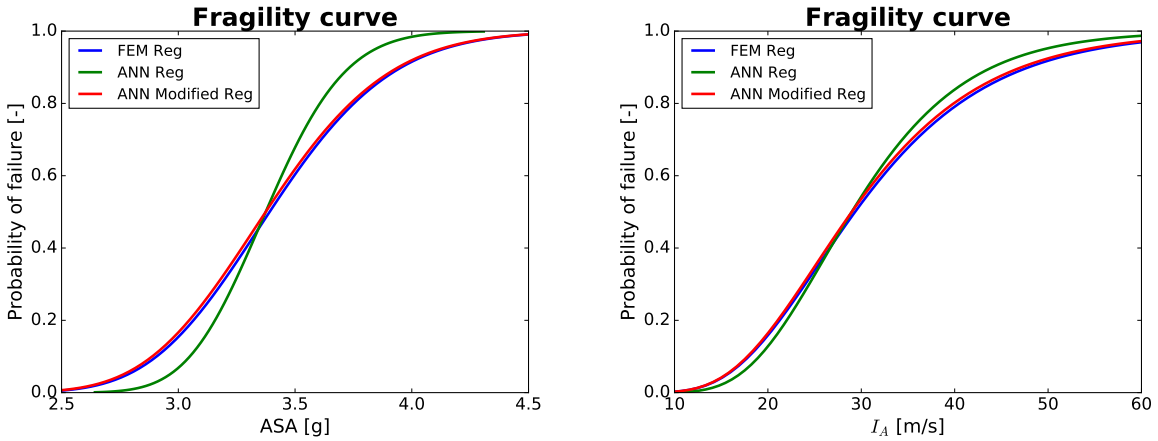

(a) Fragility curves computed with 80 T-CV data as function of ASA

(b) Fragility curves computed with 80 T-CV data as function of I_A

Figure 3.14: Fragility curves computed with 80 T-CV data

that:

- A clear difference between the fragility curves computed with FEM Reg and ANN Reg can be observed. The difference is much less evident for I_A than ASA. Nevertheless, this is not due to the fact that the ANN metamodel is poorly calibrated, because the ANN accuracy has been validated above and it is even better than other possible metamodels. If the fragility curves calculated with Reg method are not coherent for the training data between FEM and ANN, one can hardly trust the conditional probability of failure computed with the ANN based on other test data.

- The difference is due to the aleatory part of the ANN prediction uncertainty σ_{ANN}. It represents the seismic inherent randomness not identified in the inputs (ASA and I_A) of the ANN metamodel. Once σ_{ANN} is integrated in the computation of the conditional probability with Eq.3.3.4 , the computed fragility curves almost coincide with the FEM Reg curves, for both ASA and I_A. The conditional probability with Eq.3.3.4 provides also satisfactory results for the 20 test data (Figure 3.15).

- σ_{ANN} has less influence when the fragility curves are plotted for I_A. It is because I_A is less correlated to the output than ASA (Table 3.2). Consequently, $\beta^{\text{ANN}}_{R|I_A}$, which equals 0.326, is larger than $\beta^{\text{ANN}}_{R|ASA}$ (0.079), whereas σ_{ANN} (0.094) stays the same. Considering Eq.3.3.4, the impact of σ_{ANN} is less evident on the I_A curves than the ASA curves.

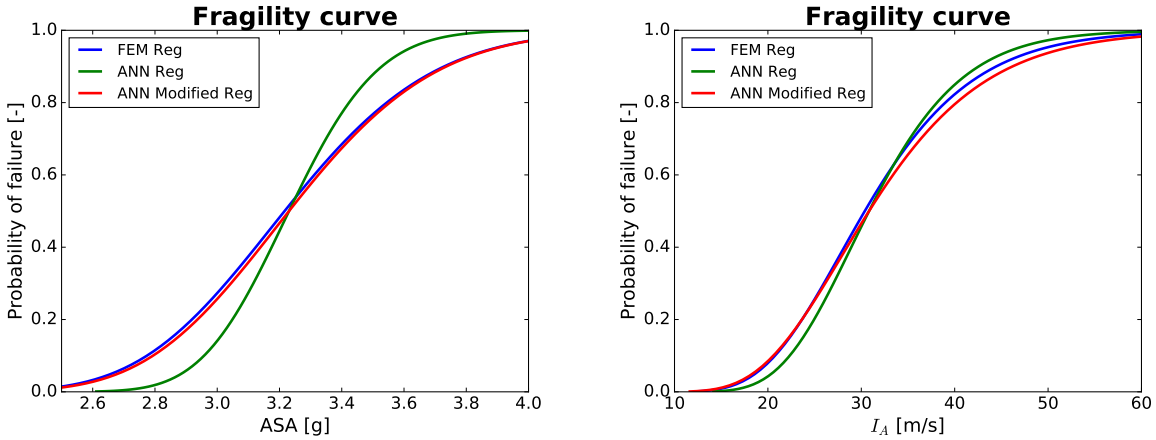

(a) Fragility curves computed with 20 test data as function of ASA

(b) Fragility curves computed with 20 test data as function of I_A

Figure 3.15: Fragility curves computed with 20 test data

These analyses show the importance of the consideration of σ_{ANN} in the computation of the fragility curves, where EDP results are provided by ANN simulations. Otherwise, the uncertainty in the fragility curves will be underestimated.

Besides, $\sigma_{\text{ANN,stat}}$ of the test data is also computed. Among the 20 test data, the positions of the first four data with the highest $\sigma_{\text{ANN,stat}}$ values are visualized in the input space in Figure 3.16. The numbers in the figure show the rank of their $\sigma_{\text{ANN,stat}}$ values in the 20 test data: '1' for the point with the highest $\sigma_{\text{ANN,stat}}$ value, '2' for the second highest, etc. It can be observed that the test data with high values of $\sigma_{\text{ANN,stat}}$ are located either at the lower boundary of the training data, or at the places where the training data are sparse, which is coherent with the property of $\sigma_{\text{ANN,stat}}$ shown in Figure 3.4.

3.4.5 Fragility Curves

After being trained, the ANN can be used to carry out fast-running simulations. For this purpose, a large number of seismic IMs have to be generated to represent the seismic motions. The following statistical properties of the lognormal distributions of ASA and I_A are obtained from the 100 triplets of seismic signals on the free surface (Table 3.5). The assumption of lognormality of the selected IMs has been validated in Section 3.4.2. With the large number of simulation results provided by the ANN, both methods presented in Section 3.3.5 can be applied for the computation of fragility curves.

Table 3.5: Statistics of ASA and I_A on the free surface

IM	Median	Log. standard deviation	ρ (ASA-I_A)
ASA [g]	2.28	0.417	0.846
I_A [m/s]	13.13	0.842	

For the lognormal based fragility curve, 10,000 ASA-I_A samples are generated with the statistics in Table 3.5. 10,000 ANN simulations are performed with these generated IMs, and the conditional probability of failure is computed with Eq.3.3.4. The computed fragility curve is described by ASA with median capacity $3.32g$ and uncertainty $\beta_{\text{Total}} = 0.127$, including $\sigma_{\text{ANN}} = 0.094$.

The pointwise fragility analysis is performed by conditional sampling of I_A for a given value of ASA, since a conditional bivariate normal distribution is also normally distributed. In the analysis, the values of ASA are selected in $[2.2g, 4.4g]$ with $\Delta\text{ASA} = 0.1g$. For every ASA value, 10,000 I_A are generated. At every ASA, the probability of failure is computed from Eq.3.3.5, and the CIs are determined with Eq.3.3.6. Fragility curves computed with both methods are shown in Figure 3.17.

Regarding the fragility curves, although there exist some differences between the lognormal based fragility curve and the MC estimation, the lognormal curve stays coherent with the pointwise MC curve. The lognormal assumption can be thus confirmed in this study. It is recalled that the source of the confidence intervals comes only from the paucity of the training data of the ANN.

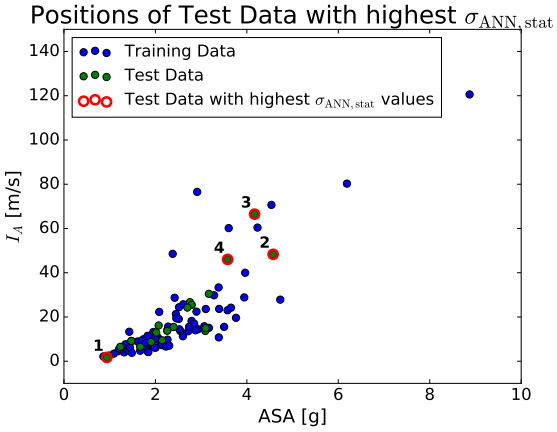

Figure 3.16: Positions of test data with highest $\sigma_{\text{ANN,stat}}$

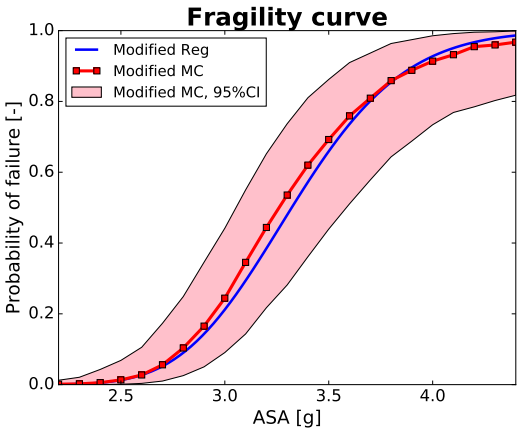

Figure 3.17: Fragility curves with ANN

3.4.6 Discussions

The proposed ANN-based fragility analysis has been applied to the K-K NPP to compute the fragility curve of an electrical cabinet. The assumptions made in this methodology are discussed what follows. The computational cost of the FEM analyses is also provided.

1. This study only considers seismic randomness in the FEM simulation. Uncertainties on structural parameters are not modeled. With other source of uncertainties, the seismic IM is less correlated to the structural output, so that the influence of the aleatory component of the metamodel uncertainty is less evident.

2. Moreover, the variability in the responses of the considered electrical cabinet is dominated by the seismic record-to-record randomness. To justify this, the material uncertainties of concrete in Table 3.6 is considered for the first 50 seismic excitations. The values of the coefficients of variation of Table 3.6 are selected according to our expertise. The lognormal model of the material parameters has been suggested and used in Kennedy et al. [1980]; Liel et al. [2009]; Calabresea and Lai [2013]; Buratti et al. [2010]; Ghosh et al. [2013]. 50 FEM simulations are performed with the material uncertainties, with the stochastic values of Table 3.6 applied to the entire structure. The corresponding fragility curve is computed with Reg method. Meanwhile, a fragility curve is calculated also with Reg method based on the first 50 FEM simulation results of this study (i.e. without the consideration of material uncertainties). Seismic excitations for both cases remain the same. The comparison of two fragility curves is shown in Figure 3.18. It can be clearly observed that there is no obvious difference between the two fragility curves, which implies that the impact of the material randomness can be neglected compared to the earthquake randomness. That is another reason why material uncertainties are not modeled in this study. With uncertainty uniquely from seismic ground motions, the selection of IMs becomes therefore crucial to ensure the accuracy of the ANN.

Table 3.6: Uncertainties in material parameters of concrete in K-K NPP

Material parameters	Distribution	Median	Coefficient of variation
Young's modulus	Lognormal	31,300 MPa	0.2
Poisson ratio	Lognormal	0.2	0.1
Density	Lognormal	2500 kg/m^3	0.05
Modal damping ratio	Lognormal	0.05	0.4

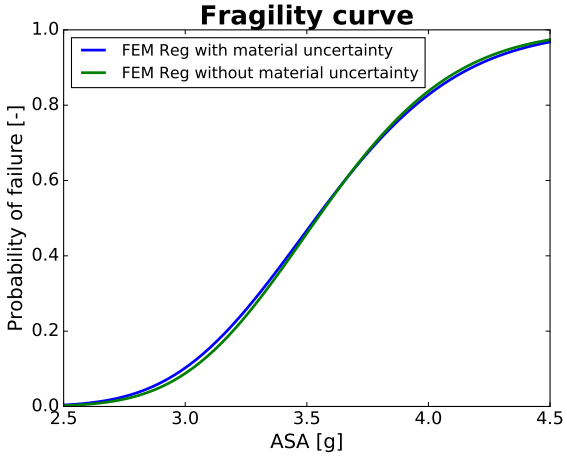

Figure 3.18: Comparison between fragility curves with or without material uncertainties

3. The ANN training errors are assumed to follow a normal distribution. The validity of this assumption is confirmed in this study. In addition, with a more mathematically

rigorous derivation, the ANN prediction uncertainty should have followed a student t distribution. This approximation by a normal distribution allows the decomposition of the ANN prediction uncertainty into two normal aleatory and epistemic components.

4. The computational cost of the FEM simulations is listed in Table 3.7. Based on the soil impedances computed by BEM, one single FEM analysis takes $(120.02 + 66.86)/100 = 1.87$ hours on an Intel Xeon E5-2600V2 CPU of 2.7GHz, which makes it almost unaffordable to run a large number of FEM simulations for the pointwise MC fragility analysis. However, once the ANN metamodel is established, the pointwise MC fragility analysis can be conducted within 0.25 hours. It has to be noticed that the ANN metamodel is constructed from the results of 100 FEM simulations, which means that $132.41 + 120.02 + 66.86 = 319.29$ hours of mechanical simulations are the prerequisites for the ANN metamodel construction.

Table 3.7: Computational cost for numerical analyses

Type of analyses	Number of analyses	Total computational time
BEM for soil impedances	4	132.41 hours
ELM analyses	100	120.02 hours
SSI analyses	100	66.86 hours
ANN simulations for MC fragility analysis	10,000 × 23	0.25 hours

3.5 Summary

A methodology of ANN metamodels for the computation of fragility curves has been proposed in this chapter. The ANN metamodel is utilized to build the statistical relation between the seismic intensity measures and the structural response. Once trained, the ANN metamodel allows carrying out a large number of simulations for both parametric and non-parametric fragility analyses, at negligible computational cost. Based on FEM simulation results, this methodology mainly consists of:

- Selection of the most relevant seismic intensity measure features. A filter approach based on semi-partial correlation coefficients is proposed in this study. It is compared with a wrapper approach based on GA. In the case study considered, the filter selection method shows slightly more advantages, in terms of accuracy and efficiency. Once the features have been retained, the ANN is trained with early stopping to prevent overfitting.

- Identification of the aleatory uncertainty and the epistemic uncertainty components in the ANN prediction uncertainties. The aleatory uncertainty is incorporated in the fragility curve, while the epistemic uncertainty is used to compute the confidence intervals.

- Computation of fragility curves and their confidence intervals, with both lognormal assumption and pointwise MC methods. The Reg and MC methods are adapted to take into

account the ANN prediction uncertainties. The non-parametric MC fragility curve is used to verify the lognormal assumption, which is widely adopted in the fragility analysis.

Instead of methods based on repeated ANN trainings realized in Ferrario et al. [2017], more efficient algorithms for the feature selection and the ANN prediction uncertainty quantification have been applied. Moreover, the ANN prediction uncertainty has been discussed thoroughly. This methodology has been applied to an industrial complex case study, i.e. Kashiwazaki-Kariwa nuclear power plant in Japan to evaluate the robustness of an electrical cabinet. The fragility curve computed with the lognormal assumption is described by ASA with median capacity $3.32g$ and uncertainty $\beta_{\text{Total}} = 0.127$. In addition, compared to the results of the pointwise MC estimation in this study, it is reasonable to assume a lognormal distribution for the fragility curves.

Bibliography

Ataei, N. and Padgett, J. E. (2015). Fragility surrogate models for coastal bridges in hurricane prone zones. *Eng. Struct.*, 103:203–213.

Baker, J. W. (2007). Correlation of ground motion intensity parameters used for predicting structural and geotechnical response. In *Proceedings of the 10th International Conference on Applications of Statistics and Probability in Civil Engineering, Tokyo.*

Biasio, M. D., Grange, S., Dufour, F., Allain, F., and Petre-Lazar, I. (2015). Intensity measures for probabilistic assessment of non-structural components acceleration demand. *Earthquake Eng. Struct. Dyn.*, 44:2261–2280.

Bishop, C. M. (1995). *Neural Networks for Pattern Recognition.* Oxford University Press.

Buratti, N., Ferracuti, B., and Savoia, M. (2010). Response surface with random factors for seismic fragility of reinforced concrete frames. *Struct. Saf.*, 32:42–51.

Calabresea, A. and Lai, C. G. (2013). Fragility functions of blockwork wharves using artificial neural networks. *Soil Dyn. Earthquake Eng.*, 52:88–102.

Campbell, K. W. and Bozorgnia, Y. (2008). NGA ground motion model for the geometric mean horizontal component of PGA, PGV, PGD and 5% damped linear elastic response spectra for periods ranging from 0.01 to 10 s. *Earthquake Spectra*, 24:139–171.

Cornell, C. A., Jalayer, F., Hamburger, R. O., and Foutch, D. A. (2002). Probabilistic basis for 2000 SAC federal emergency management agency steel moment frame guidelines. *J. Struct. Eng.*, 128:526–533.

Ditlevesen, O. and Madsen, H. (2005). *Structural Reliability Methods.*

Ellingwood, B. R. and Kinali, K. (2009). Quantifying and communicating uncertainty in seismic risk assessment. *Struct. Saf.*, 31:179–187.

EPRI (1994). Methodology for developing seismic fragilities. Technical report, Electric Power Research Institute EPRI, Palo Alto, CA. Report TR-103959.

Ferrario, E., Pedroni, N., Zio, E., and Lopez-Caballero, F. (2015). Application of metamodel-based techniques for the efficient seismic analysis of structural systems. In *Safety and Reliability of Complex Engineered Systems, ESREL*, pages 1193–1200.

Ferrario, E., Pedroni, N., Zio, E., and Lopez-Caballero, F. (2017). Bootstrapped artificial neural networks for the seismic analysis of structural systems. *Struct. Saf.*, 67:70–84.

Gehl, P. and D'Ayala, D. (2016). Development of bayesian networks for the multi-hazard fragility assessment of bridge systems. *Struct. Saf.*, 60:37–46.

Ghosh, J., Padgett, J. E., and Dueñas-Osorio, L. (2013). Surrogate modeling and failure surface visualization for ef ficient seismic vulnerability assessment of highway bridges. *Probab. Eng. Mech.*, 34:189–199.

Gidaris, I., Taflanidis, A. A., and Mavroeidis, G. P. (2015). Kriging metamodeling in seismic risk assessment based on stochastic ground motion models. *Earthquake Eng. Struct. Dyn.*, 44(14):2377–2399.

Jia, G. and A.Taflanidis, A. (2013). Kriging metamodeling for approximation of high-dimensional wave and surge responses in real-time storm/hurricane risk assessment. *Comput. Methods in Appl. Mech. Eng.*, 261–262:24–38.

Kennedy, R., Cornell, C., Campell, R., Kaplan, S., and Perla, H. (1980). Probabilistic seismic safety study of an existing nuclear power plant. *Nucl. Eng. Des.*, 59:315–338.

Kohavi, R. and John, G. H. (1997). Wrappers for feature subset selection. *Artif. Intell.*, 97:273–324.

Lagaros, N. D. and Fragiadakis, M. (2007). Fragility assessment of steel frames using neural networks. *Earthquake Spectra*, 23:735–752.

Lagaros, N. D., Tsompanakis, Y., Psarropoulos, P. N., and Georgopoulos, E. C. (2009). Computationally efficient seismic fragility analysis of geostructures. *Comput. Struct.*, 87:1195–1203.

Lallemant, D., Kiremidjian, A., and Burton, H. (2015). Statistical procedures for developing earthquake damage fragility curves. *Earthquake Eng. Struct. Dyn.*, 44:1373–1389.

Liel, A. B., Haselton, C. B., Deierlein, G. G., and Baker, J. W. (2009). Incorporating modeling uncertainties in the assessment of seismic collapse risk of buildings. *Struct. Saf.*, 31:197–211.

Lopez-Caballero, F. and Khalil, C. (2018). Vulnerability assessment for earthquake liquefaction–induced settlements of an embankment using Gaussian processes. *ASCE-ASME Journal of Risk and Uncertainty in Engineering Systems, Part A: Civil Engineering*, 4.

Mai, C., Konakli, K., and Sudret, B. (2017). Seismic fragility curves for structures using non-parametric representations. *Front. Struct. Civ. Eng.*, 11:169–186.

Mai, C. V., Spiridonakos, M. D., Chatzi, E. N., and Sudret, B. (2016). Surrogate modelling for stochastic dynamical systems by combining narx models and polynomial chaos expansions. *International Journal for Uncertainty Quantification*, 6:419–430.

Mangalathu, S., Jeon, J.-S., and DesRoches, R. (2017). Critical uncertainty parameters influencing seismic performance of bridges using lasso regression. *Earthquake Eng. Struct. Dyn.*

Mitropoulou, C. C. and Papadrakakis, M. (2011). Developing fragility curves based on neural network IDA predictions. *Eng. Struct.*, 33:3409–3421.

Noh, H. Y., Lallemant, D., and Kiremidjian, A. S. (2015). Development of empirical and analytical fragility functions using kernel smoothing methods. *Earthquake Eng. Struct. Dyn.*, 44:1163–1180.

Park, J. and Towashiraporn, P. (2014). Rapid seismic damage assessment of railway bridges using the response-surface statistical model. *Struct. Saf.*, 47:1–12.

Pedroni, N., Zio, E., and Apostolakis, G. (2010). Comparison of bootstrapped artificial neural networks and quadratic response surfaces for the estimation of the functional failure probability of a thermal–hydraulic passive system. *Reliab. Eng. Syst. Safe.*, 95(4):386–395.

Perrault, M. (2013). *Evaluation de la vulnérabilité sismique de bâtiments à partir de mesures in situ*. PhD thesis, Université de Grenoble.

Reed, R. D. and Marks, R. J. (1999). *Neural Smithing*. MIT Press.

Saha, S. K., Matsagar, V., and Chakraborty, S. (2016). Uncertainty quantification and seismic fragility of base-isolated liquid storage tanks using response surface models. *Probab. Eng. Mech.*, 43:20–35.

Seo, J., Dueñas-Osorio, L., Craig, J. I., and Goodno, B. J. (2012). Metamodel-based regional vulnerability estimate of irregular steel moment-frame structures subjected to earthquake events. *Eng. Struct.*, 45:585–597.

Seo, J. and Linzell, D. G. (2013). Use of response surface metamodels to generate system level fragilities for existing curved steel bridges. *Eng. Struct.*, 52:642–653.

Shinozuka, M., Feng, M. Q., Lee, J., and Naganuma, T. (2000). Statistical analysis of fragility curves. *J. Eng. Mech.*, 126:1224–1231.

Stewart, J. P., Chiou, S.-J., Bray, J. D., Graves, R. W., Somerville, P. G., and Abrahamson, N. A. (2001). Ground motion evaluation procedures for performance-based design. Technical report, Pacific Earthquake Engineering Research Center.

Unnikrishnan, V. U., Prasad, A. M., and Rao, B. N. (2013). Development of fragility curves using high-dimensional model representation. *Earthquake Eng. Struct. Dyn.*, 42:419–430.

Xu, H. and Gardoni, P. (2016). Probabilistic capacity and seismic demand models and fragility estimates for reinforced concrete buildings based on three-dimensional analyses. *Eng. Struct.*, 112:200–214.

Yoshida, N., Kobayashi, S., Suetomi, I., and Miura, K. (2002). Equivalent linear method considering frequency dependent characteristics of stiffness and damping. *Soil. Dyn. Earthq. Eng.*, 22:205–222.

Zentner, I. and Borgonovo, E. (2014). Construction of variance-based metamodels for probabilistic seismic analysis and fragility assessment. *Georisk*, 8:202–216.

Zentner, I., Gündel, M., and Bonfils, N. (2017). Fragility analysis methods: Review of existing approaches and application. *Nucl. Eng. Des.*, 323:245–258.

Chapter 4

A Bayesian Framework for Integrating Damage Data in Fragilities by Adaptive ANNs

The estimation of the parameters of the fragility curves requires to gather different sources of information and to quantify the uncertainties coming from these sources. This chapter is dedicated to describe a methodology for the computation of fragility curves for nuclear power plant equipment with a Bayesian updating framework. Based on the fragility curves determined by simulation-based methods explained in the previous chapters, this framework allows integrating the damage data into the computation of the fragility curves. The results of the numerical simulations provide a prior estimation of the seismic capacity of the equipment. Damage data, collected from the in-situ observation and the database of the seismic qualification utility group (SQUG), are used to construct the likelihood function for the Bayesian updating. The posterior equipment capacity is evaluated by Markov chain Monte Carlo simulation and posterior fragility curves are, then, obtained. The methodology is applied to compute the fragility curves of a low-voltage switchgear of a nuclear power plant, within the KARISMA benchmark.

Contents

4.1 Introduction

The computation of fragility curves is typically realized by statistical analysis based on different sources of information, including expert judgments, numerical simulations, empirical damage data. The safety factor method [Kennedy et al. 1980; EPRI 1994], largely used in nuclear engineering, depends on safety margins determined from simplified structural analyses and experimental data. Uncertainties are evaluated from expertise of engineers or results of qualification tests. The safety margins and their associated uncertainties are used to assess the seismic capacity of structures and equipment. This method does not require numerical simulations. However, the safety margins determined from the simplified approaches can be conservative, and thus, cannot offer a best estimate of the fragility curves.

Numerical simulations are commonly applied in the current practice of fragility analysis, e.g. by the finite element method (FEM) [Padgett and DesRoches 2008; Ellingwood and Kinali 2009; Zentner 2010]. Different sources of aleatory and epistemic uncertainties can be modeled and propagated through the numerical model. The conditional probability of failure can be computed either by pointwise Monte Carlo estimation or by assuming a parametric representation (e.g. lognormal) of fragility curves, as mentioned in Chapter 3. The underlying parameters of the fragility curves are determined based on the results of the simulations. However, because of the high complexity of numerical models, the computational cost of the numerical analyses can be very high. One way to reduce the computational burden is to use fast-running statistical metamodels, such as artificial neural networks (ANNs). Nevertheless, due to the fact that a numerical model cannot contain all the structural details and damage mechanisms, damage data of structures and equipment can be used for a more accurate computation of fragility curves.

Damage data have been also widely used for seismic fragility analysis. The damage data are obtained either from post-earthquake observations or from qualification tests. They are used to describe the performance of structures or equipment under real seismic excitations. Fragility analysis is, then, conducted by statistical analysis of the damage data. For example, fragility curves for European-type reinforced concrete buildings are determined in Rossetto and Elnashai [2003] with earthquake observational data. Using Italian seismic damage data, fragility curves for different building typologies are built in Rota et al. [2008] to provide a reliable estimate of the vulnerability of structures of different classes. In these works, the fragility curves are obtained directly by fitting the damage data into a cumulative distribution

function (CDF) of the lognormal distribution. Other studies adopt Bayesian statistics to estimate the fragility parameters [Straub and Kiureghian 2008; Gardoni et al. 2009]. In the Bayesian framework, prior distributions of the fragility parameters are assumed. Then, damage data are used to build the likelihood function. The fragility parameters can be generated by Markov chain Monte Carlo simulation (MCMC) [Hastings 1970], based on the posterior distributions obtained from Bayesian updating. The advantage of the Bayesian statistics is that it yields a probability distribution of the parameters to be estimated (so the confidence intervals can be computed), rather than a single value for the estimation of these parameters. Representative examples of the application of Bayesian statistics in seismic risk assessment can be found in Singhal and Kiremidjian [1998], Koutsourelakis [2010], Jalayer et al. [2010], EPRI [2014], Jaiswal et al. [2011], Beck and Taflanidis [2013], Buratti et al. [2017], Noh et al. [2017], Jeon et al. [2017], EPRI [2017], among others.

The objective of this chapter is to propose a framework to take into consideration both numerical simulation results and damage data in the computation of fragility curves. The methodology is divided into two parts: (i) estimation of the prior parameters with numerical simulations: to reduce the computational cost, an ANN metamodel is trained with an iterative active learning algorithm to substitute the computationally expensive FEM simulation; (ii) computation of the likelihood function with the damage data and execution of Bayesian updating to obtain the posterior distribution of the seismic capacity of the equipment. Different sources of uncertainties (aleatory and epistemic) are quantified and integrated in the computation of the fragility curves. Critical equipment of nuclear power plants are designed with high safety standards. The low probability of failure of the equipment may lead to a biased estimation of the fragility parameters, if the these parameters are solely determined by the maximum likelihood estimation [Shinozuka et al. 2000]. This requires assessing the confidence associated to the estimation, which can be achieved in the Bayesian framework.

This chapter is organized as follows. We start to describe the global methodology to account for different sources of information in the computation of fragility curves. It consists of the determination of the prior fragility curves with numerical simulations results and the Bayesian updating with damage data. The proposed methodology is later applied to evaluate the robustness of a low-voltage switchgear located in the Kashiwazaki-Kariwa nuclear power plant in Japan. Final conclusions are given at the end.

4.2 Description of the Methodology

4.2.1 Seismic Fragility Curves

Fragility curves compute the conditional probability that the engineering demand parameter (EDP) exceeds a failure threshold, for a given seismic IM:

$$P_f(\alpha) = P(y > y_{\text{crit}}|\alpha), \tag{4.2.1}$$

where y is the EDP, such as inter-story drift, y_{crit} is the failure threshold and α represents the seismic IM. The lognormal fragility model proposed in Kennedy et al. [1980] is often applied in practice. In the lognormal assumption, the shape of the fragility curve is approximated by the CDF of a lognormal distribution:

$$P_f(\alpha) = \mathbf{\Phi}(\frac{\ln \alpha - \ln \hat{A}_m}{\beta_R}) \tag{4.2.2}$$

where $\mathbf{\Phi}(\cdot)$ is the CDF of the standard normal distribution $\mathcal{N}(0,1)$, $\hat{A}_m$ denotes the median capacity. The parameter β_R represents the aleatory uncertainty related to the inherent randomness. According to Kennedy et al. [1980], an epistemic uncertainty β_U, resulting from the lack of knowledge of the structural capacity, should be also considered:

$$\hat{A}_m \sim LogN(A_m, \beta_U^2), \tag{4.2.3}$$

where A_m is the median of the lognormal distribution and $LogN$ denotes a lognormal distribution. Consequently, the $\gamma \in [0,1]$ non-exceedance confidence interval of the fragility curves can be computed by [EPRI 1994]

$$\tilde{P}_f(\alpha, \gamma) = \mathbf{\Phi}(\frac{\ln \alpha - \ln A_m + \beta_U \mathbf{\Phi}^{-1}(\gamma)}{\beta_R}). \tag{4.2.4}$$

Eq.4.2.4 allows computing the high confidence low probability of failure (HCLPF), defined as the capacity where the probability of failure reaches 5% with 95% confidence:

$$A_{\text{HCLPF}} = A_m e^{-1.645(\beta_R + \beta_U)} \tag{4.2.5}$$

The mean fragility curve, which considers both aleatory and epistemic uncertainties, is defined by

$$P_f^{\text{mean}}(\alpha) = \mathbf{\Phi}(\frac{\ln \alpha - \ln A_m}{\sqrt{\beta_R^2 + \beta_U^2}}). \tag{4.2.6}$$

The objective of the subsequent subsections is to describe the methodology to compute

fragility curves for an equipment of interest located in a specific NPP structure, which is named 'target structure' in the sequel. The numerical model of the target structure is available. The general workflow of the proposed methodology is illustrated in Figure 4.1. In this framework, reference values of β_U^{prior} and y_{crit} are obtained from the literature. To better explain the methodology, we start with the determination of prior fragility parameters based on numerical simulation results. Bayesian updating and MCMC are, then, executed with damage data to obtain the posterior curves. The assumptions made in this methodology are:

1. The fragility curves in this paper are all calculated under lognormal distribution assumptions, namely (i) the fragility curves are computed by the lognormal CDFs (Eq.4.2.2) and (ii) the epistemic uncertainty is considered lognormally distributed (Eq.4.2.3), in order to facilitate the application of the Bayesian theorem based on the damage data.
2. The seismic record-to-record variability is considered as the only source of aleatory uncertainty.
3. PGA is the IM parameter used to compute the fragility curves, since most damage data are provided with given values of PGA.
4. Without different specification, the PGA used in the fragility curve stands for the PGA value of the ground motion on the soil free surface in the proximity of the target structure.

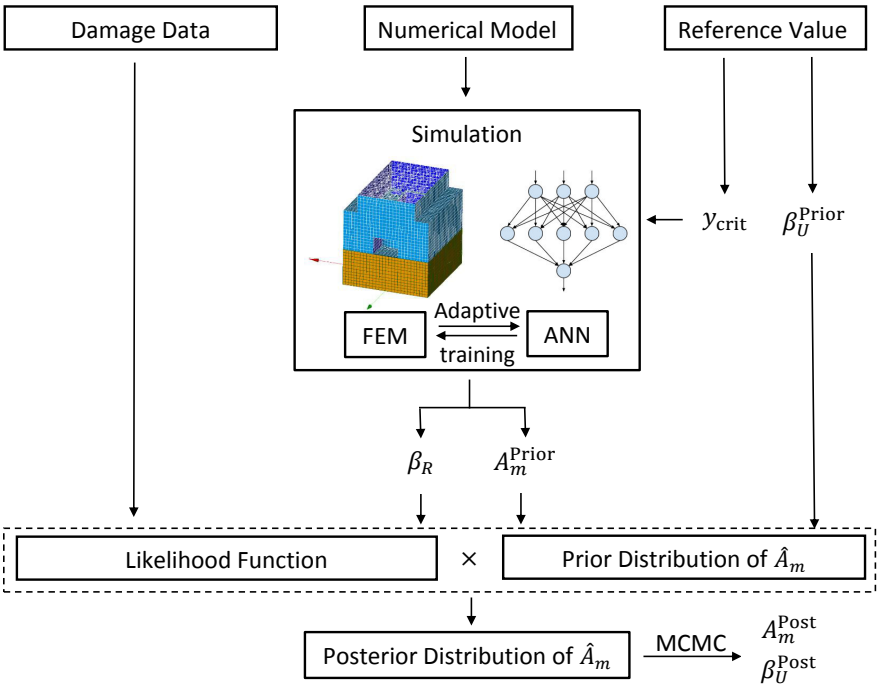

Figure 4.1: The Bayesian framework for fragility analysis

4.2.2 Determination of Prior Fragility Curve Parameters with Adaptive ANNs

Prior fragility curve parameters are determined based on the results of numerical simulations. FEM is one of the most widely used numerical methods for structural analysis. However, in case of a complex structure, the large number of degrees of freedom of the numerical model makes the resolution process highly computationally expensive. In this case, metamodels, calibrated from the existing simulation results, can be used to substitute the mechanical model, in order to improve the computational efficiency. The ANN, as in Chapter 3, is adopted.

In this subsection, the method to determine the parameters of prior fragility curves is explained. The adaptive training of ANN, explained in Chapter 2.3.2, is applied to optimize the design of experience. With the adaptive enrichment, the quality of the training data is largely improved by reducing its scarcity in the design space. Therefore, less FEM numerical simulations are needed for the calibration of the ANN metamodel.

The ANN adaptive algorithm is based on the prediction uncertainty of ANNs computed with the delta method. It adds iteratively in the training dataset the points at the location where the performance of the metamodel is limited, with a large prediction uncertainty. The iterative training of ANNs is stopped when a certain accuracy criterion is satisfied. Such an enrichment strategy not only can select the training data that better cover the whole input space, but also can enlarge the domain of the validity of the ANN metamodel, which is determined by the boundary of the input data. The working mechanism of the ANN adaptive learning algorithm is the same the one explained in Chapter 2.3.2 with the following learning function and stopping condition.

Learning function: With the ANN trained at the iteration k, ANN predictions $\hat{y}_k^i$ and the associated prediction uncertainty s_k^i can be obtained. At every iteration, the accuracy metric δ_k^i and the accuracy threshold δ_k^{crit} are computed:

$$s_{\text{ref},k} = \frac{1}{N_k} \sum_{p=1}^{N_k} s_k^p, \text{ for } p \text{ in the training set } (p = 1, ..., N_k); \tag{4.2.7}$$

$$\delta_k^i = \frac{|s_k^i - s_{\text{ref},k}|}{s_{\text{ref},k}}, \text{ for every } i \text{ in } X \ (i = 1, ..., N); \tag{4.2.8}$$

$$\delta_k^{\text{crit}} = \max_p(\delta_k^p), \text{ for } p \text{ in the training set } (p = 1, ..., N_k), \tag{4.2.9}$$

in which N is the total number of data in the initial Monte Carlo population X and N_k denotes the number of the ANN training data at the iteration k. The quantity $s_{\text{ref},k}$ is the mean value of the prediction uncertainty of the training examples at the iteration k.

It serves as the reference value to compute the accuracy metric. The accuracy metric δ_k^i calculates the relative deviation of s_k^i with respect to $s_{\mathrm{ref,k}}$. A large value of δ_k^i indicates a large prediction uncertainty s_k^i, so that the corresponding ANN prediction is less reliable. The accuracy threshold δ_k^{crit} is set as the maximal relative deviation of prediction uncertainty in the training dataset.

The set of test samples is defined by all the samples in X which are not used to train the ANN. If the accuracy of the ANN is not satisfied according to the later defined stopping condition, M samples in the test set with the largest δ_k^i values (i.e. with the largest prediction deviations) are selected to run the FEM simulations. The results of the FEM simulations are added to the ANN training data.

Stopping condition: When δ_k^i of every test sample is smaller than the accuracy threshold, i.e. $\max(\delta_k^{\mathrm{test}}) < \delta_k^{\mathrm{crit}}$, it can be considered that the samples in the ANN training set are enough to cover the whole input space of the population X. So the ANN can be considered accurate enough for the whole population X. The iterative training can be, therefore, stopped. Otherwise, a further enrichment of the training data is necessary.

The whole workflow of the adaptive ANN algorithm is summarized in Figure 4.2. With

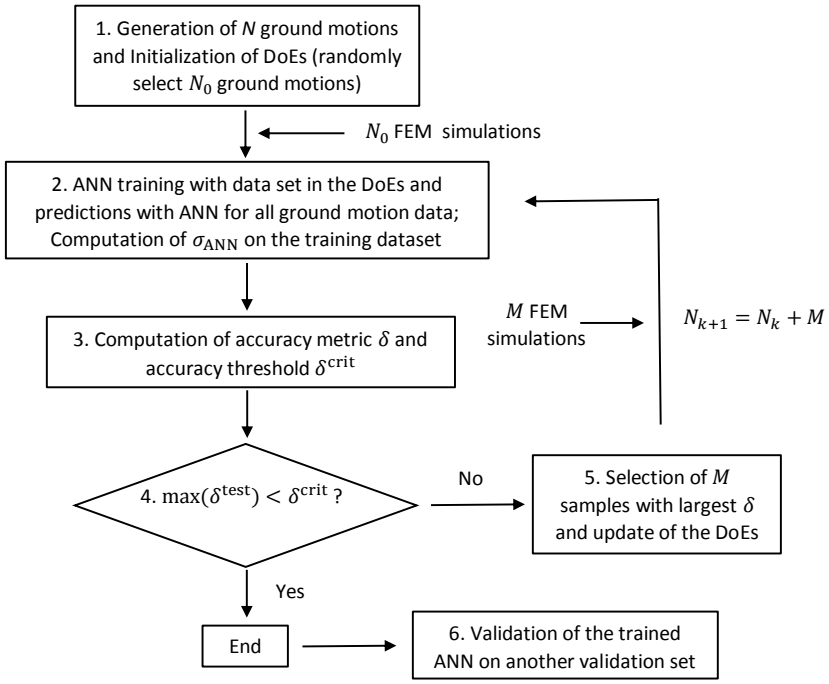

Figure 4.2: Workflow of the adaptive training of ANNs

a reasonable number of FEM simulations, an ANN is obtained at the end of the adaptive training. Then, ANN simulations can be carried out for ground motions in the whole population X to predict the structural EDPs $\hat{y}$.

Prior fragility parameters β_R and A_m^{prior} can be estimated from the ANN simulation results. The failure threshold y_{crit}, informed from the reference value in the literature, provides an estimation of A_m^{prior}. The Std of the ANN training error is integrated in the computation of fragilities to consider the metamodel uncertainty with Eq.3.3.4. Such an idea has been used in Gidaris et al. [2015] and Wang et al. [2018] to account for the metamodel error in the lognormal based fragility models. Eq.3.3.4 is reformulated for coherence with Eq.4.2.2:

$$P_f(\alpha) = \mathbf{\Phi}\left(\frac{c\ln\alpha - (\ln y_{\text{crit}} - \ln b)}{\sqrt{\hat{\sigma}_{R|IM}^2 + \sigma_{\text{ANN}}^2}}\right) = \mathbf{\Phi}\left(\frac{\ln\alpha - (\ln y_{\text{crit}} - \ln b)/c}{\sqrt{\hat{\sigma}_{R|IM}^2 + \sigma_{\text{ANN}}^2}/c}\right). \tag{4.2.10}$$

where $\hat{\sigma}_{R|IM}$ is the Std of the linear regression applied to the dataset (α, $\hat{y}$). Therefore, $A_m^{\text{prior}} = \sqrt[c]{y_{\text{crit}}/b}$ and $\beta_R = \sqrt{\hat{\sigma}_{R|IM}^2 + \sigma_{\text{ANN}}^2}/c$. The prior value of β_U of the equipment capacity is chosen in agreement with the literature, such as EPRI [2014]. With the computed value of A_m^{prior}, the prior distribution of $\hat{A}_m$ is determined: $f^{\text{prior}}(\hat{A}_m) \sim LogN(A_m^{\text{prior}}, (\beta_U^{\text{prior}})^2)$.

4.2.3 Bayesian Updating of Fragility Curves with Damage Data

Damage Database

The damage data $\underline{z}$ used in this study are taken from the seismic qualification utility group (SQUG) database. The SQUG database [EPRI 2016], built by the Electric Power Research Institute (EPRI), gathers seismic experience data related to seismic capacity of equipment in industrial facilities (not limited to NPPs) [Starck and Thomas 1990]. The data in the SQUG database are mostly obtained from post-earthquake inspections of equipment in these industrial facilities. 32 earthquakes from 1971 to 2010 are registered in the SQUG database with most of them taking place in the USA. Some strong earthquakes in Chile, Japan, Turkey, etc. are also included. The equipment in the SQUG database is divided into 20 conventional classes, including switchgears, batteries, motor control centers. A list of the 20 equipment classes is summarized in Starck and Thomas [1990].

For the data collected in the SQUG database, each observation contains the information: (i) equipment description (size, manufacturer, etc.); (ii) the earthquake and the PGA; (iii) the industrial facility where the equipment is located; (iv) the elevation h of the equipment in the facility structure; (v) the description of the performance of the equipment after the earthquake. It has to be mentioned that no details on the supporting structures are provided in the database, so that the FEM models for the structures in the SQUG database are in general not available. In our study, the damage data for the low-voltage switchgear are collected from the SQUG database. They are used in the application section for the Bayesian updating of the fragility curves.

Bayesian Framework in Fragility Analysis

Given the damage data $\underline{z}$, the posterior distribution of $\hat{A}_m$ can be computed by the Bayes' theorem:

$$f^{\text{post}}(\hat{A}_m|\underline{z}) = kL(\underline{z}|\hat{A}_m)f^{\text{prior}}(\hat{A}_m) \tag{4.2.11}$$

where $L(\underline{z}|\hat{A}_m)$ is the likelihood function determined by the observed data, and k is a constant to normalize the posterior distribution. Every observational data vector $\underline{z}^i$ has two components: the PGA value α^i of the seismic excitation and the damage state x^i of the equipment of interest after the earthquake. This latter x^i is modeled as a binary Bernoulli variable: $x^i = 0$ if no failure occurs and $x^i = 1$ if the equipment fails. According to Shinozuka et al. [2000], the likelihood function with given $\underline{z}$ is written as:

$$L(\underline{z}|\hat{A}_m) = \prod_{i=1}^{n_{\text{obs}}}[P_f(\alpha^i)]^{x^i}[1-P_f(\alpha^i)]^{1-x^i} = \prod_{i=1}^{n_{\text{obs}}}\left[\mathbf{\Phi}(\frac{\ln\alpha^i - \ln\hat{A}_m}{\beta_R})\right]^{x^i}\left[1-\mathbf{\Phi}(\frac{\ln\alpha^i - \ln\hat{A}_m}{\beta_R})\right]^{1-x^i}, \tag{4.2.12}$$

where n_{obs} is the number of the empirical data. Substituting Eq.4.2.12 into Eq.4.2.11, one can obtain the expression of the posterior distribution of $\hat{A}_m$:

$$f^{\text{post}}(\hat{A}_m|\underline{z}) \propto (\prod_{i=1}^{n_{\text{obs}}}[P_f(\alpha^i)]^{x^i}[1-P_f(\alpha^i)]^{1-x^i})f^{\text{prior}}(\hat{A}_m). \tag{4.2.13}$$

Knowing $L(\underline{z}|\hat{A}_m)$ and $f^{\text{prior}}(\hat{A}_m)$, the MCMC simulation allows sampling efficiently the posterior distribution without computing explicitly the constant k of Eq.4.2.11 [Hastings 1970]. Therefore, the essential part of the Bayesian updating is to determine the parameters in $L(\underline{z}|\hat{A}_m)$ to construct the likelihood function.

It appears that the computation of $L(\underline{z}|\hat{A}_m)$ is straightforward. However, different kinds of PGA values can be provided in the database. Before computing the likelihood function, one has to ensure that the PGA values to plug in Eq.4.2.13 describe the free surface ground motions near the target structure in which the equipment is located.

Determination of the Likelihood Function

Two groups of earthquake observational damage data are discussed in this study:

1. In-situ earthquake observational data $\underline{z}_t = (\alpha_t, x)$ of the equipment of interest in the *target* structure, where α_t denotes the PGA level recorded on the free surface near the target structure (Let us recall that the FEM model of the target structure is available).

2. SQUG earthquake observational data $\underline{z}_s = (\alpha_s, x)$ of a similar equipment positioned in other civil structures in the database, named SQUG structures in this paper. The quantity α_s denotes the PGA level recorded on the free surface near the SQUG structures.

The total workflow of the determination of the likelihood function with damage data is summarized in Figure 4.3.

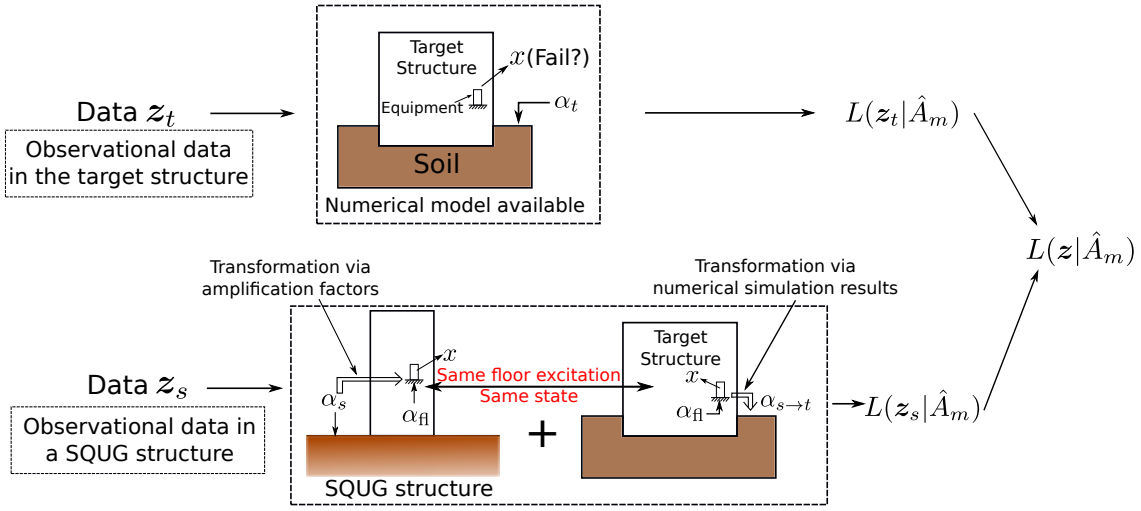

Figure 4.3: The workflow to compute the likelihood function

Likelihood function for z_t Recalling that the PGA values in Eq.4.2.13 should be α_t, data of the first category can be directly inserted into Eq.4.2.13.

$$L(\underline{z}_t|\hat{A}_m) = \prod_{i=1}^{n_t} \left[\mathbf{\Phi}\left(\frac{\ln \alpha_t^i - \ln \hat{A}_m}{\beta_R}\right) \right]^{x^i} \left[1 - \mathbf{\Phi}\left(\frac{\ln \alpha_t^i - \ln \hat{A}_m}{\beta_R}\right) \right]^{1-x^i}, \tag{4.2.14}$$

where n_t is the number of the in-situ observational data.

However, the use of the SQUG data is not straightforward. The purpose of the subsequent part is to propose a method to integrate SQUG data in Eq.4.2.13, i.e. a method to transform $\underline{z}_s$ into $\underline{z}_t$ with also the quantification of the associated uncertainty in the transformation. The essential idea of the assumption is that the damage state of the equipment after the earthquake depends on the PGA value of the floor acceleration.

Likelihood Function for z_s The transformation from $\underline{z}_s$ into $\underline{z}_t$ consists of two steps:

1. Compute the peak floor acceleration (PFA) of the SQUG structure at the location of the component, given the PGA on the free soil surface.

2. Considering that the equipment is positioned in the target structure with the same floor acceleration, compute the PGA of the free surface ground motion of the target structure.

We start with the first step of the transformation. In general, the numerical model of the SQUG structure is difficult to obtain, and only the elevation h of the location of the equipment is provided in SQUG data. Without any information on the SQUG structure, the

simple amplification factor model used in EPRI [2014] is adopted in this study:

$$\alpha_{\mathrm{fl}} = \lambda(h)\alpha_s, \tag{4.2.15}$$

where $\lambda(h)$ is the amplification factor, which is a function of the elevation. α_{fl} denotes the PFA. The quantity $\lambda(h)$ contains a median value $\bar{\lambda}(h)$ and a lognormal uncertainty $\tilde{\varepsilon}$: $\lambda(h) = \bar{\lambda}(h)\tilde{\varepsilon}$ with $\tilde{\varepsilon} \sim LogN(1, \tilde{\beta}^2)$. Here, a linear relation is selected for $\bar{\lambda}(h)$:

$$\bar{\lambda}(h) = c_h h + b_h. \tag{4.2.16}$$

The parameters c_h and b_h are determined according to the amplification factor values used in EPRI [2014]:

$$\bar{\lambda} = 1 \text{ if } h = 0; \tag{4.2.17}$$

$$\bar{\lambda} = 1.5 \text{ if } h = 12.192\text{m}. \tag{4.2.18}$$

So far, the peak floor acceleration α_{fl} and its associated uncertainty $\tilde{\varepsilon}$ have been computed. The second step of the transformation is explained in what follows. The transformation of α_{fl} to α_t is, in fact, the transformation of the PFA of the target structure into the free surface PGA. This transformation can be realized with a statistical model established from the FEM simulation results, which are used to train the adaptive ANN.

From the FEM simulation results of Section 4.2.2, the PFA values $\alpha_{\mathrm{f}}^{\mathrm{FEM}}$ and PGA values of the free surface ground motions $\alpha_{\mathrm{g}}^{\mathrm{FEM}}$ of the target structure can be extracted. Let us assume that both PFA and PGA values are lognormally distributed. This assumption is checked later in our specific case study. The lognormal assumption allows building a bi-variate normal distribution of $\ln \alpha_{\mathrm{f}}^{\mathrm{FEM}}$ and $\ln \alpha_{\mathrm{g}}^{\mathrm{FEM}}$. The marginal distributions of $\ln \alpha_{\mathrm{f}}^{\mathrm{FEM}}$ and $\ln \alpha_{\mathrm{g}}^{\mathrm{FEM}}$ are denoted by $N(\ln \mu_{\mathrm{f}}^{\mathrm{FEM}}, (\sigma_{\mathrm{f}}^{\mathrm{FEM}})^2)$ and $N(\ln \mu_{\mathrm{g}}^{\mathrm{FEM}}, (\sigma_{\mathrm{g}}^{\mathrm{FEM}})^2)$, respectively, with the correlation coefficient ρ. According to the property of the conditional bi-variate normal distribution, it can be shown that the median value of the transformed free surface PGA $\alpha_{\mathrm{fl}\to t}$ and its uncertainty $\beta_{\mathrm{fl}\to t}$ are calculated by

$$\ln \alpha_{\mathrm{fl}\to t} = \ln \mu_{\mathrm{g}}^{\mathrm{FEM}} + \rho(\ln \alpha_{\mathrm{fl}} - \ln \mu_{\mathrm{f}}^{\mathrm{FEM}}) \frac{\sigma_{\mathrm{g}}^{\mathrm{FEM}}}{\sigma_{\mathrm{f}}^{\mathrm{FEM}}}; \tag{4.2.19}$$

$$\beta_{\mathrm{fl}\to t}^2 = (1 - \rho^2)(\sigma_{\mathrm{g}}^{\mathrm{FEM}})^2. \tag{4.2.20}$$

Combining Eqs.4.2.15, 4.2.19, 4.2.20 and considering the property of the normal distribution, one can show that the median value of the transformed PGA $\ln \alpha_{s\to t}$ on the free surface of

the target structure is calculated by

$$\ln \alpha_{s\to t} = \ln \mu_{\mathrm{g}}^{\mathrm{FEM}} + \rho[\ln(\bar{\lambda}(h)\alpha_s) - \ln \mu_{\mathrm{f}}^{\mathrm{FEM}}]\frac{\sigma_{\mathrm{g}}^{\mathrm{FEM}}}{\sigma_{\mathrm{f}}^{\mathrm{FEM}}}. \tag{4.2.21}$$

and its related uncertainty is

$$\beta_{s\to t}^2 = (\frac{\sigma_{\mathrm{g}}^{\mathrm{FEM}}}{\sigma_{\mathrm{f}}^{\mathrm{FEM}}}\rho)^2\tilde{\beta}^2 + \beta_{\mathrm{fl}\to t}^2 = (\frac{\sigma_{\mathrm{g}}^{\mathrm{FEM}}}{\sigma_{\mathrm{f}}^{\mathrm{FEM}}}\rho)^2\tilde{\beta}^2 + (1-\rho^2)(\sigma_{\mathrm{g}}^{\mathrm{FEM}})^2. \tag{4.2.22}$$

In the end, the likelihood function for data $\underline{z}_s$ is derived:

$$L(\underline{z}_s|\hat{A}_m) = \prod_{i=1}^{n_{\mathrm{s}}}\left[\mathbf{\Phi}(\frac{\ln \alpha_{s\to t}^i - \ln \hat{A}_m}{\sqrt{\beta_R^2+\beta_{s\to t}^2}})\right]^{x^i}\left[1-\mathbf{\Phi}(\frac{\ln \alpha_{s\to t}^i - \ln \hat{A}_m}{\sqrt{\beta_R^2+\beta_{s\to t}^2}})\right]^{1-x^i}. \tag{4.2.23}$$

It is worth mentioning that the interpretations of β_R and $\beta_{s\to t}$ are different: the former represents the record-to-record aleatory uncertainty when the ground motion time history is characterized by a scalar PGA value, whereas the latter expresses the uncertainty of the transformed PGA value due to the underlying statistical modeling.

Consequently, the total likelihood function for the two categories of data is computed by

$$L(\underline{z}|\hat{A}_m) = L(\underline{z}_s|\hat{A}_m)L(\underline{z}_t|\hat{A}_m). \tag{4.2.24}$$

4.3 Case Study: Application to KARISMA Benchmark

This section is dedicated to apply the proposed methodology to an industrial case study. Moreover, a sensitivity analysis is conducted at the end with respect to some uncertain parameters. The equipment of interest is a low-voltage switchgear (LVSG) in the Kashiwazaki-Kariwa NPP (K-K NPP). In NPPs, the LVSG is a combination of electrical control units such as circuit breaks and relays, etc., whose function is to ensure and protect the performance of 480V-AC (alternative current) electrical systems. K-K NPP experienced the strong Niigataken-Chuetsu-Oki (NCO) earthquake with magnitude $M_w = 6.6$ in 2007. In this context, the KAshiwazaki-Kariwa Research Initiative for Seismic Margin Assessment (KARISMA) benchmark was organized by the International Atomic Energy Agency (IAEA) [IAEA 2013]. A post-earthquake inspection was carried out in order to check the performance of the equipment in K-K NPP after the earthquake [EPRI 2007].

4.3.1 KARISMA Numerical Model

The FEM model of the K-K NPP Unit 7, shown in Figure 4.4, is reused in this study. The LVSG of interest is located on the -1 floor of the K-K NPP building. The same procedures for

FEM simulations are conducted as described in Chapter 3. Two strong earthquake scenarios, which have affected the area of Kashiwazaki and Kariwa, are considered in this study: (i) the 2007 NCO earthquake scenario with $M_w = 6.6$ and source-to-site distance $r = 16$ km; (ii) the 2004 Chuetsu earthquake with $M_w = 6.8$ and source-to-site distance $r = 29$ km. Given the NCO and Chuetsu scenarios, the generation of the synthetic ground motions at the bedrock with $Vs_{30} = 720$ m/s is based on the median and 1σ spectra given by the Campbell-Bozorgnia 2008 (C&B 2008) ground motion prediction equations [Campbell and Bozorgnia 2008]. 250 triplets of 3D synthetic ground motions are generated for *each scenario* (so 500 triplets in total) and used for the uncertainty propagation. The generated motions in X direction for the NCO scenario are shown in Figure 4.5. To obtain enough failure counts for the fragility analysis, the synthetic seismic motions at the bedrock are scaled with a factor of two for the NCO scenario and a factor of three for the Chuetsu scenario.

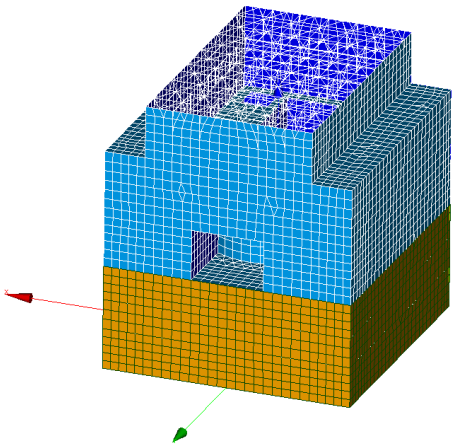

Figure 4.4: FEM model of the K-K NPP Unit 7

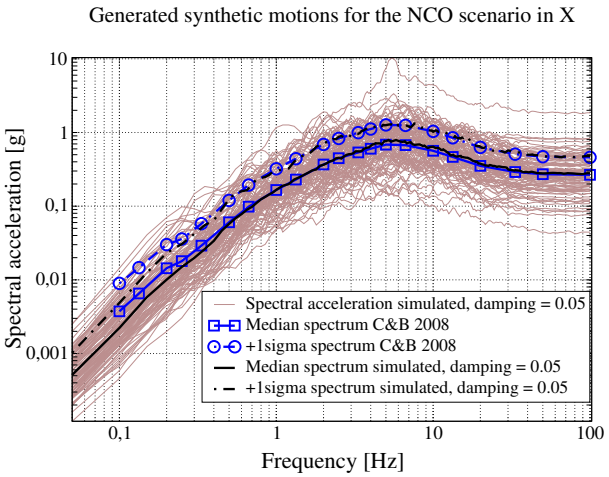

Figure 4.5: Generated motions for NCO earthquake scenario and comparison with the spectra predicted by C&B 2008

500 bedrock motions are convoluted on the free surface based 1D soil column reconvolution with the equivalent linear method (ELM) [Yoshida et al. 2002]. Meanwhile, 500 degraded soil profiles are obtained. In order to reduce the computational cost, the impedances of the soil and the seismic forces have not been computed for each soil profile using BEM. The 3D seismic signals at the bedrock are regrouped into four soil classes according to their PGA values: i. PGA$\in$[0, 0.3g) ii. PGA$\in$[0.3g, 0.5g) iii. PGA$\in$[0.5g, 1.0g) iv. PGA$\in$[1.0g, $+\infty$). The degraded soil profiles are averaged within each class and 4 soil profiles are obtained to represent four different degradation levels. The 500 ground motions on the free surface, as well as the impedances and seismic forces calculated from the four soil profiles, are used as inputs of the SSI analyses to compute the floor accelerations of the K-K NPP.

In this chapter, the failure is described by the non-operational state of the LVSG after the earthquake. Reparation of the equipment is necessary. It can be caused by the fact that

(i) relays or breakers cannot return to their operational state after the earthquake or (ii) structural damage has occurred to the equipment, for example anchorage failure at its base [EPRI 1991]. The capacity of the switchgear is given by the average floor spectral acceleration in 5-9Hz, which covers the first natural frequency of the LVSG. The maximum value of the floor spectral accelerations in the two horizontal directions, averaged over 5-9Hz is defined as the EDP y:

$$y = \frac{1}{9. - 5.} \max_{i=X,Y} \int_{5\text{Hz}}^{9\text{Hz}} S^e_{a,i}(f)\mathrm{d}f, \tag{4.3.1}$$

where $S^e_{a,i}$ denotes the floor spectral acceleration of the LVSG in the i-th direction. A value of $1.8g$ is selected for y_{crit} according to EPRI [1991], in which the failure threshold of the floor spectral acceleration $S^e_{a,i}(f)$ of the LVSG is a constant value $1.8g$ for the frequency range [3Hz, 16Hz] (so its average for the frequency range [5Hz, 9Hz] is also $1.8g$).

4.3.2 Prior Fragility Parameters

An ANN is trained iteratively with the algorithm explained in Section 4.2.2. The IMs of the 500 convoluted seismic motions on the free surface of the K-K NPP can be extracted. Three IMs are used as the inputs of the ANN: (i) PGA, which is widely used in fragility analysis; (ii) ASA [Biasio et al. 2015], the average spectral acceleration in 5-9Hz; (iii) PGV (peak ground velocity), a classical IM for the mid-frequency range. The geometric means of IMs in the two horizontal directions are used as scalar IMs for 3D ground motions. The number of the neurons in the hidden layer of the ANN is 4. In this way, the architecture of the ANN is determined: 3 input parameters (PGA, ASA, PGV), 4 hidden layer nodes and 1 output parameter (EDP defined by Eq.4.3.1). $N_0 = 30$ seismic motions from the total 500 signals are randomly selected for the initialization of the adaptive ANN training. $M = 4$ data are added in the DoE in every iteration. The ANN is trained in *log-log* space, i.e. with ln(IMs) as inputs and ln(EDP) as outputs.

The adaptive training of the ANN is stopped after 62 calls of FEM simulations. To visualize the DoEs determined by the proposed ANN algorithm, we plot the data cloud in PGA-EDP space in Figure 4.6. The convergence curve of the adaptive ANN training is shown in Figure 4.7. In this figure, the maximum value of δ of the test dataset is plotted against the iteration number k. At iteration 8, the stopping condition is satisfied and the ANN iterative training is stopped.

In order to show the advantage of the adaptive algorithm, 62 seismic motions are randomly selected from the total 500 signals. FEM simulations are conducted for the 62 randomly selected signals and the corresponding data cloud is plotted in PGA-EDP space in Figure 4.8. The PGA used in the horizontal axis is PGA on the free surface. From Figure 4.6 and Figure 4.8, one can clearly observe the improvement of the DoEs with the ANN adaptive

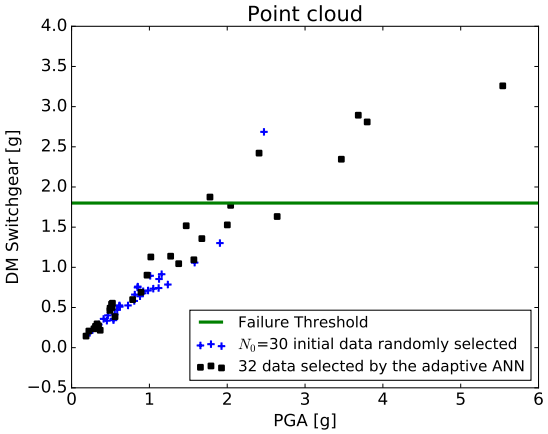

Figure 4.6: Data determined by the adaptive algorithm from 500 seismic ground motions plotted in PGA-EDP space

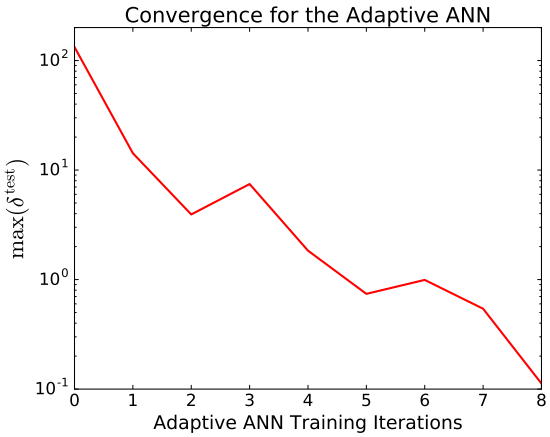

Figure 4.7: Convergence curve for the adaptive ANN training

training algorithm. The data in Figure 4.6 are better distributed in the PGA-EDP space than the data in Figure 4.8: too many data are concentrated in low PGA range in Figure 4.8, with only one point exceeding the failure threshold. On the contrary, more failures are contained in the dataset obtained by the ANN adaptive training, which is more convenient for the accuracy of the fragility analysis.

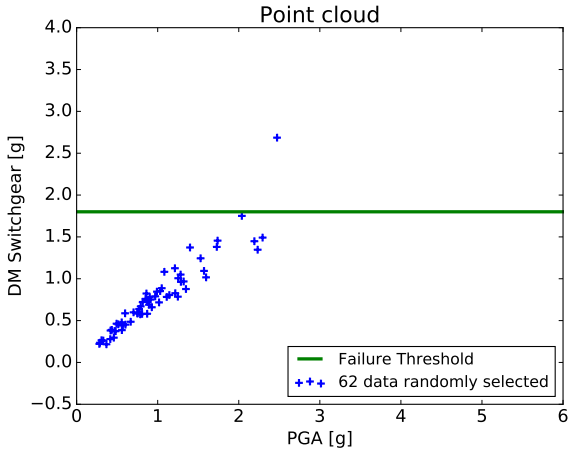

Figure 4.8: Data randomly selected from 500 seismic ground motions plotted in PGA-EDP space

The training results of the ANN are shown in Figure 4.9a. The ANN predictions of the training dataset are compared to the real FEM results (target output) *in log space*. From Figure 4.9a, one can conclude that the training results are satisfactory. Most of the results in the 'prediction-target' space are located in the proximity of the dashed diagonal line. Another 60 ground motions, which are different from the training dataset determined by the adaptive algorithm, are selected to validate the constructed ANN model. FEM and ANN simulations are performed for the 60 validation seismic signals, respectively. The validation

results are plotted in Figure 4.9b. These validated the performance of the ANN trained from the adaptive algorithm.

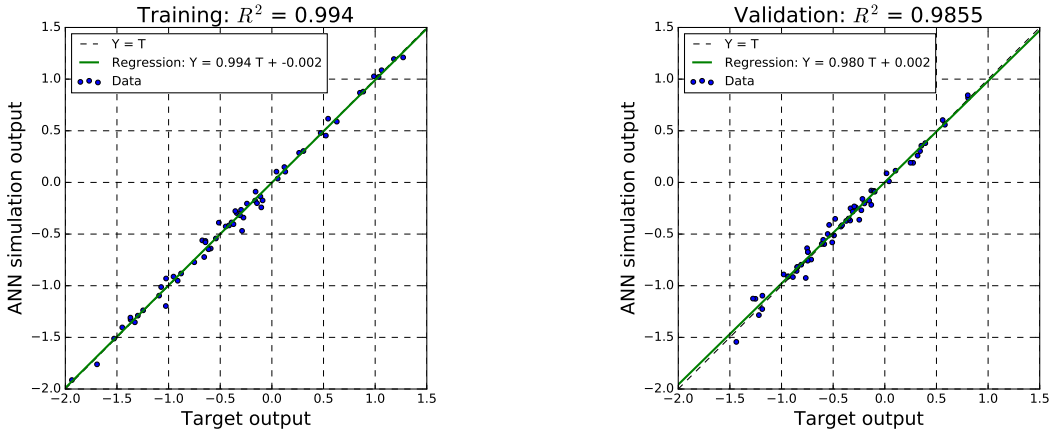

(a) ANN training results

(b) ANN validation results

Figure 4.9: Comparison of ANN results with FEM results. The comparison is conducted for $\ln \hat{y}$ and $\ln y$

A total of 500 ANN simulations are conducted for the whole ground motion population with the constructed ANN metamodel: 500 pairs of PGA-EDP are, then, obtained. The values of β_R and A_m^{prior} are estimated from the ANN simulations results with the method explained in Chapter 4.2.2, with $A_m^{\text{prior}} = 2.46g$ and $\beta_R = 0.145$. According to EPRI [2009, 2014], a reasonable estimation of β_U^{prior} concerning the uncertainty of the equipment capacity is 0.4. Consequently, the prior distribution of $\hat{A}_m$ follows $LogN(2.46g, 0.4^2)$.

4.3.3 Determination of the Likelihood Function

The LVSG damage data can be divided into two groups: one in-situ observation $\underline{z}_t$ for K-K NPP and 78 post-earthquake inspection data $\underline{z}_s$ for the LVSG in the SQUG structures. Regarding the in-situ observation, the LVSG in the K-K NPP Unit 7 was not damaged after the NCO earthquake with PGA $= 0.69g$. On the other hand, the total number of SQUG damage data for the LVSG is 78, with only one failure observed in the El Centro Steam Plant after the 1979 Imperial Valley Earthquake with local PGA value of $0.43g$. After the earthquake, it has been noticed that circuit breakers of the LVSG had refused to close. However, according to the inspection report, it is not clear that the failure of the LVSG is caused by the earthquake. It can be also due to the corrosion in the mechanical linkages, which is not earthquake-related. Therefore in the present paper, we set $x^i = 0.5$ for this potential failure, meaning that with a probability of 50% the LVSG failed during the Imperial Valley Earthquake. The local PGA values measured at different industrial structures are plotted in Figure 4.10. A summary of the SQUG data for the low voltage switchgear is given in Table 4.1.

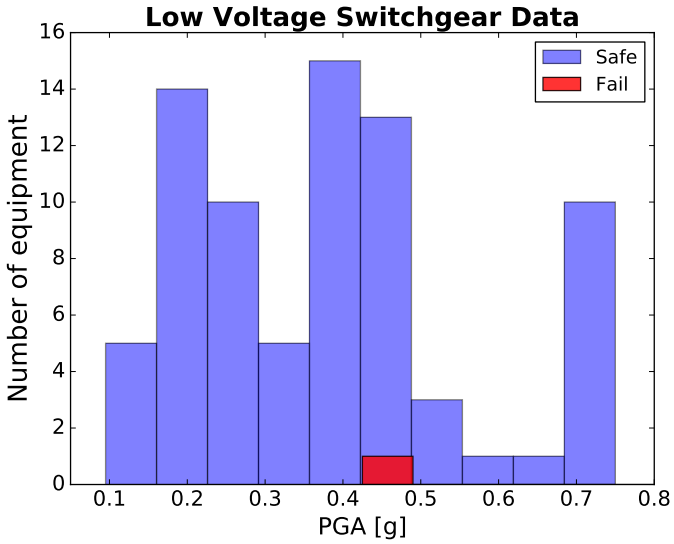

Figure 4.10: PGA values of the SQUG data for the LVSG

Table 4.1: Summary of the SQUG data for the LVSG

Earthquake	Number of the inspected LVSGs	Number of failures
1971 San Fernando Earthquake	9	0
1973 Point Mugu Earthquake	1	0
1975 Ferndale Earthquake	1	0
1979 Imperial Valley Earthquake	5	0.5
1983 Coalinga Earthquake	1	0
1984 Morgan Hill Earthquake	1	0
1985 Chile Earthquake	4	0
1985 Mexico Earthquake	1	0
1986 Adak Earthquake	2	0
1986 Chalfant Valley Earthquake	1	0
1987 Bay of Plenty Earthquake	3	0
1987 Superstition Hills Earthquake	1	0
1987 Whitter Earthquake	7	0
1989 Loma Prieta Earthquake	7	0
1992 Cape Mendocino Earthquake	2	0
1992 Landers/Big Bear Earthquake	3	0
1993 Guam Earthquake	3	0
1994 Northridge Earthquake	19	0
1995 Manzanillo Earthquake	4	0
1999 Kocaeli Turkey Earthquake	1	0
2010 Baja California Earthquake	2	0

The likelihood function $L(\underline{z}_t|\hat{A}_m)$ for the K-K NPP in-situ observation is straightforward with Eq.4.2.14. We focus on the computation of $L(\underline{z}_s|\hat{A}_m)$ in what follows.

We follow the two-step method described in Section 4.2.3 to calculate $L(\underline{z}_s|\hat{A}_m)$:

1. Step 1: computation of the PFA value of the SQUG structures with the amplification factor model, given the PGA on the soil free surface. The median values $\bar{\lambda}(h)$ for the amplification factors can be obtained by Eqs. 4.2.16, 4.2.17, 4.2.18 with the elevation values

h provided in the database. The uncertainty $\tilde{\beta}$ of the amplification factors is assumed to be 0.2, so that the true values of the amplification factors $\lambda(h)$ have a probability of 95% to lie approximately between $\frac{2}{3}\bar{\lambda}(h)$ and $1.5\bar{\lambda}(h)$. Therefore, the median PFA value and its uncertainty can be determined.

2. Step 2: transformation of the PFA to the K-K NPP free surface PGA with the bi-variate normal distribution model established from the 62 FEM simulation results.
   First, the lognormal assumption of the marginal distributions of the PFA and PGA values is checked for both floor accelerations and free field accelerations of the K-K NPP. These values of PFAs and PGAs are obtained from 62 FEM simulation results. The medians μ and logarithmic Stds σ of the assumed lognormal distributions are computed and listed in Table 4.2. The ln(PFA) and ln(PGA) values are normalized with respect to the medians and Stds and compared with $N(0,1)$ in Figure 4.11 to verify the lognormal assumption.

Table 4.2: Summary of parameters used in the transformation of PGA values

c_h	b_h	$\tilde{\beta}$	μ_g^{FEM}	σ_g^{FEM}	μ_f^{FEM}	σ_f^{FEM}	ρ
0.041	1	0.2	0.846	0.746	0.354	0.743	0.924

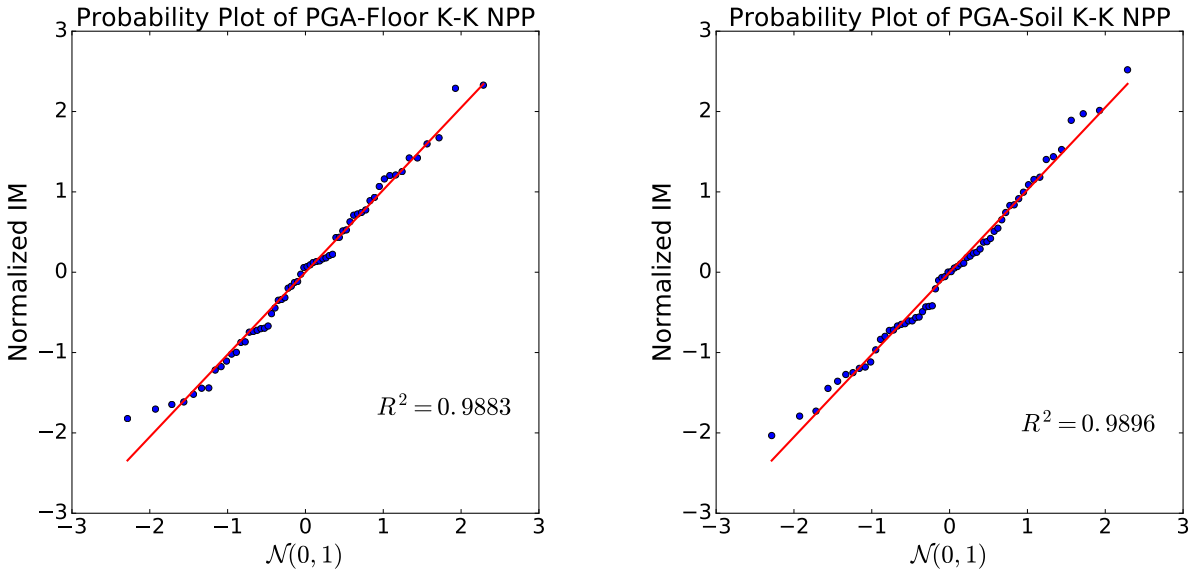

(a) Probability plot of the PFA values of the -1 floor of the K-K NPP

(b) Probability plot of the PGA values of the soil free surface of the K-K NPP

Figure 4.11: Probability plot of the normalized PGA values of the -1 floor and the normalized PGA values on the soil free surface of the K-K NPP

From the results of the probability plots, it can be concluded that the lognormal assumption for both $\alpha_{\mathrm{g}}^{\mathrm{FEM}}$ and $\alpha_{\mathrm{f}}^{\mathrm{FEM}}$ can be considered acceptable. Additionally, from Table 4.2 it can be observed that the median of the soil PGA μ_g^{FEM} is larger than the median of

the PFA μ_f^{FEM}: this is due to the fact that the LVSG is located on the -1 floor in the K-K NPP.

Furthermore, the transformed PGA values $\alpha_{s\to t}$ on the K-K NPP free surface and the relevant uncertainty $\beta_{s\to t}$ due to the transformation are computed with Eqs.4.2.21, 4.2.22. The transformed median PGA values $\alpha_{s\to t}$ are plotted in Figure 4.12. We can see an increase of the PGA values after the transformation process due to the low elevation of the target LVSG in the K-K NPP. In Figure 4.12, a linear tendency can be observed for some ($\alpha_{s\to t}$,α_s) data values. This is because their corresponding LVSGs have the same elevations h (in particular $h = 0$), so that their amplification factors in the transformation step 1 are the same. In addition, as $\beta_{s\to t}$ calculated with Eq.4.2.22 is independent of α_s, it stays the same for all 78 $\underline{z}_s$ data, with $\beta_{s\to t} = 0.299$.

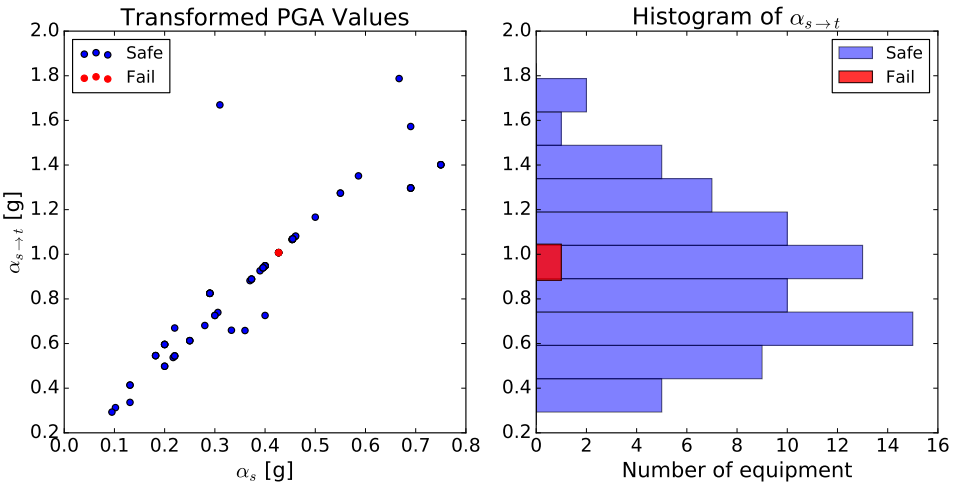

Figure 4.12: PGA values $\alpha_{s\to t}$ after the transformation into K-K NPP free surface

In the end, the transformed $\alpha_{s\to t}$ are plugged into Eq.4.2.23 to compute the likelihood function $L(\underline{z}_s|\hat{A}_m)$. We also justify the application of the fractional x^i value 0.5 for the potential failure case of El Centro steam plant. It can be regarded as two realizations of earthquake observations, with one failure and one survival. Then, the likelihood function established by the two realizations should be normalized to one observation by the square-root operation:

$$L(\underline{z}_{\text{El-Centro}}|\hat{A}_m) = \sqrt{[P_f(\alpha_{\text{El-Centro}})][1 - P_f(\alpha_{\text{El-Centro}})]} = [P_f(\alpha_{\text{El-Centro}})]^{0.5}[1-P_f(\alpha_{\text{El-Centro}})]^{0.5}. \tag{4.3.2}$$

The same procedure is also used by EPRI [2017]. As a result, the total likelihood function is computed: $L(\underline{z}|\hat{A}_m) = L(\underline{z}_t|\hat{A}_m)L(\underline{z}_s|\hat{A}_m)$

4.3.4 Posterior Fragility Curve

The posterior distribution $f^{\text{post}}(\hat{A}_m|\underline{z})$ is obtained based on the prior distribution and the likelihood function, which are calculated in Section 4.3.2 and Section 4.3.3, respectively. MCMC is used to generate 10,000 samples from $f^{\text{post}}(\hat{A}_m|\underline{z})$. A lognormal distribution is approximated for $f^{\text{post}}(\hat{A}_m|\underline{z})$ with the median and logarithmic Std of the generated 10,000 samples. The MCMC sampling of $f^{\text{post}}(\hat{A}_m|\underline{z})$ and the approximated lognormal distribution are shown in Figure 4.13. The posterior distribution of $\hat{A}_m$ has the median $A_m^{\text{post}} = 2.70g$ and the associated uncertainty $\beta_U^{\text{post}} = 0.176$. The comparison of fragility parameters of the LVSG before and after Bayesian updating is reported in Table 4.3.

Table 4.3: Posterior fragility parameters for the LVSG in K-K NPP and comparison to the prior parameters

β_R	A_m^{prior}	β_U^{prior}	$A_{\text{HCLPF}}^{\text{prior}}$	A_m^{post}	β_U^{post}	$A_{\text{HCLPF}}^{\text{post}}$
0.145	$2.46g$	0.4	$1.00g$	$2.70g$	0.176	$1.59g$

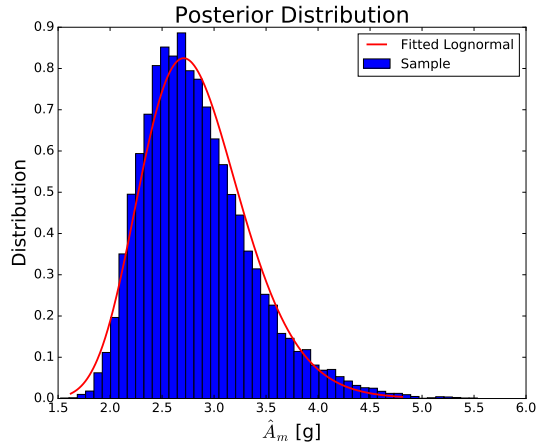

Figure 4.13: MCMC sampling of the posterior distribution of $\hat{A}_m$

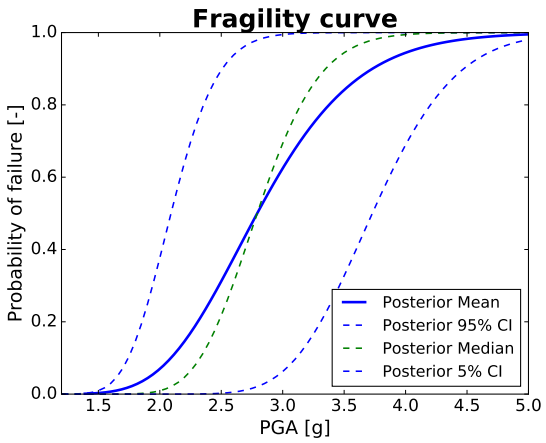

Figure 4.14: Posterior fragility curves and its confidence intervals

The posterior median and mean fragility curves are computed with Eqs.4.2.2, 4.2.6 respectively. The 0.05 and 0.95 non-exceedance confidence intervals are calculated with Eq.4.2.4. The computed fragility curves and the associated confidence intervals are shown in Figure 4.14. Compared to the prior fragility parameters, the median capacity A_m increases after Bayesian updating, because few failure cases (only one) have been observed in the post-earthquake inspection for the LVSG. The epistemic uncertainty β_U is reduced due to the supplementary information from the observational data. Relatively large confidence bounds have been shown in Figure 4.14, since despite the Bayesian updating, the value of β_U^{post} (0.176) is still larger than the aleatory uncertainty $\beta_R = 0.145$. Nevertheless, the HCLPF capacity, computed by Eq.4.2.5, is largely increased after the Bayesian updating, mainly due to the reduction of the epistemic uncertainty.

Furthermore, the influence of the selected value of β_U^{prior} on the posterior fragility curve is investigated. Different values of β_U^{prior} varying from 0.1 to 0.4 are taken for the prior $\hat{A}_m$ distributions. With the same SQUG observational data, the likelihood function remains the same. Posterior distributions of $\hat{A}_m$ are computed and plotted in Figure 4.15. It can be observed from Figure 4.15 that $\beta_U^{\text{prior}} = 0.4$ reveals in fact a relatively large uncertainty of the median capacity compared to the likelihood function $L(\underline{z}|\hat{A}_m)$ provided by the observational data. Therefore, the contribution of $L(\underline{z}|\hat{A}_m)$ to the posterior distribution is dominant if $\beta_U^{\text{prior}} = 0.4$. On the other hand, if one is very certain about the median capacity estimated from the numerical simulations (i.e. $\beta_U^{\text{prior}} = 0.1$), the influence of $L(\underline{z}|\hat{A}_m)$ on the posterior distribution is not that evident: the posterior median increases slightly in comparison with the prior median, whereas the value of β_U is hardly modified. For $\beta_U^{\text{prior}} = 0.2$ and 0.3, the posterior distribution is a trade-off between the prior distribution and the likelihood function, which is a reasonable outcome from the Bayes' theorem.

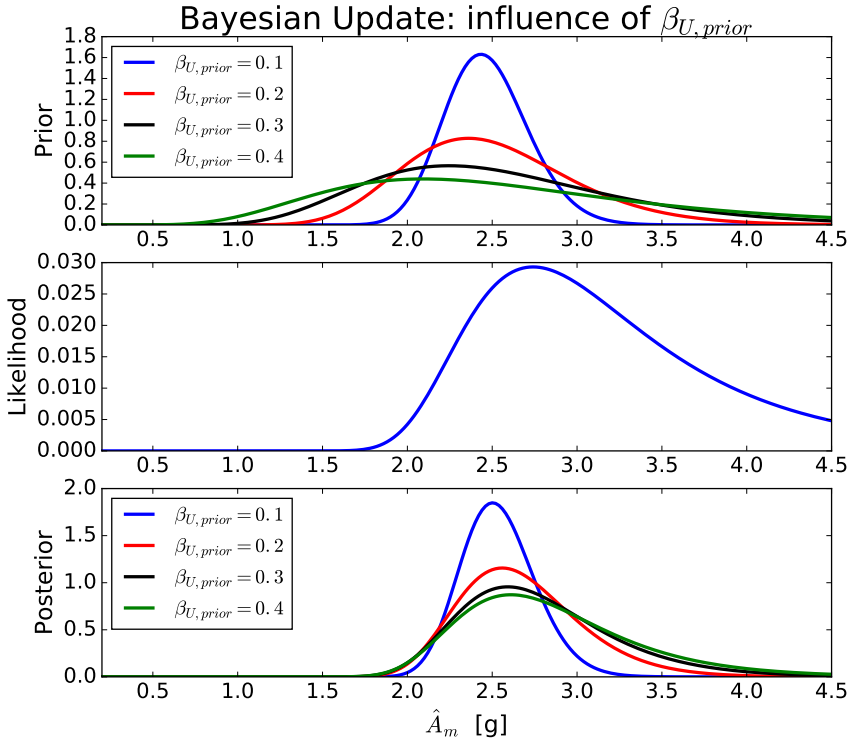

Figure 4.15: Influence of the choice of β_U^{prior} on the posterior fragility curve. Upper: prior distributions of $\hat{A}_m$ with different β_U^{prior}. Middle: likelihood function. Lower: posterior distributions of $\hat{A}_m$ with different β_U^{prior}.

Finally, we study the influence of the uncertain observational data of the El-Centro steam plant. Other than the observational value $x^i = 0.5$ applied in the previous sections, the likelihood function is also computed with $x^i = 0$ and $x^i = 1$ for the El-Centro steam plant. The posterior distributions with different levels of uncertainty on the El-Centro observational

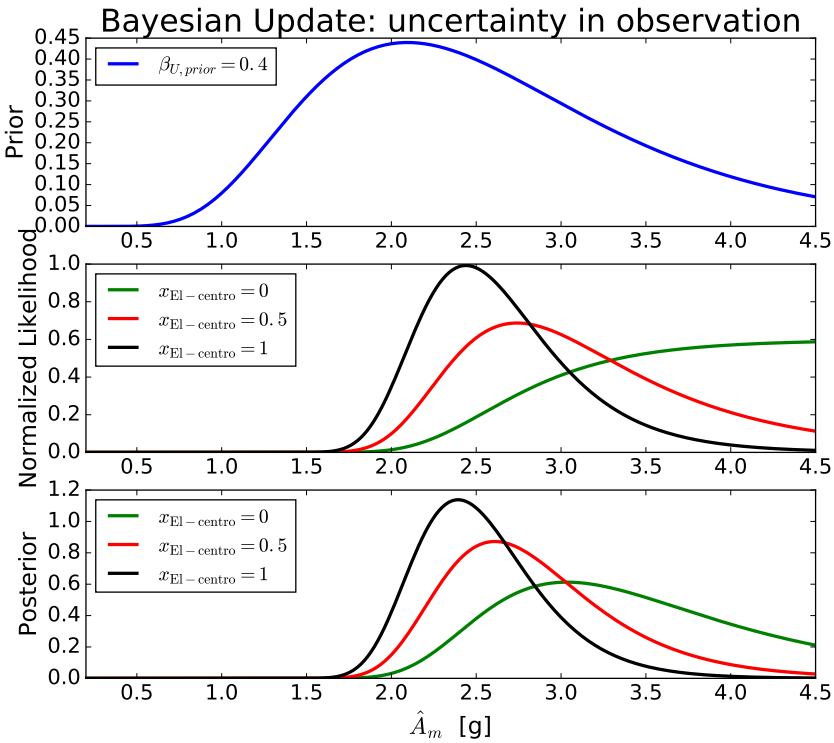

Figure 4.16: Influence of observational data of El-Centro steam plant. Upper: prior distributions of $\hat{A}_m$. Middle: likelihood function with different x^i values for the El-Centro steam plant. Lower: posterior distributions of $\hat{A}_m$.

data are plotted in Figure 4.16. From the results of Figure 4.16, a complete failure of the LVSG $x^i = 1$ in the El-Centro steam plant makes decrease the posterior $\hat{A}_m$, since the equipment is more fragile according to the observational results. On the contrary, the LVSG is more resistant if $x^i = 0$ for the El-Centro steam plant, so that an increase of the posterior $\hat{A}_m$ can be observed.

4.4 Summary

In this chapter, a Bayesian updating framework is proposed for integrating different sources of information, including numerical simulations, damage data and reference critical values informed from the literature, in the computations of seismic fragility curves. In the framework, the results from numerical simulations are used to determine the prior parameters of the fragility curves. Damage data are integrated to determine the likelihood function for the Bayesian updating. Finally, MCMC is applied to sample the posterior distribution of the updated equipment capacity. The main contributions of the work are: (i) an ANN adaptive training algorithm is proposed for a more intelligent selection of the sample in the DoEs; (ii) a method to construct the likelihood function is proposed to deal with existing damage data from SQUG database.

The methodology is applied to evaluate the fragility curve of a low-voltage switchgear in a Japanese nuclear power plant Kashiwazaki-Kariwa. The application of the adaptive ANN training provides an improved design of experiments to conduct FEM simulation. Then, the construction of the likelihood function with SQUG damage data is realized by a two-step PGA transformation. The uncertainty related to the transformation is also quantified and integrated in the computation of the likelihood function. A sensitivity analysis is finally conducted to investigate the influence of the subjectively determined prior parameters on the posterior distribution of the equipment capacity.

Bibliography

Beck, J. L. and Taflanidis, A. A. (2013). Prior and posterior robust stochastic predictions for dynamical systems using probability logic. *International Journal for Uncertainty Quantification*, 3:271–288.

Biasio, M. D., Grange, S., Dufour, F., Allain, F., and Petre-Lazar, I. (2015). Intensity measures for probabilistic assessment of non-structural components acceleration demand. *Earthquake Eng. Struct. Dyn.*, 44:2261–2280.

Buratti, N., Minghini, F., Ongaretto, E., Savoia, M., and Tullini, N. (2017). Empirical seismic fragility for the precast rc industrial buildings damaged by the 2012 Emilia (Italy) earthquakes. *Earthquake Eng. Struct. Dyn.*, 48:2317–2335.

Campbell, K. W. and Bozorgnia, Y. (2008). NGA ground motion model for the geometric mean horizontal component of PGA, PGV, PGD and 5% damped linear elastic response spectra for periods ranging from 0.01 to 10 s. *Earthquake Spectra*, 24:139–171.

Ellingwood, B. R. and Kinali, K. (2009). Quantifying and communicating uncertainty in seismic risk assessment. *Struct. Saf.*, 31:179–187.

EPRI (1991). Generic seismic ruggedness of power plant equipment (Revision 1). Technical report, Electric Power Research Institute EPRI, Palo Alto, CA.

EPRI (1994). Methodology for developing seismic fragilities. Technical report, Electric Power Research Institute EPRI, Palo Alto, CA. Report TR-103959.

EPRI (2007). EPRI independent peer review of the TEPCO seismic walkdown and evaluation of the Kashiwazaki-Kariwa nuclear power plants. Technical report, Electric Power Research Institute EPRI, Palo Alto, CA. Report TR-1016317.

EPRI (2009). Seismic fragility applications guide update. Technical report, Electric Power Research Institute EPRI, Palo Alto, CA. Report TR-1019200.

EPRI (2014). Assessment of the use of experience data to develop seismic fragilities. Technical report, Electric Power Research Institute EPRI, Palo Alto, CA. Report 3002002933.

EPRI (2016). *SQUG seismic experience database*. Electric Power Research Institute EPRI, Palo Alto, CA. http://esqug.epri.com/.

EPRI (2017). Updated equipment seismic capacities from experience data for use in the fragility calculations. Technical report, Electric Power Research Institute EPRI, Palo Alto, CA. Report 3002011627.

Gardoni, P., Mosalam, K. M., and Kiureghian, A. D. (2009). Probabilistic seismic demand models and fragility estimates for RC bridges. *J. Earthq. Eng.*, pages 79–106.

Gidaris, I., Taflanidis, A. A., and Mavroeidis, G. P. (2015). Kriging metamodeling in seismic risk assessment based on stochastic ground motion models. *Earthquake Eng. Struct. Dyn.*, 44(14):2377–2399.

Hastings, W. K. (1970). Monte carlo sampling methods using Markov chains and their applications. *Biometrika*, 57:97–105.

IAEA (2013). Review of seismic evaluation methodologies for nuclear power plants based on a benchmark exercise. Technical report, International Atomic Energy Agency.

Jaiswal, K., Wald, D., and D'Ayala, D. (2011). Developing empirical collapse fragility functions for global building types. *Earthquake Spectra*, 27:775–795.

Jalayer, F., Iervolino, I., and Manfredi, G. (2010). Structural modeling uncertainties and their influence on seismic assessment of existing RC structures. *Struct. Saf.*, 32:220–228.

Jeon, J.-S., Mangalathu, S., Song, J., and DesRoches, R. (2017). Parameterized seismic fragility curves for curved multi-frame concrete box-girder bridges using Bayesian parameter estimation. *J. Earthq. Eng.*, 0:1–26.

Kennedy, R., Cornell, C., Campell, R., Kaplan, S., and Perla, H. (1980). Probabilistic seismic safety study of an existing nuclear power plant. *Nucl. Eng. Des.*, 59:315–338.

Koutsourelakis, P. S. (2010). Assessing structural vulnerability against earthquakes using multi-dimensional fragility surfaces: A bayesian framework. *Probab. Eng. Mech.*, 25:49–60.

Noh, H.-Y., Kiremidjian, A., Ceferino, L., and So, E. (2017). Bayesian updating of earthquake vulnerability functions with application to mortality rates. *Earthq. Spectra*, 33:1173–1189.

Padgett, J. E. and DesRoches, R. (2008). Methodology for the development of analytical fragility curves for retrofitted bridges. *Earthquake Eng. Struct. Dyn.*, 37:1157–1174.

Rossetto, T. and Elnashai, A. (2003). Derivation of vulnerability functions for european-type RC structures based on observational data. *Eng. Struct.*, 25:1241–1263.

Rota, M., Pennab, A., and C.L.Strobbia (2008). Processing Italian damage data to derive typological fragility curves. *Soil. Dyn. Earthq. Eng.*, 28:933–947.

Shinozuka, M., Feng, M. Q., Lee, J., and Naganuma, T. (2000). Statistical analysis of fragility curves. *J. Eng. Mech.*, 126:1224–1231.

Singhal, A. and Kiremidjian, A. S. (1998). Bayesian updating of fragilities with application to RC frames. *J. Struct. Eng.*, 124:922–929.

Starck, R. G. and Thomas, G. G. (1990). Overview of SQUG generic implementation procedure (GIP). *Nucl. Eng. Des.*, 123:225–231.

Straub, D. and Kiureghian, A. D. (2008). Improved seismic fragility modeling from empirical data. *Struct. Saf.*, 30:320–336.

Wang, Z., Pedroni, N., Zentner, I., and Zio, E. (2018). Seismic fragility analysis with artificial neural networks: Application to nuclear power plant equipment. *Eng. Struct.*, 162:213–225.

Yoshida, N., Kobayashi, S., Suetomi, I., and Miura, K. (2002). Equivalent linear method considering frequency dependent characteristics of stiffness and damping. *Soil. Dyn. Earthq. Eng.*, 22:205–222.

Zentner, I. (2010). Numerical computation of fragility curves for NPP equipment. *Nucl. Eng. Des.*, 240:1614–1621.

Chapter 5

Computation of Ground Motion Prediction Equations with ANNs

Ground motion prediction equations (GMPEs) are used to describe seismic intensity measures as a function of source-, path- and site-related parameters. Although functional models are still widely used for their computation, a fully data-driven approach has been recently proposed based on artificial neural networks (ANNs). Moreover, the estimation errors of the predictor parameters (e.g. the magnitude and Vs_{30}) should be accounted for in the development of GMPEs. In this chapter, the uncertainty in the input parameters is considered in the computation of GMPEs by ANNs. The ANN training based on the generalized least squares principle is employed to compute the GMPEs. A simulated database is used to validate the approach and to demonstrate the effect of the input parameter uncertainties on the GMPEs. Finally, the proposed model is applied to the RESORCE data collected from Pan-Europe earthquakes. Results show that, by the proper consideration of uncertainty on the input parameters, the total GMPE uncertainties can be reduced by 4-16%, whereas the median predictions remain similar.

Contents

5.1 Introduction

Probabilistic seismic hazard analysis (PSHA) is performed to determine the seismic design load of civil structures [Bommer and Abrahamson 2006]. Within PSHA, ground motion prediction equations (GMPEs) provide median values, and associated uncertainty, of seismic intensity measures (IMs), for given values of source-, path- and site-related parameters. With the classical assumption of lognormal distributions of the IMs, seismic hazard curves can be further determined.

The GMPEs are modeled by 'mixed-effects model' with particular functional forms. The underlying model parameters are determined either by the one-stage regression [Abrahamson and Youngs 1992] or by the two-stage regression [Joyner and Boore 1993]. This can be a limitation if the computation of GMPEs for a new IM is required, as it is necessary to develop new functional models or to determine whether the existing functional forms can be generalized. Furthermore, if additional site proxies are considered, the functional forms need to be adjusted. To overcome these difficulties, non-parametric data-driven methods haven been applied to ground motion prediction. Hermkes et al. [2014] proposes GMPE models based on Gaussian process regression for application to the European RESORCE database. Models based on artificial neural networks (ANNs) have been developed in the past by Derras et al., with applications to American NGA West database [Derras et al. 2016], RESORCE database [Derras et al. 2014, 2016] and Japanese Kik-Net database [Derras et al. 2017]. In Dhanya and Raghukanth [2017], the performance of ANNs is further improved by a genetic algorithm in the computation of GMPEs. Variations of the neural network model, e.g. general regression neural networks and adaptive neuro-fuzzy inference systems, have been tested recently for applicability in the development of GMPEs [Stambouli et al. 2017; Ameur et al. 2018]. An advantage of using ANNs for the development of GMPEs is that a vector of IMs can be computed simultaneously, instead of having to develop a different functional model for each individual IM and conduct regression for estimating its parameters.

On the other hand, the existing GMPEs models with ANNs do not consider the uncertainty of input parameters (e.g. magnitude M_w and thirty-meter shear-wave velocity Vs_{30}).

In practice, epistemic uncertainties can affect the source-, path- and site-related parameters due to their determination procedures [Moss 2011]. Methods, which consider the epistemic uncertainty of the input parameters, can be divided into three categories. Crude Monte-Carlo simulations are used by Foulser-Piggott [2014], to propagate the uncertainties in the input variables. The values of the uncertain input parameters are sampled from chosen distributions and a number of GMPE regression analyses are conducted with the generated inputs. The variations of the model parameters and model output standard deviations, obtained from the different GMPE models, are analyzed, showing that the GMPE total uncertainty is little impacted by the uncertain inputs, whereas the influence on the GMPE medians can be significant. The second category applies the first order second moment (FOSM) method to the uncertain GMPE model. In this way, the variance-covariance matrix of the mixed-effects model contains supplementary epistemic uncertainty terms. The maximum likelihood problem can be solved by generalized least squares regression. This is the approach taken by Rhoades [1997], Gehl et al. [2011], for treating the uncertainty in M_w and Vs_{30}, respectively. The last category of methods consists in applying Bayesian regression in the development of the GMPEs. The uncertainties in the input parameters are described by Bayesian prior distributions. One can refer to Moss [2011], Stafford [2014], Kuehn and Abrahamson [2017] for more details concerning the Bayesian approach. These studies show a reduction of the total uncertainty σ, for example 5-10% in Moss [2011] and 1-13% in Kuehn and Abrahamson [2017]. The reduction is explained by the epistemic uncertainty in the input parameters of the GMPEs.

In this chapter, we aim to account for the input parameter uncertainties in the non-parametric ANN-based GMPE models. The approach adopted is the FOSM approach. The ANN training algorithm based on the generalized least squares principle, which is explained in Chapter 2.2, is applied to compute the GMPEs. This allows taking into consideration the non-diagonal variance-covariance matrix of the residuals in the ANN training. The proposed method is first validated by a simulated database for verification and, then, applied to the RESORCE database [Akkar et al. 2014b] for pan-European earthquakes.

In this chapter, we start with the mathematical modeling of the mixed effect model and explain furthermore the method for considering of input uncertainties with ANNs. The databases used in this chapter are later presented briefly. The proposed method is applied to the simulated database, for the purpose of validation of the methodology and analysis of the influence of the input uncertainties. For real applications, the effect of input uncertainties is studied with respect to the RESORCE database.

5.2 Treatment of input uncertainties with ANNs

5.2.1 Mixed-effects model with ANNs

We consider developing GMPEs model based on magnitude M_w, Joyner-Boore distance R_{jb} and thirty-meter shear-wave velocity Vs_{30}:

$$y_{ij} := \ln \mathrm{IM}_{ij} = \mu(M_{w,i}, \ln R_{jb,ij}, \ln Vs_{30,j}; \underline{\theta}) + \eta_i + \varepsilon_{ij}, \tag{5.2.1}$$

where y_{ij} denotes the logarithmic values of the seismic IMs, the symbol ':=' explains the definition of the variable of its left side, μ represents the regression function, i.e. the median of the GMPE model, η_i is the inter-event residual for the ith event, assumed following $\mathcal{N}(0, \tau^2)$, and ε_{ij} is the intra-event residual for the jth earthquake signal of the ith event, assumed following $\mathcal{N}(0, \phi^2)$. η_i and ε_{ij} are assumed to be independently distributed. As an earthquake event can be observed on different observation sites, we use this double index notation ij, meaning that this is the seismic intensity measure (or other relevant parameters) of the earthquake event i observed on the site j.

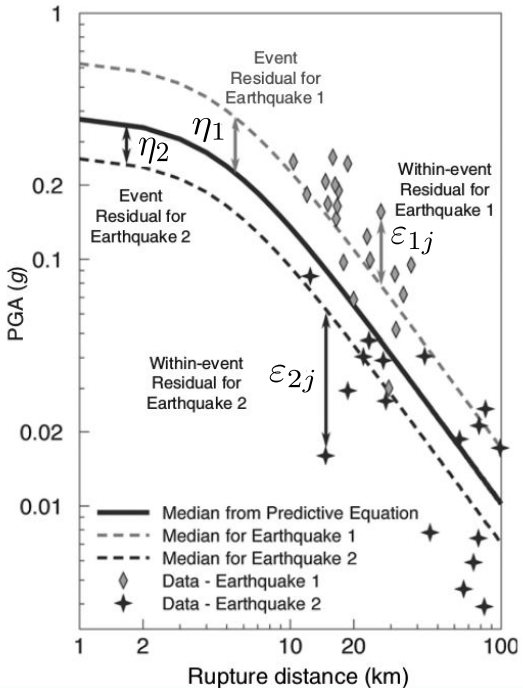

Figure 5.1: Explanation of the inter-event and intra-event residuals

The concepts of the inter- and intra-event residuals are explained with Figure 5.1. In this figure, the PGA values of two different earthquake events observed on different sites are collected and plotted with two different symbols. The inter-event residuals are the differences between the median of each earthquake (dashed lines) and the median prediction function μ (solid line). The intra-event residuals are the variations of data with respect to the median

of their corresponding earthquake event.

Without loss of generality, the logarithmic values $\ln R_{jb}$ and $\ln Vs_{30}$ are used as the inputs of the GMPE, as in Derras et al. [2014], and $\underline{\theta}$ is the vector of the parameters of the assumed functional or data-driven model. The total uncertainty σ of the GMPE is

$$\sigma = \sqrt{\tau^2 + \phi^2}. \tag{5.2.2}$$

In matrix form, Eq.5.2.1 becomes

$$\underline{y} = \underline{\mu} + \underline{\underline{Z}}\,\underline{\eta} + \underline{\varepsilon}, \tag{5.2.3}$$

where $\underline{y}$, $\underline{\mu}$, $\underline{\varepsilon}$ are $N \times 1$ matrices, with N being the total number of earthquake records, $\underline{\eta}$ is the $M \times 1$ inter-event residual matrix, with M the total number of earthquake events, and $\underline{\underline{Z}}$ is a $N \times M$ matrix, which allocates the inter-event residual to its corresponding earthquake record. This latter matrix $\underline{\underline{Z}}$ is of the form:

$$\underline{\underline{Z}} = \begin{bmatrix} \underline{\underline{Z}}_{n_1} & \underline{\underline{0}} & \cdots & \underline{\underline{0}} \\ \underline{\underline{0}} & \underline{\underline{Z}}_{n_2} & \cdots & \underline{\underline{0}} \\ \vdots & \vdots & \ddots & \vdots \\ \underline{\underline{0}} & \underline{\underline{0}} & \cdots & \underline{\underline{Z}}_{n_M} \end{bmatrix}, \quad \text{with } \underline{\underline{Z}}_{n_i} = \underbrace{\begin{bmatrix} 1 & 1 & \cdots & 1 \end{bmatrix}^T}_{n_i \text{ elements}}, \tag{5.2.4}$$

where n_i $(i = 1, 2, \cdots, M)$ represents the number of earthquake records of the ith event, $\underline{\underline{Z}}_{n_i}$ is a column vector with all the n_i elements equal to one, and the index ^{T} denotes the matrix transpose.

The solution of the mixed-effects problem (Eq.5.2.1) requires determining the model parameters $\underline{\theta}$, and the inter- and intra-event uncertainties τ and ϕ, by maximizing the following log-likelihood function $\ln L$:

$$\ln L = -\frac{N}{2}\ln 2\pi - \frac{1}{2}\ln|\underline{\underline{C}}| - \frac{1}{2}(\underline{y} - \underline{\mu})^T \underline{\underline{C}}^{-1}(\underline{y} - \underline{\mu}), \tag{5.2.5}$$

where $\underline{\underline{C}}$ is the variance-covariance matrix of the inter- and intra-event residuals:

$$\underline{\underline{C}} = \tau^2 \underline{\underline{Z}}\,\underline{\underline{Z}}^T + \phi^2 \underline{\underline{I}}_N = \sum_{i=1}^{M}{}^{+}(\phi^2 \underline{\underline{I}}_{n_i} + \tau^2 \underline{\underline{1}}_{n_i}), \tag{5.2.6}$$

in which $\underline{\underline{I}}_N$ is the identity matrix of size $N \times N$, the same for $\underline{\underline{I}}_{n_i}$. $\underline{\underline{1}}_{n_i}$ is the matrix of ones of size $n_i \times n_i$, $\sum^+$ is the matrix direct sum operation following the notation of Abrahamson

and Youngs [1992]. More precisely, $\underline{\underline{C}}$ is a blockwise-diagonal matrix under the form:

$$\underline{\underline{C}} = \begin{bmatrix} \phi^2 \underline{\underline{I}}_{n_1} + \tau^2 \underline{\underline{1}}_{n_1} & \underline{\underline{0}} & \cdots & \underline{\underline{0}} \\ \underline{\underline{0}} & \phi^2 \underline{\underline{I}}_{n_2} + \tau^2 \underline{\underline{1}}_{n_2} & \cdots & \underline{\underline{0}} \\ \vdots & \vdots & \ddots & \vdots \\ \underline{\underline{0}} & \underline{\underline{0}} & \cdots & \phi^2 \underline{\underline{I}}_{n_M} + \tau^2 \underline{\underline{1}}_{n_M} \end{bmatrix}, \tag{5.2.7}$$

with every block being a $n_i \times n_i$ square matrix:

$$\phi^2 \underline{\underline{I}}_{n_i} + \tau^2 \underline{\underline{1}}_{n_i} = \underbrace{\begin{bmatrix} \phi^2 + \tau^2 & \tau^2 & \cdots & \tau^2 \\ \tau^2 & \phi^2 + \tau^2 & \cdots & \tau^2 \\ \vdots & \vdots & \ddots & \vdots \\ \tau^2 & \tau^2 & \cdots & \phi^2 + \tau^2 \end{bmatrix}}_{\text{a } n_i \times n_i \text{ square matrix}}. \tag{5.2.8}$$

The maximization of Eq.5.2.5 is achieved by an iterative expectation-maximization (EM) algorithm. The derivation of the algorithm proposed by Abrahamson and Youngs [1992] is explained in detail in the Appendix.

Instead of functional models, ANNs can be used to perform data-driven regressions for the determination of μ, τ^2 and ϕ^2 of the GMPEs. In this study, we use classical feed-forward ANNs, which consist of a set of model parameters $\underline{\theta}$ and activation functions associated to neuron nodes. The type of activation functions are selected following [Derras et al. 2014]: hyperbolic tangent sigmoid functions are used for the hidden layer nodes and linear functions are applied to the output nodes. The model parameters $\underline{\theta}$ contain the ANN weights $\underline{w}$ and biases $\underline{b}$, which are adjusted by training to minimize the cost function, i.e. the square error between $\underline{y}$ and $\underline{\mu}$:

$$\underline{\theta}^* = \begin{bmatrix} \underline{w}^* \\ \underline{b}^* \end{bmatrix} = \arg\min_{\underline{\theta}} \frac{1}{2} \sum_i [\underline{y}^i - \underline{\mu}^i(\underline{x}; \underline{\theta})]^T [\underline{y}^i - \underline{\mu}^i(\underline{x}; \underline{\theta})], \tag{5.2.9}$$

where $\underline{x}$ is used to denote the input parameters of ANNs. In the GMPEs computation of Eq.5.2.1, this latter $\underline{x}$ represents the ground motion predictor parameters M_w, $\ln R_{jb}$ and $\ln Vs_{30}$. The index i is the ith output of the ANN, i.e. the ith IM for the GMPEs. The training of ANNs is typically achieved by gradient-based back-propagation algorithms [Rumelhart et al. 1986; Bishop 1995] to find the optimal $\underline{\theta}^*$. It is worth mentioning that one assumption of the validity of Eq.5.2.9 is that the ANN residuals should be statistically independent and identically distributed (IID). If the residuals are correlated, this correlation should be accounted for in the cost function, which gives rise to a generalized least squares

(GLS) problem for the ANN training. This case of correlated ANN residuals is addressed in detail later.

The ANN-based GMPEs computation is divided into the following steps [Derras et al. 2014]:

1. Initialization step: train an ANN to determine $\underline{\theta}$, using $\underline{x}$ and $\underline{y}$ as the inputs and outputs of the ANN.

2. With $\underline{\mu}$ computed from the determined $\underline{\theta}$, estimate τ^2 and ϕ^2 in maximizing Eq.5.2.5.

3. Given $\underline{\mu}$, τ^2 and ϕ^2, compute η_i using Eq.(10) in [Abrahamson and Youngs 1992]:

$$\eta_i = \frac{\tau^2 \sum_{j=1}^{n_i} y_{ij} - \mu_{ij}}{n_i \tau^2 + \phi^2}. \tag{5.2.10}$$

4. Train an ANN to determine $\underline{\theta}$, using $\underline{x}$ and $\underline{y} - \underline{\eta}$ as the inputs and outputs of the ANN.

5. Repeat the steps 2-4 until Eq.5.2.5 is maximized.

Normalization and denormalization procedures are performed before and after the ANN training; one can refer to Derras et al. [2014] for more details about this.

Let us study further why a classical ANN training can be applied in this algorithm. By subtracting η_i on both sides of Eq.5.2.1, only the residual term ε_{ij} remains on the right-hand side of the equation:

$$y_{ij} - \eta_i = \mu(M_{w,i}, \ln R_{jb,ij}, \ln Vs_{30,j}; \underline{\theta}) + \varepsilon_{ij}. \tag{5.2.11}$$

Therefore, the residuals are IID if $\underline{x}$ and $\underline{y} - \underline{\eta}$ are used as the inputs and outputs of the ANN. Then, the algorithm described above is valid when the variance-covariance $\underline{\underline{C}}$ is under the form of Eq.5.2.7. However, if additional terms appear on the right-hand side of Eq.5.2.1, i.e. if $\underline{\underline{C}}$ is not blockwise diagonal, a new algorithm is required to solve the mix-effects problem.

5.2.2 ANN GMPEs models with input uncertainties

The FOSM method, proposed in Rhoades [1997] and Gehl et al. [2011], is used in this study for the consideration of input uncertainties in ANN-based GMPEs model. It consists in introducing the first order Taylor expansion of the GMPE model with input uncertainties. Considering uncertainty on input parameters, the model reads

$$y_{ij} = \mu(M_{w,i}, \ln R_{jb,ij}, \ln Vs_{30,j}) + \eta_i + \varepsilon_{ij} = \mu(\hat{M}_{w,i} + \delta M_i, \ln R_{jb,ij}, \ln \hat{V}s_{30,j} + \delta Vs_j) + \eta_i + \varepsilon_{ij}. \tag{5.2.12}$$

Here, $M_{w,i}$ is the true magnitude, $\hat{M}_{w,i}$ denotes the observed magnitude (i.e. with uncertainty) and δM_i is the error related to the measurement. The same holds for Vs_{30}, $\hat{V}s_{30}$ and δVs_j,

respectively. The observation errors are assumed to follow normal distributions: $\delta M_i \sim \mathcal{N}(0, \sigma_M^2)$, $\delta Vs_j \sim \mathcal{N}(0, \sigma_{\ln Vs}^2)$. After applying the first order Taylor expansion to Eq.5.2.12, one obtains

$$\begin{aligned} y_{ij} &= \mu(\hat{M}_{w,i} + \delta M_i, \ln R_{jb,ij}, \ln \hat{V}s_{30,j} + \delta Vs_j) + \eta_i + \varepsilon_{ij} \\ &= \mu(\hat{M}_{w,i}, \ln R_{jb,ij}, \ln \hat{V}s_{30,j}) + \delta M_i \frac{\partial \mu}{\partial M_w}|_{\underline{\hat{x}}} + \delta Vs_j \frac{\partial \mu}{\partial \ln Vs}|_{\underline{\hat{x}}} + \eta_i + \varepsilon_{ij}, \end{aligned} \tag{5.2.13}$$

where $\underline{\hat{x}}$ represents the vector of the observed inputs. Considering that δM_i and δVs_j are independent from each other, the variance-covariance matrix $\underline{\underline{C}}$ related to Eq.5.2.13 contains the following elements:

1. Diagonal elements C_{kk}: $\tau^2 + \phi^2 + (\frac{\partial \mu}{\partial M_w}|_{\underline{\hat{x}}_k})^2 \sigma_M^2 + (\frac{\partial \mu}{\partial \ln Vs}|_{\underline{\hat{x}}_k})^2 \sigma_{\ln Vs}^2$;
2. Off-diagonal elements $C_{kk'}^e$, for the records k and k' sharing the same earthquake event: $\tau^2 + (\frac{\partial \mu}{\partial M_w}|_{\underline{\hat{x}}_k} \frac{\partial \mu}{\partial M_w}|_{\underline{\hat{x}}_{k'}}) \sigma_M^2$;
3. Off-diagonal elements $C_{kk'}^s$, for the records k and k' sharing the same observation site: $(\frac{\partial \mu}{\partial \ln Vs}|_{\underline{\hat{x}}_k} \frac{\partial \mu}{\partial \ln Vs}|_{\underline{\hat{x}}_{k'}}) \sigma_{\ln Vs}^2$;
4. Zero for all the other elements.

Given the off-diagonal elements $C_{kk'}^s$, the variance-covariance matrix $\underline{\underline{C}}$ is not blockwise-diagonal, so that the EM approach used by Derras et al. [2014] is not applicable in this case. Instead, as mentioned in Gehl et al. [2011], an approach based on the generalized least squares (GLS) is required for the maximization of Eq.5.2.5.

Here, the algorithm proposed in Gehl et al. [2011] is adapted for the computation of GMPEs by ANNs trained with correlated residuals. The variance-covariance matrix of the residuals is computed according to the previous part. In the subsequent parts of this chapter, the ANNs trained considering correlated residuals are called GLS ANNs. The cost function for the GLS ANNs reads

$$E(\underline{\theta}) = \frac{1}{2} \sum_i [\underline{y}^i - \underline{\mu}^i(\underline{x}; \underline{\theta})]^T [\underline{\underline{C}}^i]^{-1} [\underline{y}^i - \underline{\mu}^i(\underline{x}; \underline{\theta})], \tag{5.2.14}$$

where $\underline{\underline{C}}^i$ is the variance-covariance matrix for the ith IM. The minimization of Eq.5.2.14 can be realized by the GLS ANN training algorithm Eq.2.2.6 mentioned in Chapter 2:

$$\Delta\theta_k = \left[\sum_i [\underline{\underline{J}}_k^i]^T [\underline{\underline{C}}_k^i]^{-1} [\underline{\underline{J}}_k^i] + \lambda \underline{\underline{I}}_{n_\theta} \right]^{-1} \left[\sum_i [\underline{\underline{J}}_k^i]^T [\underline{\underline{C}}_k^i]^{-1} [\underline{r}_k^i] \right]. \tag{5.2.15}$$

A proper choice of λ is realized by cross-validation in this study.

To obtain GMPEs models considering uncertain inputs, we propose the following algorithm :

1. Initialization step $k = 0$: randomly initialize an ANN, and initialize the first variance-covariance matrix $\underline{\underline{C}}^i$ with the identity matrix $\underline{\underline{I}}$.
2. Compute $\Delta\theta_k$ according to Eq.5.2.15. Update the ANN model parameters $\theta_{k+1} = \theta_k + \Delta\theta_k$
3. With the current ANN parameters θ_{k+1}, estimate τ^2_{k+1} and ϕ^2_{k+1} in maximizing Eq.5.2.5. The maximization is performed with existing numerical optimization tools.
4. Compute the variance-covariance matrix $\underline{\underline{C}}_{k+1}$, as described before.
5. Repeat the steps 2-4 until convergence.

For the evaluation of the derivatives, we apply the finite difference method to approximate $\frac{\partial\mu}{\partial M}$, $\frac{\partial\mu}{\partial \ln Vs}$, and the back-propagation algorithm [Rumelhart et al. 1986; Bishop 1995] to compute the Jacobian matrices $\underline{\underline{J}}$.

5.2.3 Determination of inter-event and intra-event residuals

With the determined values of inter-event and intra-event uncertainties τ and ϕ, the inter-event and intra-event residuals can be calculated for every earthquake record. The computation is based on the theory of multi-variate Gaussian distributions. Let us consider the joint distribution of $\underline{y}$ and $\underline{\eta}$:

$$\begin{bmatrix} \underline{y} \\ \underline{\eta} \end{bmatrix} \sim \mathcal{N}\left(\begin{bmatrix} \underline{\mu} \\ \underline{0} \end{bmatrix}, \begin{bmatrix} \underline{\underline{C}} & \tau^2\underline{\underline{Z}} \\ \tau^2\underline{\underline{Z}}^T & \tau^2\underline{\underline{I}}_M \end{bmatrix} \right), \tag{5.2.16}$$

where $\underline{\underline{C}}$ is the variance-covariance matrix computed according to Section 5.2.2 with the determined values of τ, ϕ and the assumed values of σ_M, $\sigma_{\ln Vs}$. Considering the properties of multi-variate Gaussian distributions, the estimate of the inter-event residual vector $\hat{\underline{\eta}}$, defined by the expectation of $\underline{\eta}$ given earthquake observations $\underline{y}$, is calculated by

$$\hat{\underline{\eta}} := \mathbf{E}(\underline{\eta}|\underline{y}) = \tau^2\underline{\underline{Z}}^T\underline{\underline{C}}^{-1}(\underline{y} - \underline{\mu}), \tag{5.2.17}$$

where $\mathbf{E}(\cdot)$ is the mathematical operator used to calculate the statistical expectation. It is worth mentioning that Eq.5.2.17 is a generalized form of Eq.5.2.10, when $\underline{\underline{C}}$ is not block-wise diagonal. If the epistemic uncertainties of M_w and Vs_{30} are not modeled, namely if $\underline{\underline{C}} = \tau^2\underline{\underline{Z}}\,\underline{\underline{Z}}^T + \phi^2\underline{\underline{I}}_N$ (Eq.5.2.7), Eq.5.2.10 can be easily derived by applying the relation $\tau^2\underline{\underline{Z}}^T(\tau^2\underline{\underline{Z}}\,\underline{\underline{Z}}^T + \phi^2\underline{\underline{I}}_N)^{-1}(\underline{y} - \underline{\mu}) = (\underline{\underline{Z}}^T\underline{\underline{Z}} + \underline{\underline{I}}_M\phi^2/\tau^2)^{-1}\underline{\underline{Z}}^T(\underline{y} - \underline{\mu})$ [Dempster et al. 1981] and by performing block matrix multiplication.

In the same way, the joint distribution of $\underline{y}$ and $\underline{\varepsilon}$ is written as

$$\begin{bmatrix} \underline{y} \\ \underline{\varepsilon} \end{bmatrix} \sim \mathcal{N}\left(\begin{bmatrix} \underline{\mu} \\ \underline{0} \end{bmatrix}, \begin{bmatrix} \underline{\underline{C}} & \phi^2 \underline{\underline{I}}_N \\ \phi^2 \underline{\underline{I}}_N & \phi^2 \underline{\underline{I}}_N \end{bmatrix} \right), \tag{5.2.18}$$

and the estimate of the intra-event residual vector $\hat{\underline{\varepsilon}}$ is obtained by

$$\hat{\underline{\varepsilon}} := \mathbf{E}(\underline{\varepsilon}|\underline{y}) = \phi^2 \underline{\underline{C}}^{-1}(\underline{y} - \underline{\mu}). \tag{5.2.19}$$

5.3 Case study databases

5.3.1 RESORCE database

The RESORCE (Reference database for seismic ground motion in Europe) database collects earthquake records in broader European areas for researches and applications in earthquake engineering. Current RESORCE database contains 5882 processed accelerograms, collected from 1814 events and 1540 stations [Akkar et al. 2014b]. For the computation of the GMPE, we select ground motion records with $M_w \in [3.5, 7.6]$ and $R_{jb} \in [0, 200]$km. We focus the analyses on shallow crustal earthquakes, with depth less than 30 km. Vs_{30} is considered as the only site-related parameter in this study. Ground motions without Vs_{30} or R_{jb} values are not retained for the computation of the GMPEs. After applying these criteria, the final dataset consists of 893 earthquake records, collected from 269 events. The selected ground motion records were measured on 289 different stations. The distribution of M_w, R_{jb} and Vs_{30} of the selected dataset is illustrated in Figure 5.2. It can be observed that most of the earthquake signals are concentrated in the range of M_w values from 4.5 to 6.5. More near-fault earthquakes are selected than far-fault earthquakes. Few records are measured on stations with $Vs_{30} > 720$m/s.

We focus on the computation of GMPEs based on M_w, $\ln R_{jb}$ and $\ln Vs_{30}$, following Derras et al. [2014]. The depth and the type of the fault are not included in the GMPE, since the sensitivity analysis conducted by Derras et al. [2014] reveals that the contribution of these two parameters to the IMs is negligible. Eighteen IMs are selected as the outputs of the GMPEs, including PGA (peak ground acceleration), PGV (peak ground velocity) and sixteen different 5% damping spectral accelerations: Sa(0.3Hz), Sa(0.5Hz), Sa(0.67Hz), Sa(1Hz), Sa(1.3Hz), Sa(2Hz), Sa(2.5Hz), Sa(3.3Hz), Sa(4.2Hz), Sa(5Hz), Sa(6.7Hz), Sa(10Hz), Sa(13.3Hz), Sa(20Hz), Sa(33.3Hz) and Sa(100Hz). The geometrical mean of the two horizontal components is used as the IM value.

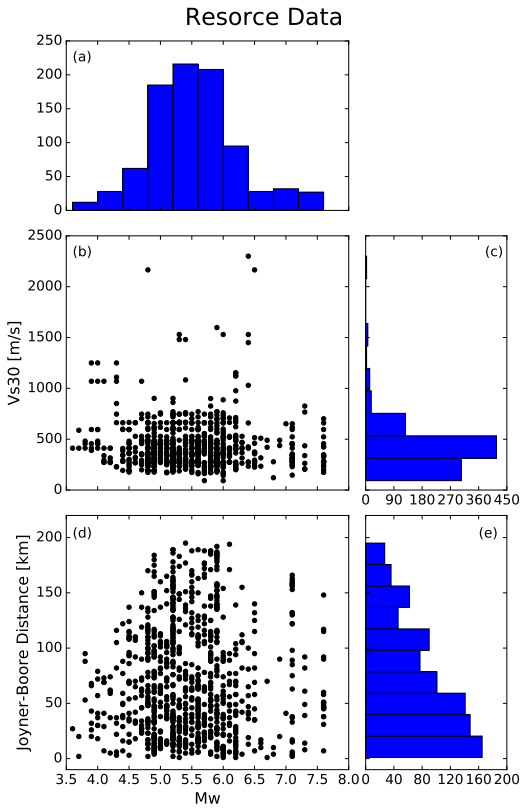

Figure 5.2: Distribution of M_w, R_{jb} and Vs_{30} of the selected earthquake records in RESORCE database. (a) Histogram of M_w of the selected RESORCE dataset; (b) Scatter plot of the selected dataset in M_w-Vs_{30} space; (c) Histogram of Vs_{30}; (d) Scatter plot of the selected dataset in M_w-R_{jb} space; (e) Histogram of R_{jb}.

5.3.2 Simulated database

A simulated database is constructed to assess the methodology and to analyze in a controlled way the effect of the input uncertainties on τ and ϕ. Based on the magnitude, distance and site parameters in the RESORCE database, the simulated database is built with assumed inter- and intra-event uncertainties $\tau = 0.2$ and $\phi = 0.3$. By comparing the values of τ and ϕ computed by the proposed algorithm to those used to generate the database, the accuracy of the methodology can be checked. In addition, we perform ten different realizations of the Monte Carlo sampling of inter- and intra-event residuals. The purpose is to evaluate the standard deviations linked to the estimation of inter- and intra-event uncertainties. The construction of the simulated database has been done as follows:

1. From 893 selected RESORCE earthquake records, extract $\hat{M}_w$, R_{jb} and $\hat{V}s_{30}$ values. The parameters are denoted by the symbol $\hat{}$ since they are observed or measured values.
2. Sample δM and δVs with $\sigma_M = 0.1$, $\sigma_{\ln Vs} = 0.3$, respectively. The real values of M_w and Vs_{30} are obtained by $M_w = \hat{M}_w + \delta M$, $\ln Vs_{30} = \ln \hat{V}s_{30} + \delta Vs$.
3. Compute the median of the $\ln$ IM by the simplified GMPE model used by Koufoudi et al.

[2015]. The values of relevant coefficients are listed in Table 5.1.

$$\mu(\ln \mathrm{IM}) = a_1 + a_2(M_w - c_1) + a_3(8.5 - M_w^2) + [a_4 + a_5(M_w - c_1)] \ln \sqrt{R_{jb}^2 + a_6^2} + b_1 \ln(\frac{Vs_{30}}{760}). \tag{5.3.1}$$

4. Sample inter-event residual η_i and intra-event residual ε_{ij} with $\tau = 0.2$, $\phi = 0.3$, respectively.
5. Compute the intensity measure values with $\ln \mathrm{IM}_{ij} = \mu_{ij}(\ln \mathrm{IM}) + \eta_i + \varepsilon_{ij}$.
6. Repeat the steps 4-5 ten times for different realizations of residuals, so that ten groups of simulated $\ln \mathrm{IM}$ values are obtained.

A simulated database, generated by ten realizations of inter- and intra-event residuals, is finally obtained.

Table 5.1: Values of coefficients used to build the simulated database. These values are obtained by computing the GMPE model for RESORCE PGA values with the functional form of Eq.5.3.1.

a_1	a_2	a_3	a_4	a_5	a_6	b_1	c_1
-3.26	1.557	0.1185	-2.565	0.2575	-7.53	-0.414	1.708

5.4 Application to the simulated database

The objective of this section is to verify the performance of the proposed algorithm in Section 5.2.2 by means the simulated database, which is generated with assumed values of τ and ϕ. The impact of the input uncertainties on the final determination of τ and ϕ is also discussed.

Three types of analyses are conducted based on the simulated database:

1. Computation of the GMPE with respect to the real inputs M_w, $\ln R_{jb}$ and $\ln Vs_{30}$.
2. Computation of the GMPE with respect to the uncertain inputs $\hat{M}_w$, $\ln R_{jb}$ and $\ln \hat{V}s_{30}$, but without accounting for the uncertainties of on the input parameters.
3. Computation of the GMPE with respect to the uncertain inputs $\hat{M}_w$, $\ln R_{jb}$ and $\ln \hat{V}s_{30}$, modeling the input uncertainties with standard deviations $\sigma_M = 0.1$, $\sigma_{\ln Vs} = 0.3$ in the computation of GMPEs. This analysis is name by 'uncertain modeling' in the sequel.

For each type of analysis, the computation of GMPE is conducted with two models, the functional model of Eq.5.3.1 and a non-parametric ANN model. The ANN model consists of 3 input nodes, 5 hidden layer nodes, and 1 output. The first two types of analyses are performed with the algorithms of Abrahamson and Youngs [1992] and Derras et al. [2014], applied to the functional model and ANN model, respectively. Regarding the uncertain

models, the functional GMPE regression is based on the GLS algorithm of Gehl et al. [2011], whereas the ANN uncertain model is built with the algorithm newly proposed in this study. The value of the damping factors λ is set to 10, estimated from the 5-fold cross-validation results of the GLS ANN training when $\underline{\underline{C}} = \underline{\underline{I}}$ (Figure 5.3).

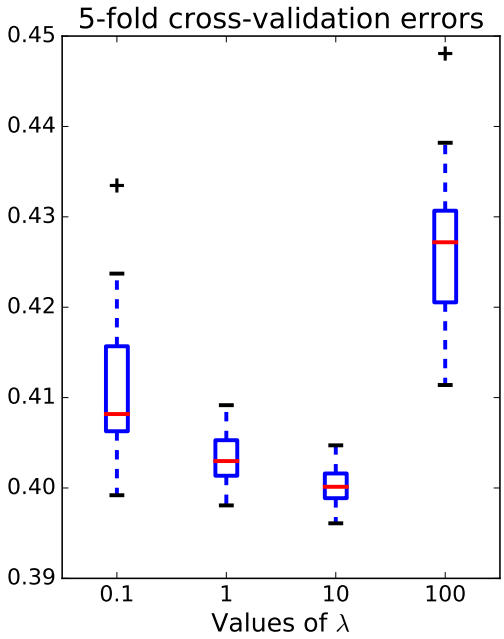

Figure 5.3: 5-fold cross-validation results for different values of λ

The three types of analyses are carried out for all of the ten simulated datasets. We estimate the mean values of the inter- and intra-event uncertainties, as well as their standard deviations from the results of the ten datasets. The values of τ, ϕ and the total uncertainty σ determined for different analyses are shown in Table 5.2. The values of τ and ϕ are determined by the mentioned algorithms and σ is calculated by $\sigma = \sqrt{\tau^2 + \phi^2}$. The values of the standard deviations are reported after the $\pm$ symbol. The results of Table 5.2 show

Table 5.2: Results of inter-event uncertainties τ and intra-event uncertainties ϕ for the simulated database

Analysis	Model	τ	ϕ	σ
Reference	-	0.2	0.3	0.36
True input values	Functional model	0.195 ± 0.023	0.297 ± 0.007	0.356 ± 0.012
	ANN	0.194 ± 0.023	0.296 ± 0.007	0.355 ± 0.012
Observed input values	Functional model	0.239 ± 0.021	0.322 ± 0.008	0.401 ± 0.013
	ANN	0.235 ± 0.020	0.320 ± 0.009	0.397 ± 0.013
$\sigma_M = 0.1$, $\sigma_{\ln Vs} = 0.3$	Functional model	0.2 ± 0.024	0.297 ± 0.008	0.359 ± 0.014
	ANN	0.198 ± 0.023	0.298 ± 0.008	0.358 ± 0.013

the influence of the input uncertainties on the values of τ and ϕ of the GMPEs computation. It can be concluded that:

1. Both ANNs and functional models provide similar estimates of the inter- and intra-event uncertainties. As the functional model is the same as the one used to generate the synthetic database, this means that the ANN can well approximate the real model in the considered case study.
2. With the true input values of M_w and Vs_{30}, both the functional model and the ANN provide good estimation of the inter- and intra-event uncertainties.
3. However, if the observed values of $\hat{M}_w$ and $\hat{V}s_{30}$ are used as the inputs of the GMPEs, and if the uncertainties associated to the observed values are not modeled, the values of τ and ϕ are overestimated (0.235 compared to 0.2 for τ, 0.320 compared to 0.3 for ϕ). This is because the input uncertainties are propagated implicitly into the GMPE model uncertainty during the GMPE computation procedure. In addition, the true values of τ and ϕ fall outside the ± 1 standard deviation range of values.
4. On the other hand, when the input uncertainty is taken into account, the overestimation is corrected by the uncertainty modeling, for both the functional model and the ANN model. This shows the necessity of modeling the input uncertainties in the GMPEs computation: otherwise, it may lead to overestimation of the inter-event and intra-event uncertainties. The proposed algorithm for the consideration of input uncertainties with ANN is also validated.

5.5 Application to RESORCE database

For the application of the input uncertainty modeling to the RESORCE dataset, the 893 selected earthquake records are divided into two sets: A training set consisting of 720 ground motions and a validation set with 173 records. The training set is used to compute the GMPEs and the corresponding inter- and intra-event uncertainty. The computed GMPEs model is validated on the validation set.

The ANN architecture used to compute the GMPEs is summarized as follows. The ANN has three input parameters: $\hat{M}_w$, R_{jb} and $\hat{V}s_{30}$. The magnitude and the shear-wave velocity are denoted with $\hat{}$, since they are considered as the observed uncertain input parameters. Five hidden layer nodes are selected, the same as Derras et al. [2014]. The damping factor λ is set to 100 from the 5-fold cross-validation executed on the 720 training data with $\underline{\underline{C}}^i = \underline{\underline{I}}$ $(i = 1, 2, ..., 18)$. We assume constant uncertainties associated to $\hat{M}_w$ and $\ln \hat{V}s_{30}$ with $\sigma_M = 0.1$, $\sigma_{\ln Vs} = 0.3$, corresponding to the average of known values of the uncertainties on the magnitude and the site information of the RESORCE dataset (0.1 and 0.265). The same values are taken in Kuehn and Abrahamson [2017] for the NGA records in which the uncertainty information is missing. The natural logarithmic values of the eighteen IMs are used as the outputs for the GMPEs computation. The damping ratio used to compute

the spectral accelerations is 5%.

5.5.1 Results

Two analyses have been performed in the computation of the GMPEs: (i) A GMPE computed directly from $\hat{M}_w$, $\ln R_{jb}$, $\ln \hat{V}s_{30}$ and 18 parameters of $\ln$ IM; (ii) A GMPE with the same input-output parameters as the first one. The uncertainties on $\hat{M}_w$ and $\ln \hat{V}s_{30}$ are modeled with the algorithm proposed in Section 5.2.2. We compare the results of these two analyses to those obtained with existing RESORCE GMPE models, including the models of Akkar et al. [2014a], Bindi et al. [2014], Bora et al. [2014], Derras et al. [2014], Hermkes et al. [2014]. The results of these five existing GMPEs are extracted from Douglas et al. [2014].

We first show the inter-event uncertainty τ, intra-event uncertainty ϕ and the total uncertainty σ of the two analyses. The τ, ϕ, σ for the 16 frequency-dependent spectral accelerations are illustrated in Figure 5.4. The legend 'ANN with uncertainty' means that the corresponding results are computed by ANN with input uncertainty modeling. The reduction ratio in Figure 5.4d calculates the relative reduction of the GMPE output standard deviations, considering the uncertain input parameters. For example:

$$r_\sigma = \frac{\sigma_{\text{ANN}} - \sigma_{\text{ANN,uncertain}}}{\sigma_{\text{ANN}}} \tag{5.5.1}$$

where r_σ represents the reduction ratio of the total uncertainty σ. In addition, the GMPE uncertainty values of PGA, PGV and three spectral accelerations Sa(0.5Hz), Sa(3.3Hz) and Sa(20Hz), representing three different frequency ranges, are listed in Table 5.3.

Table 5.3: τ, ϕ and σ values for PGA, PGV, Sa(0.5Hz), Sa(3.3Hz) and Sa(20Hz)

IMs	Uncertainties	ANN	ANN with uncertainty	Reduction ratio $r \times 100\%$
PGA	τ	0.420	0.376	10.48%
	ϕ	0.593	0.546	7.93%
	σ	0.726	0.663	8.68%
PGV	τ	0.394	0.313	20.56%
	ϕ	0.600	0.539	10.17%
	σ	0.718	0.623	13.23%
Sa(0.5Hz)	τ	0.417	0.341	18.23%
	ϕ	0.756	0.641	15.21%
	σ	0.864	0.723	16.32%
Sa(3.3Hz)	τ	0.375	0.339	9.70%
	ϕ	0.649	0.586	9.59%
	σ	0.749	0.678	9.62%
Sa(20Hz)	τ	0.444	0.401	9.68%
	ϕ	0.603	0.565	6.30%
	σ	0.749	0.693	7.48%

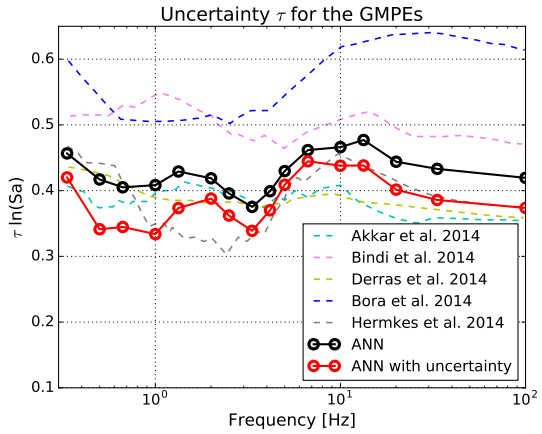

(a) Inter-event uncertainty for RESORCE data

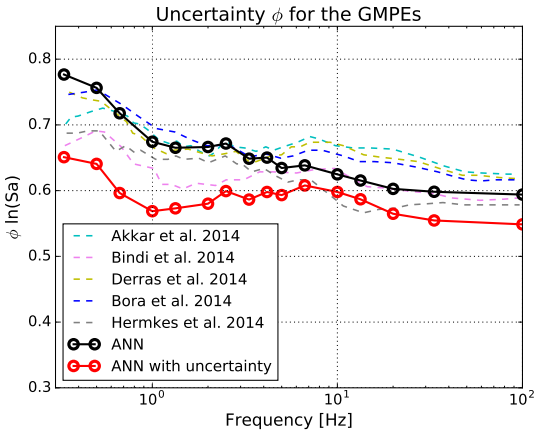

(b) Intra-event uncertainty for RESORCE data

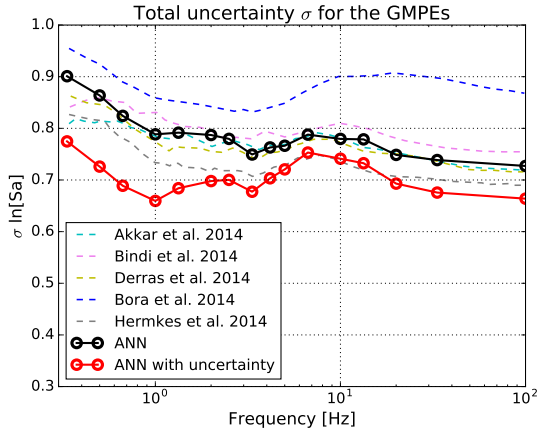

(c) Total uncertainty for RESORCE data

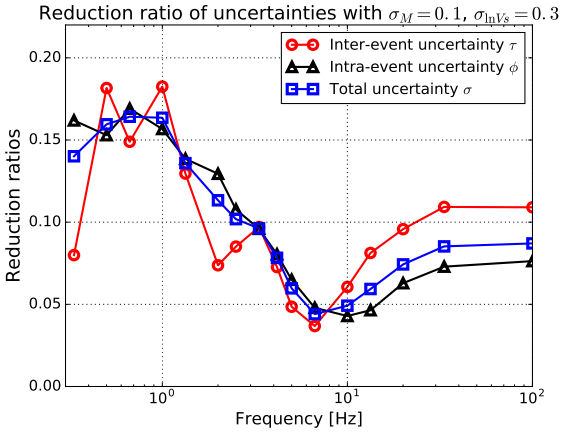

(d) Reduction ratio with the consideration of input uncertainties

Figure 5.4: Inter-event, intra-event and total uncertainties determined with the RESORCE data

From the results of Figure 5.4 and Table 5.3, it can be clearly observed that:

1. The order of magnitude of the determined τ, ϕ and σ of both ANN models stays coherent with other existing RESORCE GMPE models. The intra-event uncertainty is predominant in comparison with the inter-event uncertainty. As different GMPEs are computed with different data and different types of model, one cannot expect a perfect agreement between the results in this study and the results from other GMPEs.
2. A clear reduction of τ, ϕ and σ can be seen with the input uncertainty modeling. This is in agreement with the results obtained with the simulated database. The maximum r_σ can reach 0.16, i.e. 16% according to Figure 5.4d. The reduced part of τ, ϕ is, in fact, explained by the epistemic uncertainties introduced in the magnitude and in the share-wave velocity, which is modeled by the first order Taylor expansion with the FOSM modeling. Qualitatively, the reduction is more significant in the low frequency range than in the high frequency range. This phenomenon is further addressed in the 'Discussion' subsection.

The median GMPEs predictions for both ANN models are also plotted with two different scenarios: (i) $M_w = 5, R_{jb} = 10\text{km}, Vs_{30} = 760\text{m/s}$ and (ii) $M_w = 7$, $R_{jb} = 10\text{km}$, $Vs_{30} = 270\text{m/s}$. The comparisons between the predictions of the ANN models and other existing models are illustrated in Figure 5.5. The magnitude scaling and the distance decay of PGA and Sa(1Hz) are shown in Figure 5.6 and Figure 5.7, respectively. The magnitude scaling is computed with R_{jb}=30km, Vs_{30}=760m/s. The RESORCE data with $R_{jb} = 30 \pm 20\text{km}$, $Vs_{30} = 760 \pm 100\text{m/s}$ are also visualized in Figure 5.6. For the distance decay of PGA and Sa(1Hz), we choose $M_w = 5$, $Vs_{30} = 270\text{m/s}$ to demonstrate the impact of distance on the median predictions. The data plotted in Figure 5.7 contain the earthquake motions of $M_w = 5 \pm 0.2$, $Vs_{30} = 270 \pm 50\text{m/s}$.

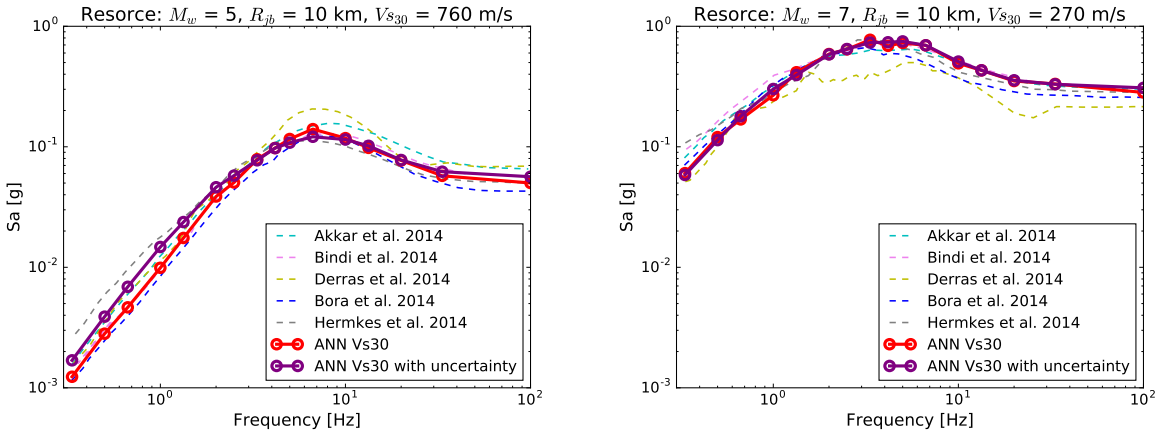

(a) $M_w = 5, R_{jb} = 10\text{km}, Vs_{30} = 760\text{m/s}$ (b) $M_w = 7$, $R_{jb} = 10\text{km}$, $Vs_{30} = 760\text{m/s}$

Figure 5.5: Comparison of median predictions of the two ANN GMPEs to existing models

In addition, we compute the inter-event and intra-event residuals of the ANN model with input uncertainty by Eq.5.2.17 and Eq.5.2.19. The results are compared to those of the ANN model without input uncertainty in Figure 5.8 and Figure 5.9, for PGA and Sa(1Hz), respectively.

Several conclusions can be drawn from Figures 5.5-5.9:

1. The ANN GMPE models, computed with or without the consideration of the input uncertainties, provide similar median predictions. This is coherent with what has been observed by Kuehn and Abrahamson [2017] using Bayesian regression. Additionally, the order of magnitude of the median predictions is in agreement with existing GMPEs computed on the basis of RESORCE database.
2. Both ANN models exhibit non-linear magnitude scaling behaviors. The effect of the magnitude scaling is less evident for PGA (an IM for high frequency range) than Sa(1Hz) (an IM for low frequency range). Although some differences exist between the ANN models and other GMPEs, the ANN models remain in the range of predictions from the other GM-

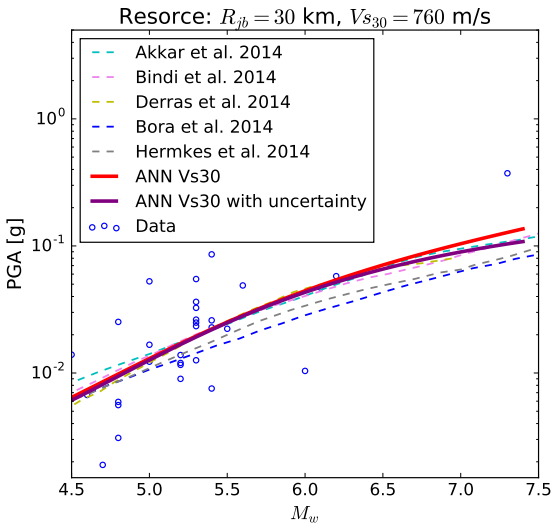

(a) Magnitude scaling of PGA, $R_{jb} = 30\text{km}, Vs_{30} = 760\text{m/s}$

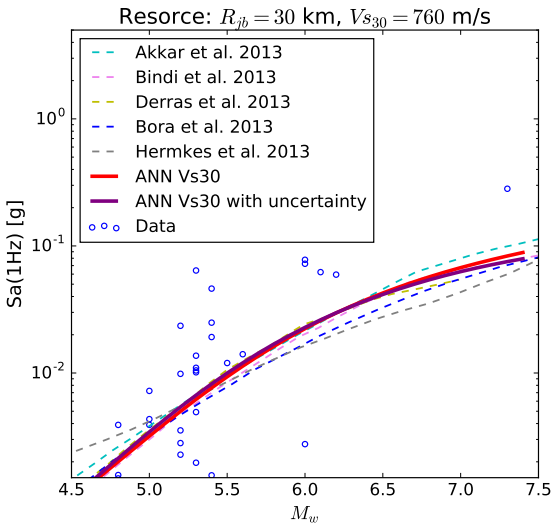

(b) Magnitude scaling of Sa(1Hz), $R_{jb} = 30\text{km}$, $Vs_{30} = 760\text{m/s}$

Figure 5.6: Magnitude scaling of PGA and Sa(1Hz). The data are selected from the earthquake records with $R_{jb} \in [10\text{km}, 50\text{km}]$ and $Vs_{30} \in [660\text{m/s}, 860\text{m/s}]$

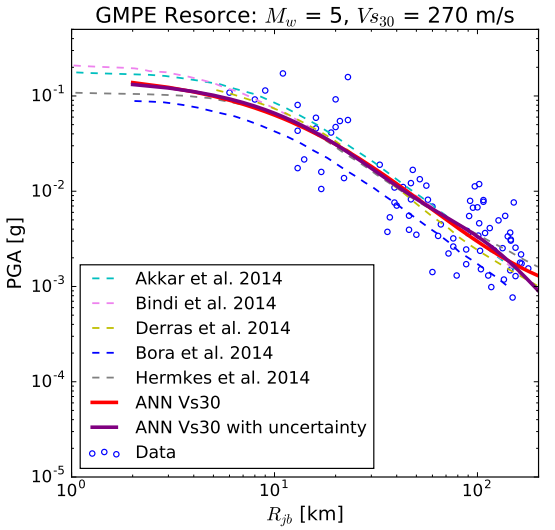

(a) Distance decay of PGA, $M_w = 5, Vs_{30} = 270\text{m/s}$

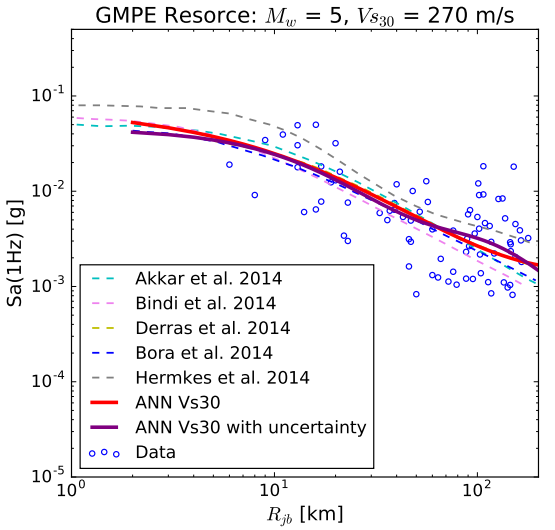

(b) Distance decay of Sa(1Hz), $M_w = 5$, $Vs_{30} = 270\text{m/s}$

Figure 5.7: Distance decay of PGA and Sa(1Hz). The data are selected from the earthquake records with $M_w \in [4.8, 5.2]$ and $Vs_{30} \in [220\text{m/s}, 320\text{m/s}]$

PEs, as shown in Figure 5.6 and Figure 5.7. Besides, considering the data cloud plotted in Figure 5.6 and Figure 5.7, the ANN models provide satisfactory regression results.

3. It can be clearly observed that the dispersion of the residuals is less important for the ANN model with input uncertainty than the classical ANN model. This is due to the reduction of the values of τ and ϕ resulting from the modeling of the input epistemic uncertainties.

The reduction effect is more evident for Sa(1Hz) than PGA.

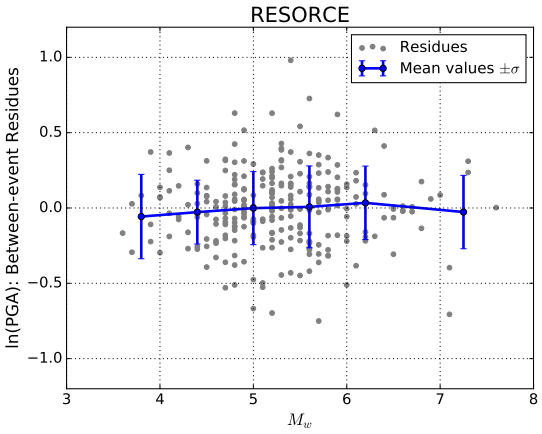

(a) Inter-event residuals for PGA computed from the ANN model with input uncertainties

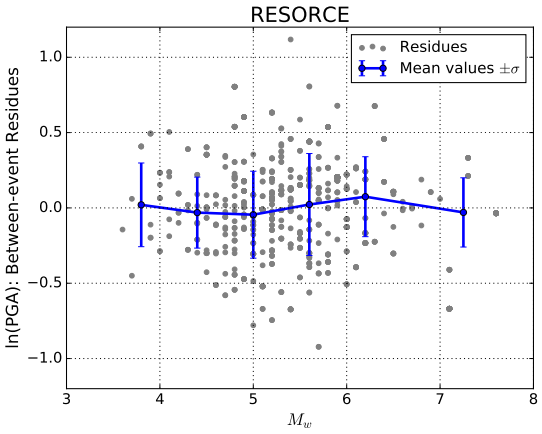

(b) Inter-event residuals for PGA computed from the ANN model without input uncertainties

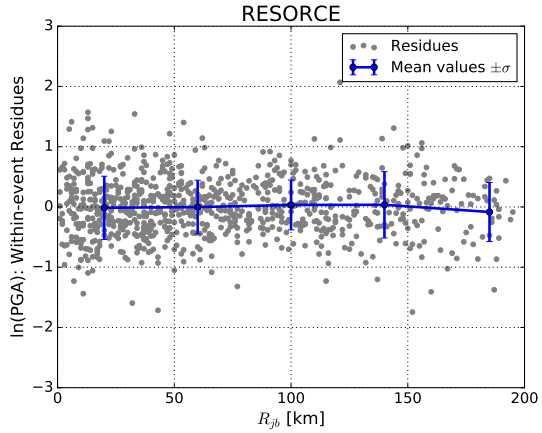

(c) Intra-event residuals for PGA computed from the ANN model with input uncertainties

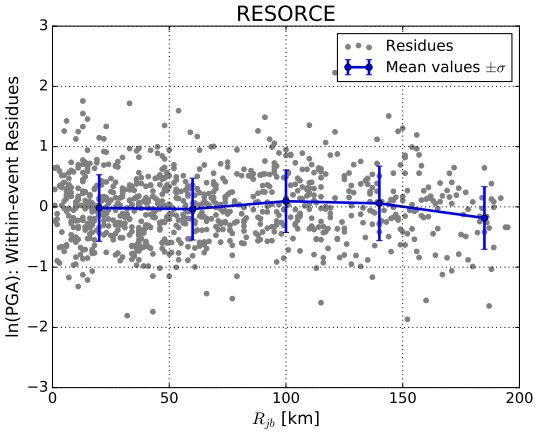

(d) Intra-event residuals for PGA computed from the ANN model without input uncertainties

Figure 5.8: Inter-event and intra-event residuals of PGA of the ANN input uncertain model, in comparison to the ANN model without input uncertainties

Finally, we validate the ANN model with input uncertainty using the 173 validation data. We recall that the validation dataset is not used to train the ANN model in the training process. Computed on the validation dataset, the value of the log-likelihood function of the ANN model with input uncertainty is -3646.48, larger than -3673.78 obtained without considering input uncertainty. The number of the validation data and the ANN architecture are the same for both models. In consequence, a larger value of the log-likelihood results in smaller values of AIC (Akaike information criterion [Akaike 1974]) and BIC (Bayesian information criterion [Schwarz 1978]). Better models are characterized by smaller AIC and BIC values, which shows the advantage of the uncertain input ANN model over the original ANN model (Table 5.4). In Figure 5.10, the predictions of the uncertain input ANN model

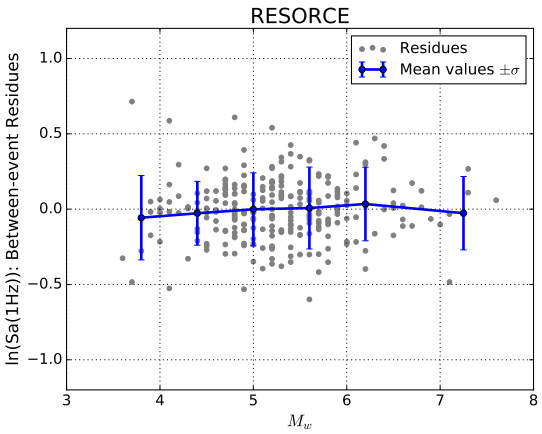

(a) Inter-event residuals for Sa(1Hz) computed from the ANN model with input uncertainties

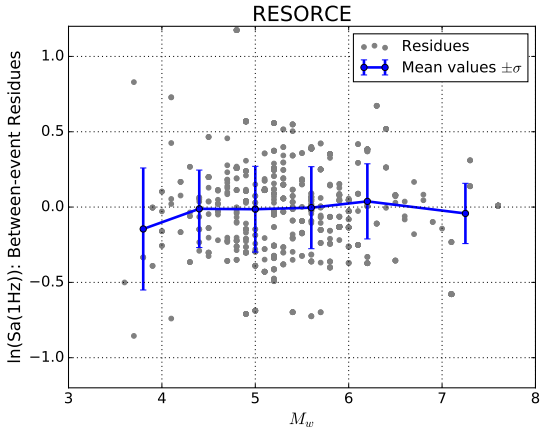

(b) Inter-event residuals for Sa(1Hz) computed from the ANN model without input uncertainties

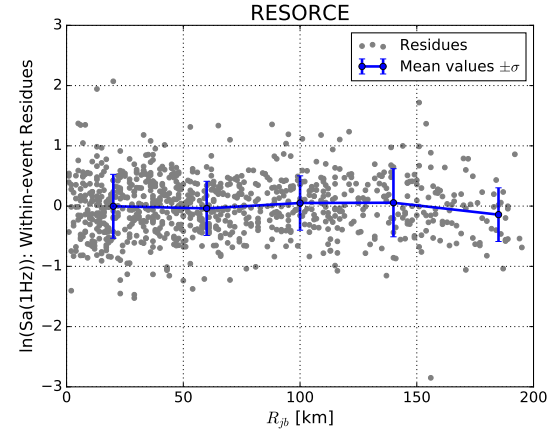

(c) Intra-event residuals for Sa(1Hz) computed from the ANN model with input uncertainties

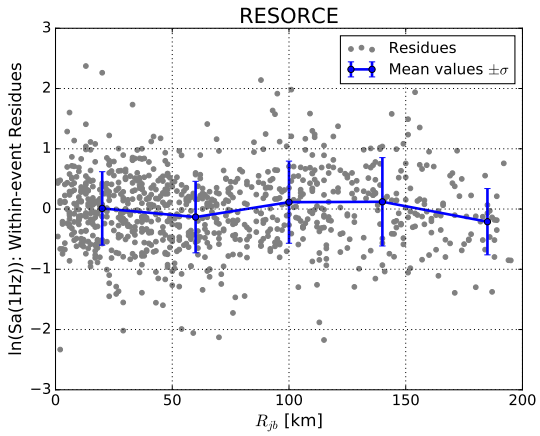

(d) Intra-event residuals for Sa(1Hz) computed from the ANN model without input uncertainties

Figure 5.9: Inter-event and intra-event residuals of Sa(1Hz) of the ANN input uncertain model, in comparison to the ANN model without input uncertainties

are compared to the original IM values of the database, for both PGA and Sa(1Hz). It can be concluded that the data clouds are located in the neighborhood of the diagonal '1-1' line, implying that the predictions of the uncertain input ANN model are satisfactory, for both PGA and Sa(1Hz).

Table 5.4: Performance of ANN models with the validation dataset

Models	Log-likelihood	AIC	BIC
ANN without input uncertainties	-3673.78	7675.56	8192.70
ANN with input uncertainties	-3646.48	7620.96	8138.10

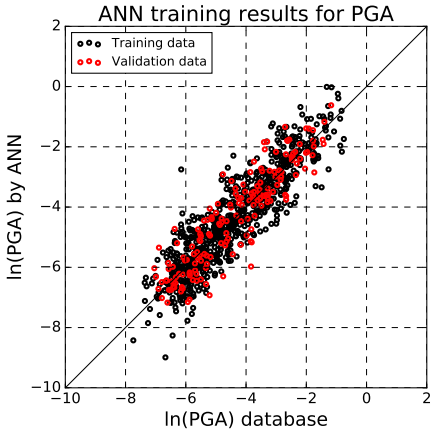

(a) Training and validation results of the uncertain input ANN model for PGA

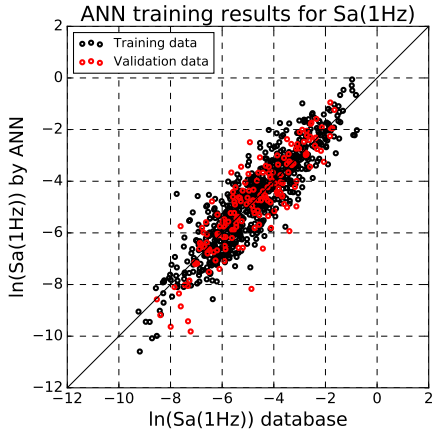

(b) Training and validation results of the uncertain input ANN model for Sa(1Hz)

Figure 5.10: Comparison between predictions of the uncertain input ANN model and the values of IMs of the database, for both training dataset and validation dataset

5.5.2 Discussions

Previous results show that the ANN model considering input uncertainties on M_w and Vs_{30} provides satisfactory regression performance with the RESORCE data. Moreover, a reduction of the GMPE uncertainty can be obtained by modeling the input uncertainties. However, there are some aspects which need to be discussed concerning this approach.

1. In our approach, we do not further separate the intra-event uncertainty into the single-site uncertainty and the site-to-site uncertainty [Baltay et al. 2017], for being able to compare the computed uncertainty values with those of existing RESORCE GMPE models. Besides, the classical ANN training in the mixed-effects problem proposed by Derras et al. [2014] does not allow a further decomposition of the intra-event uncertainty. This latter decomposition, however, can be achieved by the GLS ANN training.
2. The present approach relies on a prior estimation of the input uncertainties. Different estimations of the uncertainties associated to M_w and Vs_{30} can impact the final values of τ and ϕ. To analyze this, different values of σ_M are $\sigma_{\ln Vs}$ are selected to conduct the computation of uncertain input ANN GMPE models. First, we fix the value of $\sigma_{\ln Vs}$ to 0.3. The value of σ_M is varied to 0.15 and 0.2. The corresponding reduction ratios with the variation of σ_M are plotted in Figure 5.11. It can be observed that the inter-event uncertainty τ decreases with increasing values of σ_M and that the variation of σ_M hardly influences the intra-event uncertainty ϕ, which is consistent with the work of Rhoades [1997]. However, when σ_M is set to 0.2, the reduction ratios of the inter-event uncertainty can reach 50% to 70% in low frequency ranges. Different values of σ_M can give rise to very different estimations of the inter-event uncertainty. A second analysis is performed by fixing the value of σ_M to 0.1. Two additional values of $\sigma_{\ln Vs}$ (0.1 and 0.2) are selected

for uncertain input ANN regression. It can be seen from Figure 5.12 that the intra-event uncertainty is mainly influenced by $\sigma_{\ln Vs}$.

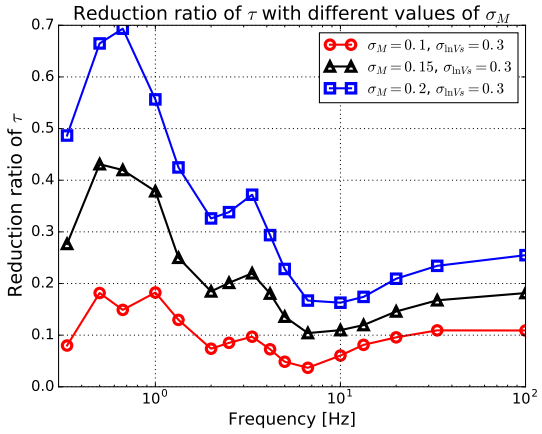

(a) Influence of σ_M on the inter-event uncertainty τ

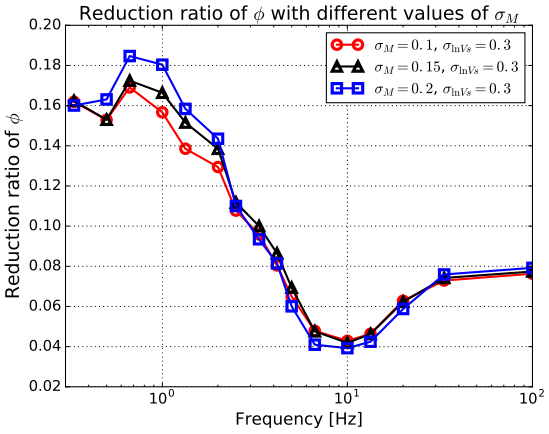

(b) Influence of σ_M on the intra-event uncertainty ϕ

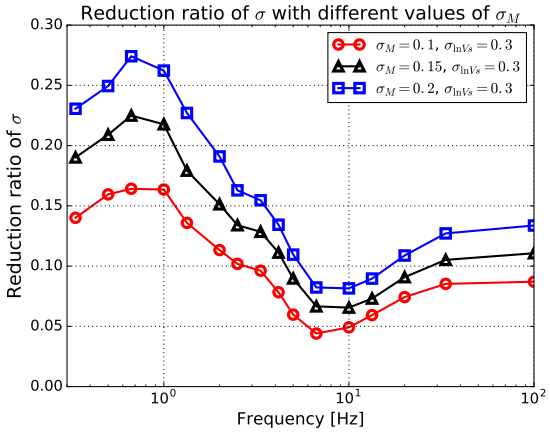

(c) Influence of σ_M on the total uncertainty σ

Figure 5.11: Influence of different values of σ_M on the reduction ratios of τ, ϕ and σ

3. It can be observed in Figure 5.4, Figure 5.11 and Figure 5.12 that, qualitatively, the reduction of the uncertainty is more important in the low frequency range than in the high frequency range. One reason is that the absolute values of the derivatives $\frac{\partial \mu}{\partial M_w}$ and $\frac{\partial \mu}{\partial \ln Vs_{30}}$ are larger for low frequency spectral accelerations than high frequency ones [Abrahamson and Silva 2007]. Considering the FOSM formulation of Eq.5.2.13, a large value of the derivative results in a large adjustment of the residuals. We show the derivatives $\frac{\partial \mu}{\partial M_w}$ and $\frac{\partial \mu}{\partial \ln Vs_{30}}$ for Sa(0.5Hz), Sa(3.3Hz) and Sa(20Hz) in Figure 5.13. The negative values of $\frac{\partial \mu}{\partial \ln Vs_{30}}$ are justified by the fact that the site effect is more evident if the soil is softer, so that the seismic intensity measures increase. The derivatives in Figure 5.13 show higher absolute values for the low frequency spectral acceleration than for the high frequency one.

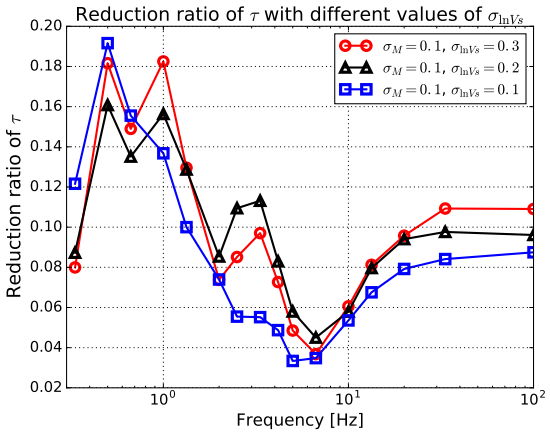

(a) Influence of $\sigma_{\ln Vs}$ on the inter-event uncertainty τ

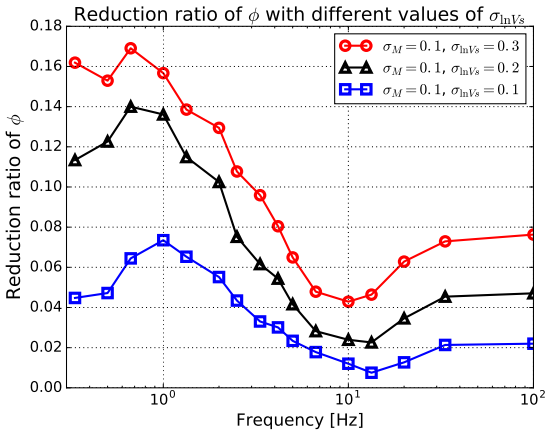

(b) Influence of $\sigma_{\ln Vs}$ on the intra-event uncertainty ϕ

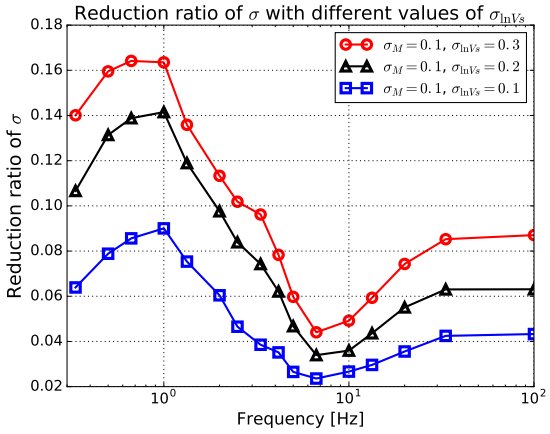

(c) Influence of $\sigma_{\ln Vs}$ on the total uncertainty σ

Figure 5.12: Influence of different values of $\sigma_{\ln Vs}$ on the reduction ratios of τ, ϕ and σ

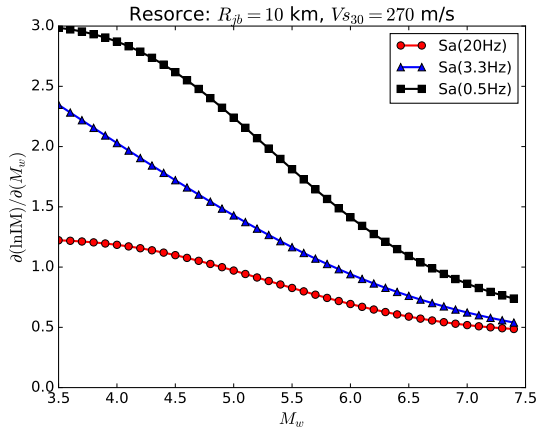

(a) Derivatives of ANN median predictions with respect to M_w

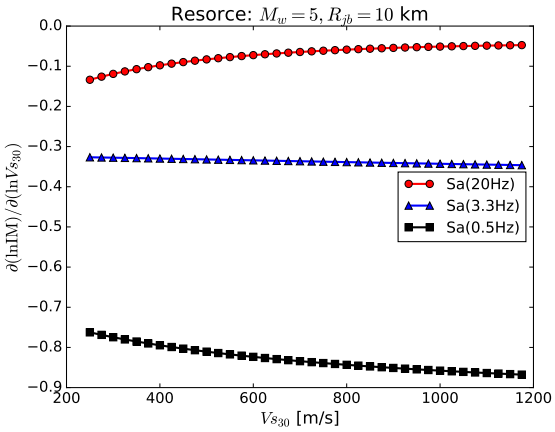

(b) Derivatives of ANN median predictions with respect to $\ln Vs_{30}$

Figure 5.13: Derivatives of ANN median predictions with respect to M_w and $\ln Vs_{30}$

4. In spite of the similarity of the median predictions of the two ANN models, the fact that the reduced value of σ, introduced by modeling the input uncertainty, can lead to different results for the computation of the hazard curves, according to Bommer and Abrahamson [2006]. This can eventually impact the results of seismic risk assessment and it shows the necessity of considering input uncertainties, if they exist, for the development of GMPEs.
5. In contrast to the Bayesian regression used in Moss [2011] and Kuehn and Abrahamson [2017], the approach proposed in this chapter does not allow an appropriate posterior estimation of the true values of M_w and Vs_{30}. This can be regarded as a limitation of the FOSM method compared to Bayesian regression. However, the application of Bayesian regression to ANNs within the context of the mixed-effects model is not trivial.

5.6 Summary

In this chapter, an approach to consider input parameter uncertainties is presented on the basis of non-parametric ANN regression for the computation of ground motion prediction equations. Based on the first order second moment method, the variance-covariance matrix contains off-diagonal terms which are introduced by the input parameter epistemic uncertainties. An ANN training algorithm is proposed based on the generalized least squares principle, to account for non-blockwise diagonal variance-covariance matrix in the ANN regression. The proposed approach is applied to a generated synthetic database, in order to analyze the impact of the input parameter uncertainty and to validate the proposed algorithm. It is, then, applied to the shallow crustal earthquakes data in the RESORCE database. These two applications show an overestimation of the GMPE inter-event and intra-event uncertainties, if the epistemic input parameter uncertainties are not taken into account. The proposed approach relies on a prior estimation of the epistemic uncertainties of the input parameters and the sensitivity analyses show the importance to assess correctly the input uncertainty for the estimation of the GMPE inter-event and intra-event uncertainties. Based on the input uncertainties $\sigma_M = 0.1$, $\sigma_{\ln Vs} = 0.3$, the reduction of the total RESORCE GMPE uncertainty is 4-16%, depending on the frequency of the spectral accelerations, whereas the median predictions are only slightly influenced. The uncertainty reduction is more significant in low frequency ranges than in high frequency ranges.

Appendix

5.A Expectation-Maximization Algorithm Applied to Mixed-effects Problems

The maximization of Eq.5.2.5 is not trivial with the presence of $\underline{\eta}$. One of the methods to solve this problem is using an iterative expectation-maximization (EM) algorithm. In this section we try to provide a theoretical derivation of the EM algorithm used by Abrahamson and Youngs [1992]. The difficulty of the maximization of Eq.5.2.5 is the determination of inter-event residual $\underline{\eta}$. Knowing this residual, the determination of the model parameter $\underline{\theta}$ can be easily achieved by classical regression methods. The essential idea of the EM algorithm is to provide an estimation of $\underline{\eta}$ given the earthquake observations $\underline{y}$, and then conduct regressions with estimated values of $\underline{\eta}$. The iterative EM algorithm is divided into two main steps, following Dempster et al. [1977]:

1. E-step (Expectation): Assuming knowing $\underline{\eta}$, compute the expected value of the log-likelihood function $\mathbf{E}_{\underline{\eta}|\underline{y}}[L]$ with the current model parameter $\underline{\theta}_k$, with respect to the conditional distribution of $f(\underline{\eta}|\underline{y})$.
   Supposing that $\underline{\eta}$ is known, the log-likelihood function Eq.5.2.5 becomes

$$\ln L = -\frac{N}{2}\ln 2\pi - \frac{1}{2}\ln|\phi^2 \underline{\underline{I}}_N| - \frac{1}{2}(\underline{y} - \underline{\mu} - \underline{\underline{Z}}\,\underline{\eta})^T[\phi^2 \underline{\underline{I}}_N]^{-1}(\underline{y} - \underline{\mu} - \underline{\underline{Z}}\,\underline{\eta}). \tag{5.A.1}$$

   Let us compute first the conditional distribution $f(\underline{\eta}|\underline{y})$. With the assumption of normal distribution of $\underline{\eta}$ and $\underline{\varepsilon}$, the joint distribution $f(\underline{y}, \underline{\eta})$ is a multi-variate normal distribution:

$$\begin{bmatrix} \underline{y} \\ \underline{\eta} \end{bmatrix} \sim f(\underline{y}, \underline{\eta}) = \mathcal{N}\left(\begin{bmatrix} \underline{\mu} \\ \underline{0} \end{bmatrix}, \begin{bmatrix} \underline{\underline{C}} & \tau^2 \underline{\underline{Z}} \\ \tau^2 \underline{\underline{Z}}^T & \tau^2 \underline{\underline{I}}_M \end{bmatrix} \right). \tag{5.A.2}$$

   Considering the property of the multi-variate normal distribution, the conditional distribution $f(\underline{\eta}|\underline{y})$ can be obtained:

$$f(\underline{\eta}|\underline{y}) = \mathcal{N}\left(\tau^2 \underline{\underline{Z}}^T \underline{\underline{C}}^{-1}(\underline{y} - \underline{\mu}), \tau^2 \underline{\underline{I}}_M - \tau^4 \underline{\underline{Z}}^T \underline{\underline{C}}^{-1} \underline{\underline{Z}}\right). \tag{5.A.3}$$

   Therefore, the expectation of $\underline{\eta}$ given earthquake observation data $\underline{y}$ is

$$\mathbf{E}_{\underline{\eta}|\underline{y}}[\underline{\eta}] = \tau^2 \underline{\underline{Z}}^T \underline{\underline{C}}^{-1}(\underline{y} - \underline{\mu}). \tag{5.A.4}$$

   By applying the relation $\tau^2 \underline{\underline{Z}}^T(\tau^2 \underline{\underline{Z}}\,\underline{\underline{Z}}^T + \phi^2 \underline{\underline{I}}_N)^{-1}(\underline{y} - \underline{\mu}) = (\underline{\underline{Z}}^T \underline{\underline{Z}} + \underline{\underline{I}}_M \phi^2/\tau^2)^{-1} \underline{\underline{Z}}^T(\underline{y} - \underline{\mu})$ [Dempster et al. 1981] and performing block matrix multiplications, Eq.5.A.4 can be further

simplified:

$$\mathbf{E}_{\underline{\eta}|\underline{y}}[\eta_i] = \frac{\tau^2 \sum_{j=1}^{n_i} y_{ij} - \mu_{ij}}{n_i \tau^2 + \phi^2}. \tag{5.A.5}$$

Now the expression of $\mathbf{E}_{\underline{\eta}|\underline{y}}[L]$ can be also derived:

$$\mathbf{E}_{\underline{\eta}|\underline{y}}[L] = \int \left[-\frac{N}{2} \ln 2\pi - \frac{1}{2} \ln |\phi^2 \underline{\underline{I}}_N| - \frac{1}{2} (\underline{y} - \underline{\mu} - \underline{\underline{Z}}\ \underline{\eta})^T [\phi^2 \underline{\underline{I}}_N]^{-1} (\underline{y} - \underline{\mu} - \underline{\underline{Z}}\ \underline{\eta}) \right] f(\underline{\eta}|\underline{y}) \mathrm{d}\underline{\eta}. \tag{5.A.6}$$

We do not perform further calculations of Eq.5.A.6 at the moment. We will see later in the M-step that the calculations can be simplified.

2. M-step (maximization): Obtain the model parameters $\underline{\theta}^{k+1}$ by maximizing $\mathbf{E}_{\underline{\eta}|\underline{y}}(L)$:

$$\underline{\theta}^{k+1} = \arg\max_{\underline{\theta}} \mathbf{E}_{\underline{\eta}|\underline{y}}[L]. \tag{5.A.7}$$

The determination of $\underline{\theta}^{k+1}$ is realized by applying $\partial \mathbf{E}_{\underline{\eta}|\underline{y}}[L]/\partial \underline{\theta} = 0$. Noting that, in Eq.5.A.6, only the model prediction $\underline{\mu}$ is influenced by $\underline{\theta}$, the computation of the derivative becomes

$$\begin{aligned}
\frac{\partial \mathbf{E}_{\underline{\eta}|\underline{y}}[L]}{\partial \underline{\theta}} &= \frac{\int -\frac{1}{2} (\underline{y} - \underline{\mu} - \underline{\underline{Z}}\ \underline{\eta})^T [\phi^2 \underline{\underline{I}}_N]^{-1} (\underline{y} - \underline{\mu} - \underline{\underline{Z}}\ \underline{\eta}) f(\underline{\eta}|\underline{y}) \mathrm{d}\underline{\eta}}{\partial \underline{\theta}} \\
&= \int \left[\frac{\partial \underline{\mu}}{\partial \underline{\theta}} \right]^T [\phi^2 \underline{\underline{I}}_N]^{-1} (\underline{y} - \underline{\mu} - \underline{\underline{Z}}\ \underline{\eta}) f(\underline{\eta}|\underline{y}) \mathrm{d}\underline{\eta} \\
&= \int \left[\frac{\partial \underline{\mu}}{\partial \underline{\theta}} \right]^T [\phi^2 \underline{\underline{I}}_N]^{-1} (\underline{y} - \underline{\mu}) f(\underline{\eta}|\underline{y}) \mathrm{d}\underline{\eta} - \int \left[\frac{\partial \underline{\mu}}{\partial \underline{\theta}} \right]^T [\phi^2 \underline{\underline{I}}_N]^{-1} \underline{\underline{Z}}\ \underline{\eta} f(\underline{\eta}|\underline{y}) \mathrm{d}\underline{\eta} \\
&= \left[\frac{\partial \underline{\mu}}{\partial \underline{\theta}} \right]^T [\phi^2 \underline{\underline{I}}_N]^{-1} (\underline{y} - \underline{\mu}) \int f(\underline{\eta}|\underline{y}) \mathrm{d}\underline{\eta} - \left[\frac{\partial \underline{\mu}}{\partial \underline{\theta}} \right]^T [\phi^2 \underline{\underline{I}}_N]^{-1} \underline{\underline{Z}} \int \underline{\eta} f(\underline{\eta}|\underline{y}) \mathrm{d}\underline{\eta}.
\end{aligned} \tag{5.A.8}$$

Considering the relation $\int f(\underline{\eta}|\underline{y}) \mathrm{d}\underline{\eta} = 1$ and $\int \underline{\eta} f(\underline{\eta}|\underline{y}) \mathrm{d}\underline{\eta} = \mathbf{E}_{\underline{\eta}|\underline{y}}[\underline{\eta}]$, Eq.5.A.8 becomes:

$$\begin{aligned}
\frac{\partial \mathbf{E}_{\underline{\eta}|\underline{y}}[L]}{\partial \underline{\theta}} &= \left[\frac{\partial \underline{\mu}}{\partial \underline{\theta}} \right]^T [\phi^2 \underline{\underline{I}}_N]^{-1} (\underline{y} - \underline{\mu}) - \left[\frac{\partial \underline{\mu}}{\partial \underline{\theta}} \right]^T [\phi^2 \underline{\underline{I}}_N]^{-1} \underline{\underline{Z}}\ \mathbf{E}_{\underline{\eta}|\underline{y}}[\underline{\eta}] \\
&= \left[\frac{\partial \underline{\mu}}{\partial \underline{\theta}} \right]^T [\phi^2 \underline{\underline{I}}_N]^{-1} \left[\underline{y} - \underline{\mu} - \underline{\underline{Z}}\ \mathbf{E}_{\underline{\eta}|\underline{y}}[\underline{\eta}] \right] = 0.
\end{aligned} \tag{5.A.9}$$

Note that solving $\partial \mathbf{E}_{\underline{\eta}|\underline{y}}[L]/\partial \underline{\theta} = 0$ in Eq.5.A.9 is equivalent to solve the problem:

$$\min_{\underline{\theta}} \frac{1}{2} \left[\underline{y} - \underline{\mu} - \underline{\underline{Z}}\ \mathbf{E}_{\underline{\eta}|\underline{y}}[\underline{\eta}] \right]^T [\phi^2 \underline{\underline{I}}_N]^{-1} \left[\underline{y} - \underline{\mu} - \underline{\underline{Z}}\ \mathbf{E}_{\underline{\eta}|\underline{y}}[\underline{\eta}] \right]. \tag{5.A.10}$$

This implies that the model parameters determined from Eq. 5.A.7 are the ordinary least squares estimates of the regression to find the model $\underline{\mu}$, with $\underline{y} - \underline{\underline{Z}}\ \mathbf{E}_{\underline{\eta}|\underline{y}}[\underline{\eta}]$ as outputs of the regression problem. It has to be mentioned that, in the method described above, there is no restriction imposed on the type of model selected for $\underline{\mu}$: It can be either a very simple linear model, or a very complex non-linear one, such as an artificial neural network, a random forest, etc.

The inter-event and intra-event uncertainties τ and ϕ can be computed once the new model parameters $\underline{\theta}_{k+1}$ are obtained. The easiest way is to use an existing numerical optimization solver to find the values of τ and ϕ, which minimize Eq.5.2.5 with the model $\underline{\mu}$ determined at the iteration $k+1$. Analytical solutions to determine τ and ϕ also exist. For the purpose of simplicity, we do not go into details for the analytical solutions. Interested readers can refer to Gumedze and Dunne [2011]; Hajjem et al. [2012] concerning this aspect.

The E-step and the M-step are iterated until the value of the log-likelihood of Eq.5.2.5 is maximized. In this way, we have derived the EM algorithm of Abrahamson and Youngs [1992] and Derras et al. [2014] used to solve the mixed-effects problem in the computation of the GMPEs:

1. Initialization step: randomly initialize the model parameters $\underline{\theta}_0$. Assuming $\underline{\eta} = \underline{0}$, conduct a regression using $\underline{x}$ and $\underline{y}$ as the inputs and outputs. $\underline{\theta}_1$ is obtained.

2. Start iterations. For the iteration k ($k \geqslant 1$), estimate τ^2 and ϕ^2 in maximizing Eq.5.2.5 with $\underline{\mu}$ computed from the determined $\underline{\theta}_k$.

3. Given $\underline{\mu}$, τ^2 and ϕ^2, compute η_i using Eq. (10) in Abrahamson and Youngs [1992]:

$$\eta_i = \frac{\tau^2 \sum_{j=1}^{n_i} y_{ij} - \mu_{ij}}{n_i \tau^2 + \phi^2} \tag{5.A.11}$$

4. Conduct a regression to determine $\underline{\theta}_{k+1}$, using $\underline{x}$ and $\underline{y} - \underline{\eta}$ as the inputs and outputs, respectively.

5. Set $k = k + 1$. Repeat the steps 2-4 until Eq.5.2.5 is maximized.

Bibliography

Abrahamson, N. A. and Silva, W. J. (2007). NGA ground motion relations for the geometric mean horizontal component of peak and spectral ground motion parameters. Technical report, Pacific Earthquake Engineering Research Center.

Abrahamson, N. A. and Youngs, R. R. (1992). A stable algorithm for regression analyses using the random effects model. *Bull. Seismol. Soc. Am.*, 82:505–510.

Akaike, H. (1974). A new look at the statistical model identification. *IEEE Trans. Autom. Control.*, 19:716–723.

Akkar, S., Sandıkkaya, M. A., and Bommer, J. J. (2014a). Empirical ground-motion models for point- and extended-source crustal earthquake scenarios in Europe and the Middle East. *Bull. Earthquake Eng.*, 12:359–387.

Akkar, S., Sandıkkaya, M. A., Senyurt, M., Sisi, A. A., Ay, B. O., Traversa, P., Douglas, J., Cotton, F., Luzi, L., Hernandez, B., and Godey, S. (2014b). Reference database for seismic ground-motion in Europe (RESORCE). *Bull. Earthquake Eng.*, 12:311–339.

Ameur, M., Derras, B., and Zendagui, D. (2018). Ground motion prediction model using adaptive neuro-fuzzy inference systems: An example based on the NGA-West 2 data. *Pure. Appl. Geophys.*, 175:1019–1034.

Baltay, A. S., Hanks, T. C., and Abrahamson, N. A. (2017). Uncertainty, variability, and earthquake physics in ground-motion prediction equations. *Bull. Seismol. Soc. Am.*, 107:1754–1772.

Bindi, D., Massa, M., Luzi, L., Ameri, G., Pacor, F., Puglia, R., and Augliera, P. (2014). Pan-European ground-motion prediction equations for the average horizontal component of PGA, PGV, and 5 %-damped PSA at spectral periods up to 3.0 s using the RESORCE dataset. *Bull. Earthquake Eng.*, 12:391–430.

Bishop, C. M. (1995). *Neural Networks for Pattern Recognition*. Oxford University Press.

Bommer, J. J. and Abrahamson, N. A. (2006). Why do modern probabilistic seismic-hazard analyses often lead to increased hazard estimates? *Bull. Seismol. Soc. Am.*, 96:1967–1977.

Bora, S. S., Scherbaum, F., Kuehn, N., and Stafford, P. (2014). Fourier spectral- and duration models for the generation of response spectra adjustable to different source-, propagation-, and site conditions. *Bull. Earthquake Eng.*, 12:467–493.

Dempster, A., Rubin, D., and Tsutakawa, R. (1981). Estimation in covariance components models. *J. Am. Stat. Assoc.*, 76:341–353.

Dempster, A. P., Laird, N. M., and Rubin, D. B. (1977). Maximum likelihood from incomplete data via the EM algorithm. *J. Am. Stat. Assoc.*, 39:1–38.

Derras, B., Bard, P. Y., and Cotton, F. (2014). Towards fully data driven ground-motion prediction models for Europe. *Bull. Earthquake Eng.*, 12:495–516.

Derras, B., Bard, P. Y., and Cotton, F. (2016). Site-condition proxies, ground motion variability, and data-driven gmpes: Insights from the NGA-West2 and RESORCE data sets. *Earthq. Spectra*, 32:2027–2056.

Derras, B., Bard, P. Y., and Cotton, F. (2017). V_{s30} , slope, H_{800} and f_0: performance of various site-condition proxies in reducing ground-motion aleatory variability and predicting nonlinear site response. *Earth Planets Space*, 69:2027–2056.

Dhanya, J. and Raghukanth, S. (2017). Ground motion prediction model using artificial neural network. *Pure. Appl. Geophys.*

Douglas, J., Akkar, S., Ameri, G., Bard, P.-Y., Bindi, D., Bommer, J. J., Bora, S. S., Cotton, F., Derras, B., Hermkes, M., Kuehn, N. M., Luzi, L., Massa, M., Pacor, F., Riggelsen, C., Sandıkkaya, M. A., Scherbaum, F., Stafford, P. J., and Traversa, P. (2014). Comparisons among the five ground-motion models developed using RESORCE for the prediction of response spectral accelerations due to earthquakes in Europe and the Middle east. *Bull. Earthquake Eng.*, 12:341–358.

Foulser-Piggott, R. (2014). Quantifying the epistemic uncertainty in ground motion models and prediction. *Soil. Dyn. Earthq. Eng.*, 65:256–268.

Gehl, P., Bonilla, L. F., and Douglas, J. (2011). Accounting for site characterization uncertainties when developing ground-motion prediction equations. *Bull. Seismol. Soc. Am.*, 101:1101–1108.

Gumedze, F. and Dunne, T. (2011). Parameter estimation and inference in the linear mixed model. *Linear Algebra Appl.*, 435:1920–1944.

Hajjem, A., Bellavance, F., and Larocque, D. (2012). Mixed-effects random forest for clustered data. *J. Stat. Comput. Simul.*, 84:1313–1328.

Hermkes, M., Kuehn, N. M., and Riggelsen, C. (2014). Simultaneous quantification of epistemic and aleatory uncertainty in GMPEs using gaussian process regression. *Bull. Earthquake Eng.*, 12:449–466.

Joyner, W. B. and Boore, D. M. (1993). Methods for regression analysis of strong-motion data. *Bull. Seismol. Soc. Am.*, 83:469–487.

Koufoudi, E., Ktenidou, O.-J., Cotton, F., Dufour, F., and Grange, S. (2015). Empirical ground-motion models adapted to the intensity measure ASA_{40}. *Bull. Earthquake Eng.*, 13:3625–3643.

Kuehn, N. M. and Abrahamson, N. A. (2017). The effect of uncertainty in predictor variables on the estimation of ground-motion prediction equations. *Bull. Seismol. Soc. Am.*, 108:358–370.

Moss, R. E. S. (2011). Reduced sigma of ground-motion prediction equations through uncertainty propagation. *Bull. Seismol. Soc. Am.*, 101:250–257.

Rhoades, D. A. (1997). Estimation of attenuation relations for strong-motion data allowing for individual earthquake magnitude uncertainties. *Bull. Seismol. Soc. Am.*, 87:1674–1678.

Rumelhart, D., Hinton, G., and Williams, R. (1986). *Learning internal representations by error propagation in Parallel Distributed Processing: Explorations in the Microstructure of Cognition*. The MIT Press.

Schwarz, G. (1978). Estimating the dimension of a model. *Ann. Stat.*, 6:461–464.

Stafford, P. J. (2014). Crossed and nested mixed-effects approaches for enhanced model development and removal of the ergodic assumption in empirical ground-motion models. *Bull. Seismol. Soc. Am.*, 104:702–719.

Stambouli, A. B., Zendagui, D., Bard, P.-Y., and Derras, B. (2017). Deriving amplification factors from simple site parameters using generalized regression neural networks: implications for relevant site proxies. *Earth Planets Space*, 69:99.

Chapter 6

Towards the Annual Failure Rate in Seismic Risk Assessment

The annual failure rate can be computed if the fragility curve and the hazard curve are provided. In this chapter, the methodology and the results from the previous chapters are reused, for the calculation of the final annual failure rate. The structure of interest is a nonlinear 3-story reinforced concrete model used in the project SMART 2013. The hazard curves are computed from the ground motion prediction equations obtained in Chapter 5. Both ground motion models, with and without the consideration of the epistemic uncertainties of input parameters, are accounted for. The adaptive artificial neural network is applied to conduct fragility analysis. The final annual failure rate is computed with respect to three different damage levels of the inter-story drift and an assumed water storage tank, which is located on the top floor of the SMART model.

Contents

6.1 Introduction

In seismic risk assessment, the annual failure rate of structures and critical components is computed by the convolution of the derivative of hazard curve and the fragility curve, based on the total probability theory:

$$\lambda = \int_0^{+\infty} |\frac{\mathrm{d}H(\alpha)}{\mathrm{d}\alpha}| P_f(\alpha) \mathrm{d}\alpha, \tag{6.1.1}$$

where λ denotes the annual rate of a consequence of interest, α represents the seismic intensity measure (IM), $H(\alpha)$ is the hazard curve and $P_f(\alpha)$ is the fragility curve. The computation of $H(\alpha)$ is based on the medians given by the ground motions prediction equations (GMPEs) and the associated standard deviations (Stds), together with the distributions of the magnitude and source-to-site distance of the earthquakes which the structure of interest can encounter.

This chapter is dedicated to provide a final application of the methodology and the model explained in the previous chapters and to move forward to the computation of the annual failure rate. The objective of this chapter is to (i) corroborate the methodology of fragility analysis by applying to a structure with a nonlinear material constitutive law. Uncertainties in material properties are also modeled; (ii) investigate the impact on the hazard curves from the reduction of the Stds of the GMPEs, due to the modeling of the epistemic uncertainties in the magnitude M_w and the site condition Vs_{30}.

This chapter is organized as follows. Firstly, we start with the presentation of the structure model studied in this chapter. The fragility analysis is, then, conducted with an adaptive ANN presented in Chapter 4. We continue to compute the hazard curves with the two GMPEs obtained in Chapter 5, with and without the consideration of the epistemic uncertainties in M_w and Vs_{30}. Finally, the final annual failure rates are computed, and we compare the annual failure rates computed with different GMPEs.

6.2 Nonlinear SMART 2013 Structure Model

In 2011, a research program aiming at better quantifying the effects of torsion and non-linearity on the dynamic response of reinforced concrete (RC) building was launched by the French Atomic Energy and Sustainable Energies Commission (CEA) and Electricité de France (EDF) [Richard et al. 2016]. In this project, a 1:4 scaled 3-story RC building was built to represent a simplified nuclear electrical building. The in-plan dimension of the 1:4 scaled model is 3.1m×2.25m, and the height of the model is 3.65m. The thickness of the shear wall on the lateral part of the building is 0.1m. The first two natural frequencies of the SMART 2013 structure are around 5.7Hz and 6.4Hz, representing the deformation of the first two eigenmodes in X and Y direction, respectively [Zentner et al. 2017]. The constructed 1:4

scaled RC building (which is called SMART model in the sequel for simplicity), as well as the finite element model, are shown in Figure 6.1.

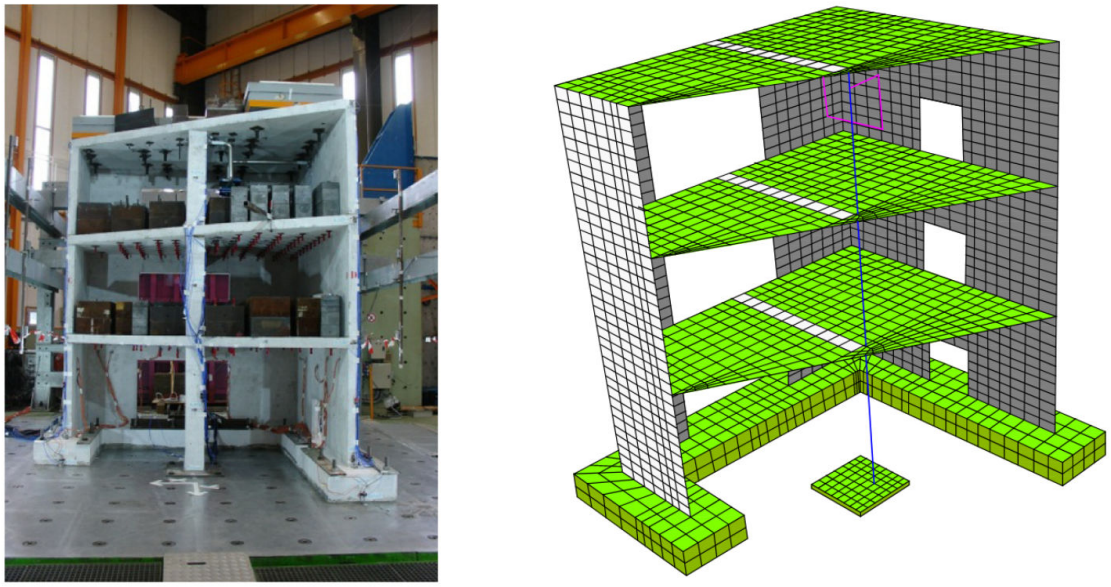

(a) Constructed SMART 2013 model (b) Corresponding SMART 2013 FEM model

Figure 6.1: SMART 2013 1:4 scaled RC building model [Richard et al. 2016]

The finite element (FE) model of the SMART model consists of 22,000 degrees of freedom, with 3230 nodes and 4400 elements, including 3D volumetric elements, 2D shell elements and beam elements. Walls and floors are modeled by shell elements, whereas beam elements are used to represent the central column. The impedances of the foundation are taken into account by springs, whose properties are the same as the ones used by Zentner et al. [2017]. The constitutive law of the RC is a homogenized nonlinear model GLRC_DM [Fayolle 2015]. Rayleigh damping is assumed, so that the damping ratio value of 3.5% can be obtained at 5Hz and 21Hz. The FE analysis of the SMART model is performed with Code_Aster, an in-house FE code developed by EDF R&D [Code_Aster 2017]. Depending on the earthquake level, the computation time for one single FE analysis can vary from 2h (almost linear RC behavior) to 6 days (highly nonlinear RC behavior) on an Intel Xeon E5-2600V2 CPU of 2.7GHz.

The uncertainties on the material properties are considered in the FE simulations for the fragility analysis. The uncertainty material parameters are: Young's modulus of the RC (E_{RC}), Poisson ratio of the RC (ν_{RC}), density of the RC (ρ_{RC}), tensile elasticity limit of the RC ($\sigma^{\mathrm{elas}}_{\mathrm{RC,\,t}}$) and elasticity limit of the steel ($\sigma^{\mathrm{elas}}_{\mathrm{steel}}$). The random material parameters are generated according the statistical properties, such as probability density functions (PDF), median values and coefficients of variation (CoV) reported in Table 6.1. These five parameters are all considered statistically mutually independent. The values of the CoVs are taken from Zentner et al. [2016] for E_{RC}, ν_{RC} and ρ_{RC}. 0.1 is assigned to the CoV value of $\sigma^{\mathrm{elas}}_{\mathrm{steel}}$,

considering the value used by Mangalathu et al. [2016]. The CoV of $\sigma^{\text{elas}}_{\text{RC, t}}$ is set to 0.2, since a similar value (0.19) is used for RC beams and columns in Liel et al. [2009].

Table 6.1: Uncertain material parameters and their probability distribution

Parameters	PDF	Median [Unit]	CoV
E_{RC}	Lognormal	26.9 [GPa]	0.2
ν_{RC}	Lognormal	0.18 [-]	0.1
ρ_{RC}	Lognormal	2300 [kg/m^3]	0.05
$\sigma^{\text{elas}}_{\text{RC, t}}$	Lognormal	3.4 [MPa]	0.2
$\sigma^{\text{elas}}_{\text{steel}}$	Lognormal	665 [MPa]	0.1

Two engineering demand parameters (EDPs) are used in this chapter to evaluate the annual failure rates: (i) the inter-story drift (ISD) δ^{ISD} of the SMART model. Three damage states (light damage, controlled damage and extended damage) are investigated according to Richard et al. [2016]. (ii) the floor spectral acceleration of an hypothetical water storage tank (WST) located on the top floor of the SMART model. The first natural frequency of the WST is assumed to be 1Hz. The average floor spectral acceleration in the frequency range [0.9Hz, 1.1Hz] is computed to consider the uncertainty on the first natural frequency:

$$y^{\text{WST}} = \frac{1}{1.1 - 0.9} \max_{i=X,Y} \int_{0.9\text{Hz}}^{1.1\text{Hz}} S^{\text{WST}}_{a,i}(f)\mathrm{d}f, \tag{6.2.1}$$

where $S^{\text{WST}}_{a,i}$ denotes the floor spectral acceleration of the WST in the i-th direction. The values of the failure threshold of the two EDPs are summarized in Table 6.2.

Table 6.2: Values of failure threshold for the computation of the annual failure rate

EDP	Damage	Failure threshold	Comments
δ^{ISD}	Slight damage	0.003m	$h/400$, with $h = 1.2$m
	Controlled damage	0.006m	$h/200$, with $h = 1.2$m
	Extended damage	0.012m	$h/100$, with $h = 1.2$m
y^{WST}	WST damage	$0.1g$	A supposed damage and failure threshold

6.3 Fragility Analysis

6.3.1 Configuration of the ANN

The methodology of the adaptive ANN described in Chapter 4.2.2 is applied to conduct the fragility analysis of the SMART model. 600 synthetic 3D ground motions are generated for twelve different earthquake scenarios. The twelve scenarios are created from the combination of four magnitudes $M_w = 5$, 5.5, 6 and 6.5 and three distances $R = 10$km, 20km and 30km. The ground motions are all generated with the site condition $Vs_{30} = 270$m/s. For

every scenario, fifty 3D ground motions are generated based on the median and 1σ spectra in agreement with the Campbell-Bozorgnia 2008 (C&B 2008) GMPEs [Campbell and Bozorgnia 2008], using the operator GENE_ACCE_SEISME in Code_Aster [Zentner 2017]. The correlation coefficient between the two horizontal components (in X and Y) is set to 0.2, with the same value used in Zentner et al. [2017]. The vertical component is not correlated to the horizontal ones. A vertical-to-horizontal ratio of $\frac{2}{3}$, suggested by Newmark and Hall [1978], is applied in the generation of the 3D ground motions. The initial population is generated with the 600 3D ground motions and 600 samples of the material parameters from the statistical properties reported in Table 6.1.

Three seismic IMs are selected to be the inputs of the ANN, representing the record-to-record randomness from the ground motions: (i) PGA; (ii) ASA(0.9-1.1Hz), to be consistent with the frequency range of the WST; (iii) Arias intensity (I_A). The two EDPs, ISD and the averaged spectral acceleration between 0.9Hz and 1.1Hz of the WST, are the outputs of the ANN. The number of the hidden layer neuron is set to five. The logarithmic values of IMs and EDPs are used for the ANN training. Therefore, the final ANN architecture is determined, with eight inputs (three IMs and five material parameters), five hidden layer nodes and two outputs. Figure 6.2 shows a summary of the architecture of the ANN, which will be training with the adaptive algorithm proposed in Chapter 4.

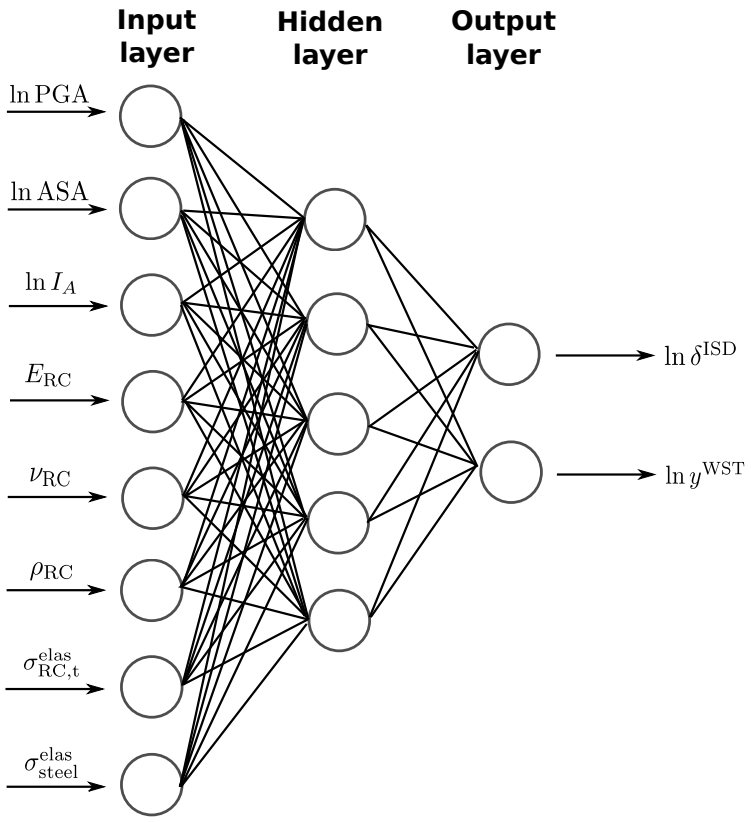

Figure 6.2: The architecture of the ANN used for the SMART model

6.3.2 Fragility Curves

Adaptive training is conducted on the ANN with the configuration of Figure 6.2. The size N_0 of the initial population of the adaptive training is 60, larger than the number of the weights and bias (57) to be determined. At every iteration, $M = 4$ samples, with the largest prediction uncertainties computed by the delta method, are added into the design of the experiments (DoEs). Finally, the adaptive training is stopped after 15 iterations with 119 calls to the FE analysis [1]. An trained ANN is therefore obtained. An additional 50 FE simulations are performed, with the ground motions and material parameters which are not used to train the ANN. The predictions (in logarithmic values) of ANN on the training and validation dataset are compared to the FE simulation results in Figure 6.3. It can be observed that the quality of the training and the validation is satisfactory, since the point clouds are located in the proximity of the '1-1' diagonal line, for both δ^{ISD} and y^{WST}.

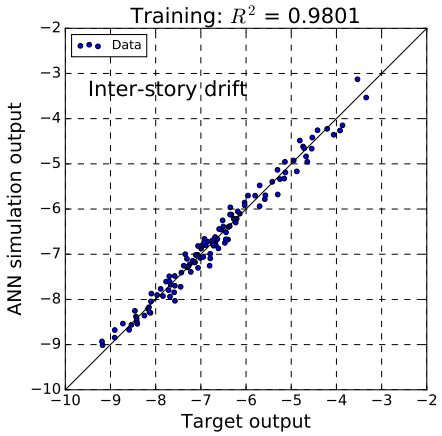

(a) ANN training results for δ^{ISD}

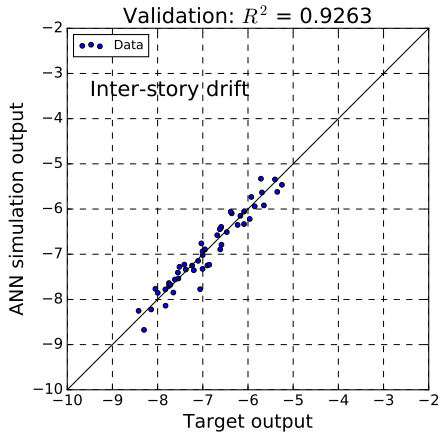

(b) ANN validation results for δ^{ISD}

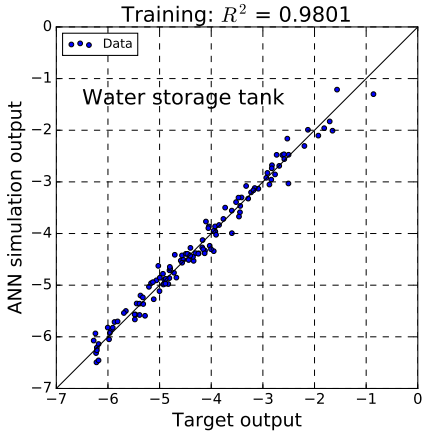

(c) ANN training results for y^{WST}

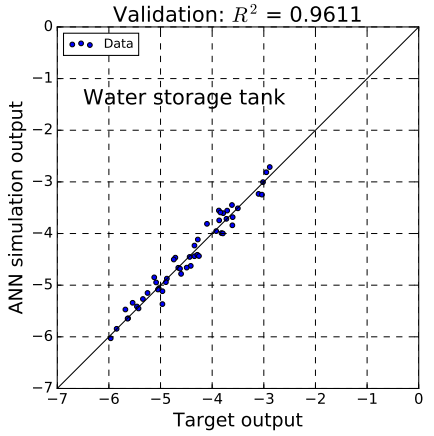

(d) ANN validation results for y^{WST}

Figure 6.3: Comparisons between ANN training/validation results and FEM results

[1] Only three data are with δ values larger than δ^{crit} before starting the last iteration, so that in the last iteration only these three samples are selected.

δ^{ISD} and y^{WST} of the training dataset are also plotted against the PGA of the ground motions in Figure 6.4 in log-log scale. It can be seen that, with the current SMART case study, due to the increased nonlinearity with the earthquake level, a linear fit of the data in log-log scale is not sufficient to describe the data trend: the EDPs increase faster than the global linear increasing rate, in particular when the PGA values are larger than $0.15g$. The values of A_m and β_R may be biased if the linear regression is performed on the whole range of PGA: the capacity A_m can be overestimated whereas β_R can be underestimated due to the larger variability of the EDPs in high PGA ranges. To solve this problem, in this chapter, the linear regression for the determination of A_m and β_R is performed for the earthquakes with PGA values larger than $0.15g$.

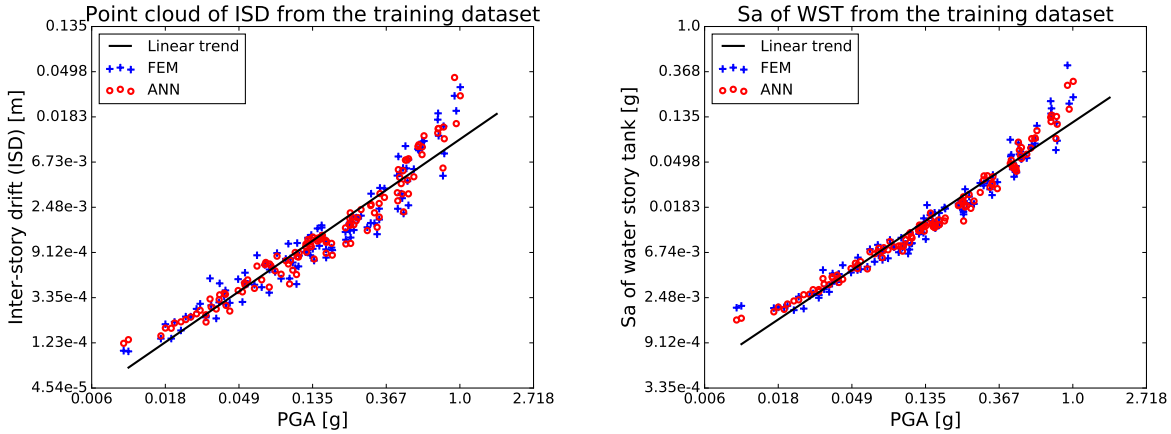

(a) Point cloud of δ^{ISD} as function of PGA (b) Point cloud of y^{WST} as function of PGA

Figure 6.4: Point cloud of δ^{ISD} and y^{WST} as function of PGA

It should be noted that, the samples selected by the adopted adaptive training depend on the generated initial population of the ground motions. With the selected scenarios, a few ground motions with low IM values are also contained in the initial population, so that some of them are retained by the adaptive ANNs. A better initial selection of the earthquake scenarios is necessary for a further improvement of the final design of experiment.

The ANN simulations are conducted for all the 600 samples in the initial population. Then, linear regression is executed on the ANN simulations results in log-log scale for the earthquakes with PGA larger than $0.15g$, as shown in Figure 6.5. The determination of the A_m and β_R for different damage levels is achieved with Eq.3.3.4. The obtained values of the fragility parameters are reported in Table 6.3. The fragility curves for the considered damage levels are plotted in Figure 6.6.

Table 6.3: Values of the parameters of the fragility curves of the SMART model

EDP	δ^{ISD}			y^{WST}
Damage	Slight damage	Controlled damage	Extended damage	Failure of WST
A_m	$0.325g$	$0.523g$	$0.842g$	$0.728g$
β_R	0.200	0.200	0.200	0.171

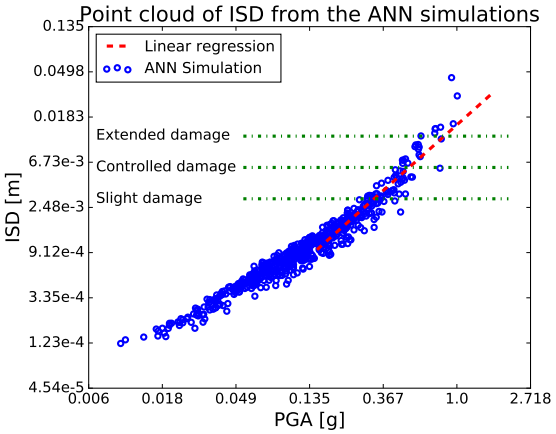

(a) ANN simulation results: point cloud of δ^{ISD} as function of PGA

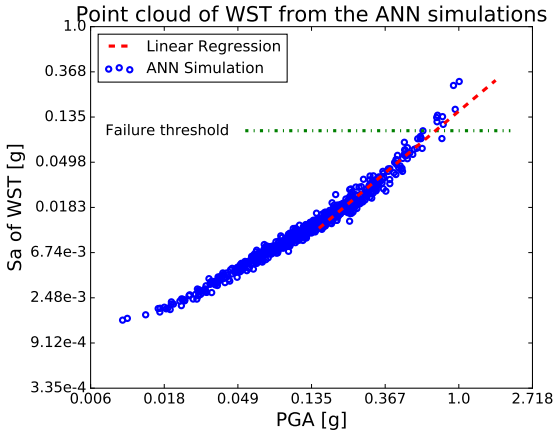

(b) ANN simulation results: point cloud of y^{WST} as function of PGA

Figure 6.5: ANN simulation results: point cloud of δ^{ISD} and y^{WST}

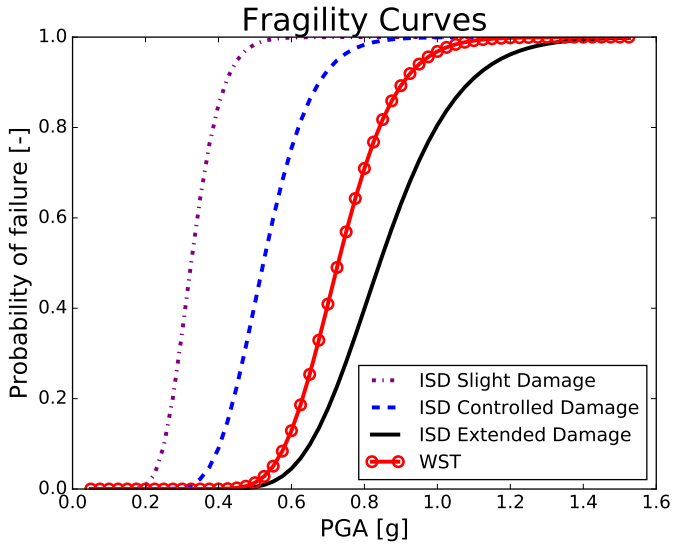

Figure 6.6: Fragility curves for the inter-story drift and the water storage tank

6.4 Hazard Curves and Annual Failure Rates

Hazard curves are used to describe the annual rate of exceeding a certain earthquake level of a given site, for a seismic intensity measure such as PGA [Baker 2008]. Probabilistic seismic hazard analysis (PSHA), is a widely applied approach for the computation of hazard curves [Cornell 1968; McGuire 2008]. In this section, based on the GMPEs calibrated by the

ANNs in Chapter 5, we aim to perform PSHA for some simplified earthquake scenarios. Basic theories about the computation of hazard curves are presented first. Then hazard curves are plotted to visualize the impact of the reduced GMPE Stds, resulting from the consideration of the epistemic uncertainties in M_w and Vs_{30}. Finally, combining results from the hazard analysis and the fragility analysis, the annual failure rates of the considered damage levels described in Section 6.3 are calculated with Eq.6.1.1.

6.4.1 Hazard Analysis: Introduction

Hazard curves are used to estimate the annual rate of exceedance of a seismic intensity level, for a given site of interest. Based on the hypothesis of the normality of the GMPEs residuals, the probability of exceeding an IM level α, given the values of M_w and Vs_{30}, can be computed by

$$P(\mathrm{IM} > \alpha | m_w, r_{jb}) = 1 - \mathbf{\Phi}(\frac{\ln \alpha - \ln \mu_{\mathrm{IM}}(m_w, r_{jb})}{\sigma_{\mathrm{IM}}}), \tag{6.4.1}$$

where $\mathbf{\Phi}(\cdot)$ is the cumulative distribution function (CDF) of the standard normal distribution, $\mu_{\mathrm{IM}}(m_w, r_{jb})$ is the median prediction of the GMPEs at magnitude value of m_w and distance value of r_{jb}, for a specific intensity measure IM, and σ_{IM} is the Std given by the GMPEs for this IM. By employing the total probability of failure, the hazard curve is calculated by

$$H(\alpha) = \lambda(\mathrm{IM} > \alpha) = \sum_i \lambda^i_{\mathrm{source}} \int_{m_w} \int_{r_{jb}} P(\mathrm{IM} > \alpha | m_w, r_{jb}) f^i_{M_w}(m_w) f^i_{R_{jb}}(r_{jb}) \mathrm{d}r_{jb} \mathrm{d}m_w, \tag{6.4.2}$$

where $\lambda(\mathrm{IM} > \alpha)$ is the annual rate for an IM exceeding the level α, $\lambda^i_{\mathrm{source}}$ is the annual occurrence rate of the earthquake source i, $f^i_{M_w}(m_w)$ and $f^i_{R_{jb}}(r_{jb})$ denote the distribution of the magnitude M_w and the distance R_{jb} of this source, respectively. The Gutenberg-Richter recurrence law [Gutenberg and Richter 1944] is often adopted to characterize the distribution of the magnitude $f_{M_w}(m_w)$. The upper limit of the earthquake magnitude is accounted for in an improved version of the Gutenberg-Richter recurrence law, named bounded Gutenberg-Richter recurrence law. These two laws are shown in Figure 6.7, along with some observed data of the earthquake magnitude. With the bounded Gutenberg-Richter law, $f_{M_w}(m_w)$ is computed by

$$f_{M_w}(m_w) = \frac{b \ln(10) 10^{-b(m_w - m_{\min})}}{1 - 10^{-b(m_{\max} - m_{\min})}}, \quad m_{\min} \leqslant m_w \leqslant m_{\max}, \tag{6.4.3}$$

where b is the slope of the Gutenberg-Richter law, and $m_{\min}$ and $m_{\max}$ are the minimum and maximum magnitudes of the considered earthquake source, respectively. The distribution of the distance can have different forms, depending on the type of the earthquake source: area

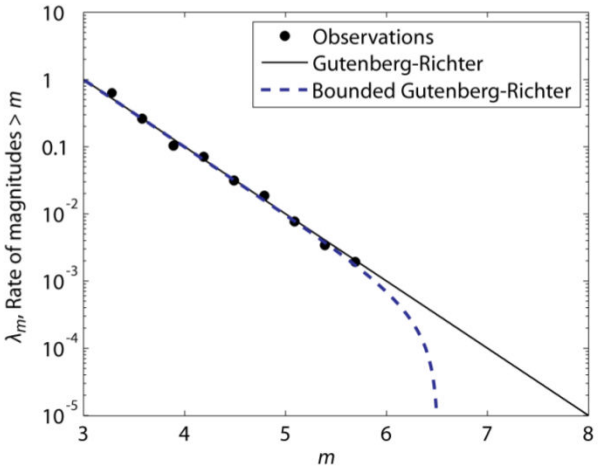

Figure 6.7: Gutenberg-Richter and bounded Gutenberg-Richter recurrence laws [Baker 2008]

source or line source. Let us take the area source as an example, as shown in Figure 6.8. The earthquake source is randomly distributed in the area between $[r_{\min}, r_{\max}]$ with equal likelihood. Therefore, the probability of the earthquake, such that the source-to-site distance is smaller than $r_{jb}(r_{jb} \geqslant r_{\min})$, is computed by:

$$F_{R_{jb}}(r_{jb}) = \mathbf{P}(R_{jb} \leqslant r_{jb}) = \frac{\pi(r_{jb}^2 - r_{\min}^2)}{\pi(r_{\max}^2 - r_{\min}^2)} = \frac{r_{jb}^2 - r_{\min}^2}{r_{\max}^2 - r_{\min}^2}, \tag{6.4.4}$$

where $F_{R_{jb}}(r_{jb})$ denotes the CDF of the R_{jb}. Therefore the probability density function $f_{R_{jb}}(r_{jb})$ can be derived:

$$f_{R_{jb}}(r_{jb}) = \frac{\mathrm{d}F_{R_{jb}}(r_{jb})}{\mathrm{d}r_{jb}} = \frac{2r_{jb}}{r_{\max}^2 - r_{\min}^2}, \quad r_{\min} \leqslant r_{jb} \leqslant r_{\max}. \tag{6.4.5}$$

The hazard curve can be finally obtained when Eqs.6.4.3 and 6.4.5 are plugged into Eq.6.4.2.

6.4.2 Hazard Curves for the SMART Model

This subsection is focused on the computation of the hazard curves, with the GMPEs determined by ANNs in Chapter 5. In this study, we suppose that the SMART model is located on a soil profile with $Vs_{30} = 270$m/s. Only one potential area earthquake source with a value of 0.02 for λ_{source} is considered. The magnitude of this earthquake is assumed in the range of [4.5, 6.5] and the value of the parameter b in Eq.6.4.3 is set to 1, so that the distribution of the magnitude can be obtained with the bounded Gutenberg-Richter recurrence law (Eq.6.4.3). Two scenarios of distances are investigated in this study: (i) $R_{jb} = 30$km without any uncertainty. In this way, the associated PDF of the distance is

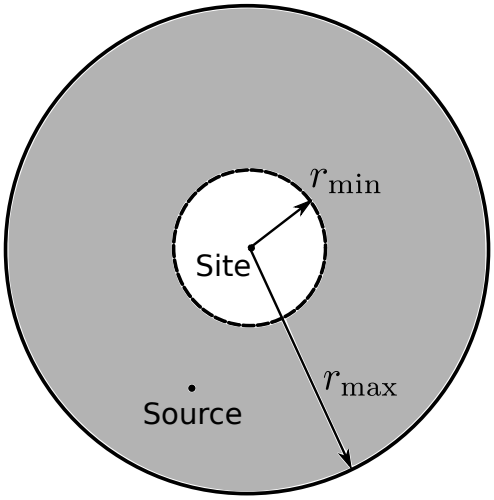

Figure 6.8: Illustration of an area source of an earthquake

$f_{R_{jb}}(r_{jb}) = \delta(r_{jb} - 30)$, where $\delta(\cdot)$ is the Dirac delta function. (ii) the value of R_{jb} is likely between 20km and 40km. Then $f_{R_{jb}}(r_{jb}) = r_{jb}/600.$, obtained with Eq.6.4.5. Both GMPEs obtained with ANNs, with and without the consideration of the uncertainties in M_w and Vs_{30}, are used in the computation of the hazard curves. The hazard curves are computed for PGA, shown in Figure 6.9. In the legend of Figure 6.9, the hazard curves computed with the GMPEs *without* consideration of the uncertainties in M_w and Vs_{30} are indicated with the word 'Certain', whereas the hazard curves computed *with* the consideration of the uncertainties are attributed with the word 'Uncertain'.

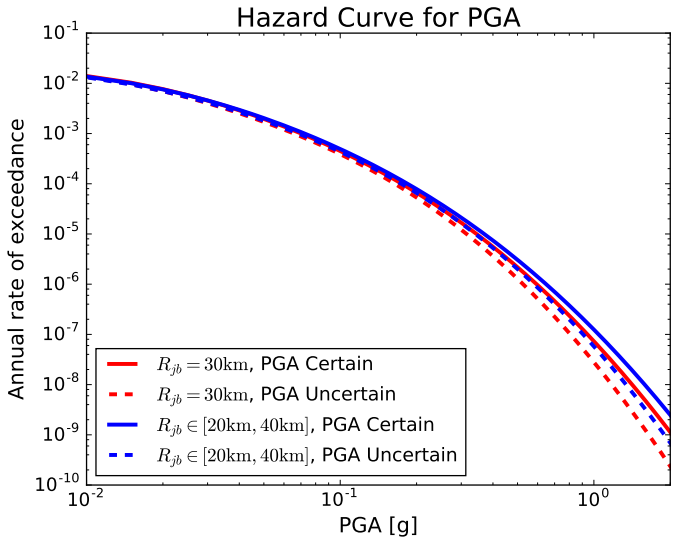

Figure 6.9: Hazard curves for the computation of PGA

In Figure 6.9, it can be concluded that, for both scenarios, the computed hazard curves with GMPEs considering input uncertainties (i.e. with the legend 'PGA Uncertain') show lower values of annual rate of exceedance, compared to those computed by GMPEs without

considering input uncertainties, in particular in high PGA ranges. This is due to the reduced GMPE Std, resulting from the modeling of the epistemic uncertainties in M_w and Vs_{30} in the computation procedure of the GMPEs.

In addition, we can also observe an increase in the annual rate of exceedance, if R_{jb} is not a deterministic value 30km and the value of R_{jb} is extended to [20km, 40km]. To better investigate the phenomenon, we compute the values of the median GMPEs values of ln(PGA) at three different distances: 20km, 30km and 40km, shown in Table 6.4. The relative differences between the values computed at 20km (or 40km) and the values at 30km are also computed and indicated in the brackets in Table 6.4. We can see that for both GMPE models, the decrease of ln(PGA) from 20km to 30km is larger than that from 30km to 40km. In spite of a linear increase of $f_{R_{jb}}(r_{jb})$ from 20km to 40km, the stronger PGA levels in shorter distance remain predominant in the computation of the hazard curves, which explains qualitatively the increase of the annual rate of exceedance when R_{jb} is extended to [20km, 40km].

Table 6.4: Values of ln(PGA) computed by GMPEs at different values of distances

GMPE Model	ln(PGA) with input uncertainty			ln(PGA) without input uncertainty		
R_{jb} [km]	20	30	40	20	30	40
$M_w = 5$	-3.539 (13.68%)	-4.100	-4.514 (-10.09%)	-3.5326 (12.82%)	-4.052	-4.464 (-10.15%)
$M_w = 5.5$	-2.892 (15.17%)	-3.409	-3.829 (-12.33%)	-2.929 (14.14%)	-3.435	-3.798 (-10.58%)
$M_w = 6$	-2.374 (16.36%)	-2.838	-3.191 (-12.42%)	-2.463 (15.36%)	-2.910	-3.269 (-12.33%)

6.4.3 Annual Failure Rates

In the end, we proceed with the computation of the annual failure rates with the damage states defined in Section 6.3 and in Section 6.4.2. The annual failure rates are computed with Eq.6.1.1. The final results of the annual failure rates computed with two different GMPEs for different damage states are reported in Table 6.5.

Table 6.5: Annual failure rates for the considered damage levels

	$R_{jb} = 30$km		$R_{jb} \in [20\text{km},\ 40\text{km}]$	
GMPEs Model	ANN Certain	ANN Uncertain	ANN Certain	ANN Uncertain
ISD Slight Damage	1.591×10^{-5}	1.168×10^{-5}	1.989×10^{-5}	1.548×10^{-5}
ISD Controlled Damage	2.516×10^{-6}	1.563×10^{-6}	3.442×10^{-6}	2.348×10^{-6}
ISD Extended Damage	2.916×10^{-7}	1.432×10^{-7}	4.475×10^{-7}	2.522×10^{-7}
WST Failure	5.218×10^{-7}	2.701×10^{-7}	7.805×10^{-7}	4.599×10^{-7}

From Table 6.5, it can be concluded that the reduced Std from the modeling of the input

uncertainty of the GMPEs leads to lower annual failure rates for the considered damage levels. Comparing the two R_{jb} cases ($R_{jb} = 30$km and $R_{jb} \in [20\text{km},\ 40\text{km}]$), the computed annual failure rates is larger in the case of $R_{jb} \in [20\text{km},\ 40\text{km}]$: this is because the potential seismic hazard for $R_{jb} \in [20\text{km},\ 40\text{km}]$, shown in Figure 6.9, is higher than that of $R_{jb} = 30$km. Besides, with a lower value of the median capacity in the fragility curves, the annual failure rate of the slight damage for ISD is the highest among all the three damage levels, whereas the annual failure rate of the extended damage for the SMART model is the lowest.

6.5 Summary

This chapter provides a final application of the proposed methodologies and models of the previous chapters, for the computation of the annual failure rate of the consequences of interest. The application case study is the structural model used in the SMART 2013 project. A nonlinear material constitutive law is employed to model the behavior reinforced concrete. An ANN is trained with the adaptive learning for the prediction of the inter-story drift and the spectral acceleration of an hypothetical water storage tank around its first natural frequency. Fragility curves are then computed for different damage levels with the predictions of the ANN. On the other hand, hazard curves are computed from the GMPEs constructed by means of ANNs, with and without the consideration of the input uncertainties. For the SMART case, it is shown that, due to the reduced GMPEs Std resulting from the modeling of the input uncertainty, lower seismic hazard is obtained, in particular for high PGA values. This leads to lower values of annual failure rate for the damages of both the inter-story drift and the water storage tank. However, it is worth mentioning again that the adopted adaptive ANN training depends to a certain degree on the initial population of the ground motions. In the SMART case study, a better quality of the initial population can further improve the design of experiments for FEM simulations.

Bibliography

Baker, J. W. (2008). An introduction to probabilistic seismic hazard analysis (PSHA). Technical report, Stanford University.

Campbell, K. W. and Bozorgnia, Y. (2008). NGA ground motion model for the geometric mean horizontal component of PGA, PGV, PGD and 5% damped linear elastic response spectra for periods ranging from 0.01 to 10 s. *Earthquake Spectra*, 24:139–171.

Code_Aster (2017). *Code Analyses des Structures et Thermomécanique pour des Etudes et des Recherches*. EDF Group. Opensource Finite Element code, http://www.code-aster.org.

Cornell, C. A. (1968). Engineering seismic risk analysis. *Bull. Seismol. Soc. Am.*, 58:1583–1606.

Fayolle, S. (2015). *GLRC_DM constitutive law*. EDF Group. Code_aster documentation R7.01.32, https://www.code-aster.org/V2/doc/default/en/man_r/r7/r7.01.32.pdf.

Gutenberg, B. and Richter, C. (1944). Frequency of earthquakes in california. *Bull. Seismol. Soc. Am.*, 34:185–188.

Liel, A. B., Haselton, C. B., Deierlein, G. G., and Baker, J. W. (2009). Incorporating modeling uncertainties in the assessment of seismic collapse risk of buildings. *Struct. Saf.*, 31:197–211.

Mangalathu, S., Jeon, J.-S., DesRoches, R., and Padgett, J. (2016). *Application of bayesian methods to probabilistic seismic demand analyses of concrete box-girder bridges*, pages 1367–1379.

McGuire, R. K. (2008). Probabilistic seismic hazard analysis: Early history. *Earthquake Eng. Struct. Dyn.*, 37:329–338.

Newmark, N. M. and Hall, W. J. (1978). Development of criteria for seismic review of selected nuclear power plants. Technical report, Nuclear Regulatory Commission.

Richard, B., Cherubini, S., Voldoire, F., Charbonnel, P.-E., Chaudat, T., Abouri, S., and Bonfils, N. (2016). SMART 2013: Experimental and numerical assessment of the dynamic behavior by shaking table tests of an asymmetrical reinforced concrete structure subjected to high intensity ground motions. *Eng. Struct.*, 109:99–116.

Zentner, I. (2017). *Operator GENE_ACCE_SEISME*. EDF Group.

Zentner, I., Banci, F., Turpin, F., and Jado, H. (2016). Définition du chargement sismique temporel et calcul de courbes de fragilité par simulation numérique – application à l'étude karisma. In *9eme Colloque Nationale AFPS*.

Zentner, I., Gündel, M., and Bonfils, N. (2017). Fragility analysis methods: Review of existing approaches and application. *Nucl. Eng. Des.*, 323:245–258.

Chapter 7

Conclusion

The main objective of the PhD thesis is to employ neural-network-based methods in seismic risk assessment, in order to (i) Reduce the computational effort in seismic fragility analysis; (ii) Compute seismic fragility curves with different sources of information, including numerical simulation results, post-earthquake observational data and reference values from the literature; (iii) Apply data-driven ground motion prediction equations (GMPEs), in particular considering the epistemic uncertainties of the magnitude M_w and the site condition Vs_{30}. To achieve these objectives, methods based on artificial neural networks (ANNs) and Bayesian statistics have been used in the work of the PhD thesis.

The work accomplished in this PhD thesis is divided into four parts. First, the application of ANNs in the fragility analysis has been investigated. Based on the finite element (FE) simulation results, the most influential seismic intensity measures (IMs) are identified by a forward selection procedure, which is driven by semi-partial correlation coefficients. An ANN is trained to establish a relation between seismic IMs and the structural engineering demand parameters of interest. The influence of the ANN prediction uncertainty on the fragility curves is also discussed. It has been found out that the ANN prediction uncertainty consists of two parts. The first part is from the simplification of the seismic inputs and it is directly integrated into the computation of the probability of failure. On the other hand, the second part is the statistical uncertainty linked to the distribution of the inputs (i.e. the IMs). This latter statistical uncertainty is used to provide the confidence intervals. In the end, a large number of IMs are sampled and used to conduct ANN simulations. Point-wise fragility curves can be computed with the results from fast-running ANN simulations. The methodology has been applied to compute the fragility curve of an assumed electrical cabinet located in the Kashiwazaki-Kariwa nuclear power plant.

In the second stage, the fragility analysis is conducted with different sources of information: simulation results, observational data from post-earthquake inspections and reference values provided in the literature. A Bayesian framework which integrates all the possible information is proposed. In this framework, an ANN is trained adaptively based on the ANN prediction uncertainty, in order to better select a reduced number of ground motions that can represent the whole ground motion space. Fragility parameters computed from the

ANN simulation results provide an estimation of the prior capacity parameter A_m^{prior} and the aleatory uncertainty β_R. The value of the prior epistemic uncertainty β_U^{prior} is selected according to the literature. The damage data, collected from post-earthquake inspections, are used to construct the likelihood function. A two-stage transformation of the IM, in particular the peak ground acceleration (PGA), is proposed to transfer the IM value registered in the database to the free field of the structure of interest. The Bayesian updating is finally performed to obtain the posterior distribution of the capacity. The framework is applied to a low-voltage switchgear in the Kashiwazaki-Kariwa nuclear power plant, and the used damage data are gathered from the database of seismic qualification utility group (SQUG). After the Bayesian updating, it can be observed that the value of the epistemic uncertainty is reduced with the additional information from the database, whereas the capacity of the low-voltage switchgear has increased since few failure cases of low-voltage switchgear are observed in the SQUG database.

The third part of the thesis is dedicated to the application of ANNs in the computation of GMPEs. The uncertainty of the magnitude M_w and the averaged thirty-meter-shear-wave velocity Vs_{30} is accounted for in the computation of the GMPEs. The modeling of the uncertainty related to M_w and Vs_{30} relies on the first order second moment approximation, which gives rise to the appearance of off-diagonal elements in the variance-covariance matrix of the residuals. An ANN training based on the generalized least-squares is designed to handle the off-diagonal terms for the maximization of the likelihood function. The proposed method is validated on a simulated database and is also applied to the RESORCE database. The application results show that the standard deviations of the GMPEs can be reduced by 4-16%, depending on the frequency of the spectral accelerations.

Finally, fragility analysis and hazard analysis are combined together to compute the annual failure rate. A nonlinear SMART model is used as a final application example. Uncertainties in the material properties are also modeled in this case study. The fragility analysis is conducted by means of the adaptive ANN training. Hazard curves are computed with the two obtained GMPE models, namely with and without the consideration of input uncertainties. Annual failure rates are computed for three levels of damages of the inter-story drift, as well as the failure of an assumed water storage tank. Application results in the considered case study show that, due to the reduced GMPEs standard deviations resulting from the modeling of the input uncertainty, lower seismic hazard is obtained, which leads to lower values of annual failure rates for the considered damages.

For further researches, a better selection of the initial population for the SMART nonlinear model can be used to improve the computation of the fragility curves of the SMART model. Furthermore, rather than using different scenarios for the generation of the earthquake exci-

tations, the deaggregation of seismic hazard can be conducted to identify the scenarios that contribute the most to the seismic hazard. Then, fragility analysis can be performed based on these scenarios. In addition, non-parametric Monte-Carlo based fragility curves can be computed to consider the heteroscedasticity of the β_R values for the SMART case study, also because in this case the assumption of the linear regression in log-log scale is not complete justified. The current approach to consider the uncertainty in the material parameters consists in sampling their values from corresponding probability distributions. Then, the same material parameter values are applied to the entire structure. One can also use the random field approach and assign realizations of the random field of the material to the structure, so that the material parameter values are different on different parts of the structure.

For the GMPE computation, other site- and fault-related parameters can be also integrated as predictor parameters in the GMPE model. It would also be interesting to estimate the error terms of δM and δVs, if possible.

ANNs can be used as a metamodel when the ground motion time histories are injected directly as the inputs. Therefore, the prediction of the ANN is also the time history of a physical quantity of interest. In this case, the recurrent neural network can be a good choice to capture the dynamic temporal behavior, due to the existence of the inner loop in the ANN architecture.

Another potential perspective is to perform vector-based fragility analysis and hazard analysis. The annual failure rate can also be computed by the convolution of the fragility surface and the joint probability density function of two IMs. The obtained annual failure rate can be compared to that calculated from scalar-based seismic risk assessment.

Part II

Publications

Wang, Z., Pedroni, N., Zentner, I., and Zio, E. (2018). Seismic fragility analysis with artificial neural networks: Application to nuclear power plant equipment. *Eng. Struct.*, 162:213–225.

Wang, Z., Zentner, I., and Zio, E. (2018). A Bayesian framework for estimating fragility curves based on seismic damage data and numerical simulations by adaptive neural networks. *Nucl. Eng. Des.*, 338:232–246.

Wang, Z., Zentner, I., and Zio, E. Ground motion prediction equations by artificial neural networks with input uncertainties (under review).

Paper I : Wang, Z., Pedorni, N., Zentner, I., and Zio, E. (2018). Seismic fragility analysis with artificial neural networks: Application to nuclear power plant equipment. *Eng. Struct.*, 162:213-225

Seismic fragility analysis with artificial neural networks: Application to nuclear power plant equipment

Zhiyi Wang[a,b,c], Nicola Pedroni[c], Irmela Zentner[a,b], Enrico Zio[c,d]

[a] *EDF Lab Saclay, France*
[b] *Institute for Mechanical Sciences and Industrial Applications, UMR 9219 CNRS-EDF-CEA-ENSTA ParisTech, France*
[c] *Chair on Systems Science and Energetic Challenge, European Foundation for New Energy of EDF, CentraleSupélec, Université Paris-Saclay, France*
[d] *Energy Department, Politecnico di Milano, Italy*

Abstract

The fragility curve is defined as the conditional probability of failure of a structure, or its critical components, at given values of seismic intensity measures (IMs). The conditional probability of failure is usually computed adopting a log-normal assumption to reduce the computational cost. In this paper, an artificial neural network (ANN) is constructed to improve the computational efficiency for the calculation of structural outputs. The following aspects are addressed in this paper: (a) Implementation of an efficient algorithm to select IMs as inputs of the ANN. The most relevant IMs are selected with a forward selection approach based on semi-partial correlation coefficients; (b) Quantification and investigation of the ANN prediction uncertainty computed with the delta method. It consists of an aleatory component from the simplification of the seismic inputs and an epistemic model uncertainty from the limited size of the training data. The aleatory component is integrated in the computation of fragility curves, whereas the epistemic component provides the confidence intervals; (c) Computation of fragility curves with Monte Carlo method and verification of the validity of the log-normal assumption. This methodology is applied to estimate the probability of failure of an electrical cabinet in a reactor building studied in the framework of the KARISMA benchmark.

Keywords: Seismic probabilistic risk assessment; Fragility curve; Artificial neural network; Feature selection; Prediction uncertainty

1. Introduction

The seismic probabilistic risk assessment (SPRA) methodology has been applied worldwide for the estimation of the seismic risk of nuclear power plants (NPPs) [1]. In the SPRA methodology, fragility curves are computed as conditional probabilities of failure of structures, or critical components, for given values of a seismic intensity measure (IM), such as the peak ground acceleration (PGA) [2]. The core damage frequency of the plant is, then, calculated by the convolution of the fragility curves with the hazard curves in fault tree and event tree analysis [2]. The computation of fragility curves requires a realistic estimation of the structure performance subject to seismic excitations via the quantification and the propagation of uncertainties existing in earthquake ground motions, structural material properties, etc. These uncertainties are categorized into two groups [3]: aleatory uncertainties, which reveal the inherent randomness of variables or stochastic processes, and epistemic uncertainties, which originate from the lack of knowledge about the model and provide a family of confidence interval curves for the fragility estimation.

In practice, a fragility curve is calculated as the conditional probability that the damage measure (DM) exceeds a critical threshold, for a given seismic IM [4, 5]:

$$P_f(\alpha) = P(y > y_{\text{crit}}|\alpha) \tag{1}$$

where y is the DM, such as inter-story drift, y_{crit} is the failure threshold and α represents the seismic IM. This conditional probability can be evaluated pointwise for different α values with the Monte Carlo method [4, 6], as well as with methods based on the log-normal hypothesis [3, 7, 8]. However, both methods require a few hundred heavy numerical simulations with the finite element method (FEM).

One way to improve the computational efficiency consists in building a metamodel to calibrate the statistical relation between seismic inputs and structural outputs. In fact, it is difficult to directly use stochastic ground motions to construct the metamodels, because the high-dimensionality of the inputs of such metamodels requires a very large size of training data to accurately approximate the input-output relation [9]. An alternative is to use seismic IMs as inputs of the metamodels to represent ground motions. Various functional models based on the calibration of IMs-DM relation have been proposed [10, 11, 12]. According to these works, a nonlinear regression metamodel seems more suitable to provide adequate nonlinearity in the IMs-DM relation. However, with this approach, the simplification of the continuous stochastic ground motion by a small set of IMs may not allow to describe all the random variability in the earthquake motion [13]. Therefore, it cannot ensure the performance of the metamodels.

Some studies regarding the application of metamodels in fragility analysis have been realized recently. Most works focus on using seismic IMs to characterize earthquake accelerations. Metamodels are constructed to calibrate the relation between DMs and uncertain inputs of the structural models, including IMs and material parameters. The construction of the metamodels is either achieved by decomposing the nonlinear input-output relation with high-dimensional model representation (HDMR) [13, 14], or realized with polynomial regression [15, 16, 17, 18, 19] or other more advanced statistical tools, such as artificial neural networks (ANNs) [20, 21, 22, 23, 24], LASSO regression [25], Bayesian networks [26], merging multivariate adaptive regression splines, radial basis function network, support vector regression [27], Kriging [9, 28], etc. On the other hand, earthquake accelerations are also used directly as inputs of the metamodel in [29] to predict structural response time histories. The construction of the metamodel is divided into two steps: the first step is to extract the characteristics of earthquake motions with nonlinear auto-regression; then the polynomial chaos expansion is applied to these characteristics to construct the metamodel. DMs are computed from the structural response time histories, and fragility curves can be thus obtained. Although this method seems different from the classical metamodeling with IMs, the idea remains the same: the nonlinear auto-regression serves as a tool to extract the features of earthquake motions and past values of the structural displacement, while these features are represented by the IMs in classical approaches. Besides regression methods, classification models like logistic regression, random forests and support vector machine are utilized in [30] to predict directly the probability of failure from the uncertain inputs. Despite the fact that seismic fragility analyses have been successfully performed with different types of metamodels, the following two points are rarely discussed: i) Systematic selection of pertinent IMs to represent seismic ground motions; ii) Quantification of the prediction uncertainty of the metamodels.

In this paper, a computationally efficient methodology for the application of ANNs to characterize the IMs-DM relation is proposed, from the selection of the most relevant IMs to the quantification of ANN prediction uncertainties. Most existing works take subjective choices of the IMs as inputs of metamodels according to their expertise (e.g. PGA or PGA with other IMs). One IM is obviously not sufficient to represent the seismic ground motion. More systematic approaches are proposed in [20, 23] to guide the selection of IMs. Different sets of IMs are selected to train ANNs in [20] and the performances of the different sets of IMs are analyzed with respect to their corresponding ANNs median training errors. Ferrario et al. proposes a wrapper approach based on genetic algorithms in [23] to select the best subset of IMs. However, these approaches can be time-consuming, because it requires repeated trainings of the metamodel. A more efficient feature selection method is proposed in this work.

The uncertainty in the metamodel predictions is also investigated. The ANN prediction uncertainty is considered to be epistemic in [31] to quantify the impact of the size of the used data. The prediction uncertainty is determined by the bootstrap approach, in which retrainings of ANNs are necessary, and it provides confidence intervals of fragility curves. On the contrary, other works integrate the metamodel uncertainty completely into $P_f(\alpha)$ by modeling the standard deviation (Std) of the residual with a dual metamodel (quadratic response surface, HDMR or Kriging) [9, 14, 18, 32]. The residual is sampled from a corresponding normal distribution, and it is added to the mean structural DM predicted by the primal metamodel. With this approach, the residual is an aleatory uncertainty, and the influence of the size of the training data is not accounted for. In addition, the number of FEM simulations required by the dual metamodel approach can be very large, because a number of FEM simulations should be performed *at every design point* with different stochastic motions to obtain the Std. Therefore, it may not be applicable to a very complex structure such as NPP. In this paper, a clearer insight of the ANN prediction uncertainty computed with the delta method is provided: it consists of an aleatory component from the simplification of the seismic inputs and an epistemic uncertainty due to the paucity of the training data. The former is considered in the computation of $P_f(\alpha)$, whereas the latter is used in the estimation of confidence intervals.

Among various types of metamodels, ANNs are chosen due to their adequate nonlinearity and their excellent universal approximation capability for continuous bounded functions [33, 34] (e.g. compared to polynomial response surfaces). Firstly, rather than a classification model like a SVM classifier, which returns only binary failed or survived information for the conditions of structures, an ANN regression model provides predictive structural responses and offers more flexibility for the fragility analysis. Furthermore, the applicability of the ANN does not depend on the probability distribution of input data, so it is a versatile model with a very wide domain of application. Finally, a metamodel based on ANN is a regression rather than an interpolation model. If representative seismic IMs are used to characterize the continuous seismic motions as inputs of the metamodel, the IMs cannot fully represent the seismic randomness and this introduces a residual term. However, an interpolation model predicts identical outputs as the original ground motions for the training data: it may thus overfit the input-output relation. This point is addressed in detail in this work.

This paper is organized as follows: in the next section, the basis about simulation-based fragility analysis methods is briefly recalled. Section 3 presents the methodology for ANN-based fragility estimation. Feature

selection techniques are highlighted in this methodology to select the most relevant seismic IMs for a better accuracy of the metamodels. ANN prediction uncertainties are separated into aleatory and epistemic components. These uncertainties are considered in the computation of the fragility curves and the related confidence intervals. An application of the proposed methodology to the Kashiwazaki-Kariwa NPP is demonstrated in Section 4 in the context of the KARISMA benchmark [35]. Conclusions are finally provided in Section 5. Only the ground motion record-to-record variability is considered in this paper, to better study the impact of the ANN prediction uncertainties on the fragility curves. In addition, without specification, the metamodel mentioned in this paper represents regression or interpolation models, instead of binary classification models.

2. Simulation-based Fragility Analysis

A simulation-based fragility analysis is composed of 3 main steps:

1. Structure modeling. This step consists in establishing a set of mathematical partial differential equations to describe the mechanical behavior of the underlying model.
2. Numerical simulation and calculation of the DM. Numerical simulations are performed to propagate the uncertainties and to compute the DM. FEM is the most widely used numerical resolution method.
3. Computation of the conditional probability of failure of the structure. This step is realized by applying a statistical analysis to the IM-DM data cloud (α, y) computed from the numerical simulation results.

In this section, the computation of the DM and the calculation of the conditional probability of failure are further discussed. The concept of the residual of the metamodel is introduced and emphasized. This concept will be later used throughout the next parts of the paper. Two commonly used methods for the computation of the conditional probability are presented. These two methods will be applied to calculate the fragility curves in an industrial complex case study in this paper.

2.1. Computation of the Damage Measure

Mechanical model. The mechanical model to compute the DM of a structure or a critical component can be described as

$$y = f(\boldsymbol{a}(t)) \tag{2}$$

where $\boldsymbol{a}(t)$ represents the seismic ground acceleration. The resolution of Eq. 2 is usually time-consuming, especially when the structural model is very complex. In this way, one needs to resort to the metamodel to reduce the computational cost of the numerical simulations.

Metamodel. In this paper, a metamodel established for IMs-DM relation is desired. It is used to replace the mechanical model in order to improve the computational efficiency:

$$\hat{y} = \hat{f}(\mathrm{IM}_1, \mathrm{IM}_2, ..., \mathrm{IM}_k) \tag{3}$$

where the symbol '$\wedge$' denotes the results calculated from the metamodel. The regression of the metamodel leads to a reduction of the variability in the metamodel prediction: $y = \hat{y} + \varepsilon$. The existence of the residual ε not only comes from the lack-of-fit of the metamodel, but also has more specific interpretations:

1. The metamodel cannot show sufficient nonlinearity to replace the mechanical model. The residual value can be very high if a linear metamodel is wrongly selected to substitute a nonlinear mechanical model.
2. IMs are adopted to represent the inherent randomness of ground motions $\boldsymbol{a}(t)$, which gives rise to a loss of information in the input variables. Different ground motion time histories with the same set of IM values lead to different structural responses, in contrast to a deterministic response predicted by the metamodel. Consequently, ε should be present for the training data in the metamodeling process. That is also the main reason why a nonlinear regression model like ANN is preferred, rather than an exact interpolation model, such as Kriging with classical kernels (Gaussian kernel, Matern kernel, etc).
3. The number of the training data for the development of the metamodel is usually limited due to the computational cost of FEM simulations.

These facts show the necessity of the quantification of the metamodel prediction uncertainty, in order to provide reliable applications of metamodels to critical structures such as NPPs.

2.2. Computation of Fragility Curves

This section is dedicated to recall the basis of two methods in the computation of fragility curves: the Monte Carlo Method and the regression method. These two methods can be applied to compute the conditional probability of failure when the data cloud (α, y) is provided.

Monte Carlo (MC) method. In this method, N seismic records with the same IM level α are collected. Structural analyses for all N seismic motions are performed, and the probability of failure for the seismic IM level α is calculated as

$$P_{\mathrm{MC}}(\alpha) = \frac{1}{N}\sum_{i=1}^{N} \mathbf{1}[y_{\mathrm{crit}} - y^i(\alpha) < 0] \tag{4}$$

where $\mathbf{1}[y_{\mathrm{crit}} - y^i(\alpha) < 0]$ equals 1 if $y_{\mathrm{crit}} - y^i(\alpha) < 0$, otherwise it equals 0.

Regression method with log-normal assumption. The log-normal assumption is commonly adopted to compute the conditional probability of failure. The regression method (Reg), or 'cloud analysis', is based on the linear regression of the data cloud (α, y) in the log-log space [5, 10, 36].

$$\ln y = c \ln \alpha + \ln b + \varepsilon \tag{5}$$

where b and c are regression parameters determined from the data cloud $(\ln \alpha, \ln y)$, and the residual ε follows a normal distribution $\mathcal{N}(0, \beta^2_{R|IM})$. $\beta_{R|IM}$ is calculated as

$$\beta_{R|IM} = \sqrt{\frac{\sum_{i=0}^{N}(\varepsilon^i - \bar{\varepsilon})^2}{N-2}} \tag{6}$$

in which $\bar{\varepsilon}$ is the mean of the regression residuals and N denotes the size of the data (α, y). The conditional probability of failure can be, thus, calculated:

$$P_f(\alpha) = \mathbf{\Phi}\left(\frac{\ln b\alpha^c - \ln y_{\mathrm{crit}}}{\beta_{R|IM}}\right) \tag{7}$$

where $\mathbf{\Phi}(\cdot)$ is the cumulative distribution function of the standard normal distribution $\mathcal{N}(0, 1)$.

Both methods MC and Reg are used in the sequel of this paper to compute fragility curves. In particular, the pointwise MC method serves to confirm the validity of the log-normal assumption.

3. Description of the ANN-based Seismic Fragility Analysis

The global procedure for the estimation of the fragility curves with ANNs is illustrated in Figure 1. The basic stages are: (1) Preparation of data set by performing FEM simulations. (2) Feature selection to extract the most important IMs as inputs of the ANN. (3) ANN training and validation. (4) ANN uncertainty quantification. (5) Computation of fragility curves with ANN simulation results.

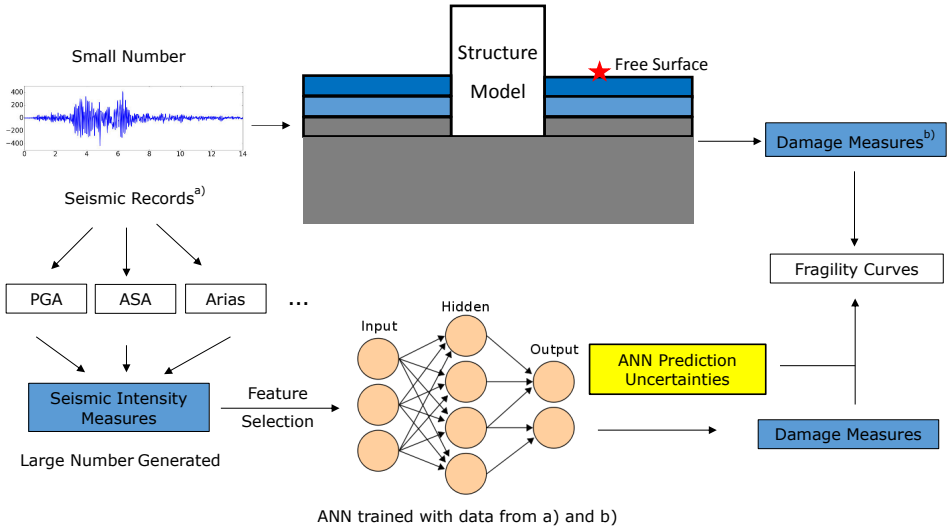

Figure 1: Work flow for the computation of fragility curves with ANN

3.1. Preparation of Data Set

This step is achieved by conducting a series of numerical simulations with the FEM. The soil-structure interaction (SSI) should be considered to offer a best estimate of the structural response. The number of simulations is thus limited due to the computational complexity of the FEM analysis, with the presence of the SSI. The basic working flow is divided into the following 5 steps illustrated in Figure 2:

1. Generation of synthetic seismic motions at the bedrock. This can be realized by generating a set of seismic motions compatible with the spectral acceleration predicted by the ground motion prediction equations (GMPEs).
2. Convolution of the bedrock accelerations to the free surface. The convolution is performed using a 1D column of soil with the consideration of soil degradation. The degradation of the soil during the earthquake is accounted for by the equivalent linear method (ELM) based on the 1D soil column [37].
3. After the convolution, surface ground motions and their corresponding degraded soil profiles are obtained. The ground motions obtained on the free surface are coherent with the site-specific degraded soil profiles. The latter is utilized as the input of the SSI analysis, whereas IMs of the ground motions on the free surface can be extracted.
4. SSI analysis is conducted and structural response time histories can be thus obtained.
5. The DMs are computed by the post-processing of the structural response time histories.

Consequently, the data set IMs-DM is available for the feature selection and further for the construction of the ANN metamodel.

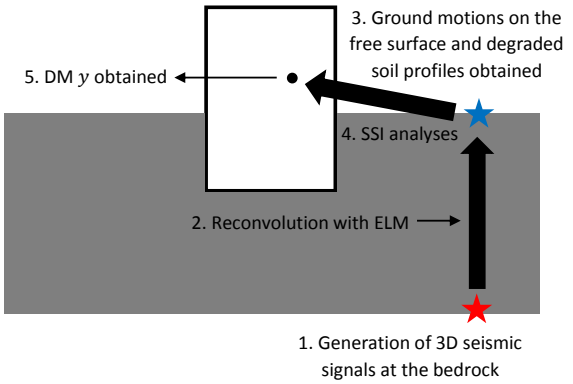

Figure 2: Work flow of FEM simulations

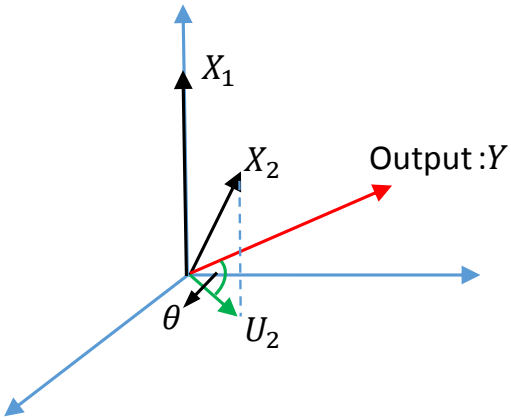

Figure 3: Computation of SPCC – $\cos(\theta)$

3.2. Feature Selection

Before the training of the ANNs, it is important to select a subset of IMs whose impact on the DM is dominant. This step, named feature selection, is crucial in the metamodel construction phase to ensure the performance of the ANNs. On the one hand, an IM irrelevant to the output should not be considered as a feature; on the other hand, with the limited size of available training data, a smaller input dimension simplifies the ANN structure and improves the generalization capacities of the network [33]. The feature selection approach applied in [23] is a wrapper approach based on the genetic algorithm (GA). The wrapper approach relies on the metamodel to select the best subset of the features (i.e. relevant IMs) [38]. However, one disadvantage of the wrapper approach is its computational burden, because this method requires a large number of repeated trainings of the ANNs.

Filter approach based on semi-partial correlation coefficients. A filter approach is proposed in this paper to improve the computational efficiency of the wrapper feature selection. In machine learning, the filter approach describes a group of methods used to select the features regardless of the metamodel. Therefore, it can be regarded as a sensitivity analysis between inputs and outputs. In the context of fragility analysis, the main difficulty in applying such an approach is the dependence between all the IMs. This correlation should be considered in the execution of the filter approach to discard the redundant information.

For this purpose, a forward selection algorithm driven by semi-partial correlation coefficients (SPCCs) is used to rank the importance of the IMs. As shown in Figure 3, in order to eliminate the dependence, the IM X_2 is projected onto the orthogonal space of the reference IM X_1. The SPCC calculates the correlation (the cosine value of the angle θ) between the projection U_2 and Y. The orthogonal relation between random variables (RVs) is interpreted by the statistical linear independence between them. Therefore, if IMs follow log-normal distributions, the orthogonal projections can be realized by means of Cholesky factorization on the correlation coefficient matrix of the underlying normally distributed RVs [39]. The adopted forward selection algorithm is as follows:

1. Define the input and the output of the algorithm: the input is the feature set $S_0 = \{X_1, \cdots, X_k\}$ ($X_i = \ln \mathrm{IM}_i$) and the output is ranked feature set S^*. Initialize the output set $S_0^* = \emptyset$.

2. Begin the iteration i (i starts from 0): for each feature X_j in S_i, compute the SPCC between X_j and the Output Y ($\ln \mathrm{DM}$), by projecting X_j onto the orthogonal space of the ranked feature set S_i^* (i.e. conditional to S_i^*). Select the feature with the largest SPCC value:

$$j^* = \arg\max_j \mathrm{SPCC}(X_j, Y|S_i^*) \tag{8}$$

$$R_i^{\mathrm{SP}} = \mathrm{SPCC}(X_{j^*}, Y|S_i^*) \tag{9}$$

When $i = 0$, $\mathrm{SPCC}(X_j, Y|\emptyset)$ actually computes the linear correlation coefficient between X_j and Y.

3. Subtract the selected X_{j^*} from the feature set: $S_i \ominus X_{j^*} \rightarrow S_{i+1}$, and add X_{j^*} into the output set: $S_i^* \oplus X_{j^*} \rightarrow S_{i+1}^*$.
4. Set $i = i + 1$ and return to Step 2 until all the IMs are selected in S^*.

The IMs are ranked in S^* according to their importance to the output, and one can select the first few IMs to train the ANN.

3.3. ANN Training and Validation

The structure of a classical, three-layer, feed-forward ANN is illustrated in Figure 4. Mathematically, this ANN consists of activation functions (linear functions, and nonlinear tanh functions) and a set of model parameters. The model parameters are the ANN weights $\boldsymbol{w}$ and biases $\boldsymbol{b}$, which are adjusted by training to minimize a cost function. The cost function computes the difference between the ANN predictions $\hat{y}$ and the targets y (e.g. FEM simulation results), summed over every training example i. For simplicity of notation, in this paper, $\boldsymbol{w}$ is used to represent all parameters of the ANNs, including weights and biases.

$$E(\boldsymbol{x}; \boldsymbol{w}) = \frac{1}{2} \sum_{i=1}^{N} (\hat{y}^i(\boldsymbol{x}; \boldsymbol{w}) - y^i)^2 \tag{10}$$

where $E(\boldsymbol{x}; \boldsymbol{w})$ denotes the cost function which the ANN aims to minimize, N is the total number of ANN training examples, and $\boldsymbol{x}$ is the ANN input vector. The ANN is trained based on the gradient vector $\boldsymbol{g}$, which can be computed efficiently by the back-propagation algorithm [33, 40]:

$$\boldsymbol{g} = \frac{\partial E(\boldsymbol{x}; \boldsymbol{w})}{\partial \boldsymbol{w}} \tag{11}$$

For the ANN training, the available data set is divided into 3 independent subsets:

- Training subset (e.g. 60% of the total data), which is used to determine the optimal weighting parameters $\boldsymbol{w}^*$ that minimize the cost function of the ANN model.

- Validation subset (e.g. 20% of the total data), which supervises the training process. The ANN training is stopped when the validation error reaches its minimum to avoid overfitting [33, 41]. This strategy is called *early stopping*.

- Test subset (e.g. 20% of the total data), which is independent of the training and validation subsets. The test subset is not used in the ANN training, but used afterwards to evaluate the generalization capacity of a trained ANN metamodel.

The ANN is suggested to be trained with IMs-DM in log-log space to facilitate the consideration of the ANN uncertainties into the fragility curves. The performance of the ANN can be evaluated by the root-mean-square error (RMSE). Once trained and validated, the ANN substitutes the FEM model to accelerate the computation process.

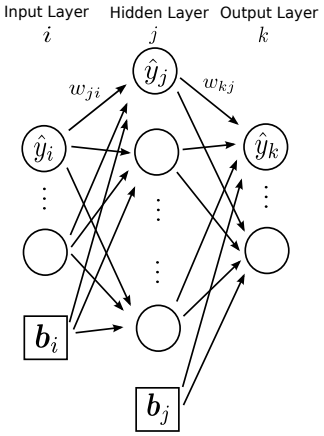

Figure 4: A multiple-layer perceptron model

3.4. ANN Uncertainty Quantification

Besides the ANN deterministic prediction $\hat{y}$, the confidence interval (CI) of this prediction can be also estimated. The main methods to evaluate the prediction intervals (PIs) of ANNs are the bootstrap method, the Bayesian approach and the delta method [42]. The delta method is adopted in this study due to its computational efficiency because it does not require repeated trainings of the ANNs with the bootstrap resampling[43]. Assuming a normal distribution of the ANN training error, this method relies on the linear Taylor expansion of the ANN model and estimates the PIs of the corresponding linear model [43, 44, 45]. In this way, the Hessian matrix of the ANN is approximated by the product of the Jacobian matrices. Mathematically, the PIs are computed with the Std of the ANN training error σ_{ANN} and the gradient vector $\boldsymbol{h}$:

$$\boldsymbol{h}^i = \frac{\partial \hat{y}^i}{\partial \boldsymbol{w}} = \frac{\partial \hat{y}^i}{\partial E(\boldsymbol{x};\boldsymbol{w})} \frac{\partial E(\boldsymbol{x};\boldsymbol{w})}{\partial \boldsymbol{w}} = \frac{\boldsymbol{g}}{\hat{y}^i - y^i} \tag{12}$$

The Jacobian matrix $\boldsymbol{J}$ of the ANN training data is, hence, constructed as

$$\boldsymbol{J} = \begin{bmatrix} \boldsymbol{h}^1 & \boldsymbol{h}^2 & \cdots & \boldsymbol{h}^i & \cdots & \boldsymbol{h}^N \end{bmatrix} \tag{13}$$

where $\boldsymbol{J}$ is a $Q \times N$ matrix, with N the number of the ANN training examples and Q the number of the weighting parameters in the ANN. Consequently, the prediction uncertainties of ANNs are calculated as

$$s^2 = \sigma^2_{\text{ANN}} + \sigma^2_{\text{ANN}} \boldsymbol{h}^T_{\text{test}} (\boldsymbol{J}\boldsymbol{J}^T)^{-1} \boldsymbol{h}_{\text{test}} \tag{14}$$

where s denotes the Std of the ANN predictions.

The source of the ANN prediction uncertainty comes from two aspects: i) The selected IMs cannot completely represent the variability of the ground motion. This eventually reduces the variability of the output. ii) The ANN accuracy due to the limited size of data to train ANNs. It is the statistical uncertainty linked to the ANN model. Let us return to the two components in s^2: the first fixed part σ^2_{ANN} represents the ANN training error, and the second part $\sigma^2_{\text{ANN,stat}} \triangleq \sigma^2_{\text{ANN}} \boldsymbol{h}^T_{\text{test}} (\boldsymbol{J}\boldsymbol{J}^T)^{-1} \boldsymbol{h}_{\text{test}}$ depends on the training and the test data.

1. The first term σ^2_{ANN} estimates the difference between the FEM simulation results and the predictions of the ANN. Given that a nonlinear regression returns a regular hyper-surface in a high dimensional space,

the predictions of the ANN show always less variability than the original FEM data. As discussed in Section 2.1, this phenomenon is mainly due to the loss of the inherent seismic randomness in the input variables, so that the nature of σ^2_{ANN} can be regarded as the aleatory uncertainty not explained by the ANN input parameters.

2. The second term $\sigma^2_{\text{ANN,stat}}$ is the statistical uncertainty linked to the limited data used to train and test the ANNs. The information of the training data is included in the $\boldsymbol{J}$ matrix and $\boldsymbol{h}_{\text{test}}$ incorporates the influence of the test data. It is thus considered as the epistemic uncertainty, and it provides the confidence intervals of the fragility curves.

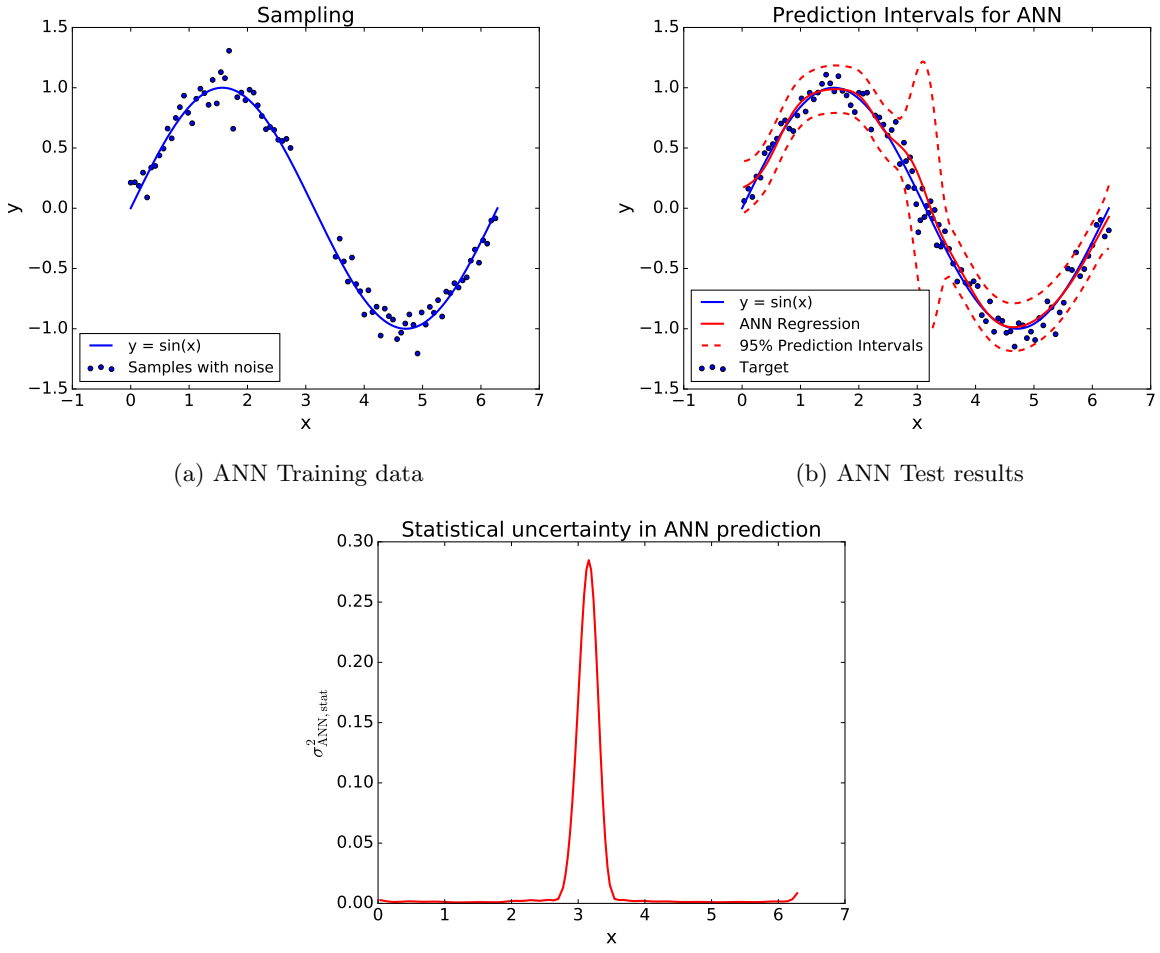

(a) ANN Training data

(b) ANN Test results

(c) ANN statistical uncertainty

Figure 5: An illustrative example for ANN prediction uncertainties: (a) 80 sparse training data $y = \sin(x) + z$, with $z \sim \mathcal{N}(0, 0.1^2)$. An ANN is trained with $(x,\ y)$. z is assumed to be the unidentified input. No training data are generated near $x = 3$, for the purpose of checking the property of $\sigma_{\text{ANN,stat}}$. (b) ANN is trained, with $\sigma_{\text{ANN}} = 0.0931$, close to the Std of z. The ANN is then tested on 100 uniformly regenerated data. (c) $\sigma_{\text{ANN,stat}}$ with a peak near $x = 3$, where no training data exist. It can be concluded that $\sigma_{\text{ANN,stat}}$ captures the scarcity of the training data.

These two aspects are illustrated with a simple case study in Figure 5. In fact, σ_{ANN} should have contained also an epistemic uncertainty contribution from the insufficient nonlinearity of the ANN. However, the high flexibility of the ANN architecture offers an universal approximation capacity to continuous bounded functions [34]. If the number of the hidden layer units is correctly determined, the error from the ANN nonlinearity

can be considered less important compared to the aleatory randomness neglected in its inputs. This can be observed from Figure 5: in spite of the existence of the unidentified input z, the ANN regression curve stays very close to $y = \sin(x)$ curve in the training data region. Consequently, this epistemic contribution is assumed negligible in this study. Next section presents the computation of fragility curves with the consideration of these two uncertainties.

3.5. Fragility Curves with ANN simulation results

The marginal distributions of the IMs are known through the GMPEs [46]. Correlation models are also available in the literature [47]. Based on GMPEs and correlation models, seismic IMs can be generated directly as inputs of the ANN. One advantage of using IMs as inputs of metamodels is that no seismic ground motions are in need for ANN simulations.

Given the large number of simulation results provided by ANN, fragility curves can be computed with methods MC and Reg. This also allows confirming the validity of the log-normal assumption used in the fragility analysis. It is important to take into account the ANN prediction uncertainty, because the regression of the ANN reduces the statistical variability of the DMs, and thus the aleatory uncertainty of the fragility curves. As a consequence, methods MC and Reg should be adapted with the consideration of the ANN prediction uncertainty.

For the Reg method, as the ANN is trained in log-log space, the aleatory residual uncertainty σ^2_{ANN} can be integrated directly into the expression of the log-normal CDF (Eq. 7). The basic steps consist of:

1. Generation of IMs as inputs of the ANN. Select one IM α as the parameter of the fragility curve.
2. Conduct ANN simulations with the generated IMs. The ANN outputs $\hat{y}$ are obtained.
3. Apply Reg method on data (α, $\hat{y}$) and determine the regression parameters b, c, $\beta^{\text{ANN}}_{R|IM}$.
4. Compute the conditional probability of failure with the consideration of σ^2_{ANN}:

$$P_f(\alpha) = \mathbf{\Phi}\left(\frac{\ln b\alpha^c - \ln y_{\text{crit}}}{\beta_{\text{Total}}}\right) = \mathbf{\Phi}\left(\frac{\ln b\alpha^c - \ln y_{\text{crit}}}{\sqrt{(\beta^{\text{ANN}}_{R|IM})^2 + \sigma^2_{\text{ANN}}}}\right) \tag{15}$$

A similar idea concerning the consideration of this metamodel uncertainty has been used in [28] for Kriging.

For the MC estimation based on the ANN simulation data, no analytical expression can be derived. One has to resort to the sampling of the residual, for both aleatory and epistemic parts. The basic steps are:

1. Generation of N groups of seismic IMs as inputs of the ANN, conditional to the IM α used as the independent parameter of the fragility curve.
2. Conduct ANN simulations with the generated IMs. The ANN outputs $\hat{y}$ are obtained.
3. Sampling of N residuals ε_{ANN} following $\mathcal{N}(0, \sigma^2_{\text{ANN}})$, and sampling of $\varepsilon^{\gamma}_{\text{ANN,stat}}$, the γ percentile of $\mathcal{N}(0, \sigma^2_{\text{ANN,stat}})$.
4. Computation of the conditional probability of failure $P_{\text{MC}}(\alpha)$ and the γ confidence interval $\tilde{P}^{\gamma}_{\text{MC}}(\alpha)$:

$$P_{\text{MC}}(\alpha) = \frac{1}{N}\sum_{i=1}^{N} \mathbf{1}[\ln y_{\text{crit}} < \ln \hat{y}^i(\alpha) + \varepsilon^i_{\text{ANN}}] \tag{16}$$

$$\tilde{P}^{\gamma}_{\text{MC}}(\alpha) = \frac{1}{N}\sum_{i=1}^{N} \mathbf{1}[\ln y_{\text{crit}} < \ln \hat{y}^i(\alpha) + \varepsilon^i_{\text{ANN}} + \varepsilon^{\gamma}_{\text{ANN,stat}}] \tag{17}$$

5. Repeat the steps 1-4 for different α values.

$P_{\mathrm{MC}}(\alpha)$ can be compared with $P_f(\alpha)$ to confirm the assumption of log-normality of the fragility curve. For the purpose of simplicity, the adapted Reg and MC methods in the ANN-based fragility analysis are denoted as 'Modified Reg' and 'Modified MC', respectively. In the sequel, the described methodology is illustrated with an industrial test case studied in the KARISMA benchmark.

4. Case Study: KARISMA benchmark

4.1. Kashiwazaki-Kariwa FEM Analysis

In 2007, the Japanese Kashiwazaki-Kariwa (K-K) NPP was affected by the Niigataken-Chuetsu-Oki earthquake (NCOE) with a magnitude $M_w = 6.6$ and an epicenter distance of 16 km. The structure of the K-K NPP is shown in Figure 6. In this paper, we are interested in the reliability of a hypothetical electrical cabinet located on the fifth floor of the Unit 7 reactor building of the NPP (Figure 6). The finite element model for the Unit 7 consists of 92,000 degrees of freedom with 10,700 nodes and 15,600 elements, including bar, beam, and different shell elements. The constitutive law of the materials is considered as linear. The NPP model is embedded 23 meters in the soil, which is accounted for in the SSI analysis. The structural analyses are carried out with Code_Aster, a finite element analysis open-source software developed by EDF group [48], while the soil part is solved with MISS based on the boundary element method (BEM) [49].

FEM analyses are performed according to the approach described in Section 3.1. 100 triplets of 3D synthetic ground motions are generated at the bedrock with $Vs_{30} = 720$ m/s and used for the uncertainty propagation. Given the NCOE scenario, the generation of the synthetic ground motions are based on scenario spectra predicted by the Campbell-Bozorgnia 2008 (C&B 2008) GMPE [46]. In order to obtain sufficient failure cases for the fragility analysis, the synthetic seismic motions at the bedrock are scaled with a factor of *three*. After analyses with ELM, 100 triplets of ground motions on the free surface and 100 degraded soil profiles are obtained.

The impedances of the soil and the seismic forces should have been computed for each soil profile using BEM. However, the high complexity of the embedded foundation makes it hard to achieve: it takes 24 hours to run the BEM simulation for one soil profile. In order to reduce the computational cost, the 3D seismic signals at the bedrock are regrouped into four soil classes according to their PGA values: i. PGA$\in$[0, 0.5g) ii. PGA$\in$[0.5g, 1.0g) iii. PGA$\in$[1.0g, 1.5g) iv. PGA$\in$[1.5g, $+\infty$). The degraded soil profiles are averaged within each class and four soil profiles are obtained to represent four different degradation levels. The SSI analyses are performed with the 100 ground motions on the free surface, as well as the impedances and seismic forces calculated from the four soil profiles, to compute the floor accelerations of the K-K NPP.

Anchorage failure of the electrical cabinet is considered in this study. The capacity is given by the floor spectral acceleration of the anchorage point around 4Hz, the assumed natural frequency of the cabinet. The maximum value of the floor spectral accelerations in the two horizontal directions, integrated over a frequency interval around 4Hz to account for the uncertainty, is defined as the DM y:

$$y = \max_{i=X,Y} \int_{3.5}^{4.5} S^e_{a,i}(f)\mathrm{d}f \tag{18}$$

where $S^e_{a,i}$ denotes the spectral acceleration of the electrical equipment in the i-th direction. Figure 7 shows the 100 calculated DMs as a function of the geometric mean of the PGAs of the horizontal seismic motions on the free surface.

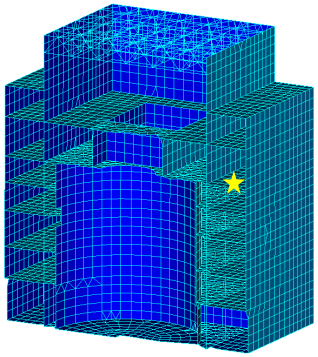

Figure 6: Location of the electrical cabinet in the K-K model (indicated by the star symbol)

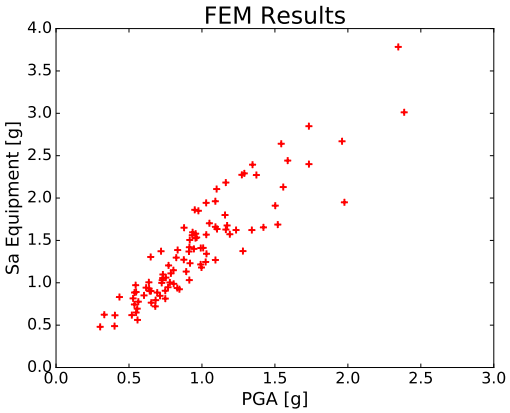

Figure 7: Point cloud of DMs (Eq. 18) calculated with FEM

4.2. Data Analysis

The 100 IMs-DM obtained from FEM simulations can be used for the construction and the training of the ANN metamodel. 8 classical IMs are chosen as candidates for the inputs of the ANN metamodel. The 8 IMs include the commonly used seismic intensity indicators PGA, PGV, PGD, $\mathrm{PS}_a(f_0)$, CAV, Arias intensity I_A, as well as the predominant period T_p used in [50] and the ASA proposed in [51]. These IMs are presented in detail in Table 1. The geometric means of IMs in the two horizontal directions are used as scalar IMs for 3D ground motions. The integration domain of the ASA is slightly modified compared to its initial definition in [51], to consider the uncertainty on the natural frequency of the electrical cabinet.

Table 1: Definitions of classical seismic intensity measures

Intensity Measures	Definitions	Comments
PGA (peak ground acceleration)	$\max \lvert a(t) \rvert$	$a(t)$: seismic acceleration
PGV (peak ground velocity)	$\max \lvert v(t) \rvert$	$v(t)$: seismic velocity
PGD (peak ground displacement)	$\max \lvert u(t) \rvert$	$u(t)$: seismic displacement
$\mathrm{PS}_a(f_0)$ (pseudo-spectral acceleration)	Spectral acceleration	f_0=4Hz, damping 5%
ASA (average spectral acceleration)	$\int_{3.5}^{4.5} \mathrm{PS}_a(f)\mathrm{d}f$	f: frequency
T_p (predominant period)	$\arg\max_T \mathrm{PS}_a(\frac{1}{T})$	$T = 1/f$
CAV (cumulative absolute velocity)	$\int_0^{t_{\max}} \lvert a(t) \rvert \mathrm{d}t$	$t_{\max}$: total seismic duration
I_A (Arias intensity)	$\frac{\pi}{2g} \int_0^{t_{\max}} a(t)^2 \mathrm{d}t$	$g = 9.81\mathrm{m/s}^2$

The correlation coefficients ρ between the eight IMs and the DM defined by 18 are listed in Table 2. It can be observed that, among all the eight chosen IMs, ASA is the most relevant IM to the DM, whereas there is a very weak correlation for T_p.

Table 2: Correlation coefficients between IMs and DM

Intensity Measures	PGA	PGV	PGD	PS_a	ASA	T_p	CAV	I_A
ρ	0.913	0.693	0.420	0.920	0.950	0.093	0.889	0.890

The statistical distributions of the eight selected IMs are examined to check their log-normality. The eight proposed IMs are normalized and compared to $\mathcal{N}(0,1)$. The normalization is realized by

$$\alpha_{\text{Norm}} = \frac{\ln \alpha - \mu_{\ln \alpha}}{\sigma_{\ln \alpha}} \tag{19}$$

where $\mu_{\ln \alpha}$ and $\sigma_{\ln \alpha}$ denote the mean and the Std of $\ln \alpha$, respectively. For simplicity of illustration, the probability plots of three IMs (PGA, ASA and I_A) are shown in Figure 8. Besides, the values of the coefficients of determination R^2 of the probability plots are given in Table 3, for all the eight IMs: the closer to the log-normal distribution the IM is, the closer to 1 the value of R^2 will be. It can be concluded that it is reasonable to apply the log-normal distribution model to all eight IMs.

This verification is performed because: i) For the selection of the subset of IMs in Section 3.2, the Cholesky factorization is executed on the covariance matrix of Gaussian random variables (RVs). As a result, if the IMs follow log-normal distributions, the Cholesky factorization can be directly applied to ln(IMs). ii) For the generation of IMs in the ANN simulation part in Section 3.5, one needs to know the marginal distribution of the IMs to be generated. In this way, it can be confirmed that the marginal distributions of the IMs are effectively log-normal. If the IMs are not log-normally distributed, an additional Nataf transformation [39] should be carried out, to transform arbitrary RVs to Gaussian RVs, in both Section 3.2 and Section 3.5.

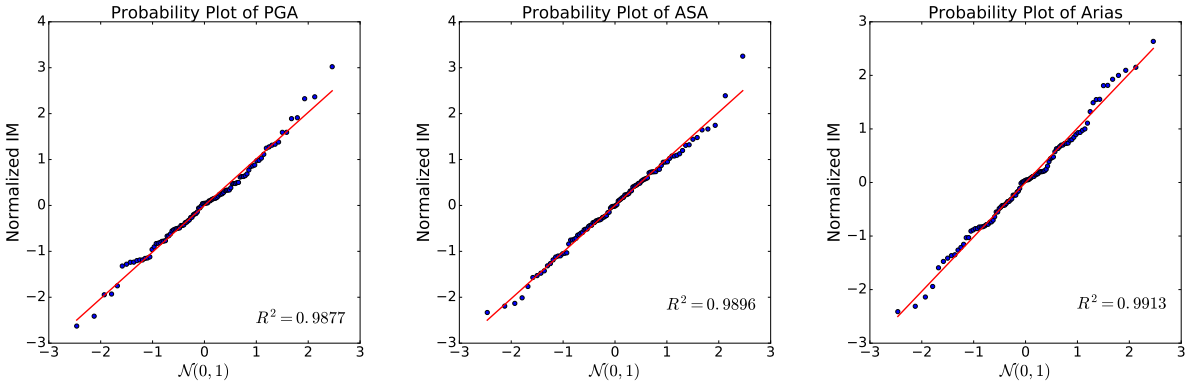

(a) Probability plot for PGA (b) Probability plot for ASA (c) Probability plot for I_A

Figure 8: Probability plots for PGA, ASA and I_A to check their log-normality

Table 3: Coefficients of determination of the probability plots

Intensity Measures	PGA	PGV	PGD	PS_a	ASA	T_p	CAV	I_A
R^2	0.9877	0.9970	0.9915	0.9866	0.9896	0.9823	0.9912	0.9913

4.3. Selection of Relevant IMs and Determination of ANN Structures

Feature selection. Due to the limited size of the data set (100 IMs-DM), it is necessary to apply feature selection to obtain a reliable ANN metamodel with good generalization capabilities. A very complex ANN with a large number of unknown weights can easily to be overfitted, given the underlying data set. The features (IMs) are selected with the SPCC filter approach proposed in Section 3.2. The result after the feature selection with SPCC is illustrated in Figure 9. From the forward selection result, ASA and I_A are

selected as the relevant features because the R^{SP} for the other IMs are less than 0.05, so that they can be regarded as non-influential if ASA and I_A have already been considered.

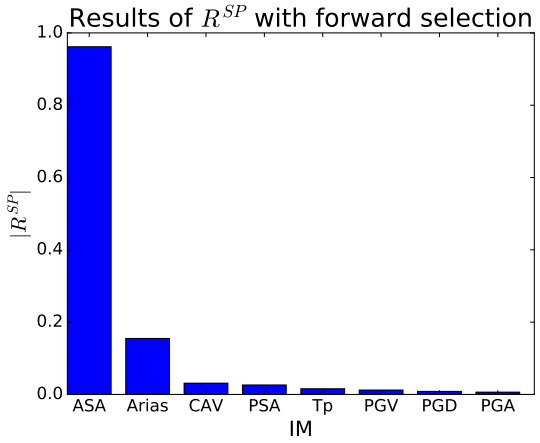

Figure 9: Results of forward selection

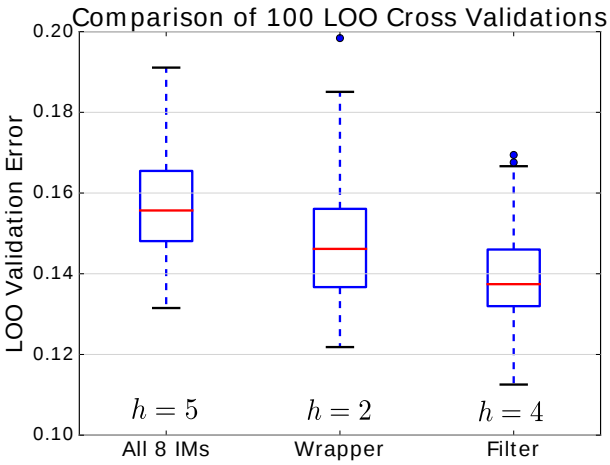

Figure 10: LOO cross-validation results for different ANNs

The number of the neurons h in the hidden layer should be determined additionally, because the filter approach only selects the most relevant feature subset. For this purpose, the total set of 100 data is separated into 2 subsets: 80 data for training and cross-validation (T-CV data), and 20 data for test. The 20 test data are not used to determine the structure of the ANN, but used later in Section 4.4 to evaluate the generalization capacity of the trained ANN. 4-fold cross-validation based on 80 T-CV data is executed on ANNs with $h = 1, 2, \ldots 8$ of hidden neurons, respectively, in order to select the optimal number: The ANN structure with the smallest 4-fold cross-validation error is chosen for the final metamodel. The optimal value of h determined by the described approach is 4.

Comparison of selected features. We compare our results to the features selected with the wrapper approach based on GA used in [23]. The final feature subset selected by GA is ASA and CAV, with $h = 2$ in the hidden layer. It can be observed that both approaches select similar seismic IMs: ASA, the most efficient IM in this study (Table 2), and an IM concerning the integration of the ground motion acceleration over the signal duration (I_A or CAV).

In order to highlight the necessity of the feature selection, the leaving-one-out (LOO) cross-validation is carried out with the ANN structures determined by the feature selection procedures, as well as the ANN without dimensionality reduction (i.e. with all eight IMs. The number of hidden nodes is $h = 5$). With random initializations of ANN weighting parameters, 100 LOO cross-validations have been performed. The box-plot of the LOO cross-validation error is shown in Figure 10. From the results, one can observe that the ANN models determined by feature selections show more accuracy. In addition, the ANN model with the filter approach performs best in the LOO cross-validation.

Therefore, in the sequel of this paper, the ANN is trained with two inputs (ASA and I_A), four hidden layer nodes and one output, which is computed according to Eq. 18. The trained ANN is used for all runs of ANN simulations. Point clouds and fragility curves will be plotted with ASA, which is the most efficient IM in this study.

4.4. Results of the ANN Training

Training results. Training based on the back-propagation algorithm is carried out with the ANN structure determined by the filter approach. The ANN toolbox used in this study is an open-source python package 'Neurolab' with the self-implemented delta method for the quantification of ANN prediction uncertainties. The 80 T-CV data in Section 4.3 is again divided into 2 subsets: 60 data for training and 20 data for validation. Early stopping is applied on the validation set to avoid overfitting. The generalization capacity of the ANN is examined on the 20 test data. The ANN is trained in *log-log space*. The results of the ANN training, as well as the point clouds of the ANN outputs $\hat{y}$ of the test data are shown in Figure 11 and Figure 12. From Figure 11, one can conclude that the training results are satisfactory. Most of the results in the 'prediction-target' space are located in the neighborhood of the dashed diagonal line. The ANN prediction results for the test data set in Figure 12 reveal a globally satisfactory prediction quality: the ANN predictions remain coherent with the FEM results. In fact, with a regression model like ANN, it is not possible to obtain the exact prediction results. In addition, it has to be pointed out that the dispersion of the ANN predictions is reduced compared to the FEM results. This is due to the loss of the aleatory uncertainty by reducing ground motions to two IMs in the ANN metamodeling. The underestimated variability in the ANN predictions will reduce the uncertainty in the fragility curve. The histogram of the normalized ANN training residuals is plotted in Figure 13. It can be observed that its distribution is close to $\mathcal{N}(0,1)$, so that the assumption of normality of the ANN residuals in the delta method can be considered reasonable in this study.

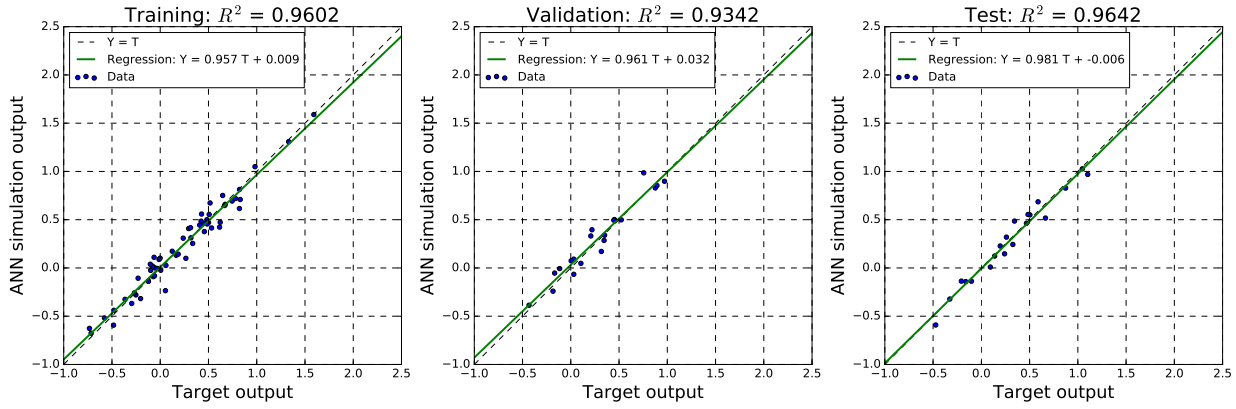

(a) Training set (b) Validation set (c) Test set

Figure 11: ANN training results

Comparison with other metamodels. The training results of the ANN are compared with those of other metamodels, including Kriging with Gaussian kernel (an interpolation model), Kriging with Gaussian and White noise kernel (a regression model) and quadratic response surface. The metamodels are constructed with 80 T-CV data and tested on 20 test data, using the python toolbox scikit-learn. The RMSE between metamodel predictions and FEM outputs is used to evaluate the accuracy of the different metamodels. The seismic IMs used are ASA and I_A, the same used for the ANN. The results are reported in Table 4.

Several conclusions can be drawn from Table 4: i) Kriging interpolation is not an appropriate metamodel for this study, since the test error is much larger than other models. The reason has already been discussed

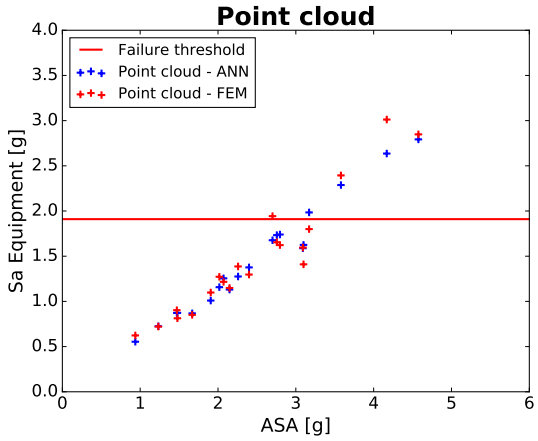

Figure 12: ANN test point cloud

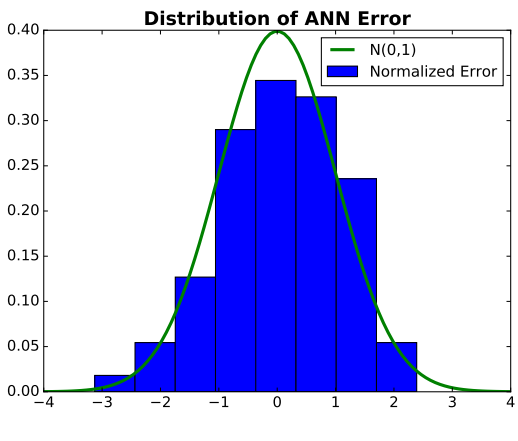

Figure 13: Distribution of ANN training residuals

Table 4: Training and test results for different metamodels

Model	RMSE Training (80 data)	RMSE Test (20 data)
ANN	0.141	0.135
Kriging interpolation (Gaussian kernel)	0	0.43
Kriging regression (Gaussian+White noise kernel)	0.153	0.145
Quadratic response surface	0.151	0.151

in Section 2.1: the zero residual in the training of Kriging overfits the model. The generalization capability of the interpolation Kriging model is thus very limited with the underlying data. ii) Once the residual is present in the training data of the Kriging regression, the performance of the Kriging is largely improved. iii) Quadratic response surface offers less nonlinearity than ANN, which is why its errors are larger. iv) Overall, ANN shows slightly better performance than other considered metamodels.

Consideration of ANN prediction uncertainties. The ANN model is validated in the previous subsections. Let us show in this part the necessity of the incorporation of the σ_{ANN} in the fragility curves. We focus on the 80 T-CV data used to train the ANN. Based on the same 80 seismic inputs, one can obtain 80 structural outputs y and $\hat{y}$, from FEM and ANN simulations respectively. Fragility curves are computed with Reg method (Eq. 7) for data set (α, y) and $(\alpha, \hat{y})$. MC method could have also been used for FEM results. However, the high complexity of the K-K model makes it very difficult to perform adequate FEM simulations for the MC estimation. This is also one of the main motivations to construct a metamodel in this study: the metamodel provides the possibility to conduct a non-parametric fragility analysis. The fragility curves are calculated for $\alpha =$ASA and $\alpha = I_A$, respectively, in order to provide further discussions. At the same time, the 'modified Reg' method (Eq. 15) is applied to the data set $(\alpha, \hat{y})$ to compute fragility curves, accounting for the aleatory residual uncertainty of the ANN predictions. From Figure 14, it can be seen that:

- A clear difference between the fragility curves computed with FEM Reg and ANN Reg can be observed. The difference is much less evident for I_A than ASA. Nevertheless, this is not due to the fact that the ANN metamodel is poorly calibrated, because the ANN accuracy has been validated above and it is even better than other possible metamodels. If the fragility curves calculated with Reg method are not coherent for the training data between FEM and ANN, one can hardly trust the conditional probability of failure computed

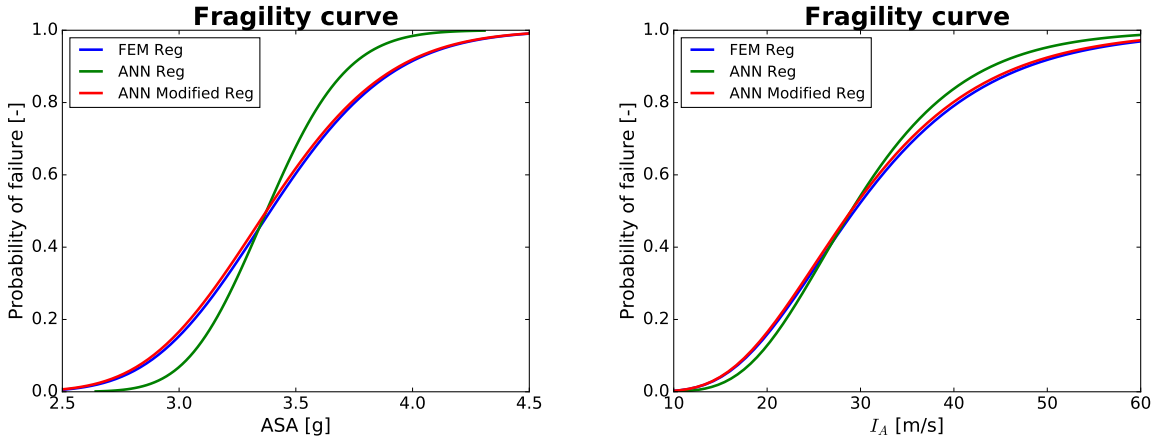

(a) Fragility curves computed with 80 T-CV data as function of ASA

(b) Fragility curves computed with 80 T-CV data as function of I_A

Figure 14: Fragility curves computed with 80 T-CV data

with the ANN based on other test data.

- The difference is due to the aleatory part of the ANN prediction uncertainty σ_{ANN}. It represents the seismic inherent randomness not identified in the inputs (ASA and I_A) of the ANN metamodel. Once σ_{ANN} is integrated in the computation of the conditional probability with Eq. 15 , the computed fragility curves almost coincide with the FEM Reg curves, for both ASA and I_A.

- σ_{ANN} has less influence when the fragility curves are plotted for I_A. It is because I_A is less correlated to the output than ASA (Table 2). Consequently, $\beta^{\text{ANN}}_{R|I_A}$, which equals 0.326, is larger than $\beta^{\text{ANN}}_{R|ASA}$ (0.079), whereas σ_{ANN} (0.094) stays the same. Considering Eq. 15, the impact of σ_{ANN} is less evident on the I_A curves than the ASA curves.

These analyses show the importance of the consideration of σ_{ANN} in the computation of the fragility curves, where DM results are provided by ANN simulations. Otherwise, the uncertainty in the fragility curves will be underestimated.

Besides, $\sigma_{\text{ANN,stat}}$ of the test data is also computed. Among the 20 test data, the positions of the first four data with the highest $\sigma_{\text{ANN,stat}}$ values are visualized in the input space in Figure 15. The numbers in the figure show the rank of their $\sigma_{\text{ANN,stat}}$ values in the 20 test data: '1' for the point with the highest $\sigma_{\text{ANN,stat}}$ value, '2' for the second highest, etc. It can be observed that the test data with high values of $\sigma_{\text{ANN,stat}}$ are located either at the lower boundary of the training data, or at the places where the training data are sparse, which is coherent with the property of $\sigma_{\text{ANN,stat}}$ shown in Figure 5.

4.5. Fragility Curves

After being trained, the ANN can be used to carry out fast-running simulations. For this purpose, a large number of seismic IMs have to be generated to represent the seismic motions. In this paper, the following statistical properties of the log-normal distributions of ASA and I_A are obtained from the 100 triplets of seismic signals on the free surface (Table 5). The assumption of log-normality of the selected IMs has been validated in Section 4.2. With the large number of simulation results provided by the ANN, both methods

presented in Section 3.5 can be applied for the computation of fragility curves.

Table 5: Statistics of ASA and I_A on the free surface

IM	Median	Log. standard deviation	ρ (ASA-I_A)
ASA [g]	2.28	0.417	0.846
I_A [m/s]	13.13	0.842	

For the log-normal based fragility curve, 10,000 ASA-I_A samples are generated with the statistics in Table 5. 10,000 ANN simulations are performed with these generated IMs, and the conditional probability of failure is computed with Eq. 15. The computed fragility curve is described by ASA with median capacity $3.32g$ and uncertainty $\beta_{\text{Total}} = 0.127$, including $\sigma_{\text{ANN}} = 0.094$.

The pointwise fragility analysis is performed by conditional sampling of I_A for a given value of ASA, since a conditional bivariate normal distribution is also normally distributed. In the analysis, the values of ASA are selected in $[2.2g, 4.4g]$ with $\Delta\text{ASA} = 0.1g$. For every ASA value, 10,000 I_A are generated. At every ASA, the probability of failure is computed from Eq. 16, and the CIs are determined with Eq. 17. Fragility curves computed with both methods are shown in Figure 16.

Regarding the fragility curves, although there exist some differences between the log-normal based fragility curve and the MC estimation, the log-normal curve stays coherent with the pointwise MC curve. The log-normal assumption can be thus confirmed in this study. It is recalled that the source of the confidence intervals comes only from the paucity of the training data of the ANN.

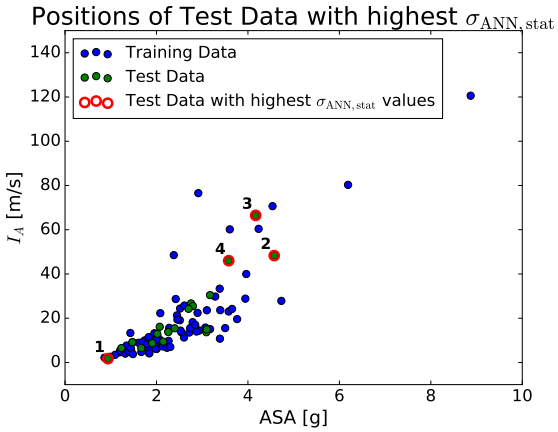

Figure 15: Positions of test data with highest $\sigma_{\text{ANN,stat}}$

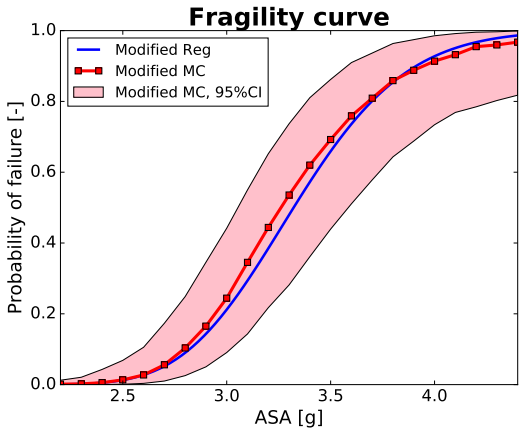

Figure 16: Fragility curves with ANN

4.6. Discussions

The proposed ANN-based fragility analysis has been applied to the K-K NPP to compute the fragility curve of an electrical cabinet. The assumptions made in this methodology are discussed what follows. The computational cost of the FEM analyses is also provided.

1. This study only considers seismic randomness in the FEM simulation. Uncertainties on structural parameters are not modeled. With other source of uncertainties, the seismic IM is less correlated to the structural output, so that the influence of the aleatory component of the metamodel uncertainty is less evident.

2. Moreover, the variability in the responses of the considered electrical cabinet is dominated by the seismic record-to-record randomness. To justify this, the material uncertainties of concrete in Table 6 is considered for the first 50 seismic excitations. The values of the coefficients of variation of Table 6 are selected according to our expertise. The log-normal model of the material parameters has been suggested and used in [3, 52, 24, 15, 27]. Additionally, the log-normal distribution can ensure that all the values of material parameters are positive, in particular for small value parameters, such as the Poisson's ratio and the modal damping ratio. 50 FEM simulations are performed with the material uncertainties, with the stochastic values of Table 6 applied to the entire structure. The material parameters do not vary for elements within the structure. The corresponding fragility curve is computed with Reg method. Meanwhile, a fragility curve is calculated also with Reg method based on the first 50 FEM simulation results of this study (i.e. without the consideration of material uncertainties). Seismic excitations for both cases remain the same. The comparison of two fragility curves is shown in Figure 17. It can be clearly observed that there is no obvious difference between the two fragility curves, which implies that the impact of the material randomness can be neglected compared to the earthquake randomness. That is another reason why material uncertainties are not modeled in this study. With uncertainty uniquely from seismic ground motions, the selection of IMs becomes therefore crucial to ensure the accuracy of the ANN.

Table 6: Uncertainties in material parameters of concrete in K-K NPP

Material parameters	Distribution	Median	Coefficient of variation
Young's modulus	Log-normal	31,300 MPa	0.2
Poisson ratio	Log-normal	0.2	0.1
Density	Log-normal	2500 kg/m^3	0.05
Modal damping ratio	Log-normal	0.05	0.4

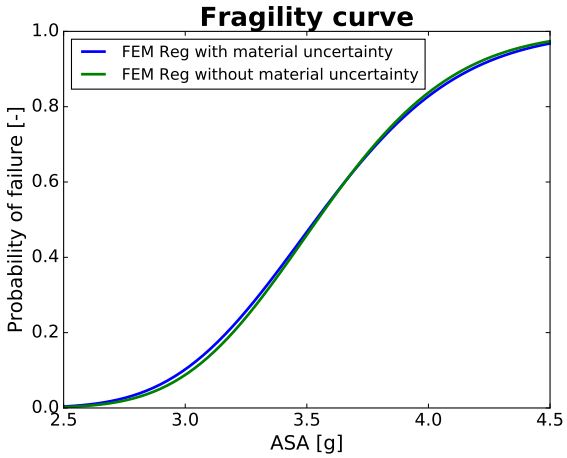

Figure 17: Comparison between fragility curves with or without material uncertainties

3. The ANN training errors are assumed to follow a normal distribution. The validity of this assumption is confirmed in this study. In addition, with a more mathematically rigorous derivation, the ANN prediction uncertainty should have followed a student t distribution. This approximation by a normal distribution allows the decomposition of the ANN prediction uncertainty into two normal aleatory and

epistemic components.

4. The computational cost of the FEM simulations is listed in Table 7. Based on the soil impedances computed by BEM, one single FEM analysis takes $(120.02 + 66.86)/100 = 1.87$ hours on an Intel Xeon E5-2600V2 CPU of 2.7GHz, which makes it almost unaffordable to run a large number of FEM simulations for the pointwise MC fragility analysis. However, once the ANN metamodel is established, the pointwise MC fragility analysis can be conducted within 0.25 hours. It has to be noticed that the ANN metamodel is constructed from the results of 100 FEM simulations, which means that $132.41 + 120.02 + 66.86 = 319.29$ hours of mechanical simulations are the prerequisites for the ANN metamodel construction.

Table 7: Computational cost for numerical analyses

Type of analyses	Number of analyses	Total computational time
BEM for soil impedances	4	132.41 hours
ELM analyses	100	120.02 hours
SSI analyses	100	66.86 hours
ANN simulations for MC fragility analysis	10,000 × 23	0.25 hours

5. The applicability of the methodology is not limited to the K-K NPP case study. It can be generalized to other structures, by adopting a proper FEM analysis for the structures in question. The same procedure from Section 3.2 to Section 3.5 can be applied to conduct the fragility analysis. However, one should pay attention to the log-normal hypothesis made in the feature selection (Section 3.2) and generation of IMs (Section 3.5). If the log-normal assumption were not valid, an additional Nataf transformation [39] of the probability distribution would have to be performed, to transform arbitrary RVs to Gaussian RVs. It is also worth emphasizing that this methodology is not restricted to ANNs: the filter feature selection is independent of the metamodel; the delta method can also be applied to other models (e.g. polynomial response surfaces) to evaluate the metamodel uncertainty. The only difference is the way to compute the gradient.

5. Summary & Conclusions

A methodology of ANN metamodels for the computation of fragility curves has been proposed in this paper. The ANN metamodel is utilized to build the statistical relation between the seismic intensity measures and the structural response. Once trained, the ANN metamodel allows carrying out a large number of simulations for both parametric and non-parametric fragility analyses, at negligible computational cost. Based on FEM simulation results, this methodology mainly consists of:

- Selection of the most relevant seismic intensity measure features. A filter approach based on semi-partial correlation coefficients is proposed in this study. It is compared with a wrapper approach based on GA. In the case study considered, the filter selection method shows slightly more advantages, in terms of accuracy and efficiency. Once the features have been retained, the ANN is trained with early stopping to prevent overfitting.

- Identification of the aleatory uncertainty and the epistemic uncertainty components in the ANN prediction uncertainties. The aleatory uncertainty is incorporated in the fragility curve, while the epistemic

uncertainty is used to compute the confidence intervals.

- Computation of fragility curves and their confidence intervals, with both log-normal assumption and pointwise MC methods. The Reg and MC methods are adapted to take into account the ANN prediction uncertainties. The non-parametric MC fragility curve is used to verify the log-normal assumption, which is widely adopted in the fragility analysis.

Instead of methods based on repeated ANN trainings realized in [31], more efficient algorithms for the feature selection and the ANN prediction uncertainty quantification have been applied. Moreover, the ANN prediction uncertainty has been discussed thoroughly. This methodology has been applied to an industrial complex case study, i.e. Kashiwazaki-Kariwa nuclear power plant in Japan to evaluate the robustness of an electrical cabinet. The fragility curve computed with the log-normal assumption is described by ASA with median capacity $3.32g$ and uncertainty $\beta_{\text{Total}} = 0.127$. In addition, compared to the results of the pointwise MC estimation in this study, it is reasonable to assume a log-normal distribution for the fragility curves.

Acknowledgement

The authors want to thank the two anonymous reviewers for their valuable comments to this work. The contribution of this work is incorporated in the project NARSIS H2020 (New Approach to Reactor Safety ImprovmentS, Horizon 2020).

References

[1] EPRI, Seismic probabilistic risk assessment implementation guide, Tech. rep., Electric Power Research Institute EPRI, Palo Alto, CA, report 1002989 (2013).

[2] EPRI, Methodology for developing seismic fragilities, Tech. rep., Electric Power Research Institute EPRI, Palo Alto, CA, report TR-103959 (1994).

[3] R. Kennedy, C. Cornell, R. Campell, S. Kaplan, H. Perla, Probabilistic seismic safety study of an existing nuclear power plant, Nucl. Eng. Des. 59 (1980) 315–338. doi:10.1016/0029-5493(80)90203-4.

[4] C. Mai, K. Konakli, B. Sudret, Seismic fragility curves for structures using non-parametric representations, Front. Struct. Civ. Eng. 11 (2017) 169186. doi:10.1007/s11709-017-0385-y.

[5] I. Zentner, M. Gündel, N. Bonfils, Fragility analysis methods: Review of existing approaches and application, Nucl. Eng. Des.In press. doi:10.1016/j.nucengdes.2016.12.021.

[6] H. Y. Noh, D. Lallemant, A. S. Kiremidjian, Development of empirical and analytical fragility functions using kernel smoothing methods, Earthquake Eng. Struct. Dyn. 44 (2015) 1163–1180. doi:10.1002/eqe.2505.

[7] D. Lallemant, A. Kiremidjian, H. Burton, Statistical procedures for developing earthquake damage fragility curves, Earthquake Eng. Struct. Dyn. 44 (2015) 13731389. doi:10.1002/eqe.2522.

[8] M. Shinozuka, M. Q. Feng, J. Lee, T. Naganuma, Statistical analysis of fragility curves, J. Eng. Mech. 126 (2000) 1224–1231. doi:10.1061/(ASCE)0733-9399(2000)126:12(1224).

[9] I. Gidaris, A. A. Taflanidis, G. P. Mavroeidis, Kriging metamodeling in seismic risk assessment based on stochastic ground motion models, Earthquake Eng. Struct. Dyn. 44 (2015) 2377–2399. doi:10.1002/eqe.2586.

[10] C. A. Cornell, F. Jalayer, R. O. Hamburger, D. A. Foutch, Probabilistic basis for 2000 SAC federal emergency management agency steel moment frame guidelines, J. Struct. Eng. 128 (2002) 526–533. doi:10.1061/(ASCE)0733-9445(2002)128:4(526).

[11] M. Perrault, Evaluation de la vulnérabilité sismique de bâtiments à partir de mesures in situ, Ph.D. thesis, Université de Grenoble (2013).

[12] H. Xu, P. Gardoni, Probabilistic capacity and seismic demand models and fragility estimates for reinforced concrete buildings based on three-dimensional analyses, Eng. Struct. 112 (2016) 200–214. doi:10.1016/j.engstruct.2016.01.005.

[13] I. Zentner, E. Borgonovo, Construction of variance-based metamodels for probabilistic seismic analysis and fragility assessment, Georisk 8 (2014) 202–216. doi:10.1080/17499518.2014.958173.

[14] V. U. Unnikrishnan, A. M. Prasad, B. N. Rao, Development of fragility curves using high-dimensional model representation, Earthquake Eng. Struct. Dyn. 42 (2013) 419–430. doi:10.1002/eqe.2214.

[15] N. Buratti, B. Ferracuti, M. Savoia, Response surface with random factors for seismic fragility of reinforced concrete frames, Struct. Saf. 32 (2010) 42–51. doi:10.1016/j.strusafe.2009.06.003.

[16] J. Seo, D. G. Linzell, Use of response surface metamodels to generate system level fragilities for existing curved steel bridges, Eng. Struct. 52 (2013) 642–653. doi:10.1016/j.engstruct.2013.03.023.

[17] J. Seo, L. Dueas-Osorio, J. I. Craig, B. J. Goodno, Metamodel-based regional vulnerability estimate of irregular steel moment-frame structures subjected to earthquake events, Eng. Struct. 45 (2012) 585–597. doi:10.1016/j.engstruct.2012.07.003.

[18] S. K. Saha, V. Matsagar, S. Chakraborty, Uncertainty quantification and seismic fragility of base-isolated liquid storage tanks using response surface models, Probab. Eng. Mech. 43 (2016) 20–35. doi:10.1016/j.probengmech.2015.10.008.

[19] J. Park, P. Towashiraporn, Rapid seismic damage assessment of railway bridges using the response-surface statistical model, Struct. Saf. 47 (2014) 1–12. doi:10.1016/j.strusafe.2013.10.001.

[20] N. D. Lagaros, M. Fragiadakis, Fragility assessment of steel frames using neural networks, Earthquake Spectra 23 (2007) 735–752. doi:10.1193/1.2798241.

[21] N. D. Lagaros, Y. Tsompanakis, P. N. Psarropoulos, E. C. Georgopoulos, Computationally efficient seismic fragility analysis of geostructures, Comput. Struct. 87 (2009) 1195–1203. doi:10.1016/j.compstruc.2008.12.001.

[22] C. C. Mitropoulou, M. Papadrakakis, Developing fragility curves based on neural network IDA predictions, Eng. Struct. 33 (2011) 3409–3421. doi:10.1016/j.engstruct.2011.07.005.

[23] E. Ferrario, N. Pedroni, E. Zio, F. Lopez-Caballero, Application of metamodel-based techniques for the efficient seismic analysis of structural systems, in: Safety and Reliability of Complex Engineered Systems, ESREL, 2015, pp. 1193–1200.

[24] A. Calabresea, C. G. Lai, Fragility functions of blockwork wharves using artificial neural networks, Soil Dyn. Earthquake Eng. 52 (2013) 88–102. doi:10.1016/j.soildyn.2013.05.002.

[25] S. Mangalathu, J.-S. Jeon, R. DesRoches, Critical uncertainty parameters influencing seismic performance of bridges using lasso regression, Earthquake Eng. Struct. Dyn.doi:10.1002/eqe.2991.

[26] P. Gehl, D. D'Ayala, Development of bayesian networks for the multi-hazard fragility assessment of bridge systems, Struct. Saf. 60 (2016) 3746. doi:10.1016/j.strusafe.2016.01.006.

[27] J. Ghosh, J. E. Padgett, L. Dueas-Osorio, Surrogate modeling and failure surface visualization for ef ficient seismic vulnerability assessment of highway bridges, Probab. Eng. Mech. 34 (2013) 189–199. doi:10.1016/j.probengmech.2013.09.003.

[28] G. Jia, A. A.Taflanidis, Kriging metamodeling for approximation of high-dimensional wave and surge responses in real-time storm/hurricane risk assessment, Comput. Methods in Appl. Mech. Eng. 261–262 (2013) 24–38. doi:10.1016/j.cma.2013.03.012.

[29] C. V. Mai, M. D. Spiridonakos, E. N. Chatzi, B. Sudret, Surrogate modelling for stochastic dynamical systems by combining narx models and polynomial chaos expansions, International Journal for Uncertainty Quantification 6 (2016) 419–430. doi:10.1615/Int.J.UncertaintyQuantification.v6.i4.

[30] N. Ataei, J. E. Padgett, Fragility surrogate models for coastal bridges in hurricane prone zones, Eng. Struct. 103 (2015) 203–213. doi:10.1016/j.engstruct.2015.07.002.

[31] E. Ferrario, N. Pedroni, E. Zio, F. Lopez-Caballero, Bootstrapped artificial neural networks for the seismic analysis of structural systems, Struct. Saf. 67 (2017) 70–84. doi:10.1016/j.strusafe.2017.03.003.

[32] P. Towashiraporn, Building seismic fragilities using response surface metamodels, Ph.D. thesis, Georgia Institute of Technology (2004).

[33] C. M. Bishop, Neural Networks for Pattern Recognition, Oxford University Press, 1995.

[34] R. D. Reed, R. J. Marks, Neural Smithing, MIT Press, 1999.

[35] IAEA, Review of seismic evaluation methodologies for nuclear power plants based on a benchmark exercise, Tech. rep., International Atomic Energy Agency (2013).

[36] B. R. Ellingwood, K. Kinali, Quantifying and communicating uncertainty in seismic risk assessment, Struct. Saf. 31 (2009) 179–187. doi:10.1016/j.strusafe.2008.06.001.

[37] N. Yoshida, S. Kobayashi, I. Suetomi, K. Miura, Equivalent linear method considering frequency dependent characteristics of stiffness and damping, Soil. Dyn. Earthq. Eng. 22 (2002) 205–222. doi:10.1016/S0267-7261(02)00011-8.

[38] R. Kohavi, G. H. John, Wrappers for feature subset selection, Artificial Intelligence 97 (1997) 273–324. doi:10.1016/S0004-3702(97)00043-X.

[39] O. Ditlevesen, H. Madsen, Structural Reliability Methods, 2005.

[40] D. Rumelhart, G. Hinton, R. Williams, Learning Internal Representations by Error Propagation in Parallel Distributed Processing: Explorations in the Microstructure of Cognition, The MIT Press, 1986.

[41] N. Pedroni, E. Zio, G. Apostolakis, Comparison of bootstrapped artificial neural networks and quadratic response surfaces for the estimation of the functional failure probability of a thermalhydraulic passive system, Reliab. Eng. Syst. Safe. 95 (2010) 386–395. doi:10.1016/j.ress.2009.11.009.

[42] E. Zio, A study of the bootstrap method for estimating the accuracy of artificial neural networks in predicting nuclear transient processes, IEEE T. Nucl. Sci. 53 (2006) 1460–1478. doi:10.1109/TNS.2006.871662.

[43] I. Rivals, L. Personnaz, Construction of confidence intervals for neural networks based on least squares estimation, Neural Networks 13 (2000) 463–484. doi:10.1016/S0893-6080(99)00080-5.

[44] G. Chryssoloiuris, M. Lee, A. Ramsey, Confidence interval prediction for neural network models, IEEE T. Neural Networ. 7 (1996) 229–232. doi:10.1109/72.478409.

[45] R. Dybowski, S. J. Roberts, Confidence intervals and prediction intervals for feed-forward neural networks, in: R. Dybowski, V. Gant (Eds.), Clinical Applications of Artificial Neural Networks, Cambridge University Press, 2001, pp. 298–326. doi:10.1016/S0933-3657(02)00081-7.

[46] K. W. Campbell, Y. Bozorgnia, NGA ground motion model for the geometric mean horizontal component of PGA, PGV, PGD and 5% damped linear elastic response spectra for periods ranging from 0.01 to 10 s, Earthquake Spectra 24 (2008) 139–171. doi:10.1193/1.2857546.

[47] J. W. Baker, Correlation of ground motion intensity parameters used for predicting structural and geotechnical response, in: Proceedings of the 10th International Conference on Applications of Statistics and Probability in Civil Engineering, Tokyo, 2007.

[48] Code_Aster, opensource Finite Element code, http://www.code-aster.org.

[49] MISS, a software in earthquake engineering and structural dynamics, http://www.mssmat.ecp.fr/miss.

[50] J. P. Stewart, S.-J. Chiou, J. D. Bray, R. W. Graves, P. G. Somerville, N. A. Abrahamson, Ground motion evaluation procedures for performance-based design, Tech. rep., Pacific Earthquake Engineering Research Center (2001).

[51] M. D. Biasio, S. Grange, F. Dufour, F. Allain, I. Petre-Lazar, Intensity measures for probabilistic assessment of non-structural components acceleration demand, Earthquake Eng. Struct. Dyn. 44 (2015) 2261–2280. doi:10.1002/eqe.2582.

[52] A. B. Liel, C. B. Haselton, G. G. Deierlein, J. W. Baker, Incorporating modeling uncertainties in the assessment of seismic collapse risk of buildings, Struct. Saf. 31 (2009) 197–211. doi:10.1016/j.strusafe.2008.06.002.

Paper II : Wang, Z., Zentner, I., and Zio, E. (2018). A Bayesian framework for estimating fragility curves based on seismic damage data and numerical simulations by adaptive neural networks. *Nucl. Eng. Des.*, 338:232-246

A Bayesian framework for estimating fragility curves based on seismic damage data and numerical simulations by adaptive neural networks

Zhiyi Wang[a,b,c,1,*], Irmela Zentner[a,b], Enrico Zio[c,d]

[a] *EDF Lab Saclay, France*
[b] *Institute for Mechanical Sciences and Industrial Applications, UMR 9219 CNRS-EDF-CEA-ENSTA ParisTech, France*
[c] *Chair on Systems Science and Energetic Challenge, European Foundation for New Energy of EDF, CentraleSupélec, Université Paris-Saclay, France*
[d] *Energy Department, Politecnico di Milano, Italy*

Abstract

In seismic risk assessment, the fragility curve is used to estimate the reliability of structures and equipment under seismic loads. The shape of fragility curves is usually approximated by the cumulative distribution function of a lognormal distribution. The estimation of the parameters of the fragility curves requires gathering different sources of information and quantifying the uncertainties coming from these sources. This paper proposes a methodology for the computation of fragility curves for nuclear power plant equipment, based on a Bayesian updating framework that combines the results of numerical simulations and damage data. An artificial neural network is trained iteratively by optimizing its prediction uncertainties over the ground motion sample space, and it is used to conduct numerical simulations. The results of the numerical simulations provide a prior estimation of the seismic capacity of the equipment. The estimation of the uncertainty related to the equipment capacity is taken from the literature. Damage data, collected from the in-situ observation and the database of the seismic qualification utility group (SQUG), are used to construct the likelihood function for the Bayesian updating. The posterior equipment capacity is evaluated by Markov chain Monte Carlo simulation and posterior fragility curves are, then, obtained. The main contributions of the work are: (i) proposal of an adaptive training algorithm of artificial neural networks to improve the design of experiments for finite element simulations; (ii) proposal of a two-step transformation method to construct the likelihood function with existing damage data from the SQUG database. The methodology is applied to compute the fragility curves of a low-voltage switchgear of a nuclear power plant, within the so-called KARISMA benchmark.

Keywords: Seismic fragility curve; Bayesian updating; Artificial neural networks; Damage data; Uncertainty

1. Introduction

Seismic probabilistic risk assessment (SPRA) is a widely applied approach to estimate the seismic risk of critical structures, such as nuclear power plants (NPPs). In the framework of SPRA, fragility analysis is conducted to evaluate the fragility curves, i.e. the conditional probabilities of failure of structures or components at given values of the seismic intensity measure (IM), e.g. the peak ground acceleration (PGA).

*Corresponding author
[1] 7 boulevard Gaspard Monge, 91120 Palaiseau, France.

The computation of fragility curves is typically realized by statistical analysis based on different sources of information, including expert judgments, numerical simulations, empirical damage data.

The safety factor method (Kennedy et al., 1980; EPRI, 1994), largely used in nuclear engineering, depends on safety margins determined from simplified structural analyses and experimental data. Uncertainties are evaluated from expertise of engineers or results of qualification tests. The safety margins and their associated uncertainties are used to assess the seismic capacity of structures and equipment. This method does not require numerical simulations. However, the safety margins determined from the simplified approaches can be conservative, and thus, cannot offer a best estimate of the fragility curves.

Numerical simulations are commonly applied in the current practice of fragility analysis, e.g. by the finite element method (FEM) (Padgett and DesRoches, 2008; Ellingwood and Kinali, 2009; Zentner, 2010). Different sources of aleatory and epistemic uncertainties can be modeled and propagated through the numerical model. The conditional probability of failure can be computed either by pointwise Monte Carlo estimation or by assuming a parametric representation (e.g. lognormal) of fragility curves. The underlying parameters of the fragility curves are determined based on the results of the simulations. However, because of the high complexity of numerical models, the computational cost of the numerical analyses can be very high. One way to reduce the computational burden is to use fast-running statistical metamodels. Various types of metamodels have been tested and applied in fragility analysis, such as Kriging (Gidaris et al., 2015), artificial neural networks (ANNs) (Lagaros et al., 2009; Ferrario et al., 2017; Mangalathu et al., 2018; Wang et al., 2018), quadratic response surfaces (Towashiraporn, 2004), polynomial chaos expansion (Mai et al., 2016), among others. Nevertheless, due to the fact that a numerical model cannot contain all the structural details and damage mechanisms, damage data of structures and equipment can be used for a more accurate computation of fragility curves.

Damage data have been also widely used for seismic fragility analysis. The damage data are obtained either from post-earthquake observations or from qualification tests. They are used to describe the performance of structures or equipment under real seismic excitations. Fragility analysis is, then, conducted by statistical analysis of the damage data. For example, fragility curves for European-type reinforced concrete buildings are determined in Rossetto and Elnashai (2003) with earthquake observational data. Using Italian seismic damage data, fragility curves for different building typologies are built in Rota et al. (2008) to provide a reliable estimate of the vulnerability of structures of different classes. In these works, the fragility curves are obtained directly by fitting the damage data into a cumulative distribution function (CDF) of the lognormal distribution. Other studies adopt Bayesian statistics to estimate the fragility parameters (Straub and Kiureghian, 2008; Gardoni et al., 2009). In the Bayesian framework, prior distributions of the fragility parameters are assumed. Then, damage data are used to build the likelihood function. The fragility parameters can be generated by Markov chain Monte Carlo simulation (MCMC) (Hastings, 1970), based on the posterior distributions obtained from Bayesian updating. The advantage of the Bayesian statistics method is that it yields a probability distribution of the parameter to be estimated (so the confidence intervals can be computed), rather than a single value for the estimation of the parameter. Representative examples of the application of Bayesian statistics in seismic risk assessment can be found in Singhal and Kiremidjian (1998), Koutsourelakis (2010), Jalayer et al. (2010), EPRI (2014), Jaiswal et al. (2011), Beck and Taflanidis (2013),

Buratti et al. (2017), Noh et al. (2017), Jeon et al. (2017), EPRI (2017), among others.

The objective of this paper is to propose a framework to take into consideration both numerical simulation results and damage data in the computation of fragility curves. The methodology is divided into two parts: (i) estimation of the prior parameters with numerical simulations: to reduce the computational cost, an ANN metamodel is trained with an iterative active learning algorithm to substitute the computationally expensive FEM simulation; (ii) computation of the likelihood function with the damage data and execution of Bayesian updating to obtain the posterior distribution of the seismic capacity of the equipment. Different sources of uncertainties (aleatory and epistemic) are quantified and integrated in the computation of the fragility curves. Critical equipment of nuclear power plants are designed with high safety standards. The low probability of failure of the equipment may lead to a biased estimation of the fragility parameters, if the these parameters are solely determined by the maximum likelihood estimation (Shinozuka et al., 2000). This requires assessing the confidence associated to the estimation, which can be achieved in the Bayesian framework.

This paper is organized as follows. Section 2 describes the global methodology to account for different sources of information in the computation of fragility curves. It consists of the determination of the prior fragility curves with numerical simulations results and the Bayesian updating with damage data. In Section 3, the proposed methodology is applied to evaluate the robustness of a low-voltage switchgear located in the Kashiwazaki-Kariwa nuclear power plant in Japan. Final conclusions are given in Section 4.

2. Description of the Methodology

2.1. Seismic Fragility Curves

Fragility curves compute the conditional probability that the engineering demand parameter (EDP) exceeds a failure threshold, for a given seismic IM:

$$P_f(\alpha) = P(y > y_{\text{crit}}|\alpha) \tag{1}$$

where y is the EDP, such as inter-story drift, y_{crit} is the failure threshold and α represents the seismic IM. The lognormal fragility model proposed in Kennedy et al. (1980); Huang et al. (2011) is often applied in practice. In the lognormal assumption, the shape of the fragility curve is approximated by the CDF of a lognormal distribution:

$$P_f(\alpha) = \mathbf{\Phi}(\frac{\ln \alpha - \ln \hat{A}_m}{\beta_R}) \tag{2}$$

where $\mathbf{\Phi}(\cdot)$ is the CDF of the standard normal distribution $\mathcal{N}(0,1)$, $\hat{A}_m$ denotes the median capacity. The parameter β_R represents the aleatory uncertainty related to the inherent randomness. According to Kennedy et al. (1980); Basu et al. (2017), an epistemic uncertainty β_U, resulting from the lack of knowledge of the structural capacity, should be also considered:

$$\hat{A}_m \sim LogN(A_m, \beta_U^2) \tag{3}$$

where A_m is the median of the lognormal distribution and $LogN$ denotes a lognormal distribution. Consequently, the $\gamma \in [0,1]$ non-exceedance confidence interval of the fragility curves can be computed by (EPRI, 1994; Kwag et al., 2014; Zentner et al., 2017)

$$\tilde{P}_f(\alpha, \gamma) = \mathbf{\Phi}(\frac{\ln \alpha - \ln A_m + \beta_U \mathbf{\Phi}^{-1}(\gamma)}{\beta_R}) \tag{4}$$

Eq.4 allows computing the high confidence low probability of failure (HCLPF), defined as the capacity where the probability of failure reaches 5% with 95% confidence:

$$A_{\text{HCLPF}} = A_m e^{-1.645(\beta_R+\beta_U)} \tag{5}$$

The mean fragility curve, which considers both aleatory and epistemic uncertainties, is defined by

$$P_f^{\text{mean}}(\alpha) = \mathbf{\Phi}(\frac{\ln \alpha - \ln A_m}{\sqrt{\beta_R^2 + \beta_U^2}}) \tag{6}$$

The objective of the subsequent subsections is to describe the methodology to compute fragility curves for an equipment of interest located in a specific NPP structure, which is named 'target structure' in the sequel. The numerical model of the target structure is available. The general workflow of the proposed methodology is illustrated in Figure 1. In this framework, reference values of β_U^{prior} and y_{crit} are obtained from the literature. To better explain the methodology, we start with the determination of prior fragility parameters based on numerical simulation results. Bayesian updating and MCMC are, then, executed with damage data to obtain the posterior curves. The assumptions made in this methodology are:

1. The fragility curves in this paper are all calculated under lognormal distribution assumptions, namely (i) the fragility curves are computed by the lognormal CDFs (Eq.2) and (ii) the epistemic uncertainty is considered lognormally distributed (Eq.3), in order to facilitate the application of the Bayesian theorem based on the damage data.
2. The seismic record-to-record variability is considered as the only source of aleatory uncertainty.
3. PGA is the IM parameter used to compute the fragility curves, since most damage data are provided with given values of PGA.
4. Without different specification, the PGA used in the fragility curve stands for the PGA value of the ground motion on the soil free surface in the proximity of the target structure.

2.2. Determination of Prior Fragility Curve Parameters with Adaptive ANNs

Prior fragility curve parameters are determined based on the results of numerical simulations. FEM is one of the most widely used numerical methods for structural analysis. However, in case of a complex structure, the large number of degrees of freedom of the numerical model makes the resolution process highly computationally expensive. In this case, metamodels, calibrated from the existing simulation results, can be used to substitute the mechanical model, in order to improve the computational efficiency. The ANN is adopted in this paper because of its excellent universal approximation capability (Reed and Marks, 1999; Bishop, 1995).

In this subsection, the method to determine the parameters of prior fragility curves is explained. In order to improve the computational efficiency, ANNs are adopted in this paper to characterize the seismic IMs-EDP relation. With the adaptive enrichment, the quality of the training data is largely improved by reducing its scarcity in the design space. Therefore, less FEM numerical simulations are needed for the calibration of the ANN metamodel.

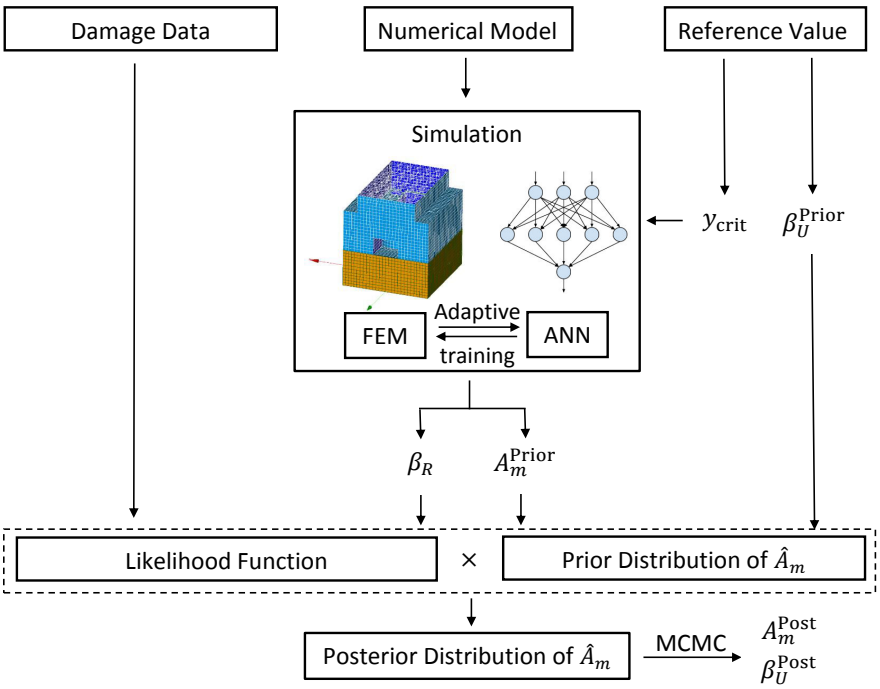

Figure 1: The Bayesian framework for fragility analysis

2.2.1. ANN training and prediction uncertainty

The objective of the application of adaptive ANNs is to establish a non-linear statistical regression model relating the seismic inputs and the EDP of interest:

$$\hat{y} = \hat{f}(\text{IM}_1, ..., \text{IM}_k) \tag{7}$$

where the symbol $\hat{}$ used in this paper denotes all the computation results relevant to ANNs: the non-linear regression model $\hat{f}$ constructed by ANNs and the EDP $\hat{y}$ computed with ANNs.

A classical feed-forward ANN consists of activation functions (linear functions, or non-linear hyperbolic tangent functions) and a set of weighting parameters $\boldsymbol{w}$ adjusted to minimize a cost function. The activation functions are connected by the weighted links in a layered structure. There are three types of layers: (i) input layer, which feeds the variables from which the ANN model is constructed; (ii) hidden layers, being single or multiple, to add parameters and nonlinearity; (iii) output layer, which provides the results of the ANN. The cost function E computes the square error between the ANN predictions $\hat{y}$ and the targets y (e.g. FEM simulation results), summed up over all training examples. The training of ANNs is typically realized by gradient-based algorithms to find the optimal weighting parameters. The gradient vector $\boldsymbol{g} = \dfrac{\partial E}{\partial \boldsymbol{w}}$ can be computed efficiently by the back-propagation algorithm (Rumelhart et al., 1986; Bishop, 1995). One can refer to Bishop (1995); Reed and Marks (1999) for detailed explanations on the basic theory about feed-forward ANNs. More details on the applied approach are also given in Wang et al. (2018).

The prediction intervals (PIs) of ANNs are estimated by the delta method (Chryssoloiuris et al., 1996; Zio, 2006). Assuming a normal distribution of the ANN training error, the standard deviation (Std) s of the ANN prediction is calculated by (Rivals and Personnaz, 2000)

$$s = \sigma_{\text{ANN}} \sqrt{1 + \boldsymbol{h}_{\text{test}}^T (\boldsymbol{J}\boldsymbol{J}^T)^{-1} \boldsymbol{h}_{\text{test}}} \tag{8}$$

where σ_{ANN} is the Std of the ANN training errors. The Jacobian matrix $\boldsymbol{J}$ is constructed by the gradient vectors $\boldsymbol{h}^i = \dfrac{\partial \hat{y}^i}{\partial \boldsymbol{w}}$ of the training examples; also $\boldsymbol{h}^i$ can be computed based on the backward-propagation method (Bishop, 1995). In Eq.8, $\boldsymbol{h}_{\text{test}}$ is the $\boldsymbol{h}$ vector for the test example, and the upper index T denotes the matrix transpose. One can refer to Rivals and Personnaz (2000) and Bishop (1995) for more details regarding the computation of $\boldsymbol{h}$ and the delta method. An important property of the prediction uncertainty computed by Eq.8 is that it shows large uncertainty at the locations where no enough training data are available. This is originated from the term $\boldsymbol{h}_{\text{test}}^T(\boldsymbol{J}\boldsymbol{J}^T)^{-1}\boldsymbol{h}_{\text{test}}$, in which the information of the training data is stored in the Jacobian matrix $\boldsymbol{J}$. One can refer to Fig. 5 of Wang et al. (2018) for an illustration example.

2.2.2. Adaptive ANN algorithm

An ANN adaptive learning algorithm is proposed in this paper to improve the design of experiments (DoEs) of FEM simulations. The algorithm is based on the prediction uncertainty of ANNs computed with the delta method. The algorithm adds iteratively in the training dataset the points at the zone of interest (e.g., at the location where the performance of the metamodel is limited, with a large prediction uncertainty). The iterative training of ANNs is stopped when a certain accuracy criterion is satisfied. The principle of such an algorithm has been used in Kriging for fragility analysis in Gidaris et al. (2015), but it is seldom used with ANNs. In fact, adaptive learning is widely used for Kriging metamodels, e.g. in Jones et al. (1998); Echard et al. (2011), because the prediction uncertainty is directly provided in the output, which is not the case for other metamodels, such as ANNs or support vector machines. For this reason, the enrichment of new training samples in most adaptive training procedures applied to ANNs is not based on the prediction uncertainty. Rather, importance sampling, directional simulation or MCMC are typically used to create new samples in the area of interest for an enriched adaptive training (Hurtado and Alvarez, 2001; Papadopoulos et al., 2012; Pedroni and Zio, 2017). However, these approaches cannot be easily applied in fragility analysis, since it is difficult to generate or to find an earthquake motion, conditional on required values of multiple IMs (e.g. PGA and Irias intensity). An alternative is to generate a large population of initial samples and to enrich the DoEs with samples in the initial population according to an enrichment criterion. Such a strategy has been studied by Xiao et al. (2018) with ANNs, in which the computation of the prediction uncertainty is based on cross-validations, requiring retrainings of ANNs. In this paper, we quantify the uncertainty linked to ANN predictions with the delta method, which can be directly obtained once the ANN is trained, and integrate the prediction uncertainty in the enrichment criterion of the DoEs, to ensure the performance of the ANN on the whole input space, with less training data. The whole workflow of the adaptive ANN algorithm is summarized in Figure 2. Combined with the FEM simulations, the ANN adaptive training algorithm is as follows:

1. Initialization of the DoEs. To prepare for the adaptive learning algorithm, a population X composed of N seismic signals should be generated. IMs are extracted for all N seismic ground motions. N_0 seismic motions are randomly selected from X to carry out FEM simulations. N_0 should be larger than the total number of the ANN parameters, including weights and biases.
2. Starting of the iterative ANN training. For iteration k ($k \geqslant 0$), the ANN is trained with N_k IMs and EDP pairs in the current DoEs. Here N_k is used to denote the number of IMs-EDP data in the DoEs at

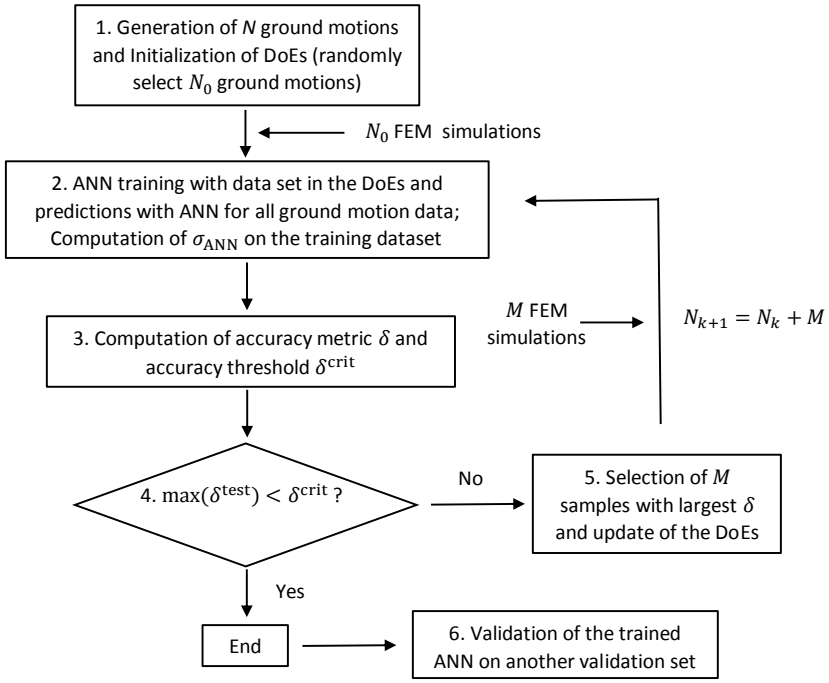

Figure 2: Workflow of the adaptive training of ANNs

the iteration k. The ANN is suggested to be trained *in the log-log space*, i.e. with ln(IMs) and ln(EDP). ANN simulation is, then, carried out for *every* IMs set in the total population X. Predictions $\hat{y}_k^i$ and the associated prediction uncertainty s_k^i can be obtained with the ANN trained at the current iteration k.

3. Computation of the accuracy metric δ_k^i and the accuracy threshold δ_k^{crit}:

$$s_{\text{ref},k} = \frac{1}{N_k} \sum_{p=1}^{N_k} s_k^p, \text{ for } p \text{ in the training set } (p = 1, ..., N_k) \tag{9}$$

$$\delta_k^i = \frac{|s_k^i - s_{\text{ref},k}|}{s_{\text{ref},k}}, \text{ for every } i \text{ in } X \ (i = 1, ..., N) \tag{10}$$

$$\delta_k^{\text{crit}} = \max_p(\delta_k^p), \text{ for } p \text{ in the training set } (p = 1, ..., N_k) \tag{11}$$

The quantity $s_{\text{ref},k}$ is the mean value of the prediction uncertainty of the training examples at the iteration k. It serves as the reference value to compute the accuracy metric. The accuracy metric δ_k^i calculates the relative deviation of s_k^i with respect to $s_{\text{ref,k}}$. A large value of δ_k^i indicates a large prediction uncertainty s_k^i, so that the corresponding ANN prediction is less reliable. The accuracy threshold δ_k^{crit} is set as the maximal relative deviation of prediction uncertainty in the training dataset.

4. Verification of the ANN accuracy. The set of test samples is defined by all the samples in X which are not used to train the ANN. When δ_k^i of every test sample is smaller than the accuracy threshold, i.e. $\max(\delta_k^{\text{test}}) < \delta_k^{\text{crit}}$, it can be considered that the samples in the ANN training set are enough to cover the whole input space of the population X. So the ANN is accurate enough for X. The iterative training can be, therefore, stopped. Otherwise, a further enrichment of the training data is necessary.

5. Enrichment of the ANN training dataset. If the accuracy of the ANN is not satisfied, M samples in the test set with the largest δ_k^i values (i.e. with the largest prediction deviations) are selected to run

the FEM simulations. The results of the FEM simulations are added to the ANN training data. Set $k = k + 1$, and go back to Step 2.

6. After being trained, the ANN is validated on another validation dataset, which is different from the training dataset.

Due to the property of the prediction uncertainty s, some ground motions with high intensities, which are often outside the validity domain of the ANNs in the first few iterations (so their prediction uncertainties are very high), can be also automatically selected by the adaptive training. With a reasonable number of FEM simulations, an ANN is obtained at the end of the adaptive training. Then, ANN simulations can be carried out for ground motions in the whole population X to predict the structural EDPs $\hat{y}$.

2.2.3. Determination of Prior Fragility Parameters

Prior fragility parameters β_R and A_m^{prior} can be estimated from the ANN simulation results. The failure threshold y_{crit}, informed from the reference value in the literature, provides an estimation of A_m^{prior}. The Std of the ANN training error is integrated in the computation of fragilities to consider the metamodel uncertainty. Such an idea has been used in Gidaris et al. (2015) and Wang et al. (2018) to account for the metamodel error in the lognormal based fragility models. Since a set of IMs, instead of the whole ground motion, is used as the input of the ANN, there is a loss of information in the input. σ_{ANN} is used to quantify this loss of the ground motion randomness, which cannot be conveyed by the IM set and therefore cannot be captured by the ANN. More details concerning the inclusion of σ_{ANN} in the fragility analysis can be found in Wang et al. (2018). More precisely, the determination of A_m^{prior} and β_R is realized by:

1. Linear regression of the data cloud $(\alpha, \hat{y})$ in log-log space (Cornell et al., 2002; Ellingwood and Kinali, 2009; Zentner et al., 2017). In the application of this paper, α denotes the PGA.

$$\ln \hat{y} = c \ln \alpha + \ln b + \varepsilon \tag{12}$$

   where b and c are regression parameters determined from the data cloud $(\ln \alpha, \ln \hat{y})$ and the residual ε follows a normal distribution $\mathcal{N}(0, \sigma_{R|IM}^2)$.

2. Computation of the conditional probability of failure, considering the Std of ANN training errors σ_{ANN}.

$$P_f(\alpha) = \mathbf{\Phi}\left(\frac{\ln b\alpha^c - \ln y_{\text{crit}}}{\sqrt{\sigma_{R|IM}^2 + \sigma_{\text{ANN}}^2}}\right) \tag{13}$$

3. Reformulating Eq.13 for coherence with Eq.2.

$$P_f(\alpha) = \mathbf{\Phi}\left(\frac{c \ln \alpha - (\ln y_{\text{crit}} - \ln b)}{\sqrt{\sigma_{R|IM}^2 + \sigma_{\text{ANN}}^2}}\right) = \mathbf{\Phi}\left(\frac{\ln \alpha - (\ln y_{\text{crit}} - \ln b)/c}{\sqrt{\sigma_{R|IM}^2 + \sigma_{\text{ANN}}^2}/c}\right) \tag{14}$$

   Therefore, $A_m^{\text{prior}} = \sqrt[c]{y_{\text{crit}}/b}$ and $\beta_R = \sqrt{\sigma_{R|IM}^2 + \sigma_{\text{ANN}}^2}/c$.

The prior value of β_U of the equipment capacity is chosen in agreement with the literature, such as EPRI (2014). With the computed value of A_m^{prior}, the prior distribution of $\hat{A}_m$ is determined: $f^{\text{prior}}(\hat{A}_m) \sim LogN(A_m^{\text{prior}}, (\beta_U^{\text{prior}})^2)$.

2.3. Bayesian Updating of Fragility Curves with Damage Data

2.3.1. Damage Database

The damage data $\boldsymbol{z}$ used in this study are taken from the seismic qualification utility group (SQUG) database. The SQUG database (EPRI, 2016), built by the Electric Power Research Institute (EPRI), gathers seismic experience data related to seismic capacity of equipment in industrial facilities (not limited to NPPs) (Starck and Thomas, 1990). The data in the SQUG database are mostly obtained from post-earthquake inspections of equipment in these industrial facilities. 32 earthquakes from 1971 to 2010 are registered in the SQUG database with most of them taking place in the USA. Some strong earthquakes in Chile, Japan, Turkey, etc are also included. The equipment in the SQUG database is divided into 20 conventional classes, including switchgears, batteries, motor control centers. A list of the 20 equipment classes is summarized in Starck and Thomas (1990).

For the data collected in the SQUG database, each observation contains the information: (i) equipment description (size, manufacturer, etc); (ii) the earthquake and the PGA; (iii) the industrial facility where the equipment is located; (iv) the elevation h of the equipment in the facility structure; (v) the description of the performance of the equipment after the earthquake. It has to be mentioned that no details on the supporting structures are provided in the database, so that the FEM models for the structures in the SQUG database are in general not available. The integration of the damage data in the Bayesian updating depends also on these supporting structures. The method to construct the likelihood function with the damage data is explained in detail in Section 2.3.3. In our study, the damage data for the low-voltage switchgear are collected from the SQUG database. They are used in the Section 3 for the Bayesian updating of the fragility curves.

2.3.2. Bayesian Framework in Fragility Analysis

Given the damage data $\boldsymbol{z}$, the posterior distribution of $\hat{A}_m$ can be computed by the Bayes' theorem:

$$f^{\text{post}}(\hat{A}_m|\boldsymbol{z}) = kL(\boldsymbol{z}|\hat{A}_m)f^{\text{prior}}(\hat{A}_m) \tag{15}$$

where $L(\boldsymbol{z}|\hat{A}_m)$ is the likelihood function determined by the observed data, and k is a constant to normalize the posterior distribution. Every observational data vector $\boldsymbol{z}^i$ has two components: the PGA value α^i of the seismic excitation and the damage state x^i of the equipment of interest after the earthquake. This latter x^i is modeled as a binary Bernoulli variable: $x^i = 0$ if no failure occurs and $x^i = 1$ if the equipment fails. According to Shinozuka et al. (2000), the likelihood function with given $\boldsymbol{z}$ is written as:

$$L(\boldsymbol{z}|\hat{A}_m) = \prod_{i=1}^{n_{\text{obs}}} [P_f(\alpha^i)]^{x^i}[1 - P_f(\alpha^i)]^{1-x^i} = \prod_{i=1}^{n_{\text{obs}}} \left[\boldsymbol{\Phi}(\frac{\ln \alpha^i - \ln \hat{A}_m}{\beta_R})\right]^{x^i} \left[1 - \boldsymbol{\Phi}(\frac{\ln \alpha^i - \ln \hat{A}_m}{\beta_R})\right]^{1-x^i} \tag{16}$$

where n_{obs} is the number of the empirical data. Substituting Eq.16 into Eq.15, one can obtain the expression of the posterior distribution of $\hat{A}_m$:

$$f^{\text{post}}(\hat{A}_m|\boldsymbol{z}) \propto (\prod_{i=1}^{n_{\text{obs}}} [P_f(\alpha^i)]^{x^i}[1 - P_f(\alpha^i)]^{1-x^i}) f^{\text{prior}}(\hat{A}_m) \tag{17}$$

Knowing $L(\boldsymbol{z}|\hat{A}_m)$ and $f^{\text{prior}}(\hat{A}_m)$, the MCMC simulation allows sampling efficiently the posterior distribution without computing explicitly the constant k of Eq.15 (Hastings, 1970). Therefore, the essential part of the Bayesian updating is to determine the parameters in $L(\boldsymbol{z}|\hat{A}_m)$ to construct the likelihood function.

It appears that the computation of $L(\boldsymbol{z}|\hat{A}_m)$ is straightforward. However, different kinds of PGA values can be provided in the database. Before computing the likelihood function, one has to ensure that the PGA values to plug in Eq.17 describe the free surface ground motions near the target structure in which the equipment is located.

2.3.3. Determination of the Likelihood Function

Two groups of earthquake observational damage data are discussed in this study:

1. In-situ earthquake observational data $\boldsymbol{z}_t = (\alpha_t, x)$ of the equipment of interest in the *target* structure, where α_t denotes the PGA level recorded on the free surface near the target structure (Let us recall that the FEM model of the target structure is available).

2. SQUG earthquake observational data $\boldsymbol{z}_s = (\alpha_s, x)$ of a similar equipment positioned in other civil structures in the database, named SQUG structures in this paper. The quantity α_s denotes the PGA level recorded on the free surface near the SQUG structures.

The total workflow of the determination of the likelihood function with damage data is summarized in Figure 3.

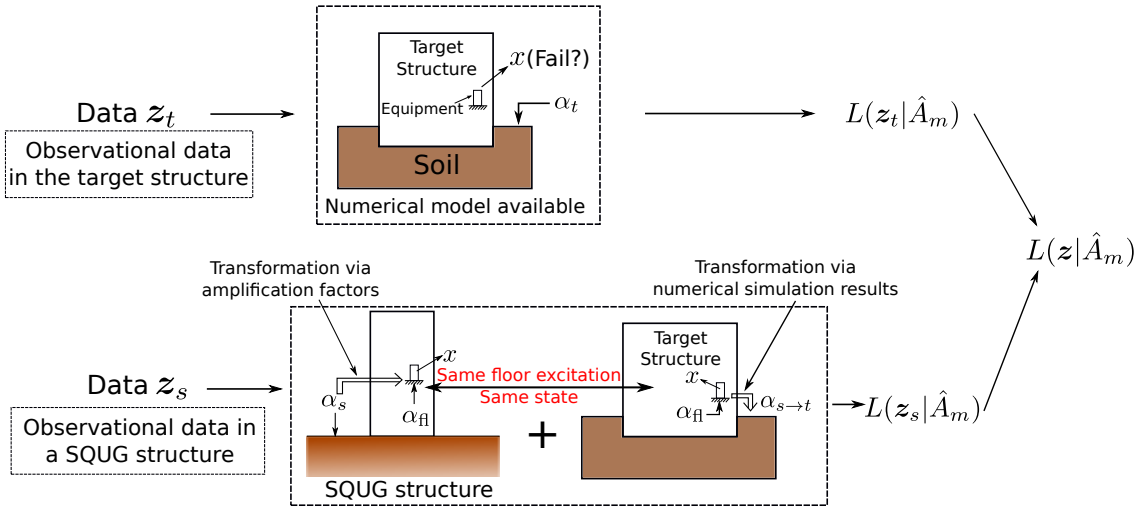

Figure 3: The workflow to compute the likelihood function

Likelihood function for z_t. Recalling that the PGA values in Eq.17 should be α_t, data of the first category can be directly inserted into Eq.17.

$$L(\boldsymbol{z_t}|\hat{A}_m) = \prod_{i=1}^{n_t} \left[\boldsymbol{\Phi}\left(\frac{\ln \alpha_t^i - \ln \hat{A}_m}{\beta_R}\right) \right]^{x^i} \left[1 - \boldsymbol{\Phi}\left(\frac{\ln \alpha_t^i - \ln \hat{A}_m}{\beta_R}\right) \right]^{1-x^i} \tag{18}$$

where n_t is the number of the in-situ observational data.

However, the use of the SQUG data is not straightforward. The purpose of the subsequent part is to propose a method to integrate SQUG data in Eq.17, i.e. a method to transform $\boldsymbol{z}_s$ into $\boldsymbol{z}_t$ with also the quantification of the associated uncertainty in the transformation. The essential idea of the assumption is that the damage state of the equipment after the earthquake depends on the PGA value of the floor acceleration.

Likelihood Function for z_s. The transformation from $\boldsymbol{z}_s$ into $\boldsymbol{z}_t$ consists of two steps:

1. Compute the PGA of the floor acceleration of the SQUG structure given the PGA on the free soil surface.

2. Considering that the equipment is positioned in the target structure with the same floor acceleration, compute the PGA of the free surface ground motion of the target structure.

We start with the first step of the transformation. In general, the numerical model of the SQUG structure is difficult to obtain, and only the elevation h of the location of the equipment is provided in SQUG data. Without any information on the SQUG structure, the simple amplification factor model used in EPRI (2014) is adopted in this study:

$$\alpha_{\text{fl}} = \lambda(h)\alpha_s \tag{19}$$

where $\lambda(h)$ is the amplification factor, which is a function of the elevation. α_{fl} denotes the PGA of the floor acceleration. The quantity $\lambda(h)$ contains a median value $\bar{\lambda}(h)$ and a lognormal uncertainty $\tilde{\varepsilon}$: $\lambda(h) = \bar{\lambda}(h)\tilde{\varepsilon}$ with $\tilde{\varepsilon} \sim LogN(1, \tilde{\beta}^2)$. Here, a linear relation is selected for $\bar{\lambda}(h)$:

$$\bar{\lambda}(h) = c_h h + b_h \tag{20}$$

The parameters c_h and b_h are determined according to the amplification factor values used in EPRI (2014):

$$\bar{\lambda} = 1 \text{ if } h = 0 \tag{21}$$

$$\bar{\lambda} = 1.5 \text{ if } h = 12.192\text{m} \tag{22}$$

So far, the floor acceleration α_{fl} and its associated uncertainty $\tilde{\varepsilon}$ have been computed. The second step of the transformation is explained in what follows. The transformation of α_{fl} to α_t is, in fact, the transformation of the floor PGA of the target structure into the free surface PGA. This transformation can be realized with a statistical model established from the FEM simulation results, which are used to train the adaptive ANN.

From the FEM simulation results of Section 2.2, PGA values of the floor accelerations $\alpha_{\text{f}}^{\text{FEM}}$ and the free surface ground motions $\alpha_{\text{g}}^{\text{FEM}}$ of the target structure can be extracted. Let us assume that both PGA values are lognormally distributed. This assumption is checked later in our specific case study. The lognormal assumption allows building a bi-variate normal distribution of $\ln \alpha_{\text{f}}^{\text{FEM}}$ and $\ln \alpha_{\text{g}}^{\text{FEM}}$. The marginal distributions of $\ln \alpha_{\text{f}}^{\text{FEM}}$ and $\ln \alpha_{\text{g}}^{\text{FEM}}$ are denoted by $N(\ln \mu_{\text{f}}^{\text{FEM}}, (\sigma_{\text{f}}^{\text{FEM}})^2)$ and $N(\ln \mu_{\text{g}}^{\text{FEM}}, (\sigma_{\text{g}}^{\text{FEM}})^2)$, respectively, with the correlation coefficient ρ. According to the property of the conditional bi-variate normal distribution, it can be shown that the median value of the transformed free surface PGA $\alpha_{\text{fl}\to t}$ and its uncertainty $\beta_{\text{fl}\to t}$ are calculated by

$$\ln \alpha_{\text{fl}\to t} = \ln \mu_{\text{g}}^{\text{FEM}} + \rho(\ln \alpha_{\text{fl}} - \ln \mu_{\text{f}}^{\text{FEM}}) \frac{\sigma_{\text{g}}^{\text{FEM}}}{\sigma_{\text{f}}^{\text{FEM}}} \tag{23}$$

$$\beta_{\text{fl}\to t}^2 = (1 - \rho^2)(\sigma_{\text{g}}^{\text{FEM}})^2 \tag{24}$$

Combining Eqs.19, 23, 24 and considering the property of the normal distribution, one can show that the median value of the transformed PGA $\ln \alpha_{s\to t}$ on the free surface of the target structure is calculated by

$$\ln \alpha_{s\to t} = \ln \mu_{\text{g}}^{\text{FEM}} + \rho[\ln(\bar{\lambda}(h)\alpha_s) - \ln \mu_{\text{f}}^{\text{FEM}}] \frac{\sigma_{\text{g}}^{\text{FEM}}}{\sigma_{\text{f}}^{\text{FEM}}} \tag{25}$$

and its related uncertainty is

$$\beta_{s\to t}^2 = (\frac{\sigma_{\mathrm{g}}^{\mathrm{FEM}}}{\sigma_{\mathrm{f}}^{\mathrm{FEM}}}\rho)^2\tilde{\beta}^2 + \beta_{\mathrm{fl}\to t}^2 = (\frac{\sigma_{\mathrm{g}}^{\mathrm{FEM}}}{\sigma_{\mathrm{f}}^{\mathrm{FEM}}}\rho)^2\tilde{\beta}^2 + (1-\rho^2)(\sigma_{\mathrm{g}}^{\mathrm{FEM}})^2 \tag{26}$$

In the end, the likelihood function for data $\boldsymbol{z}_s$ is derived:

$$L(\boldsymbol{z_s}|\hat{A}_m) = \prod_{i=1}^{n_{\mathrm{s}}} \left[\boldsymbol{\Phi}(\frac{\ln\alpha_{s\to t}^i - \ln\hat{A}_m}{\sqrt{\beta_R^2+\beta_{s\to t}^2}})\right]^{x^i} \left[1-\boldsymbol{\Phi}(\frac{\ln\alpha_{s\to t}^i - \ln\hat{A}_m}{\sqrt{\beta_R^2+\beta_{s\to t}^2}})\right]^{1-x^i} \tag{27}$$

It is worth mentioning that the interpretations of β_R and $\beta_{s\to t}$ are different: the former represents the record-to-record aleatory uncertainty when the ground motion time history is characterized by a scalar PGA value, whereas the latter expresses the uncertainty of the transformed PGA value due to the underlying statistical modeling.

Consequently, the total likelihood function for the two categories of data is computed by

$$L(\boldsymbol{z}|\hat{A}_m) = L(\boldsymbol{z}_s|\hat{A}_m)L(\boldsymbol{z}_t|\hat{A}_m) \tag{28}$$

3. Case Study: Application to KARISMA Benchmark

This section is dedicated to apply the proposed methodology to an industrial case study. Moreover, a sensitivity analysis is conducted at the end with respect to some uncertain parameters. The equipment of interest is a low-voltage switchgear (LVSG) in the Kashiwazaki-Kariwa NPP (K-K NPP). In NPPs, the LVSG is a combination of electrical control units such as circuit breaks and relays, etc, whose function is to ensure and protect the performance of 480V-AC (alternative current) electrical systems. K-K NPP experienced the strong Niigataken-Chuetsu-Oki (NCO) earthquake with magnitude $M_w = 6.6$ in 2007. In this context, the KAshiwazaki-Kariwa Research Initiative for Seismic Margin Assessment (KARISMA) benchmark was organized by the International Atomic Energy Agency (IAEA). The objective of this benchmark is to compare seismic responses calculated by numerical simulations to registered responses of K-K NPP Unit 7 (IAEA, 2013). In addition, a post-earthquake inspection was carried out in order to check the performance of the equipment in K-K NPP after the earthquake (EPRI, 2007).

3.1. KARISMA Numerical Model

The FEM model of the K-K NPP Unit 7 is shown in Figure 4. The model consists of 92,000 degrees of freedom with 10,700 nodes and 15,600 elements, including bars, beams, and different shell elements. The constitutive law of the materials is considered linear. The NPP model is embedded 23 meters in the soil, which is accounted for in the soil-structure-interaction (SSI) analysis. The LVSG of interest is located on the -1 floor of the K-K NPP building. The structural analyses are carried out with the Code_Aster, an open-source FEM software developed by Electricity of France (Code_Aster), while the soil part is solved with MISS based on the boundary element method (BEM) using MISS3D (Clouteau, 2005) available with Code_Aster via Salome_Meca platform (Salome_Meca).

Two strong earthquake scenarios, which have affected the area of Kashiwazaki and Kariwa, are considered in this study: (i) the 2007 NCO earthquake scenario with $M_w = 6.6$ and source-to-site distance $r = 16$ km; (ii) the 2004 Chuetsu earthquake with $M_w = 6.8$ and source-to-site distance $r = 29$ km. Given the NCO

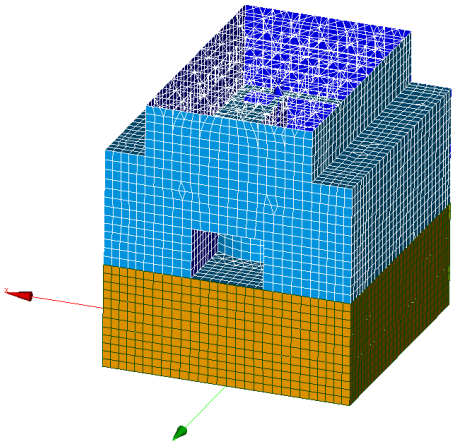

Figure 4: FEM model of the K-K NPP Unit 7

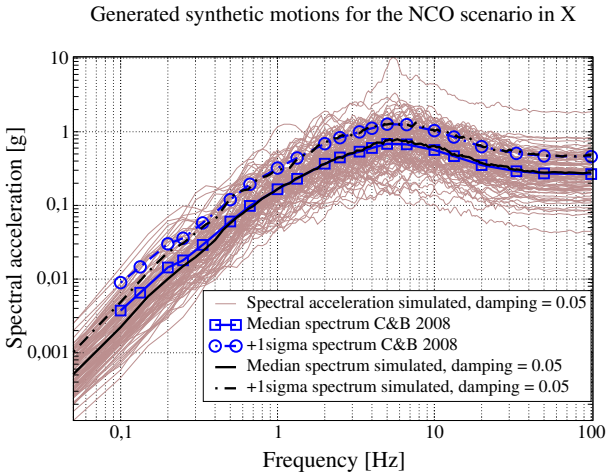

Figure 5: Generated motions for NCO earthquake scenario and comparison with the spectra predicted by C&B 2008

and Chuetsu scenarios, the generation of the synthetic ground motions at the bedrock with $Vs_{30} = 720$ m/s is based on the median and 1σ spectra given by the Campbell-Bozorgnia 2008 (C&B 2008) ground motion prediction equations (Campbell and Bozorgnia, 2008). 250 triplets of 3D synthetic ground motions are generated for *each scenario* (so 500 triplets in total) and used for the uncertainty propagation. The generated 3D ground motions of each scenario have the median and 84% percentile in agreement with the spectra provided by C&B 2008, using the operator GENE_ACCE_SEISME in Code_Aster (Zentner, 2014). A correlation coefficient of 0.2 is assumed for the two horizontal components (in X and Y), according to Zentner et al. (2017). The vertical component is not correlated to the horizontal ones. A vertical-to-horizontal ratio of $\frac{2}{3}$ is applied in the generation procedure, as suggested by Newmark and Hall (1978). The generated motions in X direction for the NCO scenario are shown in Figure 5. To obtain enough failure counts for the fragility analysis, the synthetic seismic motions at the bedrock are scaled with a factor of two for the NCO scenario and a factor of three for the Chuetsu scenario.

500 bedrock motions are convoluted on the free surface based 1D soil column reconvolution with the equivalent linear method (ELM) (Yoshida et al., 2002). Meanwhile, 500 degraded soil profiles are obtained. In order to reduce the computational cost, the impedances of the soil and the seismic forces have not been computed for each soil profile using BEM. The 3D seismic signals at the bedrock are regrouped into four soil classes according to their PGA values: (i) PGA$\in$[0, 0.3g); (ii) PGA$\in$[0.3g, 0.5g); (iii) PGA$\in$[0.5g, 1.0g); (iv) PGA$\in$[1.0g, $+\infty$). The degraded soil profiles are averaged within each class and 4 soil profiles are obtained to represent four different degradation levels. The 500 ground motions on the free surface, as well as the impedances and seismic forces calculated from the four soil profiles, are used as inputs of the SSI analyses to compute the floor accelerations of the K-K NPP.

In this paper, the failure is described by the non-operational state of the LVSG after the earthquake. Reparation of the equipment is necessary. It can be caused by the fact that (i) relays or breakers cannot return to their operational state after the earthquake or (ii) structural damage has occurred to the equipment, for example anchorage failure at its base (EPRI, 1991). The capacity of the switchgear is given by the average floor spectral acceleration in 5-9Hz, which covers the first natural frequency of the LVSG. The maximum

value of the floor spectral accelerations in the two horizontal directions, averaged over 5-9Hz is defined as the EDP y:

$$y = \frac{1}{9. - 5.} \max_{i=X,Y} \int_{5\text{Hz}}^{9\text{Hz}} S^e_{a,i}(f)\mathrm{d}f \tag{29}$$

where $S^e_{a,i}$ denotes the floor spectral acceleration of the LVSG in the i-th direction. A value of $1.8g$ is selected for y_{crit} according to EPRI (1991), in which the failure threshold of the floor spectral acceleration $S^e_{a,i}(f)$ of the LVSG is a constant value $1.8g$ for the frequency range [3Hz, 16Hz] (so its average for the frequency range [5Hz, 9Hz] is also $1.8g$).

3.2. Prior Fragility Parameters

An ANN is trained iteratively with the algorithm explained in Section 2.2.2. The IMs of the 500 convoluted seismic motions on the free surface of the K-K NPP can be extracted. Three IMs are used as the inputs of the ANN: (i) PGA, which is widely used in fragility analysis; (ii) ASA (Biasio et al., 2015), the average spectral acceleration in 5-9Hz; (iii) PGV (peak ground velocity), a classical IM for the mid-frequency range. The geometric means of IMs in the two horizontal directions are used as scalar IMs for 3D ground motions. The number of the neurons in the hidden layer of the ANN is 4. In this way, the architecture of the ANN is determined: 3 input parameters (PGA, ASA, PGV), 4 hidden layer nodes and 1 output parameter (the EDP defined by Eq.29). $N_0 = 30$ seismic motions from the total 500 signals are randomly selected for the initialization of the adaptive ANN training. $M = 4$ data are added in the DoE in every iteration. The ANN is trained in *log-log* space, i.e. with ln(IMs) as inputs and ln(EDP) as outputs.

The adaptive training of the ANN is stopped after 62 calls of FEM simulations. To visualize the DoEs determined by the proposed ANN algorithm, we plot the data cloud in PGA-EDP space in Figure 6. The PGA used in the horizontal axis is PGA on the free surface. The convergence curve of the adaptive ANN training is shown in Figure 7. In this figure, the maximum value of δ of the test dataset is plotted against the iteration number k. At iteration 8, the stopping condition is satisfied and the ANN iterative training is stopped.

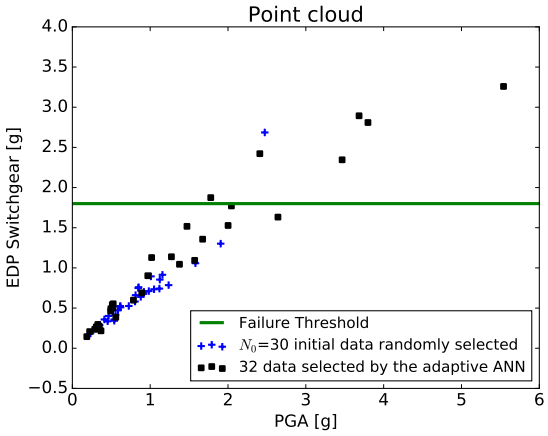

Figure 6: Data determined by the adaptive algorithm from 500 seismic ground motions plotted in PGA-EDP space

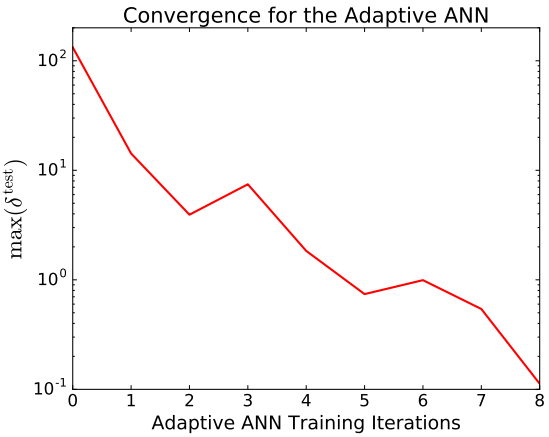

Figure 7: Convergence curve for the adaptive ANN training

In order to show the advantage of the adaptive algorithm, 62 seismic motions are randomly selected from the total 500 signals. FEM simulations are conducted for the 62 randomly selected signals and the

corresponding data cloud is plotted in PGA-EDP space in Figure 8. From Figure 6 and Figure 8, one can clearly observe the improvement of the DoEs with the ANN adaptive training algorithm. The data in Figure 6 are better distributed in the PGA-EDP space than the data in Figure 8: too many data are concentrated in low PGA range in Figure 8, with only one point exceeding the failure threshold. On the contrary, more failures are contained in the dataset obtained by the ANN adaptive training, which is more convenient for the accuracy of the fragility analysis.

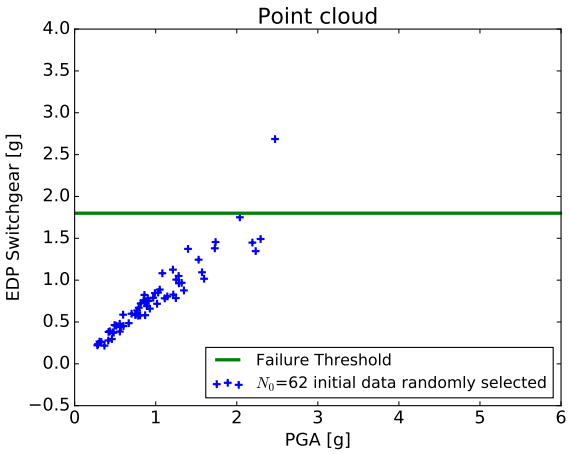

Figure 8: Data randomly selected from 500 seismic ground motions plotted in PGA-EDP space

The training results of the ANN are shown in Figure 9a. The ANN predictions of the training dataset are compared to the real FEM results (target output) *in log space*. From Figure 9a, one can conclude that the training results are satisfactory. Most of the results in the 'prediction-target' space are located in the proximity of the dashed diagonal line. Another 60 ground motions, which are different from the training dataset determined by the adaptive algorithm, are selected to validate the constructed ANN model. FEM and ANN simulations are performed for the 60 validation seismic signals, respectively. The validation results are plotted in Figure 9b: the validation results are also satisfactory.

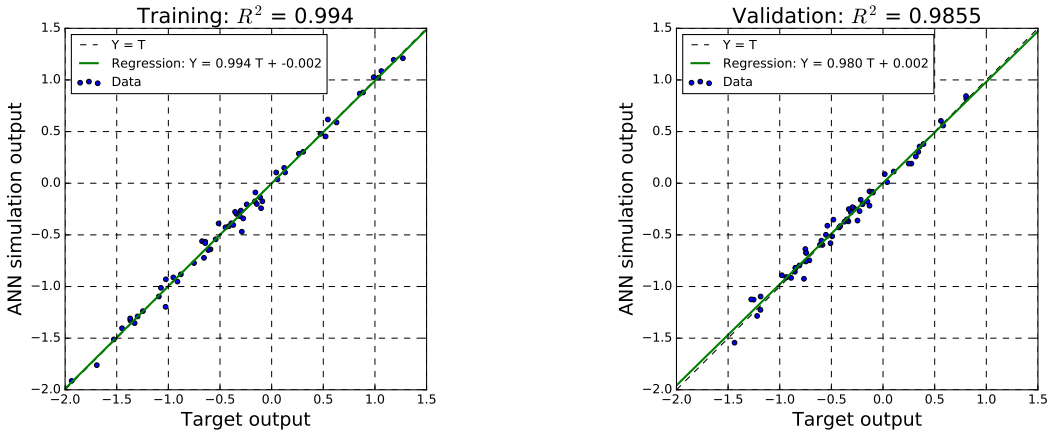

(a) ANN training results

(b) ANN validation results

Figure 9: Comparison of ANN results with FEM results. The comparison is conducted for $\ln \hat{y}$ and $\ln y$

A total of 500 ANN simulations are conducted for the whole ground motion population with the con-

structed ANN metamodel: 500 pairs of PGA-EDP are, then, obtained. The values of β_R and A_m^{prior} are estimated from the ANN simulations results with the method explained in Section 2.2.3, with $A_m^{\text{prior}} = 2.46g$ and $\beta_R = 0.145$. According to EPRI (2009, 2014), a reasonable estimation of β_U^{prior} concerning the uncertainty of the equipment capacity is 0.4. Consequently, the prior distribution of $\hat{A}_m$ follows $LogN(2.46g, 0.4^2)$.

3.3. Determination of the Likelihood Function

The LVSG damage data can be divided into two groups: one in-situ observation $\boldsymbol{z}_t$ for K-K NPP and 78 post-earthquake inspection data $\boldsymbol{z}_s$ for the LVSG in the SQUG structures. Regarding the in-situ observation, the LVSG in the K-K NPP Unit 7 was not damaged after the NCO earthquake with PGA = $0.69g$ near the Unit 7. As no detailed information on the performance of the K-K NPP equipment has been found after the 2004 Chuetsu earthquake in the SQUG database, the in-situ observational data contain only the one from the 2007 NCO earthquake. On the other hand, the total number of SQUG damage data for the LVSG is 78, with only one failure observed in the El Centro Steam Plant after the 1979 Imperial Valley Earthquake with local PGA value of $0.43g$. After the earthquake, it has been noticed that circuit breakers of the LVSG had refused to close. However, according to the inspection report, it is not clear that the failure of the LVSG is caused by the earthquake. It can be also due to the corrosion in the mechanical linkages, which is not earthquake-related. Therefore in the present paper, we set $x^i = 0.5$ for this potential failure, meaning that with a probability of 50% the LVSG failed during the Imperial Valley Earthquake. The local PGA values measured at different industrial structures are plotted in Figure 10. A summary of the SQUG data for the low voltage switchgear is given in Table 1.

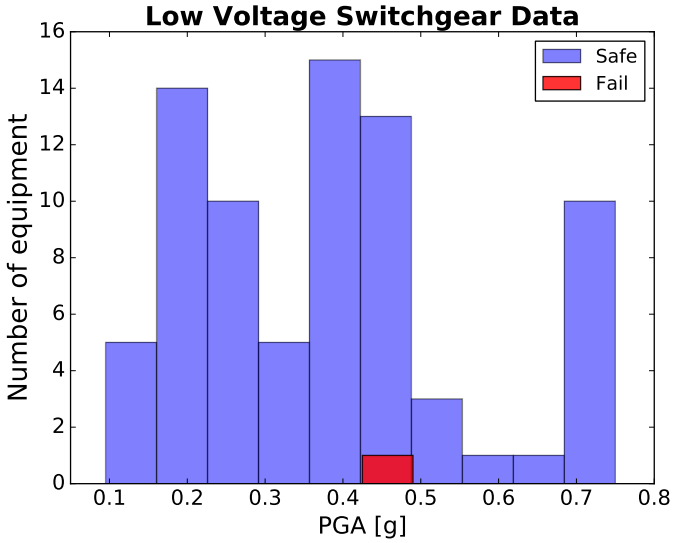

Figure 10: PGA values of the SQUG data for the LVSG

The likelihood function $L(\boldsymbol{z}_t|\hat{A}_m)$ for the K-K NPP in-situ observation is straightforward with Eq.18. We focus on the computation of $L(\boldsymbol{z}_s|\hat{A}_m)$ in what follows.

We follow the two-step method described in Section 2.3.3 to calculate $L(\boldsymbol{z}_s|\hat{A}_m)$:

1. Step 1: computation of the PGA value of the floor acceleration of the SQUG structures with the amplification factor model, given the PGA on the soil free surface. The median values $\bar{\lambda}(h)$ for the

Table 1: Summary of the SQUG data for the LVSG

Earthquake	Number of the inspected LVSGs	Number of failures
1971 San Fernando Earthquake	9	0
1973 Point Mugu Earthquake	1	0
1975 Ferndale Earthquake	1	0
1979 Imperial Valley Earthquake	5	0.5
1983 Coalinga Earthquake	1	0
1984 Morgan Hill Earthquake	1	0
1985 Chile Earthquake	4	0
1985 Mexico Earthquake	1	0
1986 Adak Earthquake	2	0
1986 Chalfant Valley Earthquake	1	0
1987 Bay of Plenty Earthquake	3	0
1987 Superstition Hills Earthquake	1	0
1987 Whitter Earthquake	7	0
1989 Loma Prieta Earthquake	7	0
1992 Cape Mendocino Earthquake	2	0
1992 Landers/Big Bear Earthquake	3	0
1993 Guam Earthquake	3	0
1994 Northridge Earthquake	19	0
1995 Manzanillo Earthquake	4	0
1999 Kocaeli Turkey Earthquake	1	0
2010 Baja California Earthquake	2	0

amplification factors can be obtained by Eqs.20, 21, 22 with the elevation values h provided in the database. The uncertainty $\tilde{\beta}$ of the amplification factors is assumed to be 0.2, so that the true values of the amplification factors $\lambda(h)$ have a probability of 95% to lie approximately between $\frac{2}{3}\bar{\lambda}(h)$ and $1.5\bar{\lambda}(h)$. Therefore, the median PGA value of the floor acceleration and its uncertainty can be determined.

2. Step 2: transformation of the PGA of the floor acceleration to the K-K NPP free surface PGA with the bi-variate normal distribution model established from the 62 FEM simulation results.

   First, the lognormal assumption of the marginal distributions of the PGA values is checked for both floor accelerations and free field accelerations of the K-K NPP. The values of PGAs are obtained from 62 FEM simulation results. The medians μ and logarithmic Stds σ of the assumed lognormal distributions are computed and listed in Table 2. The ln(PGA) values are normalized with respect to the medians and Stds and compared with $N(0,1)$ in Figure 11 to verify the lognormal assumption.

Table 2: Summary of parameters used in the transformation of PGA values

c_h	b_h	$\tilde{\beta}$	μ_g^{FEM}	σ_g^{FEM}	μ_f^{FEM}	σ_f^{FEM}	ρ
0.041	1	0.2	0.846	0.746	0.354	0.743	0.924

From the results of the probability plots, it can be concluded that the lognormal assumption for both $\alpha_{\mathrm{g}}^{\mathrm{FEM}}$ and $\alpha_{\mathrm{f}}^{\mathrm{FEM}}$ can be considered acceptable. Additionally, from Table 2 it can be observed that the median of the soil PGA μ_g^{FEM} is larger than the median of the floor PGA μ_f^{FEM}: this is due to the fact that the LVSG is located on the -1 floor in the K-K NPP.

Furthermore, the transformed PGA values $\alpha_{s\to t}$ on the K-K NPP free surface and the relevant uncertainty $\beta_{s\to t}$ due to the transformation are computed with Eqs.25, 26. The transformed median PGA

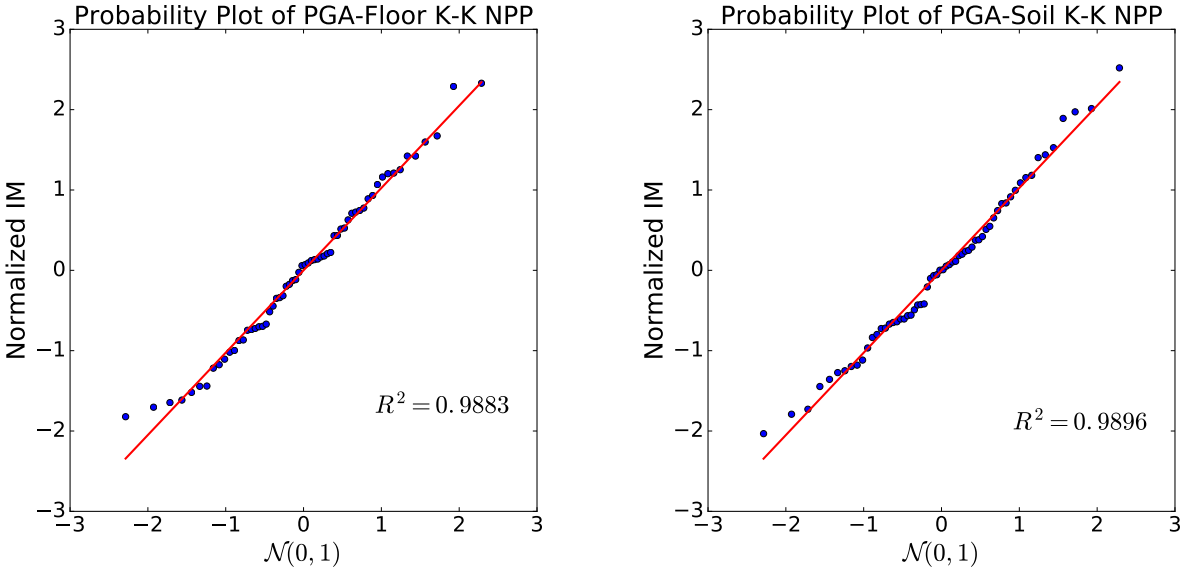

(a) Probability plot of the PGA values of the -1 floor of the K-K NPP

(b) Probability plot of the PGA values of the soil free surface of the K-K NPP

Figure 11: Probability plot of the normalized PGA values of the -1 floor and the normalized PGA values on the soil free surface of the K-K NPP

values $\alpha_{s\to t}$ are plotted in Figure 12. We can see an increase of the PGA values after the transformation process due to the low elevation of the target LVSG in the K-K NPP. In Figure 12, a linear tendency can be observed for some ($\alpha_{s\to t}$,α_s) data values. This is because their corresponding LVSGs have the same elevations h (in particular $h = 0$), so that their amplification factors in the transformation step 1 are the same. In addition, as $\beta_{s\to t}$ calculated with Eq.26 is independent of α_s, it stays the same for all 78 $\boldsymbol{z}_s$ data, with $\beta_{s\to t} = 0.299$.

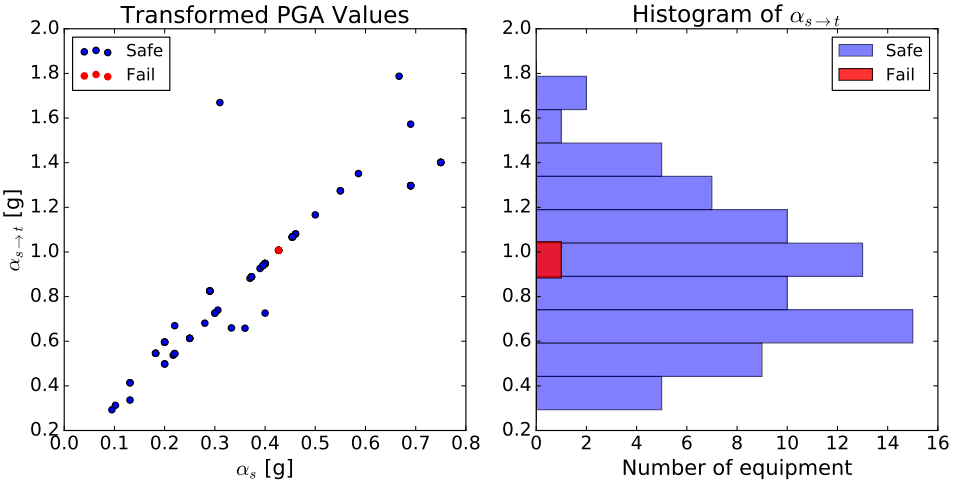

Figure 12: PGA values $\alpha_{s\to t}$ after the transformation into K-K NPP free surface

In the end, the transformed $\alpha_{s\to t}$ are plugged into Eq.27 to compute the likelihood function $L(\boldsymbol{z}_s|\hat{A}_m)$. We also justify the application of the fractional x^i value 0.5 for the potential failure case of El Centro

steam plant. It can be regarded as two realizations of earthquake observations, with one failure and one survival. Then, the likelihood function established by the two realizations should be normalized to one observation by the square-root operation:

$$L(\boldsymbol{z}_{\text{El-Centro}}|\hat{A}_m) = \sqrt{[P_f(\alpha_{\text{El-Centro}})][1 - P_f(\alpha_{\text{El-Centro}})]} = [P_f(\alpha_{\text{El-Centro}})]^{0.5}[1 - P_f(\alpha_{\text{El-Centro}})]^{0.5} \tag{30}$$

The same procedure is also used by EPRI (2017). As a result, the total likelihood function is computed: $L(\boldsymbol{z}|\hat{A}_m) = L(\boldsymbol{z}_t|\hat{A}_m)L(\boldsymbol{z}_s|\hat{A}_m)$

3.4. Posterior Fragility Curve

The posterior distribution $f^{\text{post}}(\hat{A}_m|\boldsymbol{z})$ is obtained based on the prior distribution and the likelihood function, which are calculated in Section 3.2 and Section 3.3, respectively. MCMC is used to generate 10,000 samples from $f^{\text{post}}(\hat{A}_m|\boldsymbol{z})$. A lognormal distribution is approximated for $f^{\text{post}}(\hat{A}_m|\boldsymbol{z})$ with the median and logarithmic Std of the generated 10,000 samples. The MCMC sampling of $f^{\text{post}}(\hat{A}_m|\boldsymbol{z})$ and the approximated lognormal distribution are shown in Figure 13. The posterior distribution of $\hat{A}_m$ has the median $A_m^{\text{post}} = 2.70g$ and the associated uncertainty $\beta_U^{\text{post}} = 0.176$. The comparison of fragility parameters of the LVSG before and after Bayesian updating is reported in Table 3.

Table 3: Posterior fragility parameters for the LVSG in K-K NPP and comparison to the prior parameters

β_R	A_m^{prior}	β_U^{prior}	$A_{\text{HCLPF}}^{\text{prior}}$	A_m^{post}	β_U^{post}	$A_{\text{HCLPF}}^{\text{post}}$
0.145	$2.46g$	0.4	$1.00g$	$2.70g$	0.176	$1.59g$

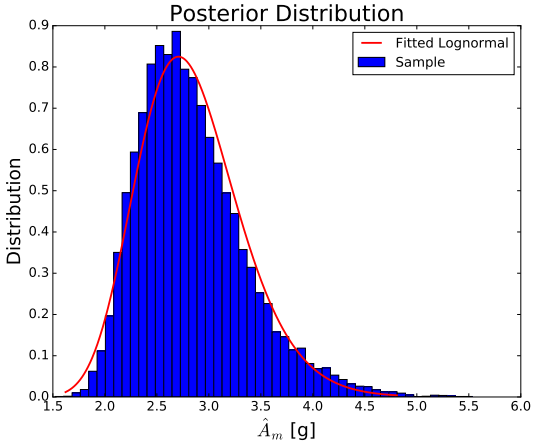

Figure 13: MCMC sampling of the posterior distribution of $\hat{A}_m$

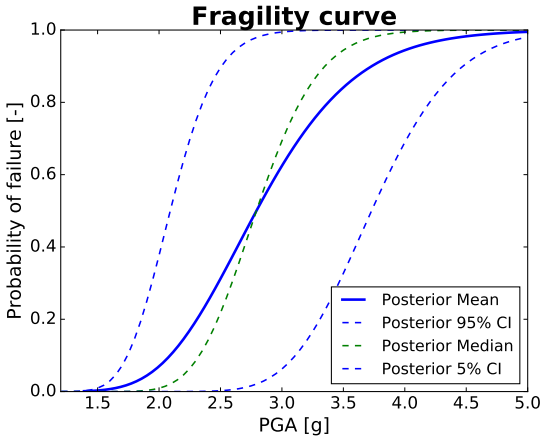

Figure 14: Posterior fragility curves and its confidence intervals

The posterior median and mean fragility curves are computed with Eqs.2, 6 respectively. The 0.05 and 0.95 non-exceedance confidence intervals are calculated with Eq.4. The computed fragility curves and the associated confidence intervals are shown in Figure 14. Compared to the prior fragility parameters, the median capacity A_m increases after Bayesian updating, because few failure cases (only one) have been observed in the post-earthquake inspection for the LVSG. The epistemic uncertainty β_U is reduced due to the supplementary information from the observational data. Relatively large confidence bounds have been shown in Figure 14,

since despite the Bayesian updating, the value of β_U^{post} (0.176) is still larger than the aleatory uncertainty $\beta_R = 0.145$. Nevertheless, the HCLPF capacity, computed by Eq.5, is largely increased after the Bayesian updating, mainly due to the reduction of the epistemic uncertainty.

Furthermore, the influence of the selected value of β_U^{prior} on the posterior fragility curve is investigated. Different values of β_U^{prior} varying from 0.1 to 0.4 are taken for the prior $\hat{A}_m$ distributions. With the same SQUG observational data, the likelihood function remains the same. Posterior distributions of $\hat{A}_m$ are computed and plotted in Figure 15. It can be observed from Figure 15 that $\beta_U^{\text{prior}} = 0.4$ reveals in fact a relatively large uncertainty of the median capacity compared to the likelihood function $L(\boldsymbol{z}|\hat{A}_m)$ provided by the observational data. Therefore, the contribution of $L(\boldsymbol{z}|\hat{A}_m)$ to the posterior distribution is dominant if $\beta_U^{\text{prior}} = 0.4$. On the other hand, if one is very certain about the median capacity estimated from the numerical simulations (i.e. $\beta_U^{\text{prior}} = 0.1$), the influence of $L(\boldsymbol{z}|\hat{A}_m)$ on the posterior distribution is not that evident: the posterior median increases slightly in comparison with the prior median, whereas the value of β_U is hardly modified. For $\beta_U^{\text{prior}} = 0.2$ and 0.3, the posterior distribution is a trade-off between the prior distribution and the likelihood function, which is a reasonable outcome from the Bayes' theorem.

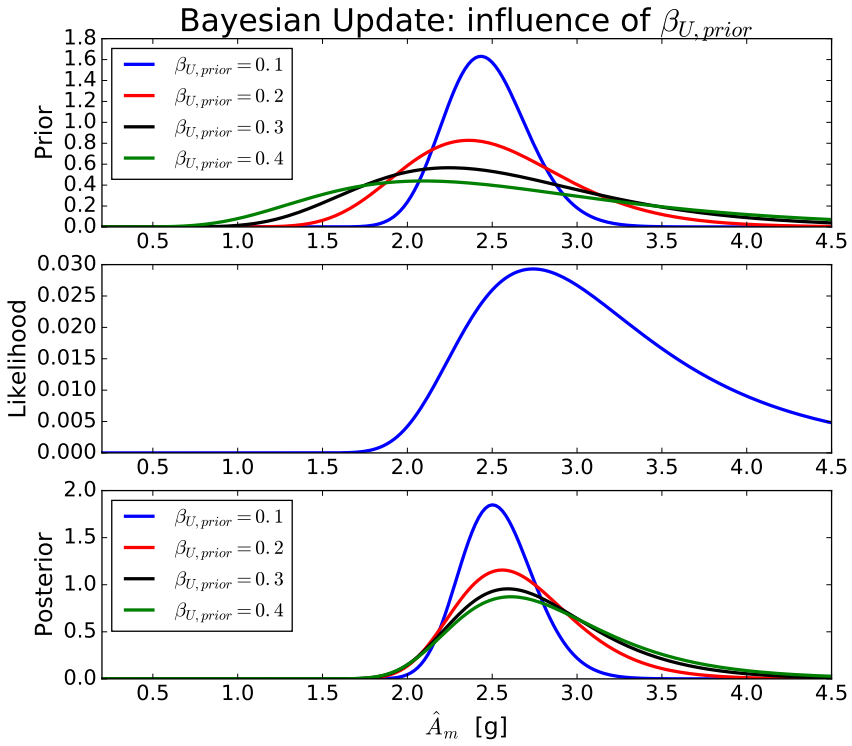

Figure 15: Influence of the choice of β_U^{prior} on the posterior fragility curve. Upper: prior distributions of $\hat{A}_m$ with different β_U^{prior}. Middle: likelihood function. Lower: posterior distributions of $\hat{A}_m$ with different β_U^{prior}.

Finally, we study the influence of the uncertain observational data of the El-Centro steam plant. Other than the observational value $x^i = 0.5$ applied in the previous sections, the likelihood function is also computed with $x^i = 0$ and $x^i = 1$ for the El-Centro steam plant. The posterior distributions with different levels of uncertainty on the El-Centro observational data are plotted in Figure 16. From the results of Figure 16, a complete failure of the LVSG $x^i = 1$ in the El-Centro steam plant makes decrease the posterior $\hat{A}_m$, since the

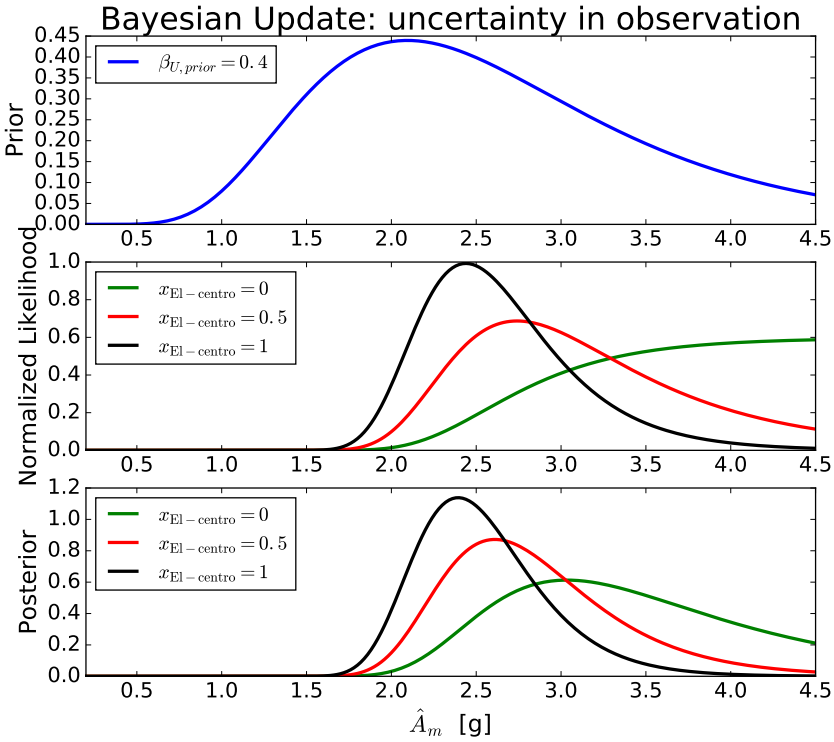

Figure 16: Influence of observational data of El-Centro steam plant. Upper: prior distributions of $\hat{A}_m$. Middle: likelihood function with different x^i values for the El-Centro steam plant. Lower: posterior distributions of $\hat{A}_m$.

equipment is more fragile according to the observational results. On the contrary, the LVSG is more resistant if $x^i = 0$ for the El-Centro steam plant, so that an increase of the posterior $\hat{A}_m$ can be observed.

3.5. Discussion

The proposed Bayesian framework has been applied to the K-K NPP to compute the fragility curve of a low-voltage switchgear. Some assumptions made in the methodology and in the application are discussed as follows:

1. As a first application of the proposed Bayesian framework, the assumption of linear material constitutive law has been applied in the FEM simulation of the K-K NPP model, since the building reveals to be very rigid and response remains mainly linear under the NCO earthquake (IAEA, 2013). However, it should be noted that the results computed from the linear material assumption do not provide best estimates of the structural responses for the higher load levels. A further step is to apply the proposed method to a nonlinear structure model but with a smaller number of degrees of freedom.
2. The derivation of the likelihood function using the two-step transformation depends on the assumptions of normality or lognormality. These assumptions are applied so that an analytical form of the final likelihood function can be derived. In real applications, if synthetic ground motions are generated from an earthquake scenario, the IMs at the free surface can be considered lognormally distributed. Nevertheless, when the ground motions, which are used to perform FEM simulations, are selected by the adaptive training, the initial lognormal distribution is disturbed. Therefore, one should be careful

to check the lognormality of the free surface PGA and the floor PGA from FEM simulations for the joint lognormal model in the second stage of the PGA transformation.

Despite this fact, it should be mentioned that, theoretically, any analytical statistical distributions can be used to compute the transformed free surface PGA value and to quantify the uncertainty in the two-step transformation. However, no analytical solution exists and Monte-Carlo simulations are needed to calculate the transformed PGA value and its uncertainty. In addition, the value of $P_f(\alpha)$ cannot be computed from a CDF of a normal distribution, if the uncertainty of the two-step transformation is not assumed lognormally distributed. Again, in this case, the only way to evaluate this $P_f(\alpha)$ is the Monte-Carlo simulation combined with the Nataf transformation (Eq.7.2.2 in Ditlevsen and Madsen (2005)).

3. It is worth mentioning that the likelihood function computed from Eq.27 is, in fact, the 'mean likelihood' considering the PGA transformation uncertainty $\beta_{s\to t}$, analogue to the capacity in the mean fragility curve of Eq.6. In a similar way of defining the non-exceedance confidence interval of fragility curves (Eq.4), the confidence interval of the likelihood function $\tilde{L}$ can also be obtained:

$$\tilde{L}(\boldsymbol{z_s}, \gamma' | \hat{A}_m) = \prod_{i=1}^{n_s} \left[\boldsymbol{\Phi}\left(\frac{\ln \alpha^i_{s\to t} + \beta_{s\to t}\boldsymbol{\Phi}^{-1}(\gamma') - \ln \hat{A}_m}{\beta_R}\right) \right]^{x^i} \left[1 - \boldsymbol{\Phi}\left(\frac{\ln \alpha^i_{s\to t} + \beta_{s\to t}\boldsymbol{\Phi}^{-1}(\gamma') - \ln \hat{A}_m}{\beta_R}\right) \right]^{1-x^i} \tag{31}$$

where $\gamma' \in [0, 1]$ is the confidence level related to the transformed PGA value. This latter modeling leads to the definition of a two-level confidence interval of the posterior fragility curves. The first level is linked to the uncertainty β_U of the capacity, whereas the second level is associated to the uncertainty $\beta_{s\to t}$ of the PGA transformation. Further explorations are necessary for this two-level confidence interval modeling.

4. In the Bayesian updating, as the prior lognormal distribution of the capacity is not a conjugate prior of the likelihood function computed by Eq.28, the posterior distribution $f^{\text{post}}(\hat{A}_m|\boldsymbol{z})$ cannot remain lognormal. A lognormal fit is, thus, applied to $f^{\text{post}}(\hat{A}_m|\boldsymbol{z})$, to be able to provide the values of A_m^{post} and β_U^{post}, which are widely used in engineering practice. In order to quantify the quality and the influence of the lognormal fit, firstly, the probability plot of the true posterior distribution against the fitted lognormal distribution is plotted. The probability plot, shown in Figure 17, compares the quantiles between the true posterior and the fitted lognormal distribution. It can be observed that the quality of the fitting, in terms of the quantile, is acceptable for $\hat{A}_m^{\text{post}}$ between $2g$ and $4g$. But the fitting quality is not very satisfactory at the two ends of the distribution.

   Furthermore, we investigate the influence of the lognormal fitting on the final fragility curves and the confidence intervals. The posterior fragility curves and the confidence intervals can be computed with the true posterior distribution. The computation of the confidence intervals is achieved by identifying the quantiles of the true distribution of $\hat{A}_m^{\text{post}}$:

$$\tilde{P}_f^{\text{True}}(\alpha, \gamma) = \boldsymbol{\Phi}\left(\frac{\ln \alpha - \ln \tilde{A}_m^{\text{True}}(\gamma)}{\beta_R}\right) \tag{32}$$

   where $\tilde{A}_m^{\text{True}}(\gamma)$ denotes the $(1-\gamma)$ quantile of the true $\hat{A}_m^{\text{post}}$. As for the mean fragility curve, no analytical form can be derived when the lognormality of $\hat{A}_m^{\text{post}}$ is not satisfied. Monte-Carlo simulation

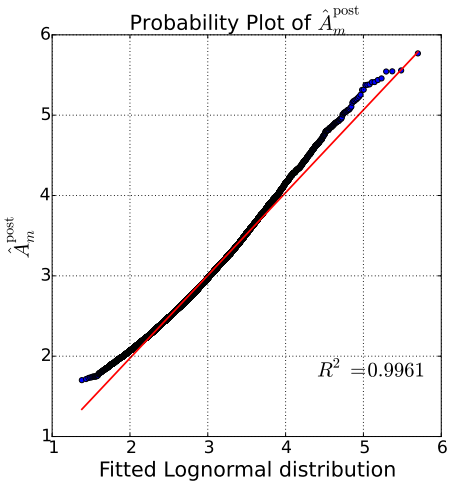

Figure 17: Probability plot of the true posterior distribution against the fitted lognormal distribution

has to be used to sample the aleatory uncertainty term ε_R. The computation of the mean fragility curve with the true posterior distribution is as follows:

(i). Sample N^{post} aleatory uncertainty term ε_R, following $LogN(1, \beta_R^2)$, where N^{post} is the number of the MCMC samples of $\hat{A}_m^{\text{post}}$.

(ii). Evaluate the probability of failure with a given value of α:

$$P_f^{\text{mean,true}}(\alpha) = \frac{1}{N^{\text{post}}} \mathbf{1}[\alpha > \hat{A}_m^{\text{post}} \varepsilon_R] \tag{33}$$

where $\mathbf{1}[\cdot]$ is the indicator function.

(iii). Select another value of α and return to the step (i).

The posterior fragility curves computed by Eqs.32, 33, shown in Figure 18, are compared to the ones obtained with the lognormal fitting. It can be observed that the fragility curves do not show evident

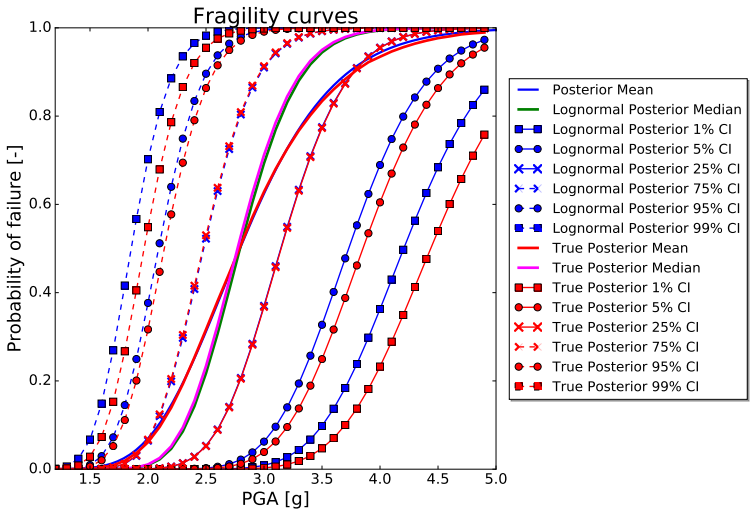

Figure 18: Comparison of fragility curves computed by the true posterior distribution and the fitted lognormal distribution

differences when γ is between 25% and 75%. However, when γ becomes very low (<5%) or very high (>95%), discrepancies start to appear. This phenomenon is due to the difference of the quantiles at the

two ends of the two distributions. Nevertheless, good coherence is obtained for the mean fragility curves: the influence of the lognormal fitting on the mean fragility curve can be neglected in the considered case study.

4. Conclusion

In this paper, a Bayesian updating framework is proposed for considering different sources of information, including numerical simulations, damage data and reference critical values informed from the literature, in the computations of seismic fragility curves. In the framework, the results from numerical simulations are used to determine the prior parameters of the fragility curves. Damage data are, then, integrated to compute the likelihood function for the Bayesian updating. Finally, MCMC is applied to sample the posterior distribution of the updated equipment capacity.

The main contributions of the work are: (i) An ANN adaptive training algorithm is proposed for a more intelligent experimental design to conduct FEM simulations. The adaptive training is based on the prediction uncertainty computed by the delta method. Relying on a relatively large initial population of ground motions, the adaptive ANN aims to select a representative subset of ground motions, which can ensure the performance of the ANN over the whole population; (ii) A method to construct the likelihood function is proposed to deal with existing damage data from the SQUG database. For post-earthquake observational data, the computation of the likelihood function is achieved by estimating an amplification factor and by assuming a joint lognormal distribution between floor PGA values and free surface PGA values. This latter lognormal assumption allows providing an analytical form of the final likelihood function.

The methodology is applied to evaluate the fragility curve of a low-voltage switchgear in a Japanese nuclear power plant Kashiwazaki-Kariwa. The application of the adaptive ANN training provides an improved design of experiments, in which more failure cases have appeared in the FEM simulation results. Then, the construction of the likelihood function with SQUG damage data is realized by the proposed two-stage PGA transformation. The uncertainty related to the transformation is also quantified and integrated in the computation of the likelihood function. Compared to the prior fragility parameters, the posterior capacity of the low-voltage switchgear has increased due to few observed failure cases, whereas the epistemic uncertainty is largely reduced with the additional information from the damage data. These two aspects give rise to a higher value of the high confidence low probability of failure capacity of the studied low-voltage switchgear. The sensitivity analysis has shown that, in this case study, the contribution of the likelihood function to the posterior estimations is predominant, if the assumed value of β_U^{prior} is larger than 0.2.

Acknowledgement

The authors want to thank Hugo Jadot for his comments and suggestions to this work. We would like also to thank the anonymous reviewers for their valuable comments and suggestions. The financial support from the project NARSIS H2020 (New Approach to Reactor Safety ImprovmentS, Horizon 2020) with the grant agreement No. 755439 is gratefully acknowledged.

References

Basu PC, Ravindra MK, Mihara Y. Component fragility for use in PSA of nuclear power plant. Nucl Eng Des 2017;323:209–27. doi:10.1016/j.nucengdes.2016.10.018.

Beck JL, Taflanidis AA. Prior and posterior robust stochastic predictions for dynamical systems using probability logic. International Journal for Uncertainty Quantification 2013;3:271–88. doi:10.1615/Int.J.UncertaintyQuantification.2012003641.

Biasio MD, Grange S, Dufour F, Allain F, Petre-Lazar I. Intensity measures for probabilistic assessment of non-structural components acceleration demand. Earthquake Eng Struct Dyn 2015;44:2261–80. doi:10.1002/eqe.2582.

Bishop CM. Neural Networks for Pattern Recognition. Oxford University Press, 1995.

Buratti N, Minghini F, Ongaretto E, Savoia M, Tullini N. Empirical seismic fragility for the precast RC industrial buildings damaged by the 2012 Emilia (Italy) earthquakes. Earthquake Eng Struct Dyn 2017;48:2317–35. doi:10.1002/eqe.2906.

Campbell KW, Bozorgnia Y. NGA ground motion model for the geometric mean horizontal component of PGA, PGV, PGD and 5% damped linear elastic response spectra for periods ranging from 0.01 to 10 s. Earthquake Spectra 2008;24:139–71. doi:10.1193/1.2857546.

Chryssoloiuris G, Lee M, Ramsey A. Confidence interval prediction for neural network models. IEEE T Neural Networ 1996;7:229–32. doi:10.1109/72.478409.

Clouteau D. Miss 6.5: Manuel Utilisateur. Lab MSSMat, CentraleSupelec; 2005. A software in earthquake engineering and structural dynamics, http://old-www.ecp.fr/mssmat/moyens/moyens_techniques_logiciels/miss/presentation_de_miss.

Code_Aster . Code Analyses des Structures et Thermomécanique pour des Etudes et des Recherches. EDF Group. Opensource Finite Element code, http://www.code-aster.org.

Cornell CA, Jalayer F, Hamburger RO, Foutch DA. Probabilistic basis for 2000 SAC federal emergency management agency steel moment frame guidelines. J Struct Eng 2002;128:526–33. doi:10.1061/(ASCE)0733-9445(2002)128:4(526).

Ditlevsen O, Madsen H. Structural Reliability Methods, 2005.

Echard B, Gayton N, Lemaire M. AK-MCS: An active learning reliability method combining Kriging and Monte Carlo simulation. Struct Saf 2011;33:145–54. doi:10.1016/j.strusafe.2011.01.002.

Ellingwood BR, Kinali K. Quantifying and communicating uncertainty in seismic risk assessment. Struct Saf 2009;31:179–87. doi:10.1016/j.strusafe.2008.06.001.

EPRI . Generic Seismic Ruggedness of Power Plant Equipment (Revision 1). Technical Report; Electric Power Research Institute EPRI, Palo Alto, CA; 1991.

EPRI . Methodology for developing seismic fragilities. Technical Report; Electric Power Research Institute EPRI, Palo Alto, CA; 1994. Report TR-103959.

EPRI . EPRI independent peer review of the TEPCO seismic walkdown and evaluation of the Kashiwazaki-Kariwa nuclear power plants. Technical Report; Electric Power Research Institute EPRI, Palo Alto, CA; 2007. Report TR-1016317.

EPRI . Seismic Fragility Applications Guide Update. Technical Report; Electric Power Research Institute EPRI, Palo Alto, CA; 2009. Report TR-1019200.

EPRI . Assessment of the Use of Experience Data to Develop Seismic Fragilities. Technical Report; Electric Power Research Institute EPRI, Palo Alto, CA; 2014. Report 3002002933.

EPRI . SQUG seismic experience database. Electric Power Research Institute EPRI, Palo Alto, CA; 2016. Http://esqug.epri.com/.

EPRI . Updated Equipment Seismic Capacities from Experience Data for Use in the Fragility Calculations. Technical Report; Electric Power Research Institute EPRI, Palo Alto, CA; 2017. Report 3002011627.

Ferrario E, Pedroni N, Zio E, Lopez-Caballero F. Bootstrapped artificial neural networks for the seismic analysis of structural systems. Struct Saf 2017;67:70–84. doi:10.1016/j.strusafe.2017.03.003.

Gardoni P, Mosalam KM, Kiureghian AD. Probabilistic seismic demand models and fragility estimates for RC bridges. J Earthq Eng 2009;7:79–106. doi:10.1080/13632460309350474.

Gidaris I, Taflanidis AA, Mavroeidis GP. Kriging metamodeling in seismic risk assessment based on stochastic ground motion models. Earthquake Eng Struct Dyn 2015;44:2377–99. doi:10.1002/eqe.2586.

Hastings WK. Monte carlo sampling methods using Markov chains and their applications. Biometrika 1970;57:97–105. doi:10.2307/2334940.

Huang YN, Whittaker A, Luco N. A probabilistic seismic risk assessment procedure for nuclear power plant: (i) Methodology. Nucl Eng Des 2011;241:3966–4003. doi:10.1016/j.nucengdes.2011.06.051.

Hurtado JE, Alvarez DA. Neural-network-based reliability analysis: a comparative study. Comput Methods Appl Mech Eng 2001;191:113–32. doi:10.1016/S0045-7825(01)00248-1.

IAEA . Review of Seismic Evaluation Methodologies for Nuclear Power Plants Based on a Benchmark Exercise. Technical Report; International Atomic Energy Agency; 2013.

Jaiswal K, Wald D, D'Ayala D. Developing empirical collapse fragility functions for global building types. Earthquake Spectra 2011;27:775–95. doi:10.1193/1.3606398.

Jalayer F, Iervolino I, Manfredi G. Structural modeling uncertainties and their influence on seismic assessment of existing RC structures. Struct Saf 2010;32:220–8. doi:10.1016/j.strusafe.2010.02.004.

Jeon JS, Mangalathu S, Song J, DesRoches R. Parameterized seismic fragility curves for curved multi-frame concrete box-girder bridges using Bayesian parameter estimation. J Earthq Eng 2017;0:1–26. doi:10.1080/13632469.2017.1342291.

Jones DR, Schonlau M, Welch WJ. Efficient global optimization of expensive black-box functions. J Global Optimiz 1998;13:455–92. doi:10.1023/A:1008306431147.

Kennedy R, Cornell C, Campell R, Kaplan S, Perla H. Probabilistic seismic safety study of an existing nuclear power plant. Nucl Eng Des 1980;59:315–38. doi:10.1016/0029-5493(80)90203-4.

Koutsourelakis PS. Assessing structural vulnerability against earthquakes using multi-dimensional fragility surfaces: A bayesian framework. Probab Eng Mech 2010;25:49–60. doi:10.1016/j.probengmech.2009.05.005.

Kwag S, Lee JM, Oh J, Ryu JS. Development of system design and seismic performance evaluation for reactor pool working platform of a research reactor. Nucl Eng Des 2014;266:199–213. doi:10.1016/j.nucengdes.2013.10.025.

Lagaros ND, Tsompanakis Y, Psarropoulos PN, Georgopoulos EC. Computationally efficient seismic fragility analysis of geostructures. Comput Struct 2009;87:1195–203. doi:10.1016/j.compstruc.2008.12.001.

Mai CV, Spiridonakos MD, Chatzi EN, Sudret B. Surrogate modelling for stochastic dynamical systems by combining narx models and polynomial chaos expansions. International Journal for Uncertainty Quantification 2016;6:419–30. doi:10.1615/Int.J.UncertaintyQuantification.v6.i4.

Mangalathu S, Heo G, Jeon JS. Artificial neural network based multi-dimensional fragility development of skewed concrete bridge classes. Eng Struct 2018;162:166–76. doi:10.1016/j.engstruct.2018.01.053.

Newmark NM, Hall WJ. Development of criteria for seismic review of selected nuclear power plants. Technical Report; Nuclear Regulatory Commission; 1978. NUREG/CR-0098.

Noh HY, Kiremidjian A, Ceferino L, So E. Bayesian updating of earthquake vulnerability functions with application to mortality rates. Earthq Spectra 2017;33:1173–89. doi:10.1193/081216EQS133M.

Padgett JE, DesRoches R. Methodology for the development of analytical fragility curves for retrofitted bridges. Earthquake Eng Struct Dyn 2008;37:1157–74. doi:10.1002/eqe.801.

Papadopoulos V, Giovanis DG, Lagaros ND, Papadrakakis M. Accelerated subset simulation with neural networks for reliability analysis. Comput Methods Appl Mech Eng 2012;223–234:70–80. doi:10.1016/j.cma.2012.02.013.

Pedroni N, Zio E. An Adaptive Metamodel-Based Subset Importance Sampling approach for the assessment of the functional failure probability of a thermal-hydraulic passive system. Appl Math Model 2017;48:269–88. doi:10.1016/j.apm.2017.04.003.

Reed RD, Marks RJ. Neural Smithing. MIT Press, 1999.

Rivals I, Personnaz L. Construction of confidence intervals for neural networks based on least squares estimation. Neural Networks 2000;13:463–84. doi:10.1016/S0893-6080(99)00080-5.

Rossetto T, Elnashai A. Derivation of vulnerability functions for european-type RC structures based on observational data. Eng Struct 2003;25:1241–63. doi:10.1016/S0141-0296(03)00060-9.

Rota M, Pennab A, C.L.Strobbia . Processing Italian damage data to derive typological fragility curves. Soil Dyn Earthq Eng 2008;28:933–47. doi:10.1016/j.soildyn.2007.10.010.

Rumelhart D, Hinton G, Williams R. Learning Internal Representations by Error Propagation in Parallel Distributed Processing: Explorations in the Microstructure of Cognition. The MIT Press, 1986.

Salome_Meca . Opensource platform for numerical simulation including pre- and post-processing. EDF Group. Https://www.code-aster.org/spip.php?article294.

Shinozuka M, Feng MQ, Lee J, Naganuma T. Statistical analysis of fragility curves. J Eng Mech 2000;126:1224–31. doi:10.1061/(ASCE)0733-9399(2000)126:12(1224).

Singhal A, Kiremidjian AS. Bayesian updating of fragilities with application to RC frames. J Struct Eng 1998;124:922–9. doi:10.1061/(ASCE)0733-9445(1998)124:8(922).

Starck RG, Thomas GG. Overview of SQUG generic implementation procedure (GIP). Nucl Eng Des 1990;123:225–31. doi:10.1016/0029-5493(90)90241-O.

Straub D, Kiureghian AD. Improved seismic fragility modeling from empirical data. Struct Saf 2008;30:320–36. doi:10.1016/j.strusafe.2007.05.004.

Towashiraporn P. Building seismic fragilities using response surface metamodels. Ph.D. thesis; Georgia Institute of Technology; 2004.

Wang Z, Pedroni N, Zentner I, Zio E. Seismic fragility analysis with artificial neural networks: Application to nuclear power plant equipment. Eng Struct 2018;162:213–25. doi:10.1016/j.engstruct.2018.02.024.

Xiao NC, Zuo MJ, Zhou C. A new adaptive sequential sampling method to construct surrogate models for efficient reliability analysis. Reliab Eng Syst Safe 2018;169:330–8. doi:10.1016/j.ress.2017.09.008.

Yoshida N, Kobayashi S, Suetomi I, Miura K. Equivalent linear method considering frequency dependent characteristics of stiffness and damping. Soil Dyn Earthq Eng 2002;22:205–22. doi:10.1016/S0267-7261(02)00011-8.

Zentner I. Numerical computation of fragility curves for NPP equipment. Nucl Eng Des 2010;240:1614–21. doi:10.1016/j.nucengdes.2010.02.030.

Zentner I. A procedure for simulating synthetic accelerograms compatible with correlated and conditional probabilistic response spectra. Soil Dyn Earthq Eng 2014;63:226–33. doi:10.1016/j.soildyn.2014.03.012.

Zentner I, Gündel M, Bonfils N. Fragility analysis methods: Review of existing approaches and application. Nucl Eng Des 2017;323:245–58. doi:10.1016/j.nucengdes.2016.12.021.

Zio E. A study of the bootstrap method for estimating the accuracy of artificial neural networks in predicting nuclear transient processes. IEEE T Nucl Sci 2006;53:1460–78. doi:10.1109/TNS.2006.871662.

Paper III : Wang, Z., Zentner, I., and Zio, E. (2018). Ground motion prediction equations by artificial neural networks with input uncertainties (under review).

Ground motion prediction equations by artificial neural networks with input uncertainties

Zhiyi Wang[a,b,c], Irmela Zentner[a,b], Enrico Zio[c,d]

[a] *EDF Lab Saclay, France*
[b] *Institute for Mechanical Sciences and Industrial Applications, CNRS-EDF-CEA-ENSTA, France*
[c] *Chair on Systems Science and Energetic Challenge, European Foundation for New Energy of EDF, CentraleSupélec, Université Paris-Saclay, France*
[d] *Energy Department, Politecnico di Milano, Italy*

Abstract

Ground motion prediction equations (GMPEs) are used to express seismic intensity measures as a function of source-, path- and site-related parameters. Although functional models are still widely used for their computation, a fully data-driven approach has been recently proposed based on artificial neural networks (ANNs). Moreover, the estimation errors of the predictor parameters (e.g. the magnitude and Vs_{30}) should be accounted for in the development of GMPEs. In the present study, the uncertainty in the input parameters is considered in the computation of GMPEs by ANNs. For this, an algorithm is proposed based on the generalized least squares principle applied to ANNs training. A simulated database is used to validate the approach and to demonstrate the effect of the input parameter uncertainties on the GMPEs. Finally, the proposed model is applied to the RESORCE data collected from Pan-Europe earthquakes. Results show that, by the proper consideration of uncertainty on the input parameters, the total GMPE uncertainties can be reduced by 4-16%, whereas the median predictions remain similar.

Keywords: Ground motion prediction equations; Artificial neural networks; Parameter uncertainty; Generalized least squares; RESORCE database

1. Introduction

Probabilistic seismic hazard analysis (PSHA) is performed to determine the seismic design load of civil structures (Bommer & Abrahamson, 2006). Within PSHA, ground motion prediction equations (GMPEs) provide median values, and associated uncertainty, of seismic intensity measures (IMs), for given values of source-, path- and site-related parameters. With the classical assumption of lognormal distributions of the IMs, seismic hazard curves can be further determined.

The GMPEs are modeled by 'mixed-effects model' with particular functional forms. The underlying model parameters are determined either by the one-stage regression (Abrahamson & Youngs, 1992) or by the two-stage regression (Joyner & Boore, 1993). This can be a limitation if the computation of GMPEs for a new IM is required, as it is necessary to develop new functional models or to determine whether the existing functional forms can be generalized. Furthermore, if additional site proxies are considered, the functional forms need to be adjusted. To overcome these difficulties, non-parametric data-driven methods haven been applied to ground motion prediction. Hermkes et al. (2014) proposes GMPE models based on Gaussian process regression for application to the European RESORCE database. Models based on artificial neural

networks (ANNs) have been developed in the past by Derras et al., with applications to American NGA West database (Derras et al., 2016), RESORCE database (Derras et al., 2014, 2016) and Japanese Kik-Net database (Derras et al., 2017). In Dhanya & Raghukanth (2017), the performance of ANNs is further improved by a genetic algorithm in the computation of GMPEs. Variations of the neural network model, e.g. general regression neural networks and adaptive neuro-fuzzy inference systems, have been tested recently for applicability in the development of GMPEs (Stambouli et al., 2017; Ameur et al., 2018). An advantage of using ANNs for the development of GMPEs is that a vector of IMs can be computed simultaneously, instead of having to develop a different functional model for each individual IM and conduct regression for estimating its parameters.

On the other hand, the existing GMPEs models with ANNs do not consider the uncertainty of input parameters (e.g. magnitude M_w and thirty-meter shear-wave velocity Vs_{30}). In practice, epistemic uncertainties can affect the source-, path- and site-related parameters due to their determination procedures (Moss, 2011). Methods, which consider the epistemic uncertainty of the input parameters, can be divided into three categories. Crude Monte-Carlo simulations are used by Foulser-Piggott (2014), to propagate the uncertainties in the input variables. The values of the uncertain input parameters are sampled from chosen distributions and a number of GMPE regression analyses are conducted with the generated inputs. The variations of the model parameters and model output standard deviations, obtained from the different GMPE models, are analyzed, showing that the GMPE total uncertainty is little impacted by the uncertain inputs, whereas the influence on the GMPE medians can be significant. The second category applies the first order second moment (FOSM) method to the uncertain GMPE model. In this way, the variance-covariance matrix of the mixed-effects model contains supplementary epistemic uncertainty terms. The maximum likelihood problem can be solved by generalized least squares regression. This is the approach taken by Rhoades (1997), Gehl et al. (2011), for treating the uncertainty in M_w and Vs_{30}, respectively. The last category of methods consists in applying Bayesian regression in the development of the GMPEs. The uncertainties in the input parameters are described by Bayesian prior distributions. One can refer to Moss (2011), Stafford (2014), Kuehn & Abrahamson (2017) for more details concerning the Bayesian approach. These studies show a reduction of the total uncertainty σ, for example 5-10% in Moss (2011) and 1-13% in Kuehn & Abrahamson (2017). The reduction is explained by the epistemic uncertainty in the input parameters of the GMPEs.

In this paper, we aim to account for the input parameter uncertainties in the non-parametric ANN-based GMPE models. The approach adopted is the FOSM approach. With this method, we propose a new ANN training algorithm based on the generalized least squares principle. This allows taking into consideration the non-diagonal variance-covariance matrix of the residuals in the ANN training. The proposed algorithm is first validated by a simulated database for verification and, then, applied to the RESORCE database (Akkar et al., 2014b) for pan-European earthquakes.

The paper is organized as follows. Section 2 explains the mathematical modeling and the method for considering of input uncertainties with ANNs. The databases used in this study are presented briefly in Section 3. The proposed algorithm is applied to the simulated database in Section 4, for the purpose of validation of the algorithm and analysis of the influence of the input uncertainties. For real applications, the effect of input uncertainties in the RESORCE database is studied in Section 5. Final conclusions are provided

in Section 6. It has to be pointed out that the objective of this study is to discuss the effect the consideration of the input uncertainties on non-parametric GMPEs models, instead of proposing a new GMPE model for the pan-European area.

2. Treatment of input uncertainties with ANNs

2.1. Mixed-effects model with ANNs

We consider developing GMPEs model based on the following parameters: magnitude M_w, Joyner-Boore distance R_{jb} and thirty-meter shear-wave velocity Vs_{30}.

$$\ln \mathrm{IM}_{ij} \triangleq y_{ij} = \mu(M_{w,i}, \ln R_{jb,ij}, \ln Vs_{30,j}; \boldsymbol{\theta}) + \eta_i + \varepsilon_{ij} \tag{1}$$

where y_{ij} denotes the logarithmic values of the seismic IMs, and μ represents the regression function, i.e. the median of the GMPE model, η_i is the inter-event residual for the ith event, assumed following $\mathcal{N}(0, \tau^2)$, ε_{ij} is the intra-event residual for the jth earthquake signal of the ith event, assumed following $\mathcal{N}(0, \phi^2)$. η_i and ε_{ij} are assumed to be independently distributed. Without loss of generality, the logarithmic values $\ln R_{jb}$ and $\ln Vs_{30}$ are used as the inputs of the GMPE, as in Derras et al. (2014), and $\boldsymbol{\theta}$ is the vector of the parameters of the assumed functional or data-driven model. The total uncertainty σ of the GMPE is

$$\sigma = \sqrt{\tau^2 + \phi^2} \tag{2}$$

In matrix form, Eq.1 becomes:

$$\boldsymbol{y} = \boldsymbol{\mu} + \boldsymbol{Z}\boldsymbol{\eta} + \boldsymbol{\varepsilon} \tag{3}$$

where $\boldsymbol{y}$, $\boldsymbol{\mu}$, $\boldsymbol{\varepsilon}$ are $N \times 1$ matrices, with N being the total number of earthquake records, $\boldsymbol{\eta}$ is the $M \times 1$ inter-event residual matrix, with M the total number of earthquake events, and $\boldsymbol{Z}$ is a $N \times M$ matrix, which allocates the inter-event residual to its corresponding earthquake record. This latter matrix $\boldsymbol{Z}$ is of the form:

$$\boldsymbol{Z} = \begin{bmatrix} \boldsymbol{Z}_{n_1} & \mathbf{0} & \cdots & \mathbf{0} \\ \mathbf{0} & \boldsymbol{Z}_{n_2} & \cdots & \mathbf{0} \\ \vdots & \vdots & \ddots & \vdots \\ \mathbf{0} & \mathbf{0} & \cdots & \boldsymbol{Z}_{n_M} \end{bmatrix}, \quad \boldsymbol{Z}_{n_i} = \underbrace{\begin{bmatrix} 1 & 1 & \cdots & 1 \end{bmatrix}^T}_{n_i \text{ elements}} \tag{4}$$

where n_i $(i = 1, 2, \cdots, M)$ represents the number of earthquake records of the ith event, $\boldsymbol{Z}_{n_i}$ is a column vector with all the n_i elements equal to one, and the index ^{T} denotes the matrix transpose.

The solution of the mixed-effects problem (Eq.1) requires determining the model parameters $\boldsymbol{\theta}$, and the inter- and intra-event uncertainties τ and ϕ, by maximizing the following log-likelihood function $\ln L$:

$$\ln L = -\frac{N}{2} \ln 2\pi - \frac{1}{2} \ln |\boldsymbol{C}| - \frac{1}{2} (\boldsymbol{y} - \boldsymbol{\mu})^T \boldsymbol{C}^{-1} (\boldsymbol{y} - \boldsymbol{\mu}) \tag{5}$$

where $\boldsymbol{C}$ is the variance-covariance matrix of the inter- and intra-event residuals:

$$\boldsymbol{C} = \tau^2 \boldsymbol{Z}\boldsymbol{Z}^T + \phi^2 \boldsymbol{I}_N = \sum_{i=1}^{M} {}^{+} (\phi^2 \boldsymbol{I}_{n_i} + \tau^2 \mathbf{1}_{n_i}) \tag{6}$$

where $\boldsymbol{I}_N$ is the identity matrix of size $N \times N$, the same for $\boldsymbol{I}_{n_i}$. $\mathbf{1}_{n_i}$ is the matrix of ones of size $n_i \times n_i$, $\sum^+$ is the matrix direct sum operation following the notation of Abrahamson & Youngs (1992). More precisely, $\boldsymbol{C}$ is a blockwise-diagonal matrix under the form:

$$\boldsymbol{C} = \begin{bmatrix} \phi^2 \boldsymbol{I}_{n_1} + \tau^2 \mathbf{1}_{n_1} & \mathbf{0} & \cdots & \mathbf{0} \\ \mathbf{0} & \phi^2 \boldsymbol{I}_{n_2} + \tau^2 \mathbf{1}_{n_2} & \cdots & \mathbf{0} \\ \vdots & \vdots & \ddots & \vdots \\ \mathbf{0} & \mathbf{0} & \cdots & \phi^2 \boldsymbol{I}_{n_M} + \tau^2 \mathbf{1}_{n_M} \end{bmatrix} \tag{7}$$

with every block being a $n_i \times n_i$ square matrix:

$$\phi^2 \boldsymbol{I}_{n_i} + \tau^2 \mathbf{1}_{n_i} = \underbrace{\begin{bmatrix} \phi^2 + \tau^2 & \tau^2 & \cdots & \tau^2 \\ \tau^2 & \phi^2 + \tau^2 & \cdots & \tau^2 \\ \vdots & \vdots & \ddots & \vdots \\ \tau^2 & \tau^2 & \cdots & \phi^2 + \tau^2 \end{bmatrix}}_{\text{a } n_i \times n_i \text{ square matrix}} \tag{8}$$

The maximization of Eq.5 is achieved by an iterative expectation-maximization (EM) algorithm. One can refer to Abrahamson & Youngs (1992) for more details about the EM algorithm used to compute the GMPE parameters.

Instead of functional models, ANNs can be used to perform data-driven regressions for the determination of μ, τ^2 and ϕ^2 of the GMPEs. In this study, we use classical feed-forward ANNs, which consist of a set of model parameters $\boldsymbol{\theta}$ and activation functions associated to neuron nodes. The type of activation functions are selected following (Derras et al., 2014): hyperbolic tangent sigmoid functions are used for the hidden layer nodes and linear functions are applied to the output nodes. The model parameters $\boldsymbol{\theta}$ contain the ANN weights $\boldsymbol{w}$ and biases $\boldsymbol{b}$, which are adjusted by training to minimize the cost function, i.e. the square error between $\boldsymbol{y}$ and $\boldsymbol{\mu}$:

$$\boldsymbol{\theta}^* = \begin{bmatrix} \boldsymbol{w}^* \\ \boldsymbol{b}^* \end{bmatrix} = \arg\min_{\boldsymbol{\theta}} \frac{1}{2} \sum_i [\boldsymbol{y}^i - \boldsymbol{\mu}^i(\boldsymbol{x}; \boldsymbol{\theta})]^T [\boldsymbol{y}^i - \boldsymbol{\mu}^i(\boldsymbol{x}; \boldsymbol{\theta})] \tag{9}$$

where $\boldsymbol{x}$ is used to denote the input parameters of ANNs. In the GMPEs computation of Eq.1, this latter $\boldsymbol{x}$ represents the ground motion predictor parameters M_w, $\ln R_{jb}$ and $\ln Vs_{30}$. The index i is the ith output of the ANN, i.e. the ith IM for the GMPEs. The training of ANNs is typically achieved by gradient-based back-propagation algorithms (Rumelhart et al., 1986; Bishop, 1995) to find the optimal $\boldsymbol{\theta}^*$. It is worth mentioning that one assumption of the validity of Eq.9 is that the ANN residuals should be statistically independent and identically distributed (IID). If the residuals are correlated, this correlation should be accounted for in the cost function, which gives rise to a generalized least squares (GLS) problem for the ANN training. This case of correlated ANN residuals is addressed in detail later.

The ANN-based GMPEs computation is divided into the following steps (Derras et al., 2014):

1. Initialization step: train an ANN to determine $\boldsymbol{\theta}$, using $\boldsymbol{x}$ and $\boldsymbol{y}$ as the inputs and outputs of the ANN.
2. With $\boldsymbol{\mu}$ computed from the determined $\boldsymbol{\theta}$, estimate τ^2 and ϕ^2 in maximizing Eq.5.
3. Given $\boldsymbol{\mu}$, τ^2 and ϕ^2, compute η_i using Eq.(10) in (Abrahamson & Youngs, 1992):

$$\eta_i = \frac{\tau^2 \sum_{j=1}^{n_i} y_{ij} - \mu_{ij}}{n_i \tau^2 + \phi^2} \tag{10}$$

4. Train an ANN to determine $\boldsymbol{\theta}$, using $\boldsymbol{x}$ and $\boldsymbol{y}-\boldsymbol{\eta}$ as the inputs and outputs of the ANN.

5. Repeat the steps 2-4 until Eq.5 is maximized.

Normalization and denormalization procedures are performed before and after the ANN training; one can refer to Derras et al. (2014) for more details about this.

Let us study further why a classical ANN training can be applied in this algorithm. By subtracting η_i on both sides of Eq.1, only the residual term ε_{ij} remains on the right-hand side of the equation:

$$y_{ij} - \eta_i = \mu(M_{w,i}, \ln R_{jb,ij}, \ln Vs_{30,j}; \boldsymbol{\theta}) + \varepsilon_{ij} \tag{11}$$

Therefore, the residuals are IID if $\boldsymbol{x}$ and $\boldsymbol{y}-\boldsymbol{\eta}$ are used as the inputs and outputs of the ANN. Then, the algorithm described above is valid when the variance-covariance $\boldsymbol{C}$ is under the form of Eq.7. However, if additional terms appear on the right-hand side of Eq.1, i.e. if $\boldsymbol{C}$ is not blockwise diagonal, a new algorithm is required to solve the mix-effects problem.

2.2. ANN GMPEs models with input uncertainties

The FOSM method, proposed in Rhoades (1997) and Gehl et al. (2011), is used in this study for the consideration of input uncertainties in ANN-based GMPEs model. It consists in introducing the first order Taylor expansion of the GMPE model with input uncertainties. Considering uncertainty on input parameters, the model reads:

$$y_{ij} = \mu(M_{w,i}, \ln R_{jb,ij}, \ln Vs_{30,j}) + \eta_i + \varepsilon_{ij} = \mu(\hat{M}_{w,i} + \delta M_i, \ln R_{jb,ij}, \ln \hat{V}s_{30,j} + \delta Vs_j) + \eta_i + \varepsilon_{ij} \tag{12}$$

Here, $M_{w,i}$ is the true magnitude, $\hat{M}_{w,i}$ denotes the observed magnitude (i.e. with uncertainty) and δM_i is the error related to the measurement. The same holds for Vs_{30}, $\hat{V}s_{30}$ and δVs_j, respectively. The observation errors are assumed to follow normal distributions: $\delta M_i \sim \mathcal{N}(0, \sigma_M^2)$, $\delta Vs_j \sim \mathcal{N}(0, \sigma_{\ln Vs}^2)$. After applying the first order Taylor expansion to Eq.12, one obtains:

$$\begin{aligned} y_{ij} &= \mu(\hat{M}_{w,i} + \delta M_i, \ln R_{jb,ij}, \ln \hat{V}s_{30,j} + \delta Vs_j) + \eta_i + \varepsilon_{ij} \\ &= \mu(\hat{M}_{w,i}, \ln R_{jb,ij}, \ln \hat{V}s_{30,j}) + \delta M_i \frac{\partial \mu}{\partial M_w}|_{\hat{\boldsymbol{x}}} + \delta Vs_j \frac{\partial \mu}{\partial \ln Vs}|_{\hat{\boldsymbol{x}}} + \eta_i + \varepsilon_{ij} \end{aligned} \tag{13}$$

where $\hat{\boldsymbol{x}}$ represents the vector of the observed inputs. Considering that δM_i and δVs_j are independent from each other, the variance-covariance matrix $\boldsymbol{C}$ related to Eq.13 contains the following elements:

1. Diagonal elements C_{kk}: $\tau^2 + \phi^2 + (\frac{\partial \mu}{\partial M_w}|_{\hat{\boldsymbol{x}}_k})^2 \sigma_M^2 + (\frac{\partial \mu}{\partial \ln Vs}|_{\hat{\boldsymbol{x}}_k})^2 \sigma_{\ln Vs}^2$
2. Off-diagonal elements $C^e_{kk'}$, for the records k and k' sharing the same earthquake event: $\tau^2 + (\frac{\partial \mu}{\partial M_w}|_{\hat{\boldsymbol{x}}_k} \frac{\partial \mu}{\partial M_w}|_{\hat{\boldsymbol{x}}_{k'}})\sigma_M^2$
3. Off-diagonal elements $C^s_{kk'}$, for the records k and k' sharing the same observation site: $(\frac{\partial \mu}{\partial \ln Vs}|_{\hat{\boldsymbol{x}}_k} \frac{\partial \mu}{\partial \ln Vs}|_{\hat{\boldsymbol{x}}_{k'}})\sigma_{\ln Vs}^2$
4. Zero for all the other elements.

Given the off-diagonal elements $C^s_{kk'}$, the variance-covariance matrix $\boldsymbol{C}$ is not blockwise-diagonal, so that the EM approach used by Derras et al. (2014) is not applicable in this case. Instead, as mentioned in Gehl et al. (2011), an approach based on the generalized least squares (GLS) is required for the maximization of Eq.5.

Here, the algorithm proposed in Gehl et al. (2011) is adapted for the computation of GMPEs by ANNs trained with correlated residuals. The variance-covariance matrix of the residuals is computed according to

the previous part. In the subsequent parts of this paper, the ANNs trained considering correlated residuals are called GLS ANNs. The cost function for the GLS ANNs reads:

$$E(\boldsymbol{\theta}) = \frac{1}{2}\sum_i [\boldsymbol{y}^i - \boldsymbol{\mu}^i(\boldsymbol{x};\boldsymbol{\theta})]^T [\boldsymbol{C}^i]^{-1} [\boldsymbol{y}^i - \boldsymbol{\mu}^i(\boldsymbol{x};\boldsymbol{\theta})] \tag{14}$$

where $\boldsymbol{C}^i$ is the variance-covariance matrix for the ith IM. By applying the gradient-based minimization $\frac{\mathrm{d}E(\boldsymbol{\theta})}{\mathrm{d}\boldsymbol{\theta}} = 0$, and using Newton-Raphson iterative scheme to solve the non-linear equation, it can be derived that

$$\Delta\theta_k = \left[\sum_i [\boldsymbol{J}_k^i]^T [\boldsymbol{C}_k^i]^{-1} [\boldsymbol{J}_k^i]\right]^{-1} \left[\sum_i [\boldsymbol{J}_k^i]^T [\boldsymbol{C}_k^i]^{-1} [\boldsymbol{r}_k^i]\right] \tag{15}$$

where k is the number of iteration steps. $\boldsymbol{J}_k^i = \frac{\partial \boldsymbol{y}_k^i}{\partial \boldsymbol{\theta}}$ is the Jacobian matrix of size $N \times n_\theta$, with n_θ being the total number of unknown model parameters in the ANNs. $\boldsymbol{r}_k^i = \boldsymbol{y}_k^i - \boldsymbol{\mu}_k^i$ denotes the prediction error at the kth iteration. Furthermore, a damping factor λ, used in the Levenberg-Marquardt algorithm (Marquardt, 1963), is adopted here to stabilize the numerical resolution, yielding:

$$\Delta\theta_k = \left[\sum_i [\boldsymbol{J}_k^i]^T [\boldsymbol{C}_k^i]^{-1} [\boldsymbol{J}_k^i] + \lambda \boldsymbol{I}_{n_\theta}\right]^{-1} \left[\sum_i [\boldsymbol{J}_k^i]^T [\boldsymbol{C}_k^i]^{-1} [\boldsymbol{r}_k^i]\right] \tag{16}$$

Eq.16 becomes a typical Gauss-Newton algorithm when $\lambda = 0$, and it approaches the classical gradient descent for $\lambda = +\infty$ (Marquardt, 1963). A small damping factor may lead to instability of the optimization process, whereas a large λ slows down the convergence speed. A proper choice of λ is realized by cross-validation in this study.

To obtain GMPEs models considering uncertain inputs, we propose the following algorithm :

1. Initialization step $k = 0$: randomly initialize an ANN, and initialize the first variance-covariance matrix $\boldsymbol{C}^i$ with the identity matrix $\boldsymbol{I}$.
2. Compute $\Delta\theta_k$ according to Eq.16. Update the ANN model parameters $\theta_{k+1} = \theta_k + \Delta\theta_k$
3. With the current ANN parameters θ_{k+1}, estimate τ_{k+1}^2 and ϕ_{k+1}^2 in maximizing Eq.5. The maximization is performed with existing numerical optimization tools.
4. Compute the variance-covariance matrix $\boldsymbol{C}_{k+1}$, as described before.
5. Repeat the steps 2-4 until convergence.

The proposed algorithm is developed based on the python open-source ANN package neurolab. To our knowledge, no existing ANN tool-boxes support GLS ANN trainings, as developed in this paper. For the evaluation of the derivatives, we apply the finite difference method to approximate $\frac{\partial \mu}{\partial M}$, $\frac{\partial \mu}{\partial \ln Vs}$, and the back-propagation algorithm (Rumelhart et al., 1986; Bishop, 1995) to compute the Jacobian matrices $\boldsymbol{J}$.

2.3. Determination of inter-event and intra-event residuals

With the determined values of inter-event and intra-event uncertainties τ and ϕ, the inter-event and intra-event residuals can be calculated for every earthquake record. The computation is based on the theory of multi-variate Gaussian distributions. Let us consider the joint distribution of $\boldsymbol{y}$ and $\boldsymbol{\eta}$:

$$\begin{bmatrix}\boldsymbol{y}\\ \boldsymbol{\eta}\end{bmatrix} \sim \mathcal{N}\left(\begin{bmatrix}\boldsymbol{\mu}\\ \boldsymbol{0}\end{bmatrix}, \begin{bmatrix}\boldsymbol{C} & \tau^2\boldsymbol{Z}\\ \tau^2\boldsymbol{Z}^T & \tau^2\boldsymbol{I}_M\end{bmatrix}\right) \tag{17}$$

where $\boldsymbol{C}$ is the variance-covariance matrix computed according to Section 2.2 with the determined values of τ, ϕ and the assumed values of σ_M, $\sigma_{\ln Vs}$. Considering the properties of multi-variate Gaussian distributions, the estimate of the inter-event residual vector $\hat{\boldsymbol{\eta}}$, defined by the expectation of $\boldsymbol{\eta}$ given earthquake observations $\boldsymbol{y}$, is calculated by

$$\hat{\boldsymbol{\eta}} \triangleq \mathbf{E}(\boldsymbol{\eta}|\boldsymbol{y}) = \tau^2 \boldsymbol{Z}^T \boldsymbol{C}^{-1}(\boldsymbol{y} - \boldsymbol{\mu}) \tag{18}$$

where $\mathbf{E}(\cdot)$ is the mathematical operator used to calculate the statistical expectation. It is worth mentioning that Eq.18 is the generalized form of Eq.10, when $\boldsymbol{C}$ is not blockwise diagonal. If the epistemic uncertainties of M_w and Vs_{30} are not modeled, namely if $\boldsymbol{C} = \tau^2 \boldsymbol{Z}\boldsymbol{Z}^T + \phi^2 \boldsymbol{I}_N$ (Eq.7), Eq.10 can be easily derived by applying the relation $\tau^2 \boldsymbol{Z}^T(\tau^2 \boldsymbol{Z}\boldsymbol{Z}^T + \phi^2 \boldsymbol{I}_N)^{-1}(\boldsymbol{y} - \boldsymbol{\mu}) = (\boldsymbol{Z}^T\boldsymbol{Z} + \boldsymbol{I}_M \phi^2/\tau^2)^{-1}\boldsymbol{Z}^T(\boldsymbol{y} - \boldsymbol{\mu})$ (Dempster et al., 1981) and by performing block matrix multiplication.

In the same way, the joint distribution of $\boldsymbol{y}$ and $\boldsymbol{\varepsilon}$ is written as

$$\begin{bmatrix} \boldsymbol{y} \\ \boldsymbol{\varepsilon} \end{bmatrix} \sim \mathcal{N}\left(\begin{bmatrix} \boldsymbol{\mu} \\ \mathbf{0} \end{bmatrix}, \begin{bmatrix} \boldsymbol{C} & \phi^2 \boldsymbol{I}_N \\ \phi^2 \boldsymbol{I}_N & \phi^2 \boldsymbol{I}_N \end{bmatrix} \right) \tag{19}$$

and the estimate of the intra-event residual vector $\hat{\boldsymbol{\varepsilon}}$ is obtained as

$$\hat{\boldsymbol{\varepsilon}} \triangleq \mathbf{E}(\boldsymbol{\varepsilon}|\boldsymbol{y}) = \phi^2 \boldsymbol{C}^{-1}(\boldsymbol{y} - \boldsymbol{\mu}) \tag{20}$$

3. Case study databases

3.1. RESORCE database

The RESORCE (Reference database for seismic ground motion in Europe) database collects earthquake records in broader European areas for researches and applications in earthquake engineering. Current RESORCE database contains 5882 processed accelerograms, collected from 1814 events and 1540 stations (Akkar et al., 2014b). For the computation of the GMPE, we select ground motion records with $M_w \in [3.5, 7.6]$ and $R_{jb} \in [0, 200]$km. We focus the analyses on shallow crustal earthquakes, with depth less than 30 km. Vs_{30} is considered as the only site-related parameter in this study. Ground motions without Vs_{30} or R_{jb} values are not retained for the computation of the GMPEs. After applying these criteria, the final dataset consists of 893 earthquake records, collected from 269 events. The selected ground motion records were measured on 289 different stations. The distribution of M_w, R_{jb} and Vs_{30} of the selected dataset is illustrated in Figure 1. It can be observed that most of the earthquake signals are concentrated in the range of M_w values from 4.5 to 6.5. More near-fault earthquakes are selected than far-fault earthquakes. Few records are measured on stations with $Vs_{30} > 720$m/s.

We focus on the computation of GMPEs based on M_w, $\ln R_{jb}$ and $\ln Vs_{30}$, following Derras et al. (2014). The depth and the type of the fault are not included in the GMPE, since the sensitivity analysis conducted by Derras et al. (2014) reveals that the contribution of these two parameters to the IMs is negligible. Eighteen IMs are selected as the outputs of the GMPEs, including PGA (peak ground acceleration), PGV (peak ground velocity) and sixteen different 5% damping spectral accelerations: Sa(0.3Hz), Sa(0.5Hz), Sa(0.67Hz), Sa(1Hz), Sa(1.3Hz), Sa(2Hz), Sa(2.5Hz), Sa(3.3Hz), Sa(4.2Hz), Sa(5Hz), Sa(6.7Hz), Sa(10Hz), Sa(13.3Hz), Sa(20Hz), Sa(33.3Hz) and Sa(100Hz). The geometrical mean of the two horizontal components is used as the IM value.

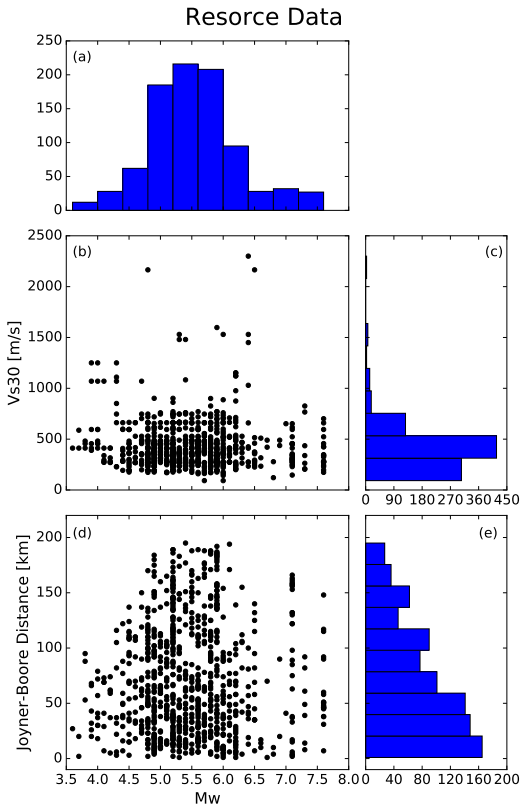

Figure 1: Distribution of M_w, R_{jb} and Vs_{30} of the selected earthquake records in RESORCE database. (a) Histogram of M_w of the selected RESORCE dataset; (b) Scatter plot of the selected dataset in M_w-Vs_{30} space; (c) Histogram of Vs_{30}; (d) Scatter plot of the selected dataset in M_w-R_{jb} space; (e) Histogram of R_{jb}.

3.2. Simulated database

A simulated database is constructed to assess the methodology and to analyze in a controlled way the effect of the input uncertainties on τ and ϕ. Based on the magnitude, distance and site parameters in the RESORCE database, the simulated database is built with assumed inter- and intra-event uncertainties $\tau = 0.2$ and $\phi = 0.3$. By comparing the values of τ and ϕ computed by the proposed algorithm to those used to generate the database, the accuracy of the methodology can be checked. In addition, we perform ten different realizations of the Monte Carlo sampling of inter- and intra-event residuals. The purpose is to evaluate the standard deviations linked to the estimation of inter- and intra-event uncertainties. The construction of the simulated database has been done as follows:

1. From 893 selected RESORCE earthquake records, extract $\hat{M}_w$, R_{jb} and $\hat{V}s_{30}$ values. The parameters are denoted by the symbol $\hat{}$ since they are observed or measured values.
2. Sample δM and δVs with $\sigma_M = 0.1$, $\sigma_{\ln Vs} = 0.3$, respectively. The real values of M_w and Vs_{30} are obtained by $M_w = \hat{M}_w + \delta M$, $\ln Vs_{30} = \ln \hat{V}s_{30} + \delta Vs$.
3. Compute the median of the $\ln \mathrm{IM}$ by the simplified GMPE model used by Koufoudi et al. (2015). The values of relevant coefficients are listed in Table 1.

$$\mu(\ln \mathrm{IM}) = a_1 + a_2(M_w - c_1) + a_3(8.5 - M_w^2) + [a_4 + a_5(M_w - c_1)] \ln \sqrt{R_{jb}^2 + a_6^2} + b_1 \ln(\frac{Vs_{30}}{760}) \quad (21)$$

4. Sample inter-event residual η_i and intra-event residual ε_{ij} with $\tau = 0.2$, $\phi = 0.3$, respectively.
5. Compute the intensity measure values with $\ln \mathrm{IM}_{ij} = \mu_{ij}(\ln \mathrm{IM}) + \eta_i + \varepsilon_{ij}$.
6. Repeat the steps 4-5 ten times for different realizations of residuals, so that ten groups of simulated $\ln \mathrm{IM}$ values are obtained.

A simulated database, generated by ten realizations of inter- and intra-event residuals, is finally obtained.

Table 1: Values of coefficients used to build the simulated database. These values are obtained by computing the GMPE model for RESORCE PGA values with the functional form of Eq.21.

a_1	a_2	a_3	a_4	a_5	a_6	b_1	c_1
-3.26	1.557	0.1185	-2.565	0.2575	-7.53	-0.414	1.708

4. Application to the simulated database

The objective of this section is to verify the performance of the proposed algorithm in Section 2.2 by means the simulated database, which is generated with assumed values of τ and ϕ. The impact of the input uncertainties on the final determination of τ and ϕ is also discussed.

Three types of analyses are conducted based on the simulated database:

1. Computation of the GMPE with respect to the real inputs M_w, $\ln R_{jb}$ and $\ln Vs_{30}$.
2. Computation of the GMPE with respect to the uncertain inputs $\hat{M}_w$, $\ln R_{jb}$ and $\ln \hat{V}s_{30}$, but without accounting for the uncertainties of on the input parameters.
3. Computation of the GMPE with respect to the uncertain inputs $\hat{M}_w$, $\ln R_{jb}$ and $\ln \hat{V}s_{30}$, modeling the input uncertainties with standard deviations $\sigma_M = 0.1$, $\sigma_{\ln Vs} = 0.3$ in the computation of GMPEs. This analysis is name by 'uncertain modeling' in the sequel.

For each type of analysis, the computation of GMPE is conducted with two models, the functional model of Eq.21 and a non-parametric ANN model. The ANN model consists of 3 input nodes, 5 hidden layer nodes, and 1 output. The first two types of analyses are performed with the algorithms of Abrahamson & Youngs (1992) and Derras et al. (2014), applied to the functional model and ANN model, respectively. Regarding the uncertain models, the functional GMPE regression is based on the GLS algorithm of Gehl et al. (2011), whereas the ANN uncertain model is built with the algorithm newly proposed in this study. The value of the damping factors λ is set to 10, estimated from the 5-fold cross-validation results of the GLS ANN training when $\boldsymbol{C} = \boldsymbol{I}$ (Figure 2).

The three types of analyses are carried out for all of the ten simulated datasets. We estimate the mean values of the inter- and intra-event uncertainties, as well as their standard deviations from the results of the ten datasets. The values of τ, ϕ and the total uncertainty σ determined for different analyses are shown in Table 2. The values of τ and ϕ are determined by the mentioned algorithms and σ is calculated by $\sigma = \sqrt{\tau^2 + \phi^2}$. The values of the standard deviations are reported after the $\pm$ symbol. The results of Table 2 show the influence of the input uncertainties on the values of τ and ϕ of the GMPEs computation. It can be concluded that:

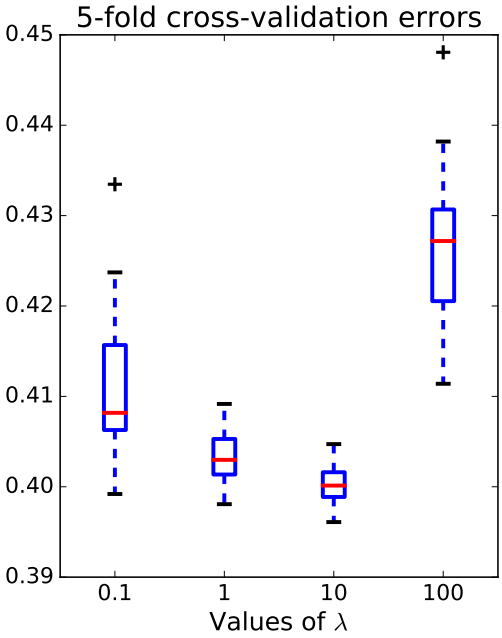

Figure 2: 5-fold cross-validation results for different values of λ

Table 2: Results of inter-event uncertainties τ and intra-event uncertainties ϕ for the simulated database

Analysis	Model	τ	ϕ	σ
Reference	-	0.2	0.3	0.36
True input values	Functional model	0.195 ± 0.023	0.297 ± 0.007	0.356 ± 0.012
	ANN	0.194 ± 0.023	0.296 ± 0.007	0.355 ± 0.012
Observed input values	Functional model	0.239 ± 0.021	0.322 ± 0.008	0.401 ± 0.013
	ANN	0.235 ± 0.020	0.320 ± 0.009	0.397 ± 0.013
$\sigma_M = 0.1$, $\sigma_{\ln Vs} = 0.3$	Functional model	0.2 ± 0.024	0.297 ± 0.008	0.359 ± 0.014
	ANN	0.198 ± 0.023	0.298 ± 0.008	0.358 ± 0.013

1. Both ANNs and functional models provide similar estimates of the inter- and intra-event uncertainties. As the functional model is the same as the one used to generate the synthetic database, this means that the ANN can well approximate the real model in the considered case study.
2. With the true input values of M_w and Vs_{30}, both the functional model and the ANN provide good estimation of the inter- and intra-event uncertainties.
3. However, if the observed values of $\hat{M}_w$ and $\hat{V}s_{30}$ are used as the inputs of the GMPEs, and if the uncertainties associated to the observed values are not modeled, the values of τ and ϕ are overestimated (0.235 compared to 0.2 for τ, 0.320 compared to 0.3 for ϕ). This is because the input uncertainties are propagated implicitly into the GMPE model uncertainty during the GMPE computation procedure. In addition, the true values of τ and ϕ fall outside the ± 1 standard deviation range of values.
4. On the other hand, when the input uncertainty is taken into account, the overestimation is corrected by the uncertainty modeling, for both the functional model and the ANN model. This shows the necessity of modeling the input uncertainties in the GMPEs computation: otherwise, it may lead to overestimation of the inter-event and intra-event uncertainties. The proposed algorithm for the consideration of input uncertainties with ANN is also validated.

5. Application to RESORCE database

For the application of the input uncertainty modeling to the RESORCE dataset, the 893 selected earthquake records are divided into two sets: A training set consisting of 720 ground motions and a validation set with 173 records. The training set is used to compute the GMPEs and the corresponding inter- and intra-event uncertainty. The computed GMPEs model is validated on the validation set.

The ANN architecture used to compute the GMPEs is summarized as follows. The ANN has three input parameters: $\hat{M}_w$, R_{jb} and $\hat{V}s_{30}$. The magnitude and the shear-wave velocity are denoted with $\hat{}$, since they are considered as the observed uncertain input parameters. Five hidden layer nodes are selected, the same as Derras et al. (2014). The damping factor λ is set to 100 from the 5-fold cross-validation executed on the 720 training data with $\boldsymbol{C}^i = \boldsymbol{I}$ $(i = 1, 2, ..., 18)$. We assume that uncertainties associated to $\hat{M}_w$ and $\ln \hat{V}s_{30}$ are $\sigma_M = 0.1$, $\sigma_{\ln Vs} = 0.3$, as in Kuehn & Abrahamson (2017). The natural logarithmic values of the eighteen IMs are used as the outputs for the GMPEs computation. The damping ratio used to compute the spectral accelerations is 5%.

5.1. Results

Two analyses have been performed in the computation of the GMPEs: (i) A GMPE computed directly from $\hat{M}_w$, $\ln R_{jb}$, $\ln \hat{V}s_{30}$ and 18 parameters of $\ln$ IM; (ii) A GMPE with the same input-output parameters as the first one. The uncertainties on $\hat{M}_w$ and $\ln \hat{V}s_{30}$ are modeled with the algorithm proposed in Section 2.2. We compare the results of these two analyses to those obtained with existing RESORCE GMPE models, including the models of Akkar et al. (2014a), Bindi et al. (2014), Bora et al. (2014), Derras et al. (2014), Hermkes et al. (2014). The results of these five existing GMPEs are extracted from Douglas et al. (2014).

We first show the inter-event uncertainty τ, intra-event uncertainty ϕ and the total uncertainty σ of the two analyses. The τ, ϕ, σ for the 16 frequency-dependent spectral accelerations are illustrated in Figure 3. The legend 'ANN with uncertainty' means that the corresponding results are computed by ANN with input uncertainty modeling. The reduction ratio in Figure 3d calculates the relative reduction of the GMPE output standard deviations, considering the uncertain input parameters. For example:

$$r_\sigma = \frac{\sigma_{\text{ANN}} - \sigma_{\text{ANN,uncertain}}}{\sigma_{\text{ANN}}} \tag{22}$$

where r_σ represents the reduction ratio of the total uncertainty σ. In addition, the GMPE uncertainty values of PGA, PGV and three spectral accelerations Sa(0.5Hz), Sa(3.3Hz) and Sa(20Hz), representing three different frequency ranges, are listed in Table 3.

From the results of Figure 3 and Table 3, it can be clearly observed that:

1. The order of magnitude of the determined τ, ϕ and σ of both ANN models stays coherent with other existing RESORCE GMPE models. The intra-event uncertainty is predominant in comparison with the inter-event uncertainty. As different GMPEs are computed with different data and different types of model, one cannot expect a perfect agreement between the results in this study and the results from other GMPEs.
2. A clear reduction of τ, ϕ and σ can be seen with the input uncertainty modeling. This is in agreement with the results obtained with the simulated database. The maximum r_σ can reach 0.16, i.e. 16%

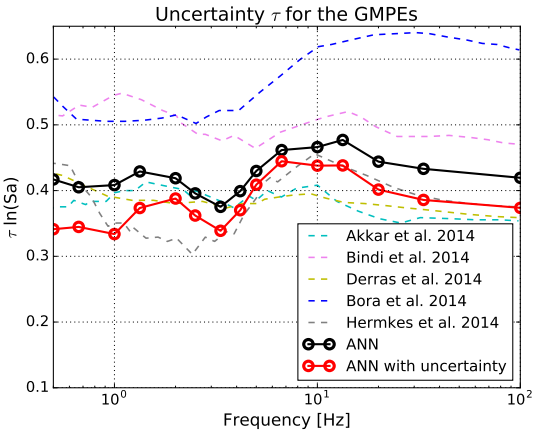

(a) Inter-event uncertainty for RESORCE data

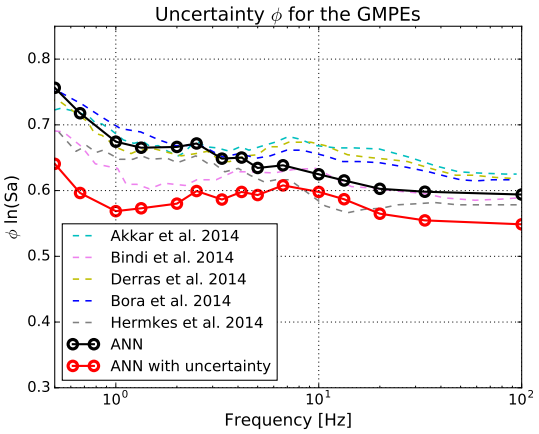

(b) Intra-event uncertainty for RESORCE data

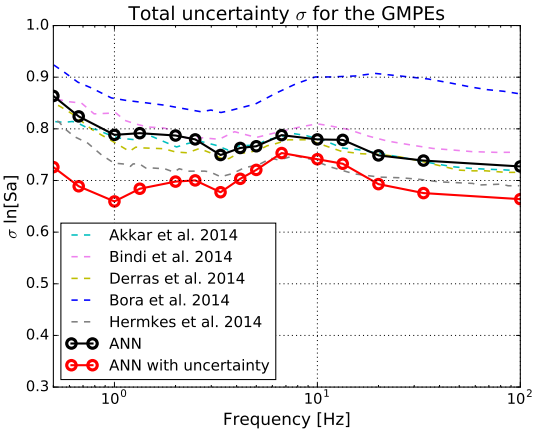

(c) Total uncertainty for RESORCE data

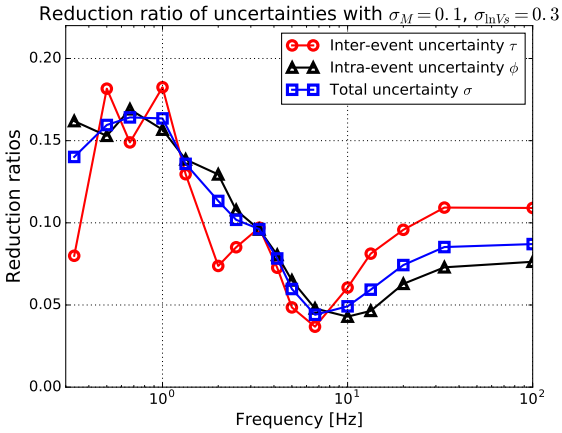

(d) Reduction ratio with the consideration of input uncertainties

Figure 3: Inter-event, intra-event and total uncertainties determined with the RESORCE data

Table 3: τ, ϕ and σ values for PGA, PGV, Sa(0.5Hz), Sa(3.3Hz) and Sa(20Hz)

IMs	Uncertainties	ANN	ANN with uncertainty	Reduction ratio $r \times 100\%$
PGA	τ	0.420	0.376	10.48%
	ϕ	0.593	0.546	7.93%
	σ	0.726	0.663	8.68%
PGV	τ	0.394	0.313	20.56%
	ϕ	0.600	0.539	10.17%
	σ	0.718	0.623	13.23%
Sa(0.5Hz)	τ	0.417	0.341	18.23%
	ϕ	0.756	0.641	15.21%
	σ	0.864	0.723	16.32%
Sa(3.3Hz)	τ	0.375	0.339	9.70%
	ϕ	0.649	0.586	9.59%
	σ	0.749	0.678	9.62%
Sa(20Hz)	τ	0.444	0.401	9.68%
	ϕ	0.603	0.565	6.30%
	σ	0.749	0.693	7.48%

according to Figure 3d. The reduced part of τ, ϕ is, in fact, explained by the epistemic uncertainties introduced in the magnitude and in the share-wave velocity, which is modeled by the first order Taylor expansion with the FOSM modeling. Qualitatively, the reduction is more significant in the low frequency range than in the high frequency range. This phenomenon is further addressed in the 'Discussion' subsection.

The median GMPEs predictions for both ANN models are also plotted with two different scenarios: (i) $M_w = 5, R_{jb} = 10\text{km}, Vs_{30} = 760\text{m/s}$ and (ii) $M_w = 7$, $R_{jb} = 10\text{km}$, $Vs_{30} = 270\text{m/s}$. The comparisons between the predictions of the ANN models and other existing models are illustrated in Figure 4. The magnitude scaling and the distance decay of PGA and Sa(1Hz) are shown in Figure 5 and Figure 6, respectively. The magnitude scaling is computed with R_{jb}=30km, Vs_{30}=760m/s. The RESORCE data with $R_{jb} = 30 \pm 20\text{km}$, $Vs_{30} = 760 \pm 100\text{m/s}$ are also visualized in Figure 5. For the distance decay of PGA and Sa(1Hz), we choose $M_w = 5$, $Vs_{30} = 270\text{m/s}$ to demonstrate the impact of distance on the median predictions. The data plotted in Figure 6 contain the earthquake motions of $M_w = 5 \pm 0.2$, $Vs_{30} = 270 \pm 50\text{m/s}$.

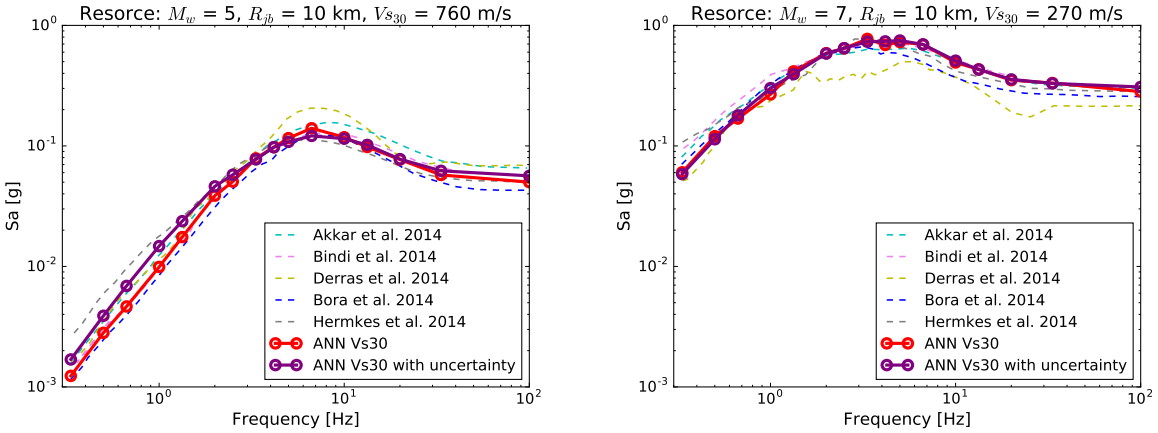

(a) $M_w = 5, R_{jb} = 10\text{km}, Vs_{30} = 760\text{m/s}$ (b) $M_w = 7$, $R_{jb} = 10\text{km}$, $Vs_{30} = 760\text{m/s}$

Figure 4: Comparison of median predictions of the two ANN GMPEs to existing models

In addition, we compute the inter-event and intra-event residuals of the ANN model with input uncertainty by Eq.18 and Eq.20. The results are compared to those of the ANN model without input uncertainty in Figure 7 and Figure 8, for PGA and Sa(1Hz), respectively.

Several conclusions can be drawn from Figures 4-8:

1. The ANN GMPE models, computed with or without the consideration of the input uncertainties, provide similar median predictions. This is coherent with what has been observed by Kuehn & Abrahamson (2017) using Bayesian regression. Additionally, the order of magnitude of the median predictions is in agreement with existing GMPEs computed on the basis of RESORCE database.
2. Both ANN models exhibit non-linear magnitude scaling behaviors. The effect of the magnitude scaling is less evident for PGA (an IM for high frequency range) than Sa(1Hz) (an IM for low frequency range). Although some differences exist between the ANN models and other GMPEs, the ANN models remain in the range of predictions from the other GMPEs, as shown in Figure 5 and Figure 6. Besides,

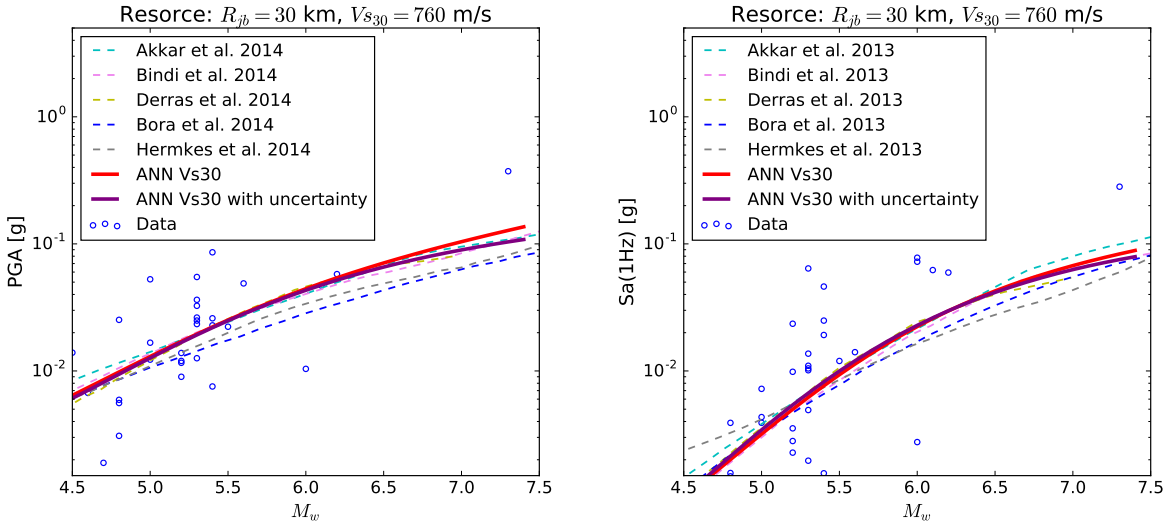

(a) Magnitude scaling of PGA, $R_{jb} = 30\text{km}, Vs_{30} = 760\text{m/s}$

(b) Magnitude scaling of Sa(1Hz), $R_{jb} = 30\text{km}$, $Vs_{30} = 760\text{m/s}$

Figure 5: Magnitude scaling of PGA and Sa(1Hz). The data are selected from the earthquake records with $R_{jb} \in [10\text{km}, 50\text{km}]$ and $Vs_{30} \in [660\text{m/s}, 860\text{m/s}]$

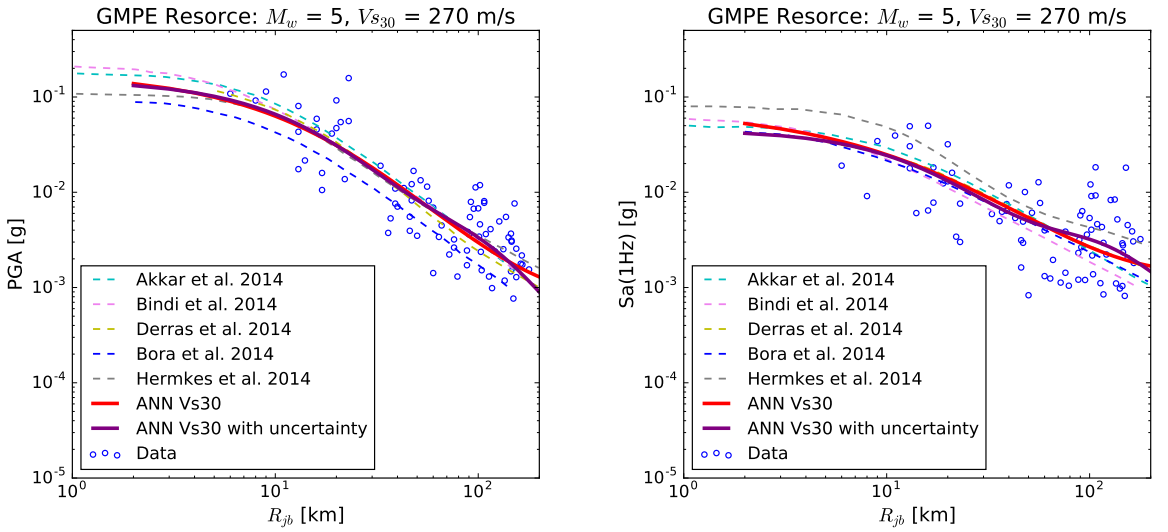

(a) Distance decay of PGA, $M_w = 5, Vs_{30} = 270\text{m/s}$

(b) Distance decay of Sa(1Hz), $M_w = 5$, $Vs_{30} = 270\text{m/s}$

Figure 6: Distance decay of PGA and Sa(1Hz). The data are selected from the earthquake records with $M_w \in [4.8, 5.2]$ and $Vs_{30} \in [220\text{m/s}, 320\text{m/s}]$

considering the data cloud plotted in Figure 5 and Figure 6, the ANN models provide satisfactory regression results.

3. It can be clearly observed that the dispersion of the residuals is less important for the ANN model with input uncertainty than the classical ANN model. This is due to the reduction of the values of τ and ϕ resulted from the modeling of the input epistemic uncertainties. The reduction effect is more evident for Sa(1Hz) than PGA.

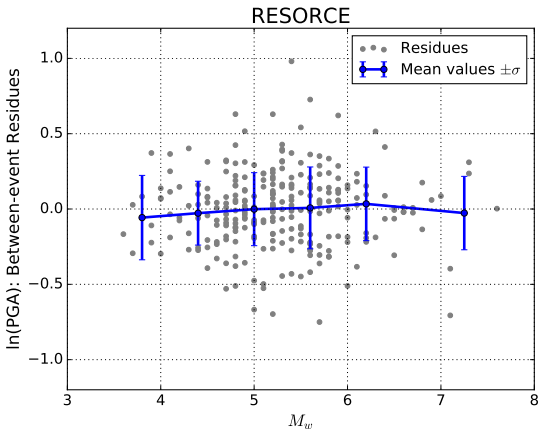

(a) Inter-event residuals for PGA computed from the ANN model with input uncertainties

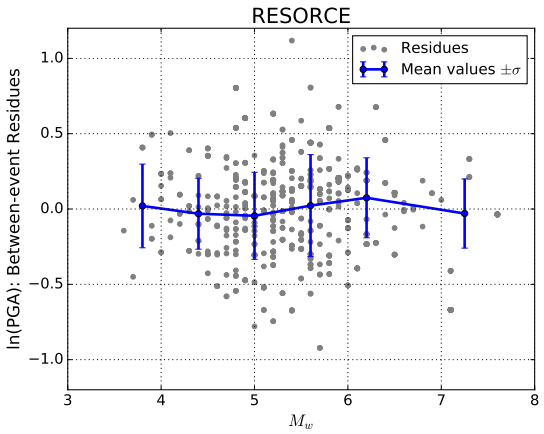

(b) Inter-event residuals for PGA computed from the ANN model without input uncertainties

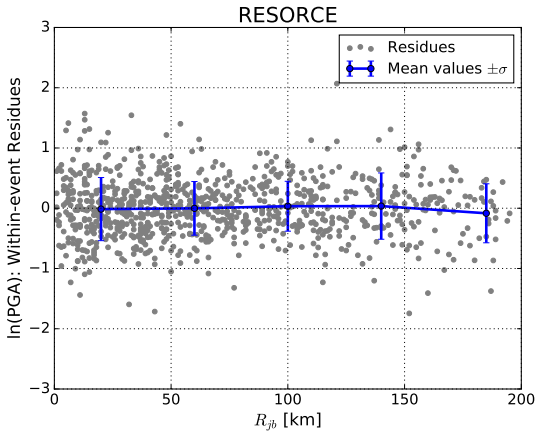

(c) Intra-event residuals for PGA computed from the ANN model with input uncertainties

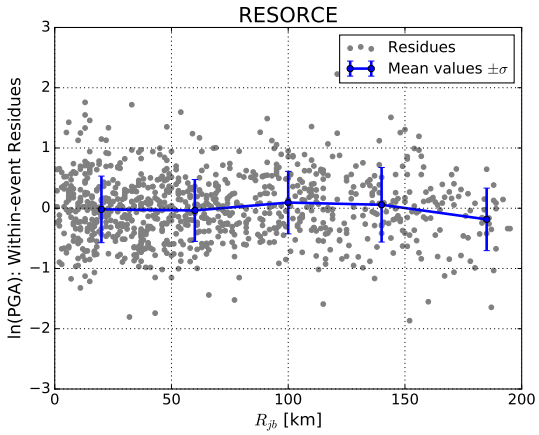

(d) Intra-event residuals for PGA computed from the ANN model without input uncertainties

Figure 7: Inter-event and intra-event residuals of PGA of the ANN input uncertain model, in comparison to the ANN model without input uncertainties

Finally, we validate the ANN model with input uncertainty using the 173 validation data. We recall that the validation dataset is not used to train the ANN model in the training process. Computed on the validation dataset, the value of the log-likelihood function of the ANN model with input uncertainty is -3646.48, larger than -3673.78 obtained without considering input uncertainty. The number of the validation data and the ANN architecture are the same for both models. In consequence, a larger value of the log-likelihood results in smaller values of AIC (Akaike information criterion (Akaike, 1974)) and BIC (Bayesian information criterion (Schwarz, 1978)). Better models are characterized by smaller AIC and BIC values, which shows the advantage of the uncertain input ANN model over the original ANN model (Table 4). In Figure 9, the predictions of the uncertain input ANN model are compared to the original IM values of the database, for both PGA and Sa(1Hz). It can be concluded that the data clouds are located in the neighborhood of the diagonal '1-1' line, implying that the predictions of the uncertain input ANN model are satisfactory, for both PGA and Sa(1Hz).

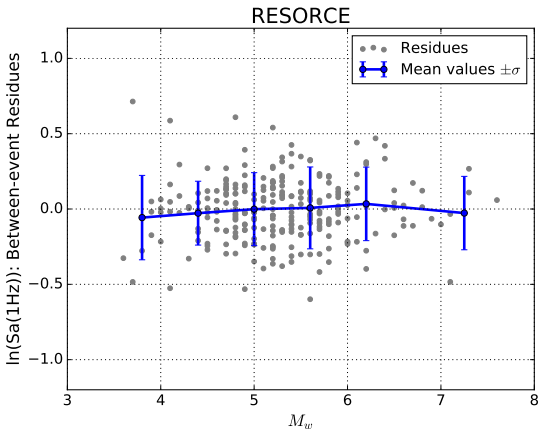

(a) Inter-event residuals for Sa(1Hz) computed from the ANN model with input uncertainties

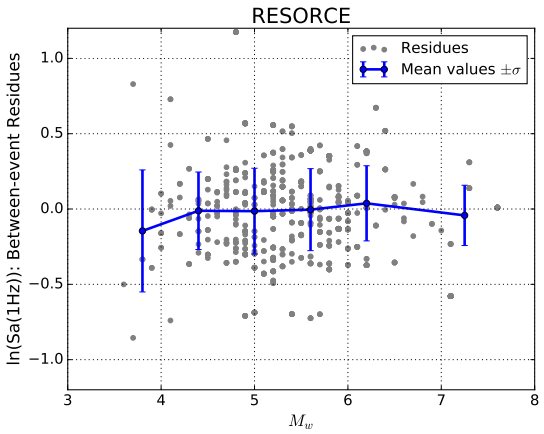

(b) Inter-event residuals for Sa(1Hz) computed from the ANN model without input uncertainties

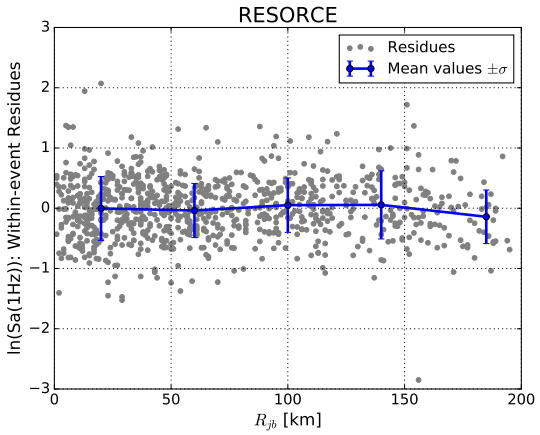

(c) Intra-event residuals for Sa(1Hz) computed from the ANN model with input uncertainties

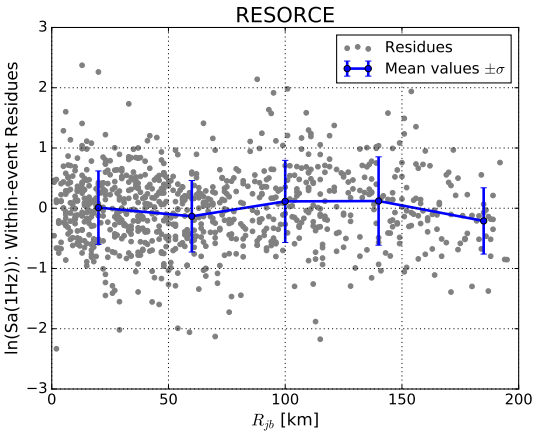

(d) Intra-event residuals for Sa(1Hz) computed from the ANN model without input uncertainties

Figure 8: Inter-event and intra-event residuals of Sa(1Hz) of the ANN input uncertain model, in comparison to the ANN model without input uncertainties

Table 4: Performance of ANN models with the validation dataset

Models	Log-likelihood	AIC	BIC
ANN without input uncertainties	-3673.78	7675.56	8192.70
ANN with input uncertainties	-3646.48	7620.96	8138.10

5.2. Discussions

Previous results show that the ANN model considering input uncertainties on M_w and Vs_{30} provides satisfactory regression performance with the RESORCE data. Moreover, a reduction of the GMPE uncertainty can be obtained by modeling the input uncertainties. However, there are some aspects which need to be discussed concerning this approach.

1. In our approach, we do not further separate the intra-event uncertainty into the single-site uncertainty and the site-to-site uncertainty (Baltay et al., 2017), for being able to compare the computed uncertainty values with those of existing RESORCE GMPE models. Besides, the classical ANN training in the

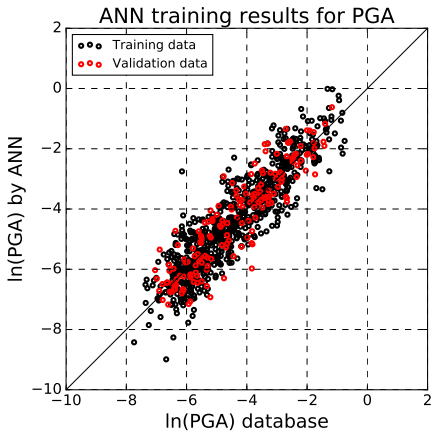

(a) Training and validation results of the uncertain input ANN model for PGA

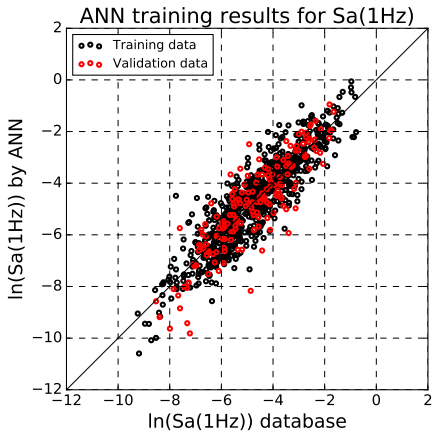

(b) Training and validation results of the uncertain input ANN model for Sa(1Hz)

Figure 9: Comparison between predictions of the uncertain input ANN model and the values of IMs of the database, for both training dataset and validation dataset

mixed-effects problem proposed by Derras et al. (2014) does not allow a further decomposition of the intra-event uncertainty. This latter decomposition, however, can be achieved by the GLS ANN training.

2. The present approach relies on a prior estimation of the input uncertainties. Different estimations of the uncertainties associated to M_w and Vs_{30} can impact the final values of τ and ϕ. To analyze this, different values of σ_M are $\sigma_{\ln Vs}$ are selected to conduct the computation of uncertain input ANN GMPE models. First, we fix the value of $\sigma_{\ln Vs}$ to 0.3. The value of σ_M is varied to 0.15 and 0.2. The corresponding reduction ratios with the variation of σ_M are plotted in Figure 10. It can be observed that the inter-event uncertainty τ decreases with increasing values of σ_M and that the variation of σ_M hardly influences the intra-event uncertainty ϕ, which is consistent with the work of Rhoades (1997). However, when σ_M is set to 0.2, the reduction ratios of the inter-event uncertainty can reach 50% to 70% in low frequency ranges. Different values of σ_M can give rise to very different estimations of the inter-event uncertainty. A second analysis is performed by fixing the value of σ_M to 0.1. Two additional values of $\sigma_{\ln Vs}$ (0.1 and 0.2) are selected for uncertain input ANN regression. It can be seen from Figure 11 that the intra-event uncertainty is mainly influenced by $\sigma_{\ln Vs}$.
3. It can be observed in Figure 3, Figure 10 and Figure 11 that, qualitatively, the reduction of the uncertainty is more important in the low frequency range than in the high frequency range. One reason is that the absolute values of the derivatives $\frac{\partial \mu}{\partial M_w}$ and $\frac{\partial \mu}{\partial \ln Vs_{30}}$ are larger for low frequency spectral accelerations than high frequency ones (Abrahamson & Silva, 2007). Considering the FOSM formulation of Eq.13, a large value of the derivative results in a large adjustment of the residuals. We show the derivatives $\frac{\partial \mu}{\partial M_w}$ and $\frac{\partial \mu}{\partial \ln Vs_{30}}$ for Sa(0.5Hz), Sa(3.3Hz) and Sa(20Hz) in Figure 12. The negative values of $\frac{\partial \mu}{\partial \ln Vs_{30}}$ are justified by the fact that the site effect is more evident if the soil is softer, so that the seismic intensity measures increase. The derivatives in Figure 12 show higher absolute values for the low frequency spectral acceleration than for the high frequency one.
4. In spite of the similarity of the median predictions of the two ANN models, the fact that the reduced

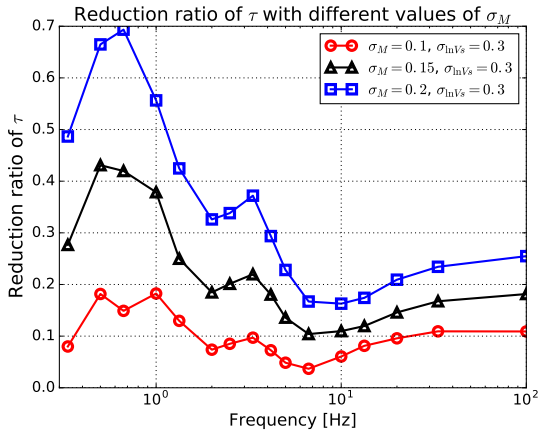

(a) Influence of σ_M on the inter-event uncertainty τ

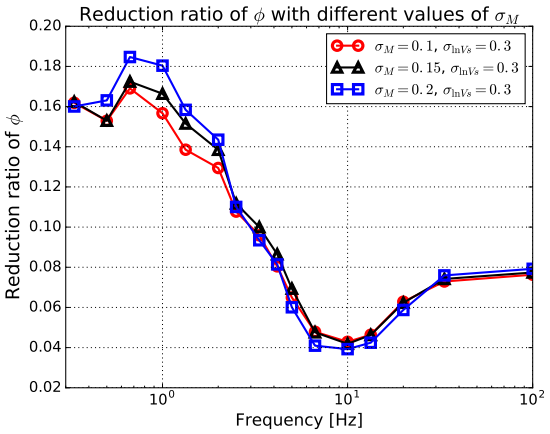

(b) Influence of σ_M on the intra-event uncertainty ϕ

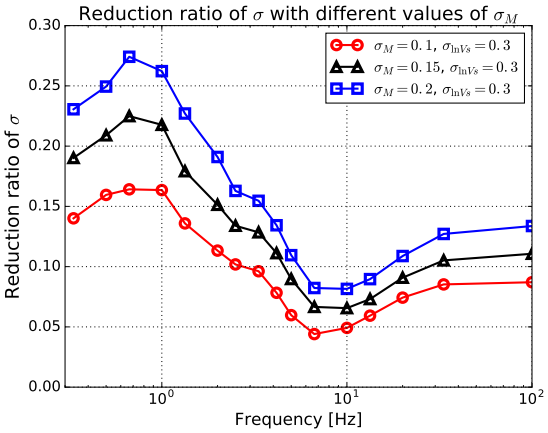

(c) Influence of σ_M on the total uncertainty σ

Figure 10: Influence of different values of σ_M on the reduction ratios of τ, ϕ and σ

value of σ, introduced by modeling the input uncertainty, can lead to different results for the computation of the hazard curves, according to Bommer & Abrahamson (2006). This can eventually impact the results of seismic risk assesment and it shows the necessity of considering input uncertainties, if they exist, for the development of GMPEs.

5. In constrast to the Bayesian regression used in Moss (2011) and Kuehn & Abrahamson (2017), the approach proposed in this paper does not allow an appropriate posterior estimation of the true values of M_w and Vs_{30}. This can be regarded as a limitation of the FOSM method compared to Bayesian regression. However, the application of Bayesian regression to ANNs within the context of the mixed-effects model is not trivial.

6. Summary & Conclusions

In this paper, an approach to consider input parameter uncertainties is presented on the basis of non-parametric ANN regression for the computation of ground motion prediction equations. Based on the first order second moment method, the variance-covariance matrix contains off-diagonal terms which are introduced by the input parameter epistemic uncertainties. An ANN training algorithm is proposed based on the

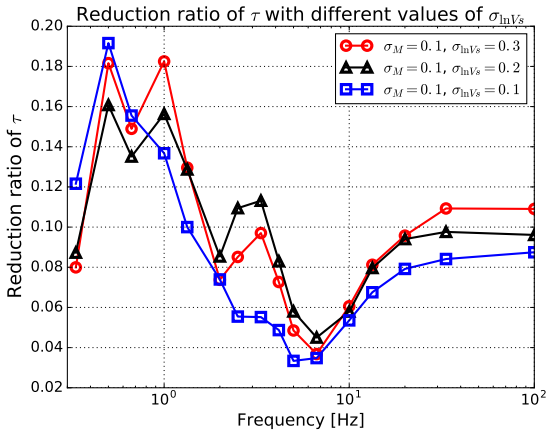

(a) Influence of $\sigma_{\ln Vs}$ on the inter-event uncertainty τ

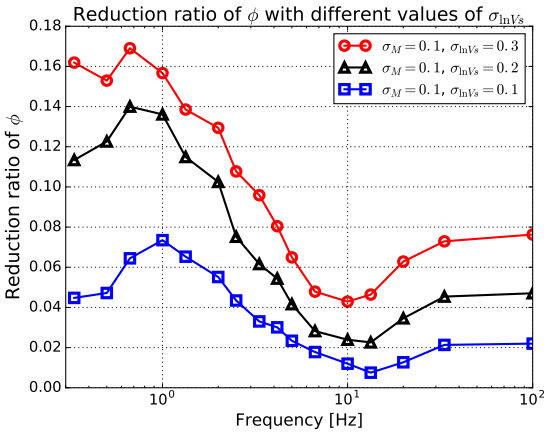

(b) Influence of $\sigma_{\ln Vs}$ on the intra-event uncertainty ϕ

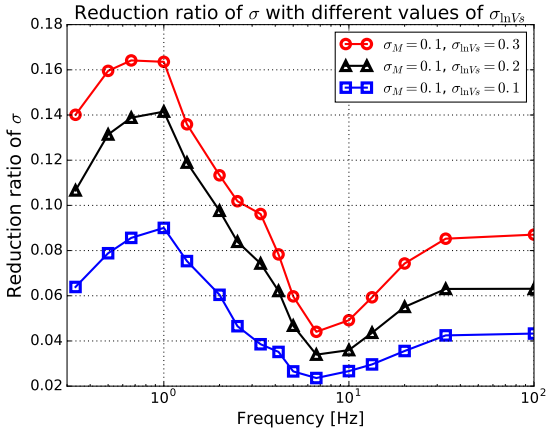

(c) Influence of $\sigma_{\ln Vs}$ on the total uncertainty σ

Figure 11: Influence of different values of $\sigma_{\ln Vs}$ on the reduction ratios of τ, ϕ and σ

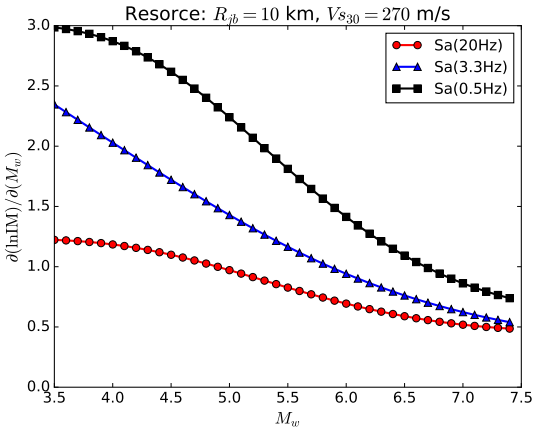

(a) Derivatives of ANN median predictions with respect to M_w

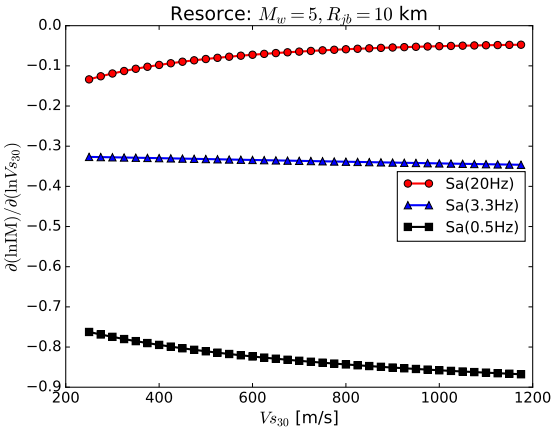

(b) Derivatives of ANN median predictions with respect to $\ln Vs_{30}$

Figure 12: Derivatives of ANN median predictions with respect to M_w and $\ln Vs_{30}$

generalized least squares principle, to account for non-blockwise diagonal variance-covariance matrix in the

ANN regression. The proposed approach is applied to a generated synthetic database, in order to analyze the impact of the input parameter uncertainty and to validate the proposed algorithm. It is, then, applied to the shallow crustal earthquakes data in the RESORCE database. These two applications show an overestimation of the GMPE inter-event and intra-event uncertainties, if the epistemic input parameter uncertainties are not taken into account. The proposed approach relies on a prior estimation of the epistemic uncertainties of the input parameters and the sensitivity analyses show the importance to assess correctly the input uncertainty for the estimation of the GMPE inter-event and intra-event uncertainties. Based on the input uncertainties $\sigma_M = 0.1$, $\sigma_{\ln Vs} = 0.3$, the reduction of the total RESORCE GMPE uncertainty is 4-16%, depending on the frequency of the spectral accelerations, whereas the median predictions are only slightly influenced. The uncertainty reduction is more significant in low frequency ranges than in high frequency ranges.

Data and Resources

The data used in this study are collected from the RESORCE database (http://www.resorce-portal.eu/). The approach developed in this study is developed based on the open-source python neurolab package (https://pythonhosted.org/neurolab/), by implementing the evaluation of the Jacobian matrices and the generalized least squares training.

Acknowledgement

This work is realized thanks to the collaboration between EDF Lab Saclay and the Chair on systems science and energetic challenge of CentraleSupélec, University Paris-Saclay, within a CIFRE contract.

References

Abrahamson, N. A., & Silva, W. J. (2007). *NGA ground motion relations for the geometric mean horizontal component of peak and spectral ground motion parameters*. Technical Report Pacific Earthquake Engineering Research Center.

Abrahamson, N. A., & Youngs, R. R. (1992). A stable algorithm for regression analyses using the random effects model. *Bull. Seismol. Soc. Am.*, *82*, 505–510.

Akaike, H. (1974). A new look at the statistical model identification. *IEEE Trans. Autom. Control.*, *19*, 716–723. doi:10.1109/TAC.1974.1100705.

Akkar, S., Sandkkaya, M. A., & Bommer, J. J. (2014a). Empirical ground-motion models for point- and extended-source crustal earthquake scenarios in Europe and the Middle East. *Bull. Earthquake Eng.*, *12*, 359–387. doi:10.1007/s10518-013-9461-4.

Akkar, S., Sandkkaya, M. A., Senyurt, M., Sisi, A. A., Ay, B. O., Traversa, P., Douglas, J., Cotton, F., Luzi, L., Hernandez, B., & Godey, S. (2014b). Reference database for seismic ground-motion in Europe (RESORCE). *Bull. Earthquake Eng.*, *12*, 311–339. doi:10.1007/s10518-013-9506-8.

Ameur, M., Derras, B., & Zendagui, D. (2018). Ground motion prediction model using adaptive neuro-fuzzy inference systems: An example based on the NGA-West 2 data. *Pure. Appl. Geophys.*, *175*, 1019–1034. doi:10.1007/s00024-017-1743-3.

Baltay, A. S., Hanks, T. C., & Abrahamson, N. A. (2017). Uncertainty, variability, and earthquake physics in ground-motion prediction equations. *Bull. Seismol. Soc. Am.*, *107*, 1754–1772. doi:10.1785/0120160164.

Bindi, D., Massa, M., Luzi, L., Ameri, G., Pacor, F., Puglia, R., & Augliera, P. (2014). Pan-European ground-motion prediction equations for the average horizontal component of PGA, PGV, and 5 %-damped PSA at spectral periods up to 3.0 s using the RESORCE dataset. *Bull. Earthquake Eng.*, *12*, 391–430. doi:10.1007/s10518-013-9461-4.

Bishop, C. M. (1995). *Neural Networks for Pattern Recognition*. Oxford University Press.

Bommer, J. J., & Abrahamson, N. A. (2006). Why do modern probabilistic seismic-hazard analyses often lead to increased hazard estimates? *Bull. Seismol. Soc. Am.*, *96*, 1967–1977. doi:10.1016/0029-5493(80)90203-4.

Bora, S. S., Scherbaum, F., Kuehn, N., & Stafford, P. (2014). Fourier spectral- and duration models for the generation of response spectra adjustable to different source-, propagation-, and site conditions. *Bull. Earthquake Eng.*, *12*, 467–493. doi:10.1007/s10518-013-9482-z.

Dempster, A., Rubin, D., & Tsutakawa, R. (1981). Estimation in covariance components models. *J. Am. Stat. Assoc.*, *76*, 341–353. doi:10.2307/2287835.

Derras, B., Bard, P. Y., & Cotton, F. (2014). Towards fully data driven ground-motion prediction models for Europe. *Bull. Earthquake Eng.*, *12*, 495–516. doi:10.1007/s10518-013-9481-0.

Derras, B., Bard, P. Y., & Cotton, F. (2016). Site-condition proxies, ground motion variability, and data-driven gmpes: Insights from the NGA-West2 and RESORCE data sets. *Earthq. Spectra*, *32*, 2027–2056. doi:10.1193/060215EQS082M.

Derras, B., Bard, P. Y., & Cotton, F. (2017). V_{s30} , slope, H_{800} and f_0: performance of various sitecondition proxies in reducing groundmotion aleatory variability and predicting nonlinear site response. *Earth Planets Space*, *69*, 2027–2056. doi:10.1186/s40623-017-0718-z.

Dhanya, J., & Raghukanth, S. (2017). Ground motion prediction model using artificial neural network. *Pure. Appl. Geophys.*, . doi:10.1007/s00024-017-1751-3.

Douglas, J., Akkar, S., Ameri, G., Bard, P.-Y., Bindi, D., Bommer, J. J., Bora, S. S., Cotton, F., Derras, B., Hermkes, M., Kuehn, N. M., Luzi, L., Massa, M., Pacor, F., Riggelsen, C., Sandkkaya, M. A., Scherbaum, F., Stafford, P. J., & Traversa, P. (2014). Comparisons among the five ground-motion models developed using RESORCE for the prediction of response spectral accelerations due to earthquakes in Europe and the Middle east. *Bull. Earthquake Eng.*, *12*, 341–358. doi:10.1007/s10518-013-9522-8.

Foulser-Piggott, R. (2014). Quantifying the epistemic uncertainty in ground motion models and prediction. *Soil. Dyn. Earthq. Eng.*, *65*, 256–268. doi:10.1016/j.soildyn.2014.06.015.

Gehl, P., Bonilla, L. F., & Douglas, J. (2011). Accounting for site characterization uncertainties when developing ground-motion prediction equations. *Bull. Seismol. Soc. Am.*, *101*, 1101–1108. doi:10.1785/0120100246.

Hermkes, M., Kuehn, N. M., & Riggelsen, C. (2014). Simultaneous quantification of epistemic and aleatory uncertainty in GMPEs using gaussian process regression. *Bull. Earthquake Eng.*, *12*, 449–466. doi:10.1007/s10518-013-9507-7.

Joyner, W. B., & Boore, D. M. (1993). Methods for regression analysis of strong-motion data. *Bull. Seismol. Soc. Am.*, *83*, 469–487.

Koufoudi, E., Ktenidou, O.-J., Cotton, F., Dufour, F., & Grange, S. (2015). Empirical ground-motion models adapted to the intensity measure asa_{40}. *Bull. Earthquake Eng.*, *13*, 3625–3643. doi:10.1007/s10518-015-9797-z.

Kuehn, N. M., & Abrahamson, N. A. (2017). The effect of uncertainty in predictor variables on the estimation of groundmotion prediction equations. *Bull. Seismol. Soc. Am.*, *108*, 358–370. doi:10.1785/0120170166.

Marquardt, D. W. (1963). An algorithm for least-squares estimation of nonlinear parameters. *J. Soc. Indust. Appl. Math.*, *11*, 431–441. doi:10.1137/0111030.

Moss, R. E. S. (2011). Reduced sigma of ground-motion prediction equations through uncertainty propagation. *Bull. Seismol. Soc. Am.*, *101*, 250–257. doi:doi:10.1785/0120090325.

Rhoades, D. A. (1997). Estimation of attenuation relations for strong-motion data allowing for individual earthquake magnitude uncertainties. *Bull. Seismol. Soc. Am.*, *87*, 1674–1678.

Rumelhart, D., Hinton, G., & Williams, R. (1986). *Learning Internal Representations by Error Propagation in Parallel Distributed Processing: Explorations in the Microstructure of Cognition*. The MIT Press.

Schwarz, G. (1978). Estimating the dimension of a model. *Ann. Stat.*, *6*, 461–464.

Stafford, P. J. (2014). Crossed and nested mixed-effects approaches for enhanced model development and removal of the ergodic assumption in empirical ground-motion models. *Bull. Seismol. Soc. Am.*, *104*, 702–719. doi:10.1785/0120130145.

Stambouli, A. B., Zendagui, D., Bard, P.-Y., & Derras, B. (2017). Deriving amplification factors from simple site parameters using generalized regression neural networks: implications for relevant site proxies. *Earth Planets Space*, *69*, 99. doi:10.1186/s40623-017-0686-3.

université PARIS-SACLAY

ÉCOLE DOCTORALE
INTERFACES
Approches Interdisciplinaires : Fondements, Applications et Innovation

Titre : Evaluation du risque sismique par approches neuronales

Mots clés : Etudes Probabilistes de Sûreté, Courbe de fragilité, Séisme, Lois d'atténuation, Réseaux de neurone, Actualisation Bayésienne.

Résumé : L'étude probabiliste de sûreté (EPS) parasismique est l'une des méthodologies les plus utilisées pour évaluer et assurer la performance des infrastructures critiques, telles que les centrales nucléaires, sous excitations sismiques. La thèse discute sur les aspects suivants: (i) Construction de méta-modèles avec les réseaux de neurones pour construire les relations entre les intensités sismiques et les paramètres de demande des structures, afin d'accélérer l'analyse de fragilité. L'incertitude liée à la substitution des modèles des éléments finis par les réseaux de neurones est étudiée. (ii) Proposition d'une méthodologie bayésienne avec réseaux de neurones adaptatifs, afin de prendre en compte les différentes sources d'information, y compris les résultats des simulations numériques, les valeurs de référence fournies dans la littérature et les évaluations post-sismiques, dans le calcul de courbes de fragilité. (iii) Calcul des lois d'atténuation avec les réseaux de neurones. Les incertitudes épistémiques des paramètres d'entrée de lois d'atténuation, tels que la magnitude et la vitesse moyenne des ondes de cisaillement de trente mètres, sont prises en compte dans la méthodologie développée. (iv) Calcul du taux de défaillance annuel en combinant les résultats des analyses de fragilité et de l'aléa sismique. Les courbes de fragilité sont déterminées par le réseau de neurones adaptatif, tandis que les courbes d'aléa sont obtenues à partir des lois d'atténuation construites avec les réseaux de neurones. Les méthodologies proposées sont appliquées à plusieurs cas industriels, tels que le benchmark KARISMA et le modèle SMART.

Title : A framework for seismic risk assessment based on artificial neural networks

Keywords : Probabilistic risk assessment, Fragility curve, Earthquake, Ground motion prediction equations, Neural networks, Bayesian updating.

Abstract : Seismic probabilistic risk assessment (SPRA) is one of the most widely used methodologies to assess and to ensure the performance of critical infrastructures, such as nuclear power plants (NPPs), faced with earthquake events. SPRA adopts a probabilistic approach to estimate the frequency of occurrence of severe consequences of NPPs under seismic conditions. The thesis provides discussions on the following aspects: (i) Construction of meta-models with ANNs to build the relations between seismic IMs and engineering demand parameters of the structures, for the purpose of accelerating the fragility analysis. The uncertainty related to the substitution of FEMs models by ANNs is investigated. (ii) Proposal of a Bayesian-based framework with adaptive ANNs, to take into account different sources of information, including numerical simulation results, reference values provided in the literature and damage data obtained from post-earthquake observations, in the fragility analysis. (iii) Computation of GMPEs with ANNs. The epistemic uncertainties of the GMPE input parameters, such as the magnitude and the averaged thirty-meter shear wave velocity, are taken into account in the developed methodology. (iv) Calculation of the annual failure rate by combining results from the fragility and hazard analyses. The fragility curves are determined by the adaptive ANN, whereas the hazard curves are obtained from the GMPEs calibrated with ANNs. The proposed methodologies are applied to various industrial case studies, such as the KARISMA benchmark and the SMART model.

Université Paris-Saclay
Espace Technologique / Immeuble Discovery
Route de l'Orme aux Merisiers RD 128 / 91190 Saint-Aubin, France